



HAL
open science

Chirality and nonlinear dynamics in polariton microresonators

Nicola Carlon Zambon

► **To cite this version:**

Nicola Carlon Zambon. Chirality and nonlinear dynamics in polariton microresonators. Pattern Formation and Solitons [nlin.PS]. Université Paris-Saclay, 2020. English. NNT : 2020UPASS053 . tel-03035028

HAL Id: tel-03035028

<https://tel.archives-ouvertes.fr/tel-03035028>

Submitted on 2 Dec 2020

HAL is a multi-disciplinary open access archive for the deposit and dissemination of scientific research documents, whether they are published or not. The documents may come from teaching and research institutions in France or abroad, or from public or private research centers.

L'archive ouverte pluridisciplinaire **HAL**, est destinée au dépôt et à la diffusion de documents scientifiques de niveau recherche, publiés ou non, émanant des établissements d'enseignement et de recherche français ou étrangers, des laboratoires publics ou privés.

Chirality and nonlinear dynamics in polariton microresonators

Thèse de doctorat de l'université Paris-Saclay

École doctorale n°572, Ondes et Matière (EDOM)
Spécialité de doctorat: Optique et photonique

Unité de recherche : Université Paris-Saclay, CNRS, Centre de Nanosciences et de
Nanotechnologies, 91120, Palaiseau, France.
Réfèrent : Faculté des sciences

Thèse présentée et soutenue à Palaiseau, le 12/03/2020, par

Nicola CARLON ZAMBON

Composition du Jury

| | |
|---|------------------------|
| Jean-Jacques GREFFET Directeur de recherche, Institut d'Optique Graduate School | Président |
| Natalia BERLOFF Professor, Cambridge University | Rapporteur & Examineur |
| Ivan FAVERO Directeur de recherche, CNRS - Université de Paris | Rapporteur & Examineur |
| Ataç İMAMOĞLU Professor, ETH Zürich | Examineur |
| Alessandro TREDICUCCI Professor, Università di Pisa | Examineur |
| Jacqueline BLOCH Directrice de recherche, Université Paris-Saclay, CNRS | Directrice de thèse |
| Alberto AMO GARCIA Chargé de recherche, Université de Lille, CNRS | Invité |

RÉSUMÉ

Les microcavités en semiconducteurs, définies par une cavité Fabry-Pérot planaire contenant un puits quantique, permettent de confiner fortement à la fois la lumière et les excitations électroniques. Dans ces hétérostructures, la lumière et la matière interagissent si fortement que les excitations fondamentales du système sont décrites par des quasi-particules hybrides lumière-matière appelées polaritons excitoniques. Les polaritons héritent les propriétés de leurs deux constituants élémentaires: la partie photonique peut être structurée spatialement en sculptant à l'échelle micrométrique l'indice de réfraction du matériau par lithographie et gravure; la composante excitonique donne au système une très forte non-linéarité Kerr. Dans cette thèse, nous avons utilisé ces deux propriétés pour réaliser une ingénierie du mode photonique grâce à des micropiliers couplés, et sonder plusieurs facettes de leurs propriétés non-linéaires.

Dans une première partie du travail, nous étudions des microcavités couplées disposées en anneau. Tirant profit d'un couplage spin-orbite synthétique et de la possibilité de polariser en spin le gain optique, nous avons démontré une émission laser dans des modes présentant un moment orbital angulaire (OAM) fini, dont la chiralité peut être contrôlée optiquement. De plus, nous mettons en évidence un comportement bistable original du microlaser, qui implique des modes présentant des valeurs différentes du OAM ainsi que des textures de polarisation différentes.

Dans la deuxième partie de la thèse, nous explorons la dynamique non-linéaire du système sous pompage cohérent. Nous déclenchons une instabilité paramétrique dans des résonateurs couplés, et analysons en détails le mécanisme physique sous-jacent. Dans le régime instable, nous observons l'établissement d'oscillations paramétriques qui donnent lieu à des bandes latérales très brillantes et contrastées dans le spectre d'émission.

Enfin dans la dernière partie du travail, nous étudions un régime de métastabilité optique dans un résonateur fortement non-linéaire. Ce régime se manifeste par l'apparition de sauts aléatoires entre deux valeurs du nombre moyen de photons dans le résonateur. Pour certaines conditions de pompage, nous observons un ralentissement critique de la dynamique métastable, signature d'une transition de phase dissipative. Par des expériences d'hystérésis dynamique, nous évaluons les exposants critiques de cette transition de phase. Finalement, nous proposons une correspondance ("mapping") entre la dynamique métastable d'un résonateur Kerr, et les renversements aléatoires dans le temps d'un bit logique. Nous pouvons alors définir et mesurer la production d'entropie lors d'une trajectoire unique d'une expérience d'hystérésis dynamique. Ces mesures nous ont permis de valider, dans le cadre de cette correspondance, le théorème intégral de fluctuations pour la production d'entropie hors équilibre.

Ce travail couvre une grande variété de sujets, d'aspects les plus fondamentaux de la dynamique non linéaire dans un système photonique, à des idées innovantes pour réaliser des dispositifs photoniques, qui pourraient dans le futur être optimisés pour un fonctionnement à température ambiante.

ACKNOWLEDGEMENTS

During my second year of master, I was looking for the possibility of working on my final project abroad. Essentially out of curiosity and wanderlust, partly because under-financing of research narrowed down opportunities too much in Italy to my eyes. I am fascinated by optics, because, quoting a dear friend, “makes physics visible”: one day, I rather casually found an article describing the possibility to tailor the properties of a light flow to emulate a black-hole event-horizon. Amazing. I reached out to the authors and that’s how all this started. What I found at my arrival in LPN (now C2N) labs is a deeply humane environment, boundary condition for doing research in a serene yet stimulating context. For this, I am especially grateful to Jacqueline and Alberto, who first introduced and welcomed me to the group, but also to the many other people whom I had the pleasure to meet over these past few years in the lab. The ‘bonheur’, the day-to-day discussions in front of the coffee machine or at lunch about science, music and politics but also gin-making and life experiences is probably what enriched me the most, and will always hold dear in my heart.

In the rollercoaster of exciting results and intuitions interleaving delusions and set-backs inherent to the research process, I feel much indebted to Jacqueline, not only for her constant support in difficult moments, but also because as a supervisor she let me the freedom and precious time to explore, to fail, to reason about the origin of the problems. Whenever I had a question, needed feedback or to discuss you have always found a moment for me, regardless of a merciless agenda; I do not think this comes for granted, thank you. Even when our views diverged significantly you, Jacqueline, have granted me the benefit of a doubt and finally the possibility to pursue my ideas to the end; all of this, I believe, has been overly important for my personal and scientific growth. While physics appears to be a complex language with a cumbersome grammar, you have shown me that, deep down, the message is often simple; once understood, it can be conveyed using few words, two lines on paper or the hands. I have ever since admired this elegant intuition of yours.

I want to thank Alberto for the enthusiasm he has always communicated to me when discussing about science but also society and politics, for his advice and support during the first months at LPN, for providing me all the time with critical inputs on my work, even after moving to PhLAM laboratories in Lille. In our discussions, you have always managed to reveal another point of view I was unaware of, allowing me to re-contextualize my thoughts and finally look at a bigger picture. I am truly lucky to have met also two special persons during these years, Said R.K. Rodriguez and Philippe St-Jean. We started working together as colleagues, you are now among my dearest friends. I learned from you a large part of the experimental know-how and the long hours spent discussing together educated my way of thinking; even now that our ways parted, you will somehow always be with me. I must thank Sylvain Ravets, for as he joined the group, he shared his expertise, always up for giving a hand or keen tips; your timely feedbacks and empathy, Sylvain, has been important for me in difficult moments. Precious have been the discussions, laughers, beers and help of Valentin, Marijana and Nicolas with whom I shared my journey as PhD student. I hope you enjoyed the time together as much as I did. I owe some special thanks to Valentin and Philippe who

stoically withstood my snoring in several conferences and showed me that I am not yet ready for off track skiing.

All the experiments presented in this manuscript would have not been possible without Aristide Lemaître, Luc Le Gratiet, Abdelmounaim Harouri and Isabelle Sagnes who have developed and perfected over the years the growth and sample fabrication process. Thank you, Aristide, for answering all my curiosities about the art of epitaxial growth as well as dry-aging duck breast, for the ‘pause cigarette’ and for being an endless source of jokes (thanks god I’m not from Québec). Thank you, Luc and Abdou, for sharing with me always a nice word and for your support during all these years. Thank you, Isabelle, for the sparkling energy you bring in, it has motivated me at several points. Despite the difficulties related to moving of the lab and an often overly-packed agenda, you all have constantly managed to find some time to develop new samples, so necessary to advance in my project; I am deeply grateful to you for this.

I would also like to acknowledge the many, enriching discussions I had with Filippo Vicentini, Carlos Antón Solanas, Niccolò Somaschi, Juan Carlos Loredó, Paul Hilaire, Fabrice Lamberti, Martin Esmann, Ilse Maillette de Buy Wenniger and Mathias Marconi. I have learned a lot discussing with you, like the impressively complicated phase-diagram of honey and or the technique of Pink Floyd-assisted mode-locking of a laser. Thank you, Ilse, for the helpful comments on the introductory chapters of this manuscript. As well, I am grateful to Daniel Kimura, Olivier Krebs, Loïc Lanco and Pascale Senellart, your feedback and answers to my curiosity has fed my thoughts. Finally, I want to thank all the other people I crossed during these years at LPN first and C2N then: all of you contributed somehow to the ‘bonheur’ I have mentioned before and that has been so important to me.

While working at most among the projects presented in this manuscript, I had the chance to collaborate with the groups of Cristiano Ciuti from Université de Paris, Guillaume Malpuech from Institut Pascal and Alexia Auffèves from Institut Néel. The added value and insight they brought to the projects has been determining and profoundly instructive. I am looking forward to continue the exchange of ideas with you in the future. I must further thank Cristiano and especially some members of his group: Filippo, Florent, Cassia, Nicola, Fabrizio and Alberto for welcoming me to their offices whenever the metro line disruption made impossible to reach C2N, for sharing coffee and chocolate and for the nice time spent together while at conferences.

To tell the truth, all this journey would have been twice as hard and half as funny without all the people I bumped into outside the precinct of the lab: Ciccio, Cate, Saggi and the rest of the Erasmus group, Elea, Megan, the Filippo’s angels, all the friends orbiting around the barbecue garden in Le Lilas, the people of la casa del Gusto and the Thello Gang. Thank you for spicing up my time in Paris, if I now look outside the window and smile, it is also because of you. I must acknowledge dry gin for blessing the midsummer night’s dream that brought Silvia, Filippo, Fra and Alberto to me (except the closet part of your plan). Living with you the horizontal life has been a such a dream that when I look back I almost fear to wake up right away on the sofa (don’t laugh)... just without you. Wherever our uncertain futures will bring us, see you there. I certainly now fully appreciate someone else’s saying: as often happens with the most beautiful adventures in life, also this journey started by chance.

I want to dedicate this manuscript to my roots, living on the other side of the Alps: lo dedico ai miei genitori, per la loro sensibilità, per il loro incoraggiamento nell'intraprendere ogni nuova avventura che mi si apriva davanti, libero di esprimermi. Lo dedico alla mia nonna Gigia, che sapeva vedere la bellezza nelle piccole cose, e a Giuliano, il cui ricordo riesce sempre, maledettamente, a strapparmi un sorriso ed una lacrima. Ai miei tanti zii, di sangue e di fatto, per essermi sempre vicini col pensiero. Ai miei amici di sempre, con cui ho condiviso ogni gioia e fragilità e che compongono la mia foto di gruppo, sempre mossa e fuori fuoco, così come a noi piace. A chi mi ha amato.

Davanti a voi, la felicità è un'idea semplice.

| | | |
|----------|---|-----------|
| 1 | Introduction - Understanding and Harnessing Complexity | 1 |
| 2 | Strong light-matter coupling in semiconductor heterostructures | 7 |
| 2.1 | Semiconductor microcavities | 7 |
| 2.1.1 | Distributed Bragg Reflectors | 9 |
| 2.1.2 | Dielectric Fabry-Perot Microcavities | 11 |
| 2.2 | Quantum well excitons | 14 |
| 2.2.1 | Excitons in shallow QWs | 17 |
| 2.2.2 | Optical selection rules | 20 |
| 2.2.3 | Exciton quantization and interactions | 22 |
| 2.3 | Exciton Polaritons | 23 |
| 2.3.1 | Hamiltonian description | 25 |
| 2.3.2 | Quasi-resonant excitation | 29 |
| 2.3.3 | Non-resonant excitation | 30 |
| 2.3.4 | Polariton linewidth | 33 |
| 2.4 | Polariton mode engineering | 36 |
| 2.4.1 | Micropillar cavities | 38 |
| 2.4.2 | Coupling the micropillars | 39 |
| 2.4.3 | Emulation of lattice hamiltonians | 41 |
| 2.4.4 | Master equation | 43 |
| 2.5 | Summary | 46 |
| 2.6 | Appendix A: Finite element simulations | 47 |
| 3 | Experimental and numerical techniques | 51 |
| 3.1 | Sample preparation | 51 |
| 3.1.1 | Design | 52 |
| 3.1.2 | Fabrication | 54 |
| 3.2 | Experimental Setup | 56 |
| 3.2.1 | Real and momentum space imaging | 59 |
| 3.2.2 | Scaling of the microcavity linewidth | 61 |
| 3.3 | Modeling quasi-resonant experiments | 63 |
| 3.3.1 | Mean-field equations | 63 |

| | | |
|----------|--|------------|
| 3.3.2 | Truncated Wigner approximation | 68 |
| 3.3.3 | Matrix representation of the Liouvillian | 71 |
| 4 | Optically controlling the emission chirality of microlasers | 75 |
| 4.1 | Introduction | 76 |
| 4.2 | Ring-type photonic molecules | 80 |
| 4.2.1 | Fine structure of the optical modes | 82 |
| 4.2.2 | A spin polarized gain medium | 85 |
| 4.3 | Demonstration of the OAM control scheme | 88 |
| 4.3.1 | Selection of the OAM lasing manifold | 91 |
| 4.3.2 | Temperature robustness | 93 |
| 4.4 | OAM bistability | 95 |
| 4.4.1 | Dynamical rate equations | 96 |
| 4.5 | Summary and Perspectives | 99 |
| 4.6 | Appendix A: The angular momentum of light | 101 |
| 4.7 | Appendix B: Retrieving the phase maps | 106 |
| 4.8 | Appendix C: Eigenmodes via a group theory approach | 107 |
| 5 | Parametric instabilities in coupled nonlinear microcavities | 111 |
| 5.1 | Introduction | 112 |
| 5.1.1 | Semiclassical coupled mode model | 114 |
| 5.2 | Experiments with coupled micropillar cavities | 117 |
| 5.2.1 | Retrieving the eigenstate fractions | 117 |
| 5.2.2 | Resonant spectroscopy | 119 |
| 5.2.3 | Nonlinear regime | 121 |
| 5.2.4 | Parametric Instability | 123 |
| 5.3 | Summary and Perspectives | 126 |
| 6 | Metastability in a driven Kerr resonator | 127 |
| 6.1 | Introduction | 128 |
| 6.1.1 | An apparent contradiction | 128 |
| 6.1.2 | The relation with dissipative phase transitions | 132 |
| 6.2 | Probing a dissipative phase transition | 134 |
| 6.2.1 | Characterization of the microcavity | 134 |
| 6.2.2 | Dynamical hysteresis experiments | 136 |
| 6.2.3 | Scaling of the tunneling time | 140 |
| 6.3 | A parallel with stochastic thermodynamics | 144 |
| 6.3.1 | The Logical Bit | 145 |
| 6.3.2 | Measuring the entropy production | 148 |
| 6.4 | Summary and Perspectives | 151 |
| 7 | Conclusion and Outlook | 153 |
| | Publications | 157 |
| | Bibliography | 159 |

Introduction - Understanding and Harnessing Complexity

In the fifties, the capability of electronic computing machines to solve problems of unprecedented complexity became clear to the whole scientific community. One of the first numerical studies appeared in the 1955 milestone article by E. Fermi, J. Pasta, S. M. Ulam and M. Tsingou [1]. The authors employed the MANIAC-I computer in Los Alamos labs to study the dynamics of a linear chain of 64 anharmonically coupled oscillators. The simulation highlighted "very little -if any- tendency of equipartition of energy among the degrees of freedom". In his memories, Ulam recalls the awe of Fermi when the first results were plotted and reports his belief that future fundamental theories may involve nonlinear operators. In absence of closed analytical solution, the role of computing machines would have been to lead scientists where complexity overwhelmed intuition.

Over the past sixty years the synergetic development of scientific computing and microelectronics industry boosted the predictive capabilities in all research disciplines. Computers allowed giant steps in the comprehension of nature's complexity and impacted society with its technological and behavioral byproducts. Despite the impressive computational power of modern microprocessor clusters, some problems remain impossible to solve due to the tremendous requirements in terms of storage memory and computational overhead. This finding stimulated a discussion about the definition of the computational complexity of a problem and of possible strategies to overcome present limitations [2].

Narrowing the discussion to the mathematical description of a physical object, the presence of nonlinearities or interactions between its elementary constituents is fundamental for the definition of the degree of complexity of the problem [3]. If not, one can study the properties of an isolated constituent of the object, later invoking the linear superposition principle to infer its global properties. In this sense, we could define a complex system as an object whose properties cannot be understood only in relation with the behaviour of its indivisible constituents. This statement may be reductive when considering objects whose descriptions cannot leave aside the laws of quantum mechanics. In this latter case, even if the physics is entirely encoded in linear opera-

tors, the dimensionality of the state vector on which they act makes the computational overhead of each algebraic operation unbearable. One example is the boson sampling problem, the quantum version of Galton's board experiment [4, 5]. Interacting quantum many-body phases of matter gather both of these aspects of complexity, representing a formidable problem to tackle. Yet, the understanding of collective phenomena arising in these exotic phases of matter might help to solve some fundamental questions concerning, for instance, the locality issue [6, 7] and the unconventional superconductivity mechanism [8].

One possible approach to reduce the computational complexity deriving from the Hilbert space dimensionality curse, would be to develop a (digital) quantum computer where the information units can be in a state superposition (qubit) and the boolean logic is substituted by some set of unitary transformations (gates) [9, 10]. This initial idea, after more than a quarter century of collective effort, culminated this year with the first, exciting demonstration of quantum supremacy using a 53-qubit device [11, 12]. A digital quantum computer can be programmed to simulate any local quantum system [13, 14]. Still, not every problem can be efficiently encoded using the presently available few-qubit gates, as the duration of the algorithm cycle would be pushed beyond the coherence time of the qubit, eventually yielding a faulty result [15, 16]. The development of reliable quantum compilers optimizing the number of gates used to obtain a target result seems of prominent importance [17].

A second approach, especially suited for condensed matter problems, relies on emulating the properties of a system of interest with another system that is easier to control and measure. One example is the implementation of prototypical lattice hamiltonians such as the Bose- and Fermi-Hubbard models [18, 19, 20] or the Heisenberg-Ising models [21, 22, 23] using ultra-cold atoms in optical lattices [24], trapped ions [25] and superconducting circuits [26], just to name a few platforms. The distinctive trait of an analog emulator is the ability to experimentally control each parameter of the system, to perform both global and local measurements of its properties and to prepare it in a controlled initial state [27]. On the one hand, photonic systems, being inherently lossy, offer several opportunities in terms of state-preparation and detection [28, 29]. On the other hand, photon-photon interactions in vacuum are negligible at optical frequencies [30], thus calling for the development of an interacting structured light platform. With interacting structured light, we mean the possibility to engineer spectrally and spatially the optical modes of the system, while some nonlinearity allows for energy exchange among them.

In this direction, harnessing light-matter interactions to engineer matter-mediated photon interactions demonstrated to be a promising avenue. To understand the link between the two interaction mechanisms, one may consider a simple example: two laser beams crossing at the interface of a dielectric nonlinear medium, that is, a medium whose refractive index depends on the local density of the electromagnetic field. Since the presence of each of the beams modifies the refractive index of the medium, according to Snell's law, the propagation direction of each transmitted pulse is affected by the presence of the other, see Fig. 1.1. Depending on the sign of the nonlinear term in the refractive index, this behavior mimics an either attractive or repulsive interaction between the two light beams. Although these nonlinear effects are typically small, a significant enhancement can be obtained by forcing photons to interact multiple times with matter in optical cavities. Furthermore, cavities can be used to engineer the photonic modes by modifying the boundary conditions for the confined electromagnetic

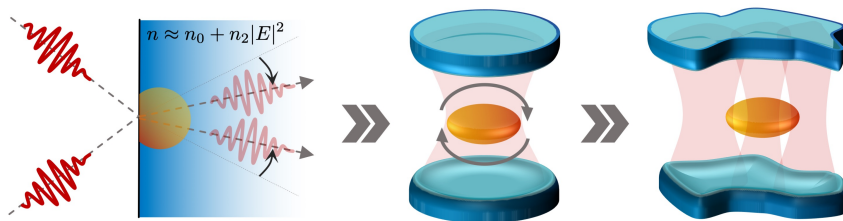


Figure 1.1: Light-matter interactions: towards an interacting structured light platform

field. Overall, the above considerations indicate a possible roadmap towards interacting structured light, as we illustrate in Fig. 1.1.

There are several strategies to implement this roadmap; in this manuscript we will focus on the integrated photonic platform developed in C2N laboratories, relying on the strong light-matter coupling of quantum-well excitons with cavity photons in semiconductor heterostructures. Heterostructures are layered stacks of different materials (here AlGaAs/InGaAs alloys) grown by molecular beam epitaxy. A careful choice of the materials and layer thicknesses allows the fabrication of high finesse planar Fabry-Perot cavities. These cavities embed a quantum-well (QW) hosting bound electron-hole pairs called excitons. Excitons are optically active: by tuning the resonant frequency of the cavity in vicinity of the exciton transition, repeated cycles of emission and re-absorption may happen before a photon is able to escape the heterostructure. If the energy exchange rate between the QW and the cavity exceeds any other loss mechanism, the strong coupling regime is reached and the exciton-photon interaction becomes non-perturbative.

A direct consequence of the strong light-matter coupling regime is that the fundamental excitations of the heterostructure are not anymore the bare QW excitons and cavity photons, but exciton-polaritons, hybrid light-matter quasiparticles inheriting properties from both their constituents [31, 32]. The excitonic component provides effective interactions in the form of a strong Kerr type nonlinearity and a susceptibility to both magnetic and electric fields, while the photonic component results in a light effective mass and allows to probe the system through its emission. Moreover, for moderate excitation powers, polaritons obey bosonic statistics: they can condense and macroscopically occupy a single quantum state [33, 34, 35, 36]. Furthermore, when polaritons are coherently injected in microcavities they collectively behave as an interacting two dimensional quantum fluid [37]. A spectacular variety of hydrodynamic effects has been observed in this configuration ranging from superfluid flow [38, 39] and vortex nucleation [40, 41], to the creation of bright or dark solitons [42, 43].

The hybrid light-matter nature of polariton excitations, provides us with several strategies for implementing local potentials [44, 45, 46]. Controlling the potential landscape allows tailoring the dispersion relation or trapping polaritons, a necessary feature for the analog implementation of lattice hamiltonians [47]. The strategy adopted in our group is to engineer the refractive index landscape by etching to the substrate some pattern on the microcavity. The large refractive index mismatch between vacuum and the semiconductor, tightly confines polaritons within the unetched regions. By carefully designing the etching pattern, one can fabricate synthetic lattices emulating a wide range of 1D and 2D Hamiltonians [48, 49, 50]. Although two-polariton interactions are

still too small to accommodate strongly correlated quantum phases [51, 52, 53], recent experiments demonstrating weak-blockade and the engineering of dipolar interactions are encouraging [54, 55, 56]. The versatility and scalability of this semiconductor-based platform not only makes it an interesting candidate for the emulation of complex systems [47, 57], but also valid platform for the development of novel structured or topological light sources [58, 59, 60].

In this dissertation we study systems composed of a single or few coupled microcavities. Despite the apparent simplicity, these structures present a rich and complex phenomenology. We concentrated our investigation around two main subjects. The first is more related to the possibility of structuring the properties of light in coupled microcavities: we want to engineer optical modes supporting chiral photonic currents. The second, is the emergence of spontaneous dynamical phenomena due to the interplay of nonlinearities and dissipation with a coherent pumping. The contents are organized in five chapters and a concluding section.

The first chapter is a general survey on the physics of semiconductor heterostructures. Initially, we separately describe the properties of photons confined in Fabry-Perot cavities defined by dielectric interferential mirrors and of quantum-well excitons. Then, we show that such heterostructures operate in the strong light-matter coupling regime, thus supporting hybrid polariton excitations and describe their linear and nonlinear properties. We discuss the resonant and non-resonant polariton injection schemes: in both cases, we summarize the diverse phenomenology characterizing the nonlinear regime of the system. Finally, we detail the strategy developed in C2N to engineer the transverse optical modes of the microcavities via a selective etching technique. We show how this allows us to emulate a wide range of lattice hamiltonians.

The second chapter presents the samples design criteria and the fabrication protocol as well as the details of the experimental setup. We present two representative measurements: in the first, we use a non-resonant excitation scheme to image in direct and reciprocal space the energy resolved emission of an array of coupled microcavities. In the second, we perform resonant spectroscopy experiments on single micropillar structures. We use this experiment to probe the polariton linewidth as a function of its energy detuning from the exciton transition. The last section of the chapter describes the theoretical framework and the numerical techniques used for modeling quasi-resonant experiments.

In the third chapter we investigate arrays of coupled microcavities arranged in a ring geometry. As these structures present a discrete rotational symmetry, they support modes whose phase winds an integer multiple of times 2π across the structure. The emission from these modes presents a twisted wavefront, associated to a non-zero orbital angular momentum (OAM) of light. Unfortunately, modes with opposite OAM sign (chirality) come in energy-degenerate doublets due to the mirror symmetry of the structure, globally cancelling the OAM of the emission. Harnessing an analog spin-orbit coupling effect, combined with the possibility of spin-polarizing the optical gain provided by the quantum well, we are able to optically break time-reversal symmetry. As a result, we show that we can trigger lasing in modes carrying a net OAM and to optically control the chirality of the emission. Furthermore, while investigating the saturation regime of the microlasers, we demonstrate a bistable behavior involving two modes with distinct OAM and polarization patterns.

In the fourth chapter we report the observation of a parametric instability in the out-of-equilibrium steady state of two coupled Kerr resonators coherently driven by a laser. The resonators are implemented with two overlapping micropillar cavities hosting polariton excitations. For suitable driving conditions, we steer the system into the unstable regime, where we observe the appearance of intense and well resolved sidebands in the emission spectrum. This feature is a characteristic signature of self-sustained oscillations of the intracavity field. The mechanism responsible for the instability, relates to the opening of a resonant scattering channel from the pump toward two modes as their energy gets renormalized by the nonlinearity.

In the fifth chapter we probe the optical metastability of highly nonlinear single micropillar cavities. We first discuss how the interplay of dissipation and nonlinearities originates the metastability, which manifests in jumps of the cavity occupation between the two -otherwise stable- branches of the classical bistability. For specific driving conditions one observes a critical slowing down of the dynamics, which can be associated with the onset of a dissipative phase transition. Following a theoretical proposal, we use dynamical hysteresis experiments to characterize the exponents of the phase transition. In the second part of the chapter, we propose to map the metastable dynamics of the microresonator with the one of a logical bit subject to random bit-flip events. This allows us drawing a parallel with stochastic thermodynamics, which we leverage to evaluate the entropy production in dynamical hysteresis experiments at a single trajectory level. Finally, we benchmark the validity of the mapping against a general result of stochastic thermodynamics, namely, the integral fluctuation theorem for the entropy production. This work has been done in collaboration with the groups of C. Ciuti (Université de Paris) and A. Auffève (Institut Néel, Grenoble).

In the last chapter we summarize the main results and outline future research directions.

Strong light-matter coupling in semiconductor heterostructures

In this introductory chapter we survey the key aspects of light-matter interactions in AlGaAs/InGaAs based semiconductor heterostructures. The first two sections separately describe the confinement of photons in dielectric Fabry-Perot microcavities and of excitons in shallow InGaAs quantum wells. In both systems, the scaling of the key figures of merit is addressed theoretically. When the resonant frequency of the cavity is tuned in vicinity of an optically active excitonic transition, the strong light-matter coupling regime can be achieved. In this regime, the fundamental excitations of the system can be described as hybrid light-matter quasiparticles, called Exciton-Polaritons.

In the third section we discuss a general criterion to discriminate between the different light-matter interactions regimes and the theoretical framework for the description of polaritons. We review the rich phenomenology characterizing this hybrid platform which we organize according to the two possible excitation schemes (non-resonant and quasi-resonant injection). In the last section, we introduce the strategy developed in our group to engineer the transverse modes of the microcavity. Capitalizing on this ability, we show that we can emulate some lattice hamiltonians using arrays of coupled micropillar cavities. Finally, we introduce the general theoretical framework describing the dynamics of coupled polariton microcavities within an open quantum system perspective.

2.1 Semiconductor microcavities

The simplest realization of an optical cavity consists of two parallel planar mirrors with equal reflectivity \mathcal{R} , facing each other and enclosing a medium of thickness L_c and refractive index n_c . For a monochromatic plane-wave at normal incidence and wavelength λ , the partial reflections formed at each mirror interface constructively interfere if the phase accumulated in a round-trip ($4\pi n_c L_c / \lambda$) amounts to multiples of 2π . Then, a standing wave pattern forms within the cavity and sharp resonances can be observed in the transmission and reflection spectrum when $\lambda = 2n_c L_c / q$ with

$q \in \mathbb{Z}$. The energy difference between two subsequent resonances defines the cavity free spectral range (FSR). At resonance and normal incidence conditions, a simple relation can be derived for the average escape time of a photon from the cavity [61]

$$\tau_c = \frac{L_c n_c}{c} \frac{1 - \mathcal{R}}{\sqrt{\mathcal{R}}} \quad (2.1)$$

here c is the speed of light. The full-width at half maximum of the resonances is therefore $\gamma_c = \tau_c^{-1}$. The ratio of the cavity FSR with the spectral width of the peaks γ_c defines the cavity finesse.

$$\mathcal{F} = \pi \frac{\sqrt{\mathcal{R}}}{1 - \mathcal{R}} \quad (2.2)$$

This number quantifies the average number of roundtrips the photon travels in the cavity before escaping it and is related to the resonator quality factor by $\mathcal{Q} = q\mathcal{F}$. A remarkable consequence of the confinement of the electromagnetic field is that the optical power circulating in the resonator is significantly larger than the input power. At resonance the enhancement factor is $\eta_c = (1 - \mathcal{R})^{-1}$ [61]. Finally, let's consider the more general case of a plane wave incident with a wavevector \mathbf{k} at some angle with respect to the mirror normal axis \hat{z} . The confinement along \hat{z} results in the quantization of the corresponding component of the wavevector inside the cavity $k_z = q\pi/L_c$, still, the in-plane component of \mathbf{k} can take a continuum of values due to the in-plane translational symmetry of the system. For a photon in a homogeneous dielectric medium with refractive index n_c , the photon dispersion relation is $E(\mathbf{k}) = \hbar c|\mathbf{k}|/n_c$. Expanding the modulus of the wavevector in a transverse and in-plane components, we can write the dispersion relation for the cavity modes.

$$\hbar\omega_{q,\mathbf{k}} = \frac{\hbar c}{n_c} \sqrt{\left(\frac{q\pi n_c}{L_c}\right)^2 + |\mathbf{k}_{\parallel}|^2} \approx \hbar\omega_{q,0} + \frac{\hbar^2 |\mathbf{k}_{\parallel}|^2}{2m_c} \quad (2.3)$$

Here \mathbf{k}_{\parallel} is the in-plane component of the wavevector, we defined $m_c = n_c^2 \hbar\omega_{q,0}/c^2$ and the right-most term is an expansion valid for $|\mathbf{k}_{\parallel}| \ll |\mathbf{k}|$. Because of the analogy with the parabolic dispersion relation of a massive particle in free space, the coefficient m_c can be regarded as the cavity-photon effective mass. For the fundamental mode of a cavity filled with a dielectric medium having $n_c = 2$ and operating at optical frequencies $m_c/m_e \sim 10^{-5}$, where m_e denotes the electron rest mass. Hereafter we will implicitly consider only the $q = 1$ transverse cavity mode, and to ease the notation we drop the subscript of the in-plane momentum vector. Given the energy dispersion relation, one can write the Hamiltonian for the electromagnetic field as

$$\mathcal{H}_c = \int \frac{d^2\mathbf{k}}{(2\pi)^2} \hbar\omega_{\mathbf{k}} \hat{a}_{\mathbf{k},\sigma}^\dagger \hat{a}_{\mathbf{k},\sigma} \quad (2.4)$$

The operators $\hat{a}_{\mathbf{k},\sigma}^\dagger$ and $\hat{a}_{\mathbf{k},\sigma}$ respectively create or destroy a photon with in-plane momentum \mathbf{k} , polarization state σ and obey the canonical commutation rules for bosons [37]. We consider for the moment a polarization-independent dispersion relation. This is a fair assumption in the case of metallic mirrors, but is not always verified for dielectric ones, as we will see in the last pages of this section.

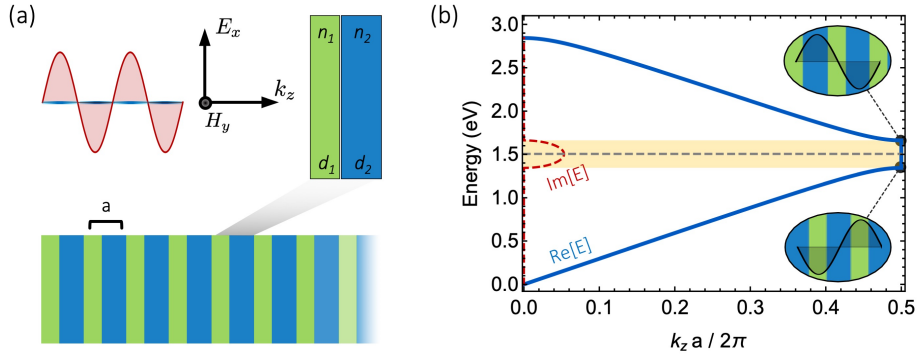


Figure 2.1: **1D Photonic Crystals** (a) A transverse electromagnetic (TEM) wave propagates in a material with a periodic dielectric constant along the z axis. The structure period is a and is composed by alternating layers of thickness $d_{1,2}$ and refractive index $n_{1,2}$. (b) Photonic band structure for quarter wave stacks ($d_1 n_1 = d_2 n_2 = \lambda_0/4$) with $n_1 = 1.0$, $n_2 = 1.5$, and $hc/\lambda_0 = 1.5$ eV. The insets show the electric field profile at the two band edges.

2.1.1 Distributed Bragg Reflectors

We would now desirably implement a cavity combining a large finesse ($\mathcal{F} \sim 10^5$) and a small cavity mode volume ($L_c \mu\text{m}$). For reasons which will become clear in the next pages, these are both key figures of merit for our platform. One dimensional photonic crystals, i.e. materials presenting a periodic dielectric constant along one spatial direction, come forth as an excellent solution combining both requirements. Indeed, by engineering the characteristic function of the dielectric constant, is possible to open photonic band gaps where the material acts as a perfect mirror due to the absence of propagating modes [62, 63]. These layered structures can be grown with a variety of techniques allowing the fabrication of large area dielectric mirrors and Fabry-Perot cavities presenting a few-micron cross section. A simple example of 1D photonic crystal structure is presented in Fig. 2.1-(a). It is a multilayer structure composed of alternating materials with refractive indices $n_{1,2}$ and thicknesses $d_{1,2}$. The length $d_1 + d_2$ defines the lattice constant a , aligned along the z axis. A transverse electromagnetic (TEM) wave is propagating at normal incidence, given its wavevector $k_z = 2\pi/\lambda$, one may wonder what is the group velocity of radiation in the material. Writing the electric (E_x) and magnetic (H_y) field as a function of the forward and backward traveling waves, one can relate their values at left and right of an interface via

$$\begin{pmatrix} E_x(d) \\ H_y(d) \end{pmatrix} = \begin{pmatrix} \cos(k_z d) & \sin(k_z d)/k_z \\ -k_z \sin(k_z d) & \cos(k_z d) \end{pmatrix} \begin{pmatrix} E_x(0) \\ H_y(0) \end{pmatrix}. \quad (2.5)$$

If we denote $\mathcal{M}_{1,2}$ the value of the characteristic matrix in the two different layers, the TEM wave propagation trough one unit cell will be given by $\mathcal{M}_1 \cdot \mathcal{M}_2 = \mathcal{M}_{BZ}$, which is all we need to relate in the first Brillouin zone the energy $E = \hbar c k_z$ of the incident wave to its wavevector in the material. Using the properties of the trace and determinant of \mathcal{M}_{BZ} we can (implicitly) write the dispersion relation as

$$a k_z = \arccos \left[\cos(k_1 d_1) \cos(k_2 d_2) - \frac{1}{2} \left(\frac{k_2}{k_1} + \frac{k_1}{k_2} \right) \sin(k_1 d_1) \sin(k_2 d_2) \right] \quad (2.6)$$

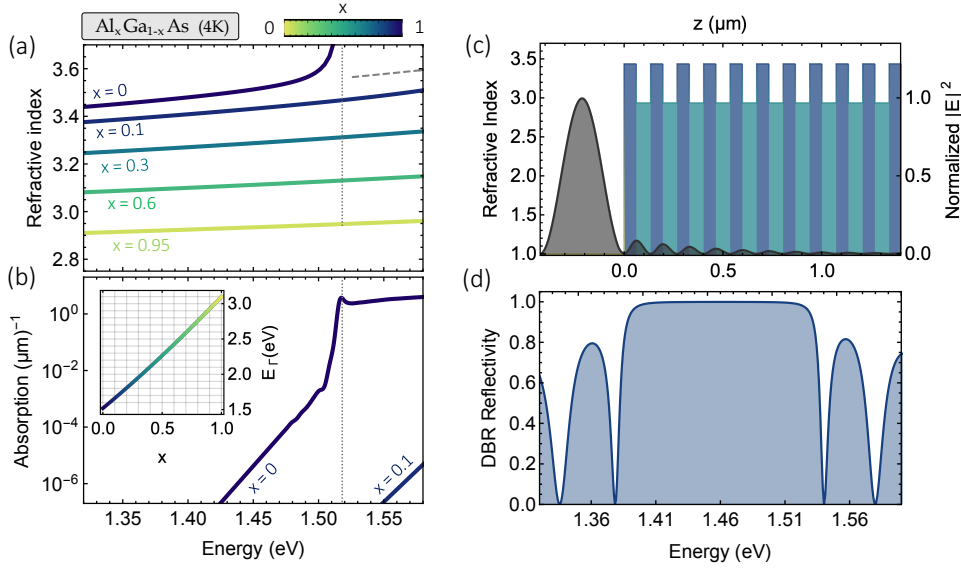


Figure 2.2: **Distributed Bragg reflectors.** (a) Refractive index at 4K as a function of the photon energy and Aluminum concentration x for $\text{Al}_x\text{Ga}_{1-x}\text{As}$ alloys. (b) Corresponding absorption coefficients, the inset shows the Γ point energy gap as a function of Aluminum concentration. (c) Refractive index and mode profile for monochromatic light (1.46 eV) at normal incidence on a DBR with 20.5 $\text{Al}_{0.1}\text{Ga}_{0.9}\text{As}/\text{Al}_{0.95}\text{Ga}_{0.05}\text{As}$ pairs. (d) Reflectivity profile of the DBR.

where $k_{1,2} = k_z/n_{1,2}$. Fig. 2.1-(a) shows an example of photonic bandstructure of a multilayer structure composed by quarter-wave optical thickness stacks ($d_1n_1 = d_2n_2 = \lambda_0/4$) with $n_{1,2} = (1.0, 1.5)$ and $\hbar\omega_0 = hc/\lambda_0 = 1.5$ eV. Interestingly, when approaching the band gap opened around $\hbar\omega_0$, the real part of the wavevector reaches the edge of the Brillouin zone, becoming a standing wave as shown in the insets of Fig. 2.1-(b). Inside the gap, the wavevector acquires an imaginary component, corresponding to an evanescent field in the multilayer film. Since the incident wave cannot propagate in this gap, it is entirely reflected, and the multilayer structure behaves as a perfect mirror. It is possible to demonstrate that the width of the gap $\delta\omega$ is maximal for a quarter-wave stack arrangement and increases as a function of the refractive index contrast between the two layers [63], namely

$$\frac{\delta\omega}{\omega_0} = \frac{4}{\pi} \arcsin\left(\frac{|n_1 - n_2|}{n_1 + n_2}\right). \quad (2.7)$$

At the mid-gap energy the partial waves created at each layer interface destructively interfere since $(n_1d_1 + n_2d_2)k_z = \pi p$ with $p \in \mathbb{Z}$ (Bragg condition). Because of the analogy with the diffraction from crystalline solids, these multilayer structures are often referred as distributed Bragg reflectors (DBRs). In this manuscript, we focus on $\text{Al}_x\text{Ga}_{1-x}\text{As}$ based DBRs which are epitaxially grown in C2N laboratories and are the core element of our semiconductor heterostructure design.

In Fig. 2.2-(a) we show the refractive index of $\text{Al}_x\text{Ga}_{1-x}\text{As}$ alloys as a function of the incident photon energy for different Al concentrations at 4K. The curves are an adaptation of the room-temperature Sellmeier equations in references [64, 65] to best fit the experimental data at cryogenic temperature, obtained for GaAs and AlAs

in [66] and [67], respectively. The absorption coefficient, plotted in Fig. 2.2-(b), was extrapolated from [68] and, for small Al concentrations, we assumed that the absorption spectrum does not change profile, but shifts in energy together with the Γ -point gap of the $\text{Al}_x\text{Ga}_{1-x}\text{As}$ alloy. The vertical dashed line corresponds to the bulk GaAs gap $E_\Gamma = 1.519$ eV.

When considering a finite number of layers, optical absorption, finite angles of incidence and the wavelength dependence of refractive index, it is common to rely on generalized version of the characteristic (or "transfer") matrix (2.5) for the calculation of the optical response of the multilayer structure [69]. In Fig. 2.2-(c) we show the refractive index profile of a DBR reflector formed by 20.5 layer pairs, with $x = (0.10, 0.95)$ and a central wavelength $\lambda_0 = 850$ nm. The black profile shows the (instantaneous) electric field profile for a TEM wave at normal incidence and oscillating at the mid-gap frequency. Fitting the peaks of the electric field we derive the characteristic penetration depth in the mirror $L_{DBR} = 426$ nm, well approximated by the analytical expression $L_{DBR} \sim \lambda_0/4(n_1 - n_2)$ [70, 71]. This quantity is important for the definition of the mode volume in dielectric microcavities. Fig. 2.2-(d) shows the normal incidence reflectivity spectra of the DBR. Remarkably, even with 20.5 pairs (~ 2.7 μm total thickness) the reflectivity at λ_0 reaches $\mathcal{R}_0 \approx 0.9994$.

2.1.2 Dielectric Fabry-Perot Microcavities

If now we perturb the DBR periodic layer structure by inserting midway a defect layer of optical thickness ($d_3 n_3$) $\approx \lambda_0$ it is reasonable to expect, on the basis of the band-structure description of the previous section, that it will support a confined mode evanescently coupled to the mirror edges, that is, a cavity mode. In Fig. 2.3-(a) we show the refractive index profile of a structure formed by two $x = (0.10, 0.95)$ DBRs with 28 and 32 periods, respectively, and separated by a λ_0 optical thickness GaAs spacer. We also include a 2 μm GaAs layer representing the substrate wafer and a quarter-wavelength antireflective coating (right-most greenish layer). The shaded black line shows the intensity profile of the confined optical mode excited by a normal incidence TEM wave.

Fig. 2.3-(b) shows the reflectivity of the microcavity as a function of the incident light energy. The pronounced dip at $E_c = \hbar c \lambda_0 = 1.459$ eV corresponds to the cavity resonance; see Fig. 2.3-(c) for a zoom-in around E_c . The spectral profile of the dip is Lorentian with a linewidth $\gamma_c \sim 0.01$ meV corresponding to a cavity finesse exceeding 10^5 . Importantly, we notice that $\mathcal{R} + \mathcal{T} \neq 1$ at resonance since we included absorption in the transfer matrix calculation. When designing the microcavity structure it is important to recount for absorption as it ultimately limits the maximal achievable finesse and affects the peak transmission. The main absorption channels in such heterostructures are the residual absorption (Urbach) tails near the semiconductor bandgap, roughness-induced scattering at the interfaces and residual doping [68, 72, 73].

The cavity dispersion relation (2.3) holds also for dielectric microcavities, with the only difference being the replacement of the cavity length L_c and refractive index n_c with two effective values [70]. The first modification ($L_c \rightarrow L_{\text{eff}}$) recounts for the electromagnetic field penetration depth inside the DBRs which -unlike the case of metallic mirrors- is sizable, as Fig. 2.3-(a) demonstrates. More specifically, the effective cavity thickness is $L_{\text{eff}} = (2L_{DBR} + L_c) \approx 1.09$ μm , where L_{DBR} corresponds to the decay

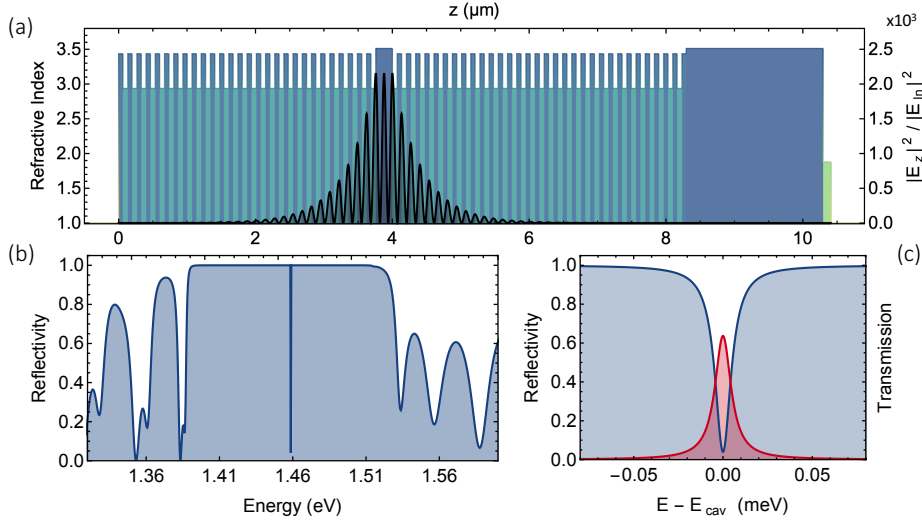


Figure 2.3: **Fabry-Perot microcavity.** (a) Refractive index profile for a λ Fabry-Perot cavity enclosed within two $\text{Al}_{0.1}\text{Ga}_{0.9}\text{As}/\text{Al}_{0.95}\text{Ga}_{0.05}\text{As}$ DBRs with 28 (top) and 32 (bottom) pairs. The spacer and substrate are crystalline GaAs, the right-most greenish layer is a Silicon Oxynitride $\lambda/4$ anti-reflective coating. The cavity mode profile at resonance is traced in black. (b) Reflectivity spectrum of the cavity showing a pronounced dip at $E_0 = 1.459$ eV. (c) Reflectivity and transmission spectrum of the cavity mode.

length of the electric field in the DBRs and $L_c = \lambda_0/n_{\text{GaAs}} \approx 0.24\mu\text{m}$. In our case, L_{eff} is largely determined by L_{DBR} , which is inversely proportional to the refractive index contrast between adjacent layers. The second modification ($n_c \rightarrow n_{\text{eff}}$) takes in account the non homogeneity of the refractive index landscape: n_{eff} can be computed weighting the local refractive index by the normalized mode profile. For the cavity described in Fig. 2.3 one gets $n_{\text{eff}} = 3.36$, consistent with the analytical estimate in [72].

An intriguing feature of dielectric cavities unveils when the DBRs central wavelength differs slightly with respect to the spacer optical thickness. In Fig. 2.4 we consider such a cavity, similar to the one described in Fig. 2.4, except for the reduced number of mirror pairs and where an extra optical thickness δz is added to the cavity spacer. Fig. 2.4-(a) shows the normal incidence transmission spectrum of this cavity for several values of δz ranging between 0 and 100 nm, color-coded from red to blue. As expected, an increase in L_{eff} corresponds to a redshift of the resonance by $\delta\lambda_c \sim \delta z/4$; correspondingly the linewidth γ broadens since the DBR reflectivity is maximal only at the mid-gap wavelength. The scaling of $\delta\lambda_c$ and γ as a function of δz is presented in Fig. 2.4-(b). For each value of δz , we calculate the resonance peak obtained separately for the transverse-electric (TE) and transverse-magnetic (TM) linear polarization components, at different values of the angle of incidence, allowing to retrieve two cavity dispersion relations. The results are shown Fig. 2.4-(c) for $\delta z = (0, 100)$ nm. Interestingly, we observe an energy splitting between the TE and TM dispersion as soon as $\delta z \neq 0$. This energy splitting, hereafter Δ_{so} , is due to the angle and polarization dependence of the penetration depth in the DBRs. In the small in-plane wavevector limit, $\Delta_{\text{so}} \propto k^2$ [71], and for a given k , it increases linearly with δz with a slope of $1.30(2)$ meV μm , as shown in Fig. 2.4-(d). Notice that the slope $\Delta_{\text{so}}/\delta z$ depends on the DBRs design parameters.

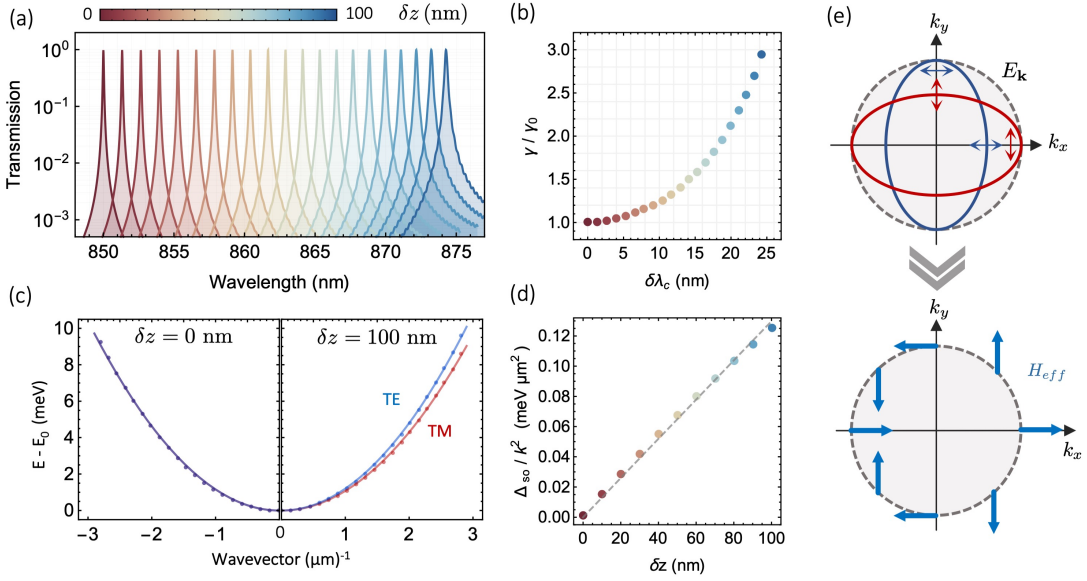


Figure 2.4: **Polarization effects in microcavities.** (a) Transmission spectra for a Fabry-Perot cavity formed by two $x = (0.10, 0.95)$ DBRs with 20 (24) pairs on the top (bottom) mirror. The cavity spacer optical thickness is increased by an amount δz . (b) Scaling of the resonance redshift and cavity linewidth as a function of δz . (c) Calculated cavity dispersion relations at $\delta z = 0$ nm (left panel) and $\delta z = 100$ nm (right panel) for both linear polarizations (TE-TM). (d) Scaling of the polarization-dependent energy splitting Δ_{so}/k^2 with δz . (e) Schematic representation of an isoenergetic cut in momentum space through the dispersion relation for the TE and TM components (relative to the xz plane) of incident light. Corresponding effective magnetic field (H_{eff}) pattern along the elastic circle $E_{\mathbf{k}} = \text{const.}$ [74].

For a plane-wave whose polarization axis is fixed along either the $\text{TE}_{(xz)}$ or $\text{TM}_{(xz)}$ polarizations (i.e. relative to the xz plane) an isoenergetic cut of the dispersion relation describes an ellipse in the in-plane wavevector space. Indeed, as the wavevector direction is rotated from k_x to k_y , the TE polarization state relative to the xz plane becomes the TM one for yz , see Fig. 2.4-(e). We can write the dispersion relation for light with an arbitrary polarization state by decomposing it in the $(\text{TE} - \text{TM})_{xz}$ basis. This corresponds to an additional term to Eq. (2.4), in the form of a coupling between the polarization and in-plane wavevector [75, 74, 37].

$$\mathcal{H}_{so} = \int \frac{d^2\mathbf{k}}{(2\pi)^2} \frac{\Delta_{so}}{|\mathbf{k}|^2} [\sigma_x(k_x^2 - k_y^2) + 2\sigma_y k_x k_y] \hat{a}_{\mathbf{k},\sigma}^\dagger \hat{a}_{\mathbf{k},\sigma'} \quad (2.8)$$

here, $\sigma_{x,y}$ are Pauli matrices and σ, σ' are the polarization states of the photons. Notice that in this pseudo-spin (polarization) basis, \mathcal{H}_{so} has only off-diagonal terms, whereas the cavity dispersion relation of Eq. (2.4) corresponds to diagonal terms. This also means that except when $\Delta_{so} = 0$, the eigenstates of a dielectric cavity are never circularly polarized. Furthermore, inserting the decomposition $\mathbf{k} = (k \cos \phi, k \sin \phi)$ in Eq. (2.8), it can be rewritten as a coupling term between an effective magnetic field $\mathbf{H}_{\text{eff}} = \Delta_{so}(\cos(2\phi), \sin(2\phi))$, schematically represented in Fig. 2.4-(e), and the photon polarization (pseudo-spin) [75]. For this reason Eq. (2.8) is often referred as an effective spin-orbit Hamiltonian. Such parallel has been thoroughly explored in literature,

allowing for instance the observation of optical analogues of the Spin-Hall effect [76, 77, 78] and spin-vortex textures [79]. Other mechanisms leading to synthetic spin-orbit interactions for photons are reviewed in [80]. In Chapter 4 we will capitalize on this analog spin-orbit coupling to engineer the polarization properties of the optical modes in microstructures presenting a discrete rotational symmetry.

2.2 Quantum well excitons

This section will focus on the description of the optical properties of semiconductor heterostructures with a reduced dimensionality. In particular, we will consider few-nanometer layers of $\text{In}_p\text{Ga}_{1-p}\text{As}$ alloys embedded in a GaAs matrix. For reasons which will soon be clear, such layers act as a quantum well (QW) for the electronic excitations, hosting hydrogen-like bound states which are optically active. $\text{In}_p\text{Ga}_{1-p}\text{As}$ QWs inherit several of their properties from the bulk material they are made of. In particular, since both GaAs and InAs are direct bandgap semiconductors, close to high symmetry points of their electronic bandstructure and for the small In concentrations relevant in this manuscript, a study of bulk GaAs is sufficient to infer the properties of $\text{In}_p\text{Ga}_{1-p}\text{As}$. The groundstate properties of bulk GaAs can be calculated within the Born-Oppenheimer approximation, relying on the huge separation between the characteristic timescales of the nuclear and electronic dynamics. With this assumption the total hamiltonian is the sum of three terms $\mathcal{H}_i + \mathcal{H}_{ie} + \mathcal{H}_e$. We will not enter the details of their expression which can be found in many introductory textbooks for solid-state physics (e.g. [81]), but we want to briefly recall their physical origin. The first term takes in account the interaction between nuclei and core electrons which determines the form of the effective ion-ion interaction potential. The groundstate of \mathcal{H}_i determines zinc-blende crystalline structure of bulk GaAs, corresponding to two face centered cubic Bravais lattices for each of the two atomic species translated by one quarter of the cell parameter ($\approx 5.65 \text{ \AA}$). The second term \mathcal{H}_{ie} , describes the interaction between valence electrons, which occupy the outer incomplete shells of the electron cloud and the ions when they are displaced from their equilibrium positions (i.e. electron-phonon interactions), and is responsible for the electronic energy relaxation mechanisms. In III-V semiconductors at cryogenic temperatures this term can be either neglected, or included at a perturbative level. The last term, \mathcal{H}_e describes both the interaction between electrons and ions frozen on their equilibrium positions and electron-electron Coulomb interactions.

The solution of this latter many-body hamiltonian, alone constitutes a formidable task. A standard approach [81] is to use a mean-field approximation where each valence electron is subject to an averaged effective potential coming from the ions and the rest of the electrons. The material-dependent effective potential is usually simulated within the framework of density functional theory [82, 83, 84]. In this way, \mathcal{H}_e becomes a single particle (Kohn-Luttinger) hamiltonian \mathcal{H}_e^{KL} for the electronic wavefunctions [85], which can be diagonalized using a number of approximate methods detailed in [81, 86]. For instance in Fig. 2.5-(a) we show the electronic bandstructure of GaAs obtained with a $\mathbf{k} \cdot \mathbf{p}$ method in [87]. As a reference, the Brillouin zone in reciprocal space for a zinc-blende type lattice is shown in the top-right part of the panel. In vicinity of $\mathbf{k} = 0$ (Γ point), a 1.519 eV energy gap opens between the highest valence band and the lowest conduction band. One conduction and three valence bands approach closely the gap at the Γ -point. Indeed in a zinc-blende crystal, the valence electrons form four bonds

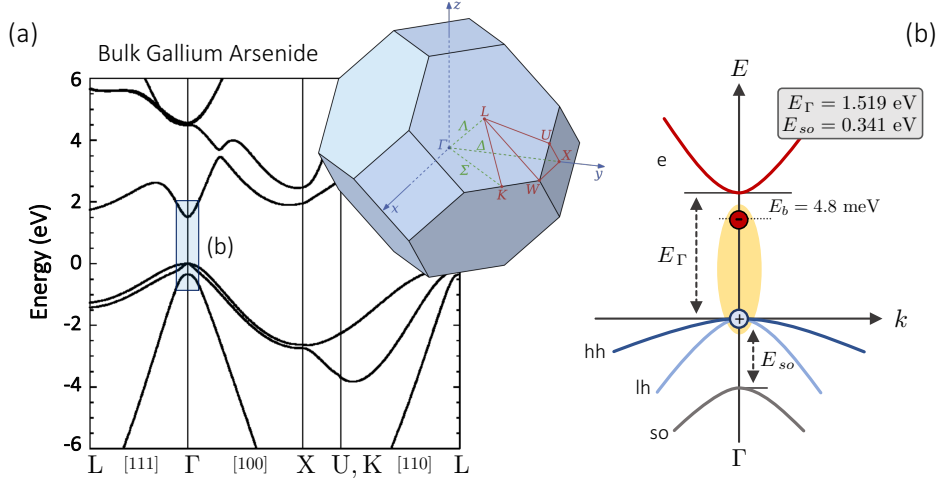


Figure 2.5: **GaAs electronic properties** (a) Bandstructure of bulk GaAs computed with a 30-band $\mathbf{k} \cdot \mathbf{p}$ method, adapted from [87]. Inset: first Brillouin zone of a zinc-blende crystal. (b) Schematic representation of the conduction (e), heavy-hole (hh), light-hole (lh) and split-off (so) bands within a parabolic band approximation.

arranged in a tetrahedral covalent bonding structure. Since the incomplete outer shell is $4s^24p^1$ for Gallium and $4s^24p^3$ for Arsenide, valence electrons have p-type character in their ground state forming sp^3 hybridized covalent bonds, whereas the conduction band originates from s-type orbitals [81]. If we restrict ourselves to these four bands in vicinity of this high-symmetry point in reciprocal space, the bands can be approximated using a second order expansion in small wavevectors [86]. The parabolic dispersion relation for the lowest conduction band reads

$$E_c(\mathbf{k}) = E_\Gamma + \frac{\hbar^2 \mathbf{k}^2}{2m_c^*}. \quad (2.9)$$

Here E_Γ is the bandgap energy and m_c^* is the effective mass for an electron in the conduction band. In a similar fashion, for the three other valence bands

$$E_{v,i}(\mathbf{k}) = -E_i(\mathbf{0}) - \frac{\hbar^2 \mathbf{k}^2}{2m_i^*}. \quad (2.10)$$

Two of the bands, often referred as heavy-hole (hh) and light-hole (lh) bands for $\mathbf{k} = \mathbf{0}$ are degenerate at zero energy but have different effective masses $m_{hh}^* > m_{lh}^*$, the third, or split-off (so) band, lies below the other by $E_{so}(\mathbf{0}) = 0.341$ eV. This parabolic four-band model is schematized in Fig. 2.5-(b). Both the energy separation of the so-band, and the different values of the effective masses, find a physical origin in spin-orbit interaction term of the single electron Kohn-Luttinger Hamiltonian [86]. This interaction indeed depends on the specific angular momentum of the orbitals forming each band. Indeed, the conduction band has s-type Bloch orbitals with orbital angular momentum $\ell = 0$ and electron spin $s_z \pm 1/2$, therefore total angular momentum $|J, J_z\rangle = |1/2, \pm 1/2\rangle$. Having the valence bands a p-type character $|\ell| = 1$ and from the composition rules we get three doubly degenerate bands: hh with $|3/2, \pm 3/2\rangle$, lh with $|3/2, \pm 1/2\rangle$ and so with $|1/2, \pm 1/2\rangle$. A similar reasoning can be applied to bulk InAs.

| | E_Γ (eV) | E_{so} (eV) | m_c^*/m_0 | m_{hh}^*/m_0 | m_{lh}^*/m_0 | m_{so}^*/m_0 |
|------|-----------------|---------------|-------------|----------------|----------------|----------------|
| GaAs | 1.519 | 0.341 | 0.063 | 0.51 | 0.082 | 0.15 |
| InAs | 0.420 | 0.41* | 0.023 | 0.41 | 0.026 | 0.16* |

Table 2.1: **Bulk GaAs and InAs Γ -point parameters:** effective masses are expressed in units of the rest electron mass m_0 . All values are stated for $T < 10$ K, except the ones marked with a star symbol, which were measured at room temperature. Band gaps are taken from [88, 89], the other parameters summarize [84, 90, 91, 92].

The fundamental parameters of this four band model are summarized in Tab. 2.2 for the two materials. Since the Fermi energy of a semiconductor lies within the bandgap, its ground state has insulating character at zero temperature, having the valence bands completely filled. The first excited state of a semiconductor, consists in the promotion of one valence band electron to the conduction band, thus creating a vacancy (hole) in the valence band which can be effectively seen as a positively charged particle [86, 81]. Hereafter we will neglect the split-off band excitations since they have significantly larger energies than the hh and lh, and we are interested only in $E \sim E_\Gamma$ excitations.

When an electron is promoted from the top of valence band to the bottom of the conduction band, it feels a mutual attraction to the hole due to Coulomb interaction. The Hamiltonian for the electron-hole system is

$$\mathcal{H} = E_\Gamma + \frac{p_e^2}{2m_e^*} + \frac{p_h^2}{2m_h^*} - \frac{e^2}{\kappa|r_e - r_h|} \quad (2.11)$$

where $p_{e,h}$ and $r_{e,h}$ are the momentum and position operators of the electron and hole, e is the electric charge quantum and $\kappa/4\pi = \epsilon\epsilon_0$ the static dielectric permittivity of GaAs ($\epsilon = 12.4$), accounting for the screening of Coulomb interaction due to background electrons. Eq. (2.11) can be separated in a free-particle term for the center of mass dynamics and a hydrogen-like problem for the relative motion of the electron-hole pair [86]. The solution of the associated Schrödinger problem is known: the eigenmodes of the system are hydrogen like electron-hole bound states, called excitons. Denoting $M = m_e^* + m_h^*$ the total mass, $\mu = m_e^*m_h^*/M$ the reduced mass of the electron hole pair and $a_B = \hbar^2\kappa^2/\mu e^2 \approx 12$ nm the fundamental exciton Bohr-radius, the dispersion relation for a bulk exciton with principal quantum number n yields

$$E_x(\mathbf{K}) = E_\Gamma + \frac{\hbar^2\mathbf{K}^2}{2M} - \frac{R^*}{n^2} \quad (2.12)$$

where \mathbf{K} is the center of mass wavevector and $R^* = \hbar^2/2\mu a_B^2 \approx 4.8$ meV is the Rydberg constant for the exciton. Notice that $k_B T \ll R^*$ in order to observe these bound states, which are otherwise readily ionized by phonons. Using the angular momentum composition rules for the electron-hole pairs one finds that excitons can have a total angular momentum $J = 0, 1, 2$. Since the semiconductor groundstate has $J = 0$ and photons have a total angular momentum $J = 1$, the only optically active transitions are towards $J = 1$ "bright" excitons, while the other exciton are dark-states. For instance $J = 2$ heavy-holes and $J = 0$ light-holes excitons are dark. Notice that this picture is only exact at the Γ point where \mathcal{H}_e^{KL} commutes with the angular momentum operators J^2 and J_z .

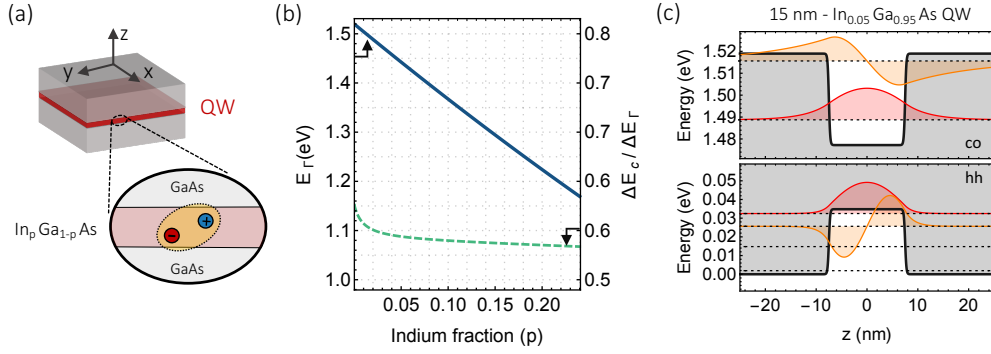


Figure 2.6: **InGaAs Quantum Wells.** (a) Graphic representation of a quantum well for electron and holes, formed by a few nanometer thick layer of a material embedded in a host semiconductor matrix characterized by a larger bandgap. (b) Dependence on the molar Indium fraction (p) of the bandgap (E_Γ , solid line, from [89, 93]) and of the conduction band mismatch (ΔE_c , dashed line, from [94, 95, 96]) for a GaAs/InGaAs heterointerface. (c) Calculated energies (dotted lines) and envelope functions $\chi_{e,h}(z)$ of electrons and heavy-holes (solid lines) along the growth axis z of a $p = 0.05$ heterostructure. Correspondingly, solid gray lines trace the conduction and valence band profile.

2.2.1 Excitons in shallow QWs

We shall now consider a $\text{In}_p\text{Ga}_{1-p}\text{As}$ layer of thickness L embedded in a GaAs matrix and lying parallel to the xy plane, see the sketch in Fig. 2.6-(a). In this layer, the bandgap energy E_Γ is locally lowered with respect to GaAs, because of the presence of InAs in the alloy. The scaling of E_Γ depends on the relative In molar fraction p and is traced as a solid line in Fig 2.6-(b) (adapted from [89, 93]). If we call ΔE_Γ bandgap offset along z , the offset in the valence and conduction band at the Γ point satisfies $\Delta E_\Gamma = \Delta E_v + \Delta E_c$, with relative weights determined by the matching of the Fermi energies at the heterointerface [81]. In Fig 2.6-(b) we plot $\Delta E_c / \Delta E_\Gamma$ as a function of p (dashed green line), interpolating between the results of refs. [94, 95, 96]. An example of the Γ -point conduction and valence band profile along z is shown in Fig 2.6-(c) for a 15 nm thick $\text{In}_{0.05}\text{Ga}_{0.95}\text{As}$ layer (solid black lines).

If we model the conduction and valence band offsets with two smoothed box-like potentials $V_{e,h}$ acting on the electron and hole $z_{e,h}$ position, label E'_Γ the bandgap in the QW and we keep for the rest the notations used for Eq. (2.11), the Hamiltonian of the system has the following form

$$\mathcal{H} = E'_\Gamma + \frac{p_e^2}{2m_c^*} + \frac{p_h^2}{2m_h^*} - \frac{e^2}{\kappa|r_e - r_h|} + V_e(z_e) + V_h(z_h). \quad (2.13)$$

Due to the in-plane translational invariance the center of mass momentum along the QW plane is a good quantum number. Then, Hamiltonian can be separated in four terms $\mathcal{H} = \mathcal{H}_0^x + \mathcal{H}_z^e + \mathcal{H}_z^h + \mathcal{H}_C^x$. The first term $\mathcal{H}_0^x = E'_\Gamma + \hbar^2 \mathbf{K}^2 / 2M$ encodes the in-plane center of mass motion ($M = m_e^* + m_h^*$) and is separable, unfortunately the other three generally are not.

Denoting μ the electron-hole system reduced mass and ρ the relative distance of electron and hole in the QW plane, one can write them as

$$\mathcal{H}_z^{e,h} = \frac{p_z^2}{2m^*} + V_{e,h}(z) \quad (2.14)$$

$$\mathcal{H}_C^x = \frac{p_\rho^2}{2\mu} - \frac{e^2}{\kappa\sqrt{\rho^2 + (z_e - z_h)^2}} \quad (2.15)$$

The first two terms are particle in a box problems, whereas the last term takes into account the relative in-plane motion and Coulomb interaction of electron and holes and is non-separable due to the $(z_e - z_h)$ dependence. This term can be safely neglected if two conditions are met. First, electron and hole have to be tightly confined in the QW layer and second, the quantum well thickness L_{QW} has to be smaller or order of the bulk-exciton Bohr radius [86]. In this case one can solve separately the three Schrödinger equations associated to each hamiltonian. Two of them are particle in a box problems for the electron and hole with eigenmodes $\chi_{e,h}(z)$ and the third is a radial hydrogen equation in two dimensions with solutions $\phi(\rho)$. Therefore the exciton envelope wavefunction has the form $\psi_x = \mathcal{N}^{-1/2} e^{i\mathbf{K}\cdot\mathbf{R}} \chi_h(z)\chi_e(z)\phi(\rho)$ where \mathcal{N} is a normalization constant, \mathbf{K} and \mathbf{R} are the center of mass position and wavevector, respectively. The QW exciton dispersion relation reads

$$E_x(\mathbf{K}) = E'_\Gamma + \Delta E_e + \Delta E_h + \frac{\hbar^2 \mathbf{K}^2}{2M} - \frac{R_{2D}^*}{n^2} \quad (2.16)$$

Except for the offsets $\Delta E_{e,h}$ due to the electron and hole confinement along the QW direction ($\propto L_{QW}^{-2}$), the main difference here is that the Bohr radius for the 2D Hydrogen problem is two times smaller than the bulk one, correspondingly, the exciton binding energy R_{2D}^* is four times larger. Also, because ΔE_h is inversely proportional to the effective mass of the particle, light- and heavy-holes split in energy even at $\mathbf{K} = 0$. Since we are interested only in the fundamental excitation of the system, we will hereafter focus only on heavy-hole excitons.

More generally, if the thin QW hypothesis is dropped then ψ_x becomes non separable in $(z_e - z_h)$ and ρ . Assuming that the electrons and holes are still tightly confined in the quantum well, i.e. $E_{e,h} \ll \Delta E_{c,v}$, one can still write $\chi_h(z) = \chi_e(z) \sim \cos(\pi z_{e,h}/L)$ but ϕ now depends both on $z_{e,h}$ and ρ . Using a variational ansatz, one can still find the QW exciton Bohr radius and binding energy, see for instance ref. [97]. On the other hand, if both $L_{QW} \sim a_B$ and the electron and hole potential wells are shallow, the envelope functions $\chi_{e,h}(z)$ present important evanescent tails and a rather lengthy analytic expression, significantly complicating the calculation.

An alternative approach (except when $L_{QW}/a_B \gg 1$) relies on the definition of an effective pseudo-potential for the relative in plane motion of electron and holes [98]. First, one needs to solve the particle in a box problem for the electron and hole in absence of the Coulomb term and get their approximate envelope wavefunctions $\chi_{e,h}(z_{e,h})$, see Fig. 2.6-(c). Then we calculate the pseudo-potential as

$$V_{\text{eff}}(\rho) = -\frac{e^2}{\kappa} \int dz_e dz_h \frac{|\chi_e(z_e)|^2 |\chi_h(z_h)|^2}{\sqrt{\rho^2 + (z_e - z_h)^2}} \quad (2.17)$$

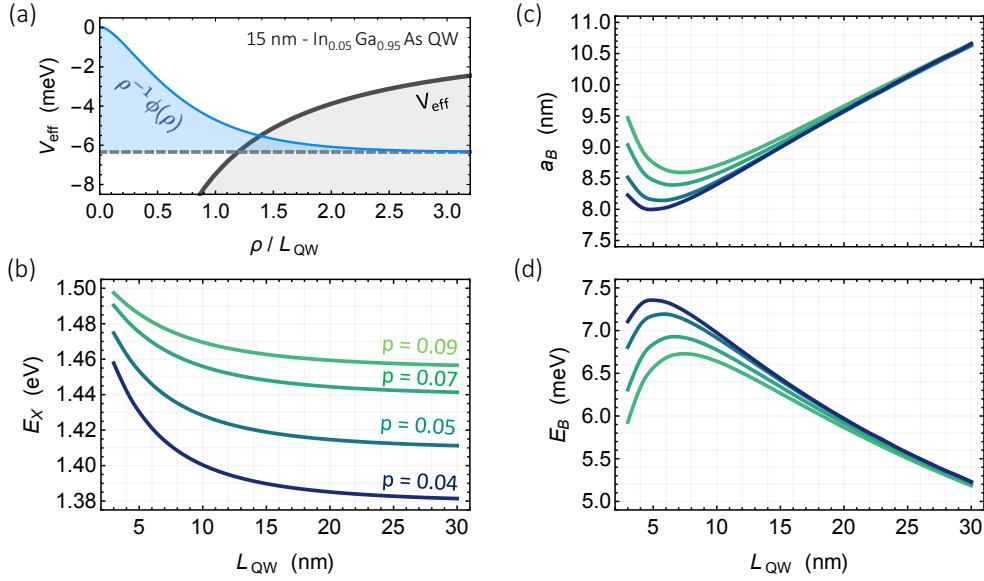


Figure 2.7: **Shallow InGaAs QW properties.** (a) The pseudo potential defined by Eq. (2.17) -in gray- is plotted together with the associated lowest energy radial eigenfunction $\phi(\rho)$ (light-blue profile). Inset: QW parameters. (b,c,d) Show the calculated fundamental hh-exciton energy (b), Bohr radius (c) and binding energy (d) as a function of the QW thickness for four representative values of the In fraction, ranging from 0.04 to 0.09 and color-coded from blue to green. All the results correspond to the ten self-consistent iteration of the pseudo-potential algorithm.

In this way we marginalize $z_{e,h}$ and the Hamiltonian \mathcal{H}_C^x becomes again a radial problem. \mathcal{H}_C^x lowest eigenvalue defines the exciton binding energy E_B and the corresponding radial eigenmode ϕ_ρ can be used to deduce the in-plane Bohr radius as $a_B \approx \int d\rho \phi(\rho) / \int d\rho \phi(\rho) / \rho$. If necessary, the procedure can be iterated self-consistently, by deepening $V_{e,h}(z)$ by half E_B , to simulate the effect of the binding energy on the penetration depth of $\chi_{e,h}$ in the GaAs matrix.

In Figure 2.7 we summarize the result of a systematic numerical study on shallow InGaAs quantum wells (i.e. small Indium content). Panel (a) presents the pseudo-potential $V_{\text{eff}}(\rho)$ calculated for a 15nm $\text{In}_{0.05}\text{Ga}_{0.95}\text{As}$ QW associated to the electron and hole envelope wavefunctions shown in Fig. 2.6-(c). The fundamental eigenvalue associated to the radial problem is traced with a dashed line and the corresponding eigenmode profile has been shaded in light-blue colors. In Fig. 2.7-(b) we trace the calculated $\mathbf{K} = 0$ energy for the heavy-hole exciton (including the binding term) as a function of the well thickness and for different values of the Indium molar fraction ($0.04 < p < 0.09$). Finally, in Fig. 2.6-(c,d) we show, for the same parameters, the Bohr radius and heavy-hole exciton binding energy. For large values of the quantum well thickness they both tend to the bulk values $a_B \approx 12$ nm and $E_B \approx 4.8$ meV, below $L_{\text{QW}} \sim 6$ nm instead there is a strong deviation with respect to the quasi-2D exciton analytical predictions. This is due to the fact that in shallow QWs the electron and hole confinement energies $\Delta E_{e,h}$ become of the same order of the band offsets $\Delta E_{c,v}$. In this situation, long evanescent tails develop in the GaAs matrix, which tend to delocalize the electron and holes, thus increasing the effective exciton Bohr radius and consequently decreasing the binding energy [93, 98].

Later on in this manuscript we will work with semiconductor microcavities embedding a quantum well. Two types of quantum wells have been used: 17 nm thick $\text{In}_{0.04}\text{Ga}_{0.96}\text{As}$ and 15 nm thick $\text{In}_{0.05}\text{Ga}_{0.95}\text{As}$. From Fig. 2.7 we see that for both QWs a representative value of the Bohr radius is 9 nm. The estimation of the exciton Bohr radius is particularly interesting, as it both allows to estimate the exciton oscillator strength and to get an order of magnitude of resonant exciton-exciton interactions. The first is fundamental to quantify the coupling of exciton to electromagnetic radiation [70, 99]. The latter is responsible for the large Kerr-type nonlinearity of cavity polaritons [37, 100].

2.2.2 Optical selection rules

As previously anticipated, some exciton states are bright in the sense that angular momentum selection rules allow them to be both optically excited and to spontaneously emit a photon during electron-hole recombination. These optical transitions must respect an additional set of rules and have a magnitude depending on the exciton microscopic details. This section summarizes the main results, whose derivation can be found in [70, 81, 86, 101]. The description of light-matter interactions relies on the substitution of a minimal coupling ansatz $\mathbf{p} \rightarrow (\mathbf{p} + e\mathbf{A}/c)$ in the exciton hamiltonian, where \mathbf{p} is the electron momentum, e its electric charge and \mathbf{A} the electromagnetic vector potential. This yields an additional light-matter interaction term

$$\mathcal{H}_I = -e \frac{\mathbf{p} \cdot \mathbf{A}}{m} + \frac{e^2 |\mathbf{A}|^2}{2m} \approx -e \frac{\mathbf{p} \cdot \mathbf{A}}{m} \quad (2.18)$$

where m is the electron mass and in the last passage we dropped the quadratic term in the vector potential, which is negligible for weak fields and as long as the wavelength of incident light is much larger than the Bohr radius. Within this dipolar approximation the optical selection rules are the following [81]:

- 1 - In-plane linear momentum must be conserved in the emission or absorption process due to the in-plane translational symmetry of the problem. An exciton with in-plane wavevector K can couple only with a photon with the same in-plane momentum k_γ . Equating the photon energy to the exciton dispersion relation with $K = k_\gamma$ (i.e. neglecting the radiative linewidth), tells us that exciton states with $K \gtrsim 30 \mu\text{m}^{-1}$ are non radiative.
- 2 - Angular momentum must be conserved, which is true only for "bright" $J = 1$ excitons, at least in vicinity of the Γ point.
- 3 - Due to the parity of the confined wavefunctions in electron and hole sub-band with principal quantum number n_e and n_h , the only allowed transition are those satisfying $(n_e + n_h)/2 \in \mathbb{N}$.

To quantify the strength of the exciton interaction with the electromagnetic field we need to compute the probability per unit of time of having the photon absorbed in the QW or reciprocally emitted in the exciton recombination. The calculation of this scattering amplitude can be done using the Fermi golden rule [70, 86]. After the calculation, one can associate this rate to an oscillator strength per unit area

$$\frac{f_{\text{osc}}}{S} = \frac{2}{mE} |\langle u_v | \epsilon \cdot \mathbf{p} | u_c \rangle|^2 |\phi(0)|^2 \left| \int dz \chi_e(z) \chi_h(z) \right|^2 \quad (2.19)$$

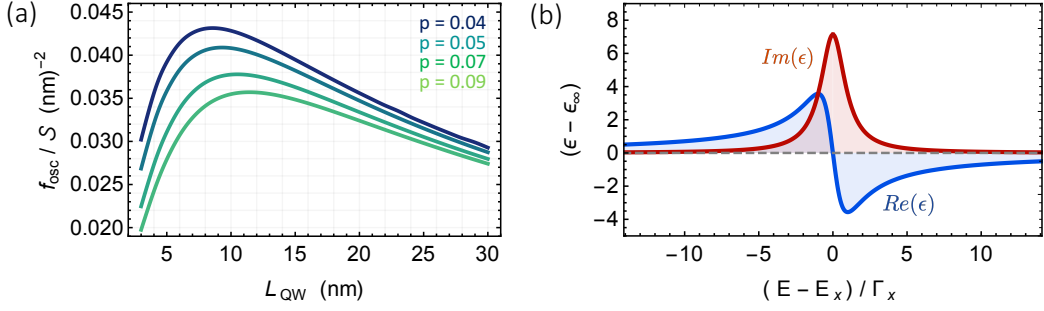


Figure 2.8: **QW optical response** (a) Oscillator strength per unit area of a shallow $\text{In}_p\text{Ga}_{1-p}\text{As}$ QW as a function of the well thickness. (b) Excitonic contribution to the static dielectric function of a 15 nm QW with a 5% In fraction. Here, E_x and Γ_x are the exciton energy and homogeneous linewidth, respectively.

where E is the transition energy, $u_{c,v}$ are the valence and conduction Bloch bands corresponding to the transition, ϵ is the polarization vector associated to the vector potential, \mathbf{p} the electron momentum, ϕ is the eigenmode solution of the exciton radial problem and $\chi_{e,h}$ are the envelope wavefunctions for the electron and hole along z . The Kane matrix element $|\langle u_v | \epsilon \cdot \mathbf{p} | u_c \rangle|$ is the only difficult one to calculate and is related to the specific electron-hole transition [86, 93]. Since radiative modes are limited in close vicinity of the Γ point an approximate value for this scattering term can be calculated and gives $2|\langle u_v | \epsilon \cdot \mathbf{p} | u_c \rangle|^2/m \approx 25.7$ eV [99]. All the other overlap terms are easy to calculate using the numeric pseudo-potential technique detailed in the previous section. It is interesting to point out that since the exciton fundamental state presents a radial probability distribution which is roughly exponential [see Fig. 2.7-(a)], it means that $|\phi(0)|$ is inversely proportional to the exciton Bohr radius. Therefore, the oscillator strength scales with a_B^{-2} and is larger for heavy-hole than for light-hole excitons. In Fig. 2.8-(a) we plot the oscillator strength calculated with the pseudo-potential method for the same quantum well width and Indium fraction parameters of Fig. 2.7. A typical value for our experiments is thus $f_{\text{osc}}/S \approx 0.037$ nm^{-2} . The oscillator strength is also related to the emission/absorption probability per unit of time, or radiative exciton lifetime $\tau_x = 2\hbar/\Gamma_x$. Denoting α the fine-structure constant of the electromagnetic field, and m_0 the electron rest-mass, the homogeneous exciton linewidth reads [70]

$$\Gamma_x = 2\alpha \frac{(\hbar c)^2}{(m_0 c^2)} \frac{f_{\text{osc}}}{S} \quad (2.20)$$

For the QW parameters relevant to our experiments we get $\Gamma_x \approx 0.04$ meV ($\tau_x \approx 20$ ps). Together with the oscillator strength, Γ_x allows to build a simple Lorentz-Drude linear dispersion model describing the optical response of a semiconductor QW at the level of its dielectric polarizability [70, 93]. This can be done by inserting an energy dependent contribution to the static dielectric constant of the QW material ϵ_∞ with the form

$$\epsilon(E) = \epsilon_\infty + \frac{f_{\text{osc}}}{SL_{\text{QW}}} \frac{e^2 \hbar^2}{m_0 \epsilon_0 E_x} \frac{1}{(E_x - E) - i\Gamma_x} \quad (2.21)$$

notice that we are assuming $E_x \gg \Gamma_x$ and $|E_x - E| \ll (E + E_x)$. As an example we plot the real and imaginary part of $(\epsilon - \epsilon_\infty)$ in Fig. 2.8-(b). Inhomogeneous broadening of the exciton transition, described by a probability density function $\mathcal{P}(E'_x)$ can be taken as well into account defining $\epsilon_{\text{inh}}(E) = \int dE'_x \epsilon(E - E'_x) \mathcal{P}(E'_x)$.

2.2.3 Exciton quantization and interactions

For small exciton densities, each fermionic electron-hole state is weakly occupied: it is possible to use a bosonization procedure to show that excitons behave at the leading order as composite bosons described by ladder operators ($\hat{b}_{\mathbf{k}}, \hat{b}_{\mathbf{k}}^\dagger$) whose commutator satisfies $\langle [\hat{b}, \hat{b}^\dagger] \rangle \approx 1$ [102, 103, 101]. Since the number of available states in the QW scales roughly as the in plane spatial extent of the electron and hole wavefunction, this approximation is reasonable if $n_0 a_B^2 \ll 1$ [101, 104], that is, when the exciton density n_0 is such that the average spacing between excitons is much larger than their Bohr radius. Considering a typical Bohr radius of 9 nm for the QW parameters relevant to this manuscript, one gets $n_0 \ll 1.2 \cdot 10^{12} \text{ cm}^{-2}$. At higher densities the fermionic nature of the elementary constituents of the exciton starts to play a role: phase-space filling and the screening of the electron-hole Coulomb interaction, gradually leads to the dissociation of excitons into a electron-hole plasma [105, 106].

When the exciton density is significantly below the critical value n_0 , a bosonization procedure allows to write also the many-body states in the excitonic basis [107, 34, 105, 103]. The many-body electron-hole wavefunction is used only to evaluate the scattering amplitudes of each interaction channels. The microscopic description of the different processes is rather complex, we refer to [107, 34, 105, 100, 108, 109] for the details. For the purposes of this manuscript, what is important is that for $n_0 a_B^2 \ll 1$ and relative wavevectors q such that $q a_B \ll 1$ (e.g. for radiative exciton states), the dominant interaction channel is direct (Pauli) exchange [107]. The exciton hamiltonian can thus be written as the sum of two terms. The first, corresponds to the free exciton part

$$\mathcal{H}_x = \int \frac{d^2 \mathbf{k}}{(2\pi)^2} E_x(\mathbf{k}) \hat{b}_{\mathbf{k},\sigma}^\dagger \hat{b}_{\mathbf{k},\sigma} \quad (2.22)$$

where $E_x(\mathbf{k})$ is the parabolic in-plane dispersion of the exciton. The second, includes resonant exchange interactions, and can be written in the form of a two-body contact interaction [37, 34]

$$\begin{aligned} \mathcal{H}_{xx} &= \frac{1}{2} \int \frac{d^2 \mathbf{q}}{(2\pi)^2} \int \frac{d^2 \mathbf{k} d^2 \mathbf{k}'}{(2\pi)^4} U_{\sigma,\sigma'}^q \hat{b}_{\mathbf{k}-\mathbf{q},\sigma}^\dagger \hat{b}_{\mathbf{k}'+\mathbf{q},\sigma'}^\dagger \hat{b}_{\mathbf{k}',\sigma'} \hat{b}_{\mathbf{k},\sigma} \\ &= \frac{1}{2} \int d^2 \mathbf{r} U_{\sigma,\sigma'}^0 \hat{b}_{\mathbf{r},\sigma}^\dagger \hat{b}_{\mathbf{r},\sigma'}^\dagger \hat{b}_{\mathbf{r},\sigma'} \hat{b}_{\mathbf{r},\sigma} \end{aligned} \quad (2.23)$$

The latter expression follows by approximating $U_{\sigma,\sigma'}^{\mathbf{q}}$ with $U_{\sigma,\sigma'}^0$ for $q a_B \ll 1$ and defining $\hat{b}_{\mathbf{r},\sigma}$ as the Fourier conjugate of $\hat{b}_{\mathbf{k},\sigma}$ [37, 107]. The rotational invariance of a contact potential ensures that the scattering is spin-preserving. In particular the triplet channel (parallel spins) has the largest magnitude and is repulsive, whereas the singlet channel (opposite spins), is attractive [109]. The triplet channel interaction strength per unit surface was estimated at the leading perturbative order in [107, 34] yielding $U = 6e^2 a_B / \epsilon$ or $\sim 6 \mu\text{eV} \mu\text{m}^{-2}$ for the QW parameters relevant to the manuscript. This estimate implicitly assumes a 2D exciton wavefunction, which may be inaccurate to describe the wide QWs investigated in this manuscript where $L_{QW} \sim 2a_B$. Repeating the calculation in the limiting case of 3D exciton, E. Estrecho and collaborators found the an approximate upper bound $U_{3D} \sim 7U_{2D}$ [110].

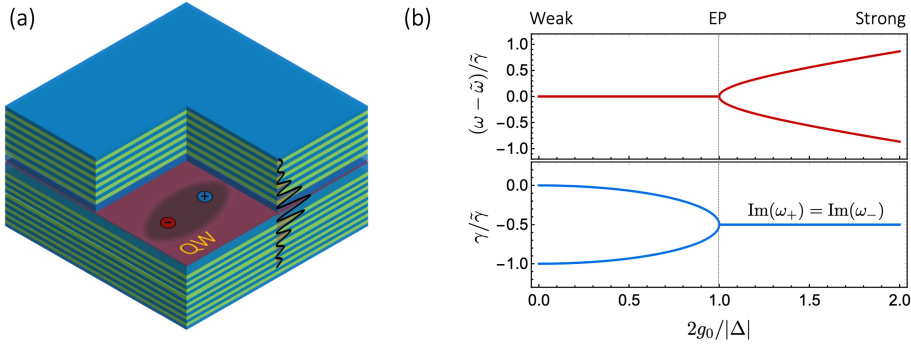


Figure 2.9: **Light-matter coupling in semiconductor microcavities** (a) Schematic representation of a semiconductor microcavity embedding a QW at the antinode of the optical field. (b) Real and imaginary part of the eigenvalues of the coupled oscillator model as a function of the coupling strength g_0 . The oscillator parameters are $\omega_1/\omega_2 = 1$, $\gamma_1/\omega_1 = 10^{-3}$ and $\gamma_2 = 0$. Here $\tilde{\omega}$ is the average complex frequency of the bare resonator modes and $\tilde{\Delta}$ is their complex detuning.

2.3 Exciton Polaritons

In the two previous sections we separately presented the properties of semiconductor Fabry-Perot cavities and quantum wells. We explained that QW excitons are coupled to the electromagnetic field, provided some optical selection rules are verified. In particular, the in-plane wavevector and spin angular momentum must be conserved for radiative recombination processes. Since the two semiconductor heterostructures are intrinsically compatible we can now imagine embedding a QW in vicinity of an antinode of the microcavity field, see Fig. 2.9-(a). For an ideal cavity with no linear polarization splitting (cf. Sec. 2.1.2), only two degenerate circularly polarized modes exist for a given in-plane wavevector. Each radiative channel of an exciton couples to a single optical mode $\hat{a}_{\mathbf{k},\sigma} \rightleftharpoons \hat{b}_{\mathbf{k},\sigma}$. This allows us, without loss of generality, to temporarily consider just one these modes, for instance $\mathbf{k} = 0$ and $\sigma = +1$. Once a photon is emitted in the cavity mode there are only two possibilities. First, it can escape the cavity at a rate γ_c proportional to the cavity linewidth. Second, it can be converted back to a QW exciton at a rate g_0 proportional to the exciton oscillator strength [111, 112].

The physical consequences of light-matter coupling between QW excitons and cavity photons depends drastically on the ratio of the recombination rate g_0 with respect to all the other decay channels. To have an insight on the possible scenarios we can rely on a simple semiclassical model describing exciton and photons as coupled Lorentz oscillators, leaving the quantum description for the next pages [70, 71]. A semiclassical description is indeed valid in the limit of low exciton densities as both the cavity and exciton hamiltonian are harmonic and the (dipolar) coupling between the two is bilinear in the fields. We denote $\omega_{1,2}$ the resonant frequency, and $\gamma_{1,2}$ the damping rate of the two coupled Lorentz oscillators. The linear response of the system at a frequency $\omega \gg \gamma_{1,2}$ is governed by the solutions of a secular equation $|\mathcal{H} - \omega I| = 0$ [111, 113], the determinant yields

$$(\omega_1 - i\gamma_1 - \omega)(\omega_2 - i\gamma_2 - \omega) = g_0^2 \quad (2.24)$$

where g_0 is the relative coupling strength. Notice that if resonator 1 (2) describes the photon (exciton) field amplitude, γ_1 is simply the cavity decay rate; γ_2 instead, is a phenomenological term corresponding to all non-radiative decay channels of the exciton, since the radiative recombination rate is already included in the coupling term g_0 [111]. The solutions of Eq. (2.24) can be expressed in terms of the average complex frequency $2\tilde{\omega} = (\omega_1 + \omega_2) - i(\gamma_1 + \gamma_2)$ and detuning $\tilde{\Delta} = (\omega_1 - \omega_2) - i(\gamma_1 - \gamma_2)$ as

$$\omega_{\pm} = \tilde{\omega} \pm \frac{1}{2} \sqrt{4g_0^2 + \tilde{\Delta}^2} \quad (2.25)$$

In Fig. 2.9-(b) we show the real and imaginary part of the solutions ω_{\pm} as a function of the coupling strength g_0 for two resonant oscillators $\omega_1 = \omega_2$ characterized by the loss rates $\gamma_1/\omega_1 = 10^{-3}$ and $\gamma_2 = 0$. Interestingly, since the square root in Eq. (2.25) is imaginary for $g_0^2 < (\gamma_1 - \gamma_2)^2/4$, the two bare oscillator resonances are not changed by the coupling term. The progressive increase with g_0 of the decay rate $\text{Im}(\omega_-)$ of the matter-like resonance can be seen as the classical analogue of the Purcell effect [112, 114, 115]. This scenario, characterized by a perturbative effect of the coupling to the dynamics of each oscillator, is often called weak coupling regime.

Otherwise, if $g_0^2 > (\gamma_1 - \gamma_2)^2/4$, the decay rates of the normal modes of the system coalesce $\text{Im}(\omega_{\pm}) = (\gamma_1 + \gamma_2)/2$ while their frequencies split-up. In other words the energy exchange between resonators is so efficient that both mode experience the same average loss even if $\gamma_1 \neq \gamma_2$. At the same time, coherent energy exchange (Rabi oscillations) between the two renormalizes the bare resonator frequencies, the normal modes of the system now corresponding to collective in-phase and out-of-phase linear superpositions of the bare resonator eigenmodes [111]. In this strong-coupling regime, the new hybrid eigenstates of the system, often called polaritons, inherit properties both from the cavity and the exciton field [31].

It is worth mentioning that for $g_0^2 = (\gamma_1 - \gamma_2)^2/4$ the eigenvalues ω_{\pm} are degenerate. The non hermitian matrix associated to the secular equation (2.24) can no longer be diagonalized since the ω_{\pm} manifold parametrized by $\tilde{\Delta}$ is non analytic [113]. Such singularities in the complex detuning parameter space are called exceptional points [EP in Fig. 2.9-(b)] and are gathering renewed interest for instance in the context of \mathcal{PT} symmetric photonic systems in photonics (i.e. when $\gamma_1 = -\gamma_2$), anomalous dispersion engineering in metamaterials, or in the design of non-reciprocal devices, see for an overview [116, 117]. Moreover, if g_0 becomes of the order of $\omega_{1,2}$, one enters the so-called ultrastrong coupling regime, where the coupled-Lorentz oscillator picture breaks down. In this regime, only recently demonstrated in experiments [118, 119], a quantum treatment of light-matter coupling predicts spectacular effects such as the breakdown of the electromagnetic gauge invariance [120], for a viewpoint we refer to [121, 122].

In semiconductor microcavities embedding a single QW the light-matter coupling rate g_0 is governed by the exciton oscillator strength and cavity length. In the limit of symmetric and large cavity DBR reflectivity a semiclassical calculation yields [111]

$$g_0 \approx \sqrt{\frac{2\Gamma_x c}{\hbar n_{\text{eff}} L_{\text{eff}}}} \quad (2.26)$$

where Γ_x is the exciton radiative linewidth [Eq. (2.20)] and $n_{\text{eff}} L_{\text{eff}}$ is the effective optical thickness of a dielectric Fabry-Perot cavity. The dependence in Γ_x is intuitive: a

faster radiative decay rate means faster exciton-photon interconversion. The proportionality to the cavity free spectral range, or inverse round-trip time $\tau_{rt} = 2c/nL$, can be as well understood in a semiclassical picture as the average time before an emitted photon crosses the QW plane being possibly re-absorbed: the smaller τ_{rt} , the larger g_0 . Recalling the values of Γ_x , n_{eff} and L_{eff} derived in Sections 2.1-2.2 for a typical microcavity embedding a single 15 nm thick InGaAs QW with a 5% In fraction we get $g_0 \approx 1.7$ meV, roughly two orders of magnitude larger of the typical cavity linewidth $\gamma_c \sim (20 - 30)$ μeV . We can therefore expect these semiconductor heterostructures to operate deep in the strong light-matter coupling. According to Eq. (2.25) the energy splitting between the hybrid normal modes of the system is $\hbar\Omega_R \approx 2\hbar g_0$. Such large expected values of the light-matter interaction constant in semiconductor heterostructures motivated early experimental works, culminating in 1992 with the observation of the exciton vacuum Rabi splitting in a semiconductor microcavity [32].

2.3.1 Hamiltonian description

In the low density regime the semiclassical and quantum descriptions are equivalent, because of the bosonic nature of the system excitations and of the harmonicity of the excitation ladder. Otherwise, when exciton-exciton interactions become sizable, this picture may become inaccurate. In this section, we move to a second quantization description of the cavity and exciton fields which is the starting point to comprehensively describe the dynamics of the system. Since the light matter coupling rate satisfies $g_0 \gg \gamma_{c,x}$, we can assume that losses have a perturbative effect on the eigenstates of the system, thus their contribution is temporarily neglected, leaving the open quantum system description for a later discussion. For simplicity we set to zero the polarization splitting term in the cavity dispersion relation: the pseudo-spin degree of freedom becomes degenerate and is thus omitted in the notation. Then, the total hamiltonian is given by the sum of the bare photon [Eq. (2.4)], bare exciton [Eq. (2.22)-(2.23)] and light-matter coupling term \mathcal{H}_{cx} .

$$\mathcal{H}_{cx} = \int \frac{d^2\mathbf{k}}{(2\pi)^2} \frac{\hbar\Omega_R}{2} \left(\hat{a}_{\mathbf{k}}^\dagger \hat{b}_{\mathbf{k}} + \hat{b}_{\mathbf{k}}^\dagger \hat{a}_{\mathbf{k}} \right) \quad (2.27)$$

where the exciton ($\hat{b}_{\mathbf{k}}$) and cavity photon ($\hat{a}_{\mathbf{k}}$) ladder operators are evaluated at equal in-plane momentum \mathbf{k} due to the optical selection rules for QWs (cf. Sec. 2.2.2). Notice that ($\hat{a}\hat{b} + c.c.$) terms are not included within a rotating-wave approximation, accurate if $\Omega_R/\omega_{x,c} \ll 1$. The bosonic many-body state of the system is decomposed in a Fock state basis $|\hat{n}_{c,\mathbf{k}}, \hat{n}_{x,\mathbf{k}'}\rangle$. The only term which couples the exciton and photon subspaces is \mathcal{H}_{cx} , but only for equal k . The exciton-exciton interaction hamiltonian [Eq. (2.23)] instead couples different wavevector components of the \hat{n}_x subspace. Dealing simultaneously with this two features, without loss of generality, is difficult and greatly complicates the notation.

We can proceed in two steps: first, we set interaction to zero and study the linear eigenmodes of the system. Then, we introduce interactions in a specific scenario which is relevant to the manuscript, that is, when we limit our study to a single polariton branch. If $\mathcal{H}_{xx} = 0$, a change of the basis is enough to put the total hamiltonian in a diagonal form [31]. This new normal basis is associated to the operators (\hat{p}, \hat{q}), related to the bare photon and exciton ones via the isomorphism

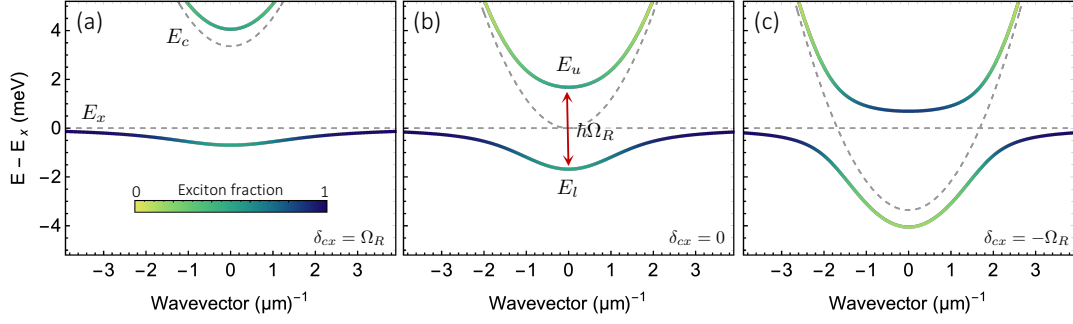


Figure 2.10: **Polariton dispersion relation** (a,b,c) The upper and lower polariton branches $E_{u,l}$ are plotted against in-plane wavevector for three representative values of exciton-cavity detuning: $\delta_{cx} = \Omega_R$ (a), $\delta_{cx} = 0$ (b) and $\delta_{cx} = -\Omega_R$ (c). The exciton fraction dependence on momentum is color-coded in each branch. Dashed lines correspond to the bare cavity (E_c) and exciton (E_x) dispersion relations, in all the plots $\hbar\Omega_R = 3.36$ meV.

$$\begin{pmatrix} \hat{p}_{\mathbf{k}} \\ \hat{q}_{\mathbf{k}} \end{pmatrix} = \begin{pmatrix} C_{\mathbf{k}} & X_{\mathbf{k}} \\ -X_{\mathbf{k}} & C_{\mathbf{k}} \end{pmatrix} \begin{pmatrix} \hat{a}_{\mathbf{k}} \\ \hat{b}_{\mathbf{k}} \end{pmatrix} \quad (2.28)$$

The Hopfield coefficients $C_{\mathbf{k}}, X_{\mathbf{k}}$, satisfy the condition $|C_{\mathbf{k}}|^2 + |X_{\mathbf{k}}|^2 = 1$, granting a unitary character to the transformation and depend on the bare exciton-cavity detuning $\delta_{cx} = (\omega_c - \omega_x)$ and Rabi frequency Ω_R as

$$|X_{\mathbf{k}}|^2 = \frac{1}{2} \left(1 + \frac{\delta_{cx}}{\sqrt{\Omega_R^2 + \delta_{cx}^2}} \right) = 1 - |C_{\mathbf{k}}|^2 \quad (2.29)$$

Under this transformation the total hamiltonian becomes

$$\mathcal{H}_{tot} = \int \frac{d^2\mathbf{k}}{(2\pi)^2} \hbar\omega_l(\mathbf{k}) \hat{p}_{\mathbf{k}}^\dagger \hat{p}_{\mathbf{k}} + \hbar\omega_u(\mathbf{k}) \hat{q}_{\mathbf{k}}^\dagger \hat{q}_{\mathbf{k}} \quad (2.30)$$

describing a system of free bosonic quasiparticles, obeying a dispersion relation identical to Eq. (2.25) but where the oscillator frequencies $\omega_{1,2}$ are replaced with the exciton and photon dispersion relations $\omega_{c,x}(\mathbf{k})$, yielding

$$\omega_{u,l}(\mathbf{k}) = \frac{(\omega_c(\mathbf{k}) + \omega_x(\mathbf{k}))}{2} \pm \frac{1}{2} \sqrt{(\Omega_R)^2 + (\omega_x(\mathbf{k}) - \omega_c(\mathbf{k}))^2} \quad (2.31)$$

These branches satisfy $\omega_u > \omega_l$ for all \mathbf{k} , it is thus common to refer to them as the upper and lower branches of the polariton dispersion. The term polariton indicates the hybrid light-matter character of the quasi-particles excitation on these branches, which are linear superpositions [Eq. (2.28)] of the cavity and exciton fields, weighted by the Hopfield coefficients. In Fig. 2.10 we plot these polariton dispersion relations for three values of exciton-cavity detuning $\delta_{cx} = (\Omega_R, 0, -\Omega_R)$, the exciton fraction along each branch is color-coded. For negative detuning [Fig. 2.10-(c)] we can observe the characteristic anti-crossing of the bands, which is one of the distinctive features of strong coupling.

From Fig. 2.10, we can get two useful informations. First, an expansion in small wavevectors of the the lower branch allows to define within a parabolic band approximation the polariton effective mass. Some algebra yields

$$\frac{1}{m_l^*} = \frac{|X_0|^2}{M} + \frac{|C_0|^2}{m_c} \approx \frac{|C_0|^2}{m_c} \quad (2.32)$$

The last approximation is legitimate because the exciton mass M is much larger than the photon effective mass m_c . This tells us that, for $\delta_{cx} \lesssim 0$, the lower polariton effective mass is extremely light, being roughly four orders of magnitude smaller than the electron rest mass. For instance at zero detuning $m_l^* \approx 2m_c \approx 6.4 \cdot 10^{-5}m_e$. Correspondingly, the thermal de Broglie wavelength is expected to be significantly larger for polaritons than standard bosonic atomic species, in principle allowing to observe bosonic condensation at much favorable experimental conditions.

The second important observation supported by Fig. 2.10 is that, for the same in-plane momentum, the upper and lower bands are never closer in energy than $\hbar\Omega_R$. For a small exciton-cavity detuning, this statement is true even if one considers two different wavevectors k and $k' = (k - q)$, such that $(k, k') \ll a_B^{-1}$. Provided that the total exciton-exciton interaction energy for two given polariton modes is smaller than the polariton band separation, which is the case in most experimental situations, one can truncate the polariton basis to describe only interactions within polaritons belonging to the lower band [37, 34]. The exciton-exciton interaction term becomes straightforward to write since, after the truncation, $\hat{b} = (C\hat{q} - X\hat{p}) \approx -X\hat{p}$. Therefore, the polariton-polariton interaction hamiltonian \mathcal{H}_{pp} within the lower band has the same form of resonant exciton interactions discussed in Sec. 2.2.3. The only difference is that the interaction constant is now multiplied by the excitonic fraction of the lower polaritons participating to the scattering event

$$U_{\sigma,\sigma'}^q = X_{k-q}X_{k'+q}X_{k'}X_k U_{\sigma,\sigma'}^q \quad (2.33)$$

Here the polarization indexes are necessary since the singlet channel couples polaritons with different pseudo-spin components. Moreover, recalling that for $qa_B \ll 1$ the interaction constant is $U_{\sigma,\sigma'}^q \approx U_{\sigma,\sigma'}^0$, and working in vicinity of the lower polariton band minimum, the interaction term can be approximated by the contact form [37, 107, 34]

$$\mathcal{H}_{pp} = \frac{1}{2} \int d^2\mathbf{r} U_{\sigma,\sigma'}^0 |X_0|^4 \hat{p}_{\mathbf{r},\sigma}^\dagger \hat{p}_{\mathbf{r},\sigma'}^\dagger \hat{p}_{\mathbf{r},\sigma'} \hat{p}_{\mathbf{r},\sigma} \quad (2.34)$$

In summary, for small in-plane wavevectors, polaritons behave as free bosons with a light mass of the order of few times the cavity photon effective mass (m_c) and subject to two-body contact-type interactions inherited via the excitonic component and thus proportional to $|X_0|^4$.

We are now interested in deriving the mean-field equations governing the dynamics of the system. Several ways are possible: one is to use an Hartree approximation of the many-body state and minimize the free energy of the system imposing the wavefunction normalization as Lagrange multiplier [123, 124]. Alternatively, one can write down the action of the system

$$\mathcal{S} = \int dt \int d^2\mathbf{r} \sum_{\sigma,\sigma'} i\hbar \hat{p}_{\mathbf{r},\sigma}^\dagger \partial_t \hat{p}_{\mathbf{r},\sigma} - (\mathcal{H}_p + \mathcal{H}_{pp} + \mathcal{V}_p) \quad (2.35)$$

Where \mathcal{V}_p is a stationary potential, added for the moment by hand and accounting for the possibility of modifying the energetic landscape of the microcavity. Then, we can impose that the infinitesimal variation of the action

$$\delta\mathcal{S} = \int dt \int d^2\mathbf{r} \sum_{\sigma,\sigma'} \left(\frac{\delta\mathcal{S}}{\delta\hat{p}_\sigma} \delta\hat{p}_{\sigma'} + \delta\hat{p}_{\sigma'}^\dagger \frac{\delta\mathcal{S}}{\delta\hat{p}_\sigma^\dagger} \right) \quad (2.36)$$

is vanishing for a test field $\psi_{\mathbf{r},\sigma}$ (saddle-point approximation), which must satisfy the Euler-Lagrange equation of motion for ψ . Since $\psi_{\mathbf{r},\sigma}$ minimizes the action at any time along the dynamics, we are neglecting all fluctuations. Indeed, according to the Ehrenfest's theorem, the evolution of the expectation value of quantum observables, up to second order, follows the equations of motion of the associated classical hamiltonian. Using Eq. (2.35), (2.36) and $\int d^2\mathbf{r} \hat{p}^\dagger \nabla^2 \hat{p} = - \int d^2\mathbf{r} \nabla \hat{p}^\dagger \cdot \nabla \hat{p}$, within the parabolic band approximation of the polariton hamiltonian yields

$$i\hbar\partial_t\psi_\sigma = \left[\hbar\omega_l(0) - \frac{\hbar^2\nabla^2}{2m_l^*} + V(\mathbf{r}) + (\mathcal{U}^t\psi_\sigma^*\psi_\sigma + \mathcal{U}^s\psi_{\sigma'}^*\psi_{\sigma'}) \right] \psi_\sigma \quad (2.37)$$

Here, we omitted the explicit dependence of ψ on the spatial coordinates. Furthermore, since the triplet channel \mathcal{U}^t typically dominates over the singlet channel \mathcal{U}^s [109], the above equation can be reduced to a scalar equation for the evolution of $\psi(\mathbf{r})$. In this scalar form Eq. (2.37) is identical to the Gross-Pitaevskii equation (GPE) describing a pure Bose-Einstein condensate of interacting particles within a Hartree approximation and the hydrodynamic nucleation of vortices in liquid Helium [124]. Indeed, a change of variables allows writing these equations in an alternative form, elucidating the parallel with hydrodynamic equations. We start by writing $\psi = \sqrt{\rho}e^{i\phi}$, where ρ is the local polariton density and ϕ the field phase. Multiplying the scalar version of Eq. 2.37 by ψ^* and subtracting its complex conjugate, one gets the continuity equation for the polariton density

$$\partial_t\rho + \nabla \cdot (\rho\mathbf{v}) = 0 \quad (2.38)$$

where $\mathbf{v} = \hbar\nabla\phi/m_l^*$ is the velocity of polaritons. This continuity equations tells us that motion of polaritons corresponds to a flow, since the velocity is the gradient of a scalar quantity. Similarly, inserting $\psi = \sqrt{\rho}e^{i\phi}$ in Eq. 2.37 and taking its real part, one can derive an equation for $\partial_t\phi$, which can then related to \mathbf{v} . Some algebra yields

$$m_l^*\partial_t\mathbf{v} + \frac{1}{2}m\nabla^2\mathbf{v} = \frac{\hbar^2}{2m_l^*}\nabla \left(\rho^{-1/2}\nabla^2\sqrt{\rho} \right) - \nabla V - \mathcal{U}^t\nabla\rho. \quad (2.39)$$

For and an irrotational flow it is possible to reduce this expression to the Euler equation for an inviscid fluid [123]. This parallel earned polaritons the evocative name of quantum fluids of light [37]. Due to the presence of a nonlinear term, the Gross-Pitaevskii equation describes a surprisingly vast phenomenology, from nonlinear waves in optics to fluid mechanics [125, 126, 124]. Moreover, polaritons are not a conservative system due to losses, which conversely means polariton can also be injected (or pumped) in the microcavity.

At a semiclassical level, losses can be included in Eq. (2.37) introducing a non-Hermitian term in the polariton hamiltonian producing a decay over time of the average

polariton density [37, 70]

$$\mathcal{H}_{Loss} = -i\frac{\gamma}{2} \langle \hat{p}^\dagger \hat{p} \rangle \quad (2.40)$$

where γ is the polariton linewidth. This amounts to an additional imaginary term $-i\gamma\psi/2$ in the GPE, damping the polariton density ρ over time. This is a purely phenomenological inclusion, but shall be later justified within the Lindblad master equation formalism in Sec. 2.4.4.

We now focus on the choice of the excitation scheme, as the behavior of the system in the high density regime, critically depends on it. This contextually offers us a key to organize the variety of phenomena which can be observed in exciton-polariton systems.

2.3.2 Quasi-resonant excitation

In quasi-resonant excitation schemes, a coherent laser beam illuminates the microcavity in vicinity of some polariton mode, directly coupling to the photonic component. Energy-momentum conservation in the structure ensures that a monochromatic pump can couple only to the modes sharing its same frequency, intensity-phase profile and polarization, i.e. when it is mode-matched. For the lower polariton branch, denoting $u_c(\mathbf{r})$ and $u_L(\mathbf{r})$ the envelope functions of the cavity and laser field at a frequency ω_0 , we can define the input-coupling efficiency a $\eta = \int d^2\mathbf{r} C u_c^*(\mathbf{r}) u_L(\mathbf{r})$. For a symmetric cavity, with a homogeneous linewidth γ_c , and a incident laser field $F_t = \mathcal{F} e^{i\omega_0 t} u_L(\mathbf{r})$, the coherent drive can be included as a time-dependent hamiltonian in the form [127]

$$\mathcal{H}_{Drive} = i\hbar\eta\sqrt{\gamma_c/2\mathcal{F}}(\hat{p}^\dagger e^{i\omega_0 t} - \hat{p} e^{-i\omega_0 t}) \quad (2.41)$$

The inclusion of losses [Eq. (2.40)] and of the coherent driving field [Eq. (2.41)] in the GPE (2.37) yields the following generalized GPE ($\hbar = 1$ units)

$$i\partial_t\psi = \left[\omega_l(0) - \frac{\nabla^2}{2m_l^*} + V(\mathbf{r}) + \mathcal{U}|\psi|^2 - i\frac{\gamma}{2} \right] \psi + i\eta\sqrt{\gamma_c/2\mathcal{F}} e^{i\omega_0 t} \quad (2.42)$$

For a small, constant excitation power, the nonlinear term proportional to the polariton density can be neglected. Moving to the frame rotating at the pump frequency $\psi(t) = \psi_0 e^{i\omega_0 t}$ allows writing Eq. 2.42 as a time-independent relation in the frequency domain. This equation contains the information on the linear response of the system at the frequency of the drive. For instance, if we consider a weak homogeneous illumination of a planar cavity ($V(\mathbf{r}) = 0$) and we sweep the pump frequency, we can probe the $\mathbf{k} = 0$ polariton mode spectral properties. Indeed Eq. 2.42 reduces to

$$0 = \left[(\omega_0 - \omega_l(0)) - i\frac{\gamma}{2} \right] \psi + i\eta\sqrt{\gamma_c/2\mathcal{F}} \quad (2.43)$$

Solving for ψ and inserting it in the definition of the cavity transmission coefficient $\mathcal{T} = \gamma_c|\psi|^2/2\mathcal{F}^2$, one finds a Lorentian spectrum with a full-width at half maximum equal to γ . Throughout this manuscript, we will systematically use low-power resonant experiments to characterize the linear spectrum of the polariton modes.

In the high density regime, the interplay of drive and dissipation with polariton-polariton interactions results in a variety of phenomena. Some, related to the nonlinear optics domain, such as polariton parametric amplification [128, 129] and oscillation [130, 131, 132] as well as optical bistability [133], squeezing [134, 135] and four-wave mixing [136]. Others, relate to the hydrodynamic behavior of polaritons. While investigating the (Bogolyubov) dispersion relation of small perturbations on top of the coherently excited polariton flow, I. Carusotto and C. Ciuti observed that it becomes linear for specific driving conditions [137]. According to the Landau criterion, this suggested the existence of a superfluid phase, which was experimentally revealed by the absence of backscattering in the flow around a defect [38]. In particular, the possibility to control the fluid velocity and density profile using the angle of incidence and spatial profile of the laser excitation, demonstrated to be an invaluable tool to probe its hydrodynamic excitations [41, 40, 42, 43]. More recently, in a pulsed excitation experiment, organic exciton-polariton superfluidity was reported at room temperature [138]. A nice historical overview on the nonlinear behaviour of polariton quantum fluids can be found in [37]. Importantly, for a quasi-resonant excitation, the phase of the polariton fluid under the excitation spot is imposed by the laser. This prevents the observation of phenomena such as bosonic condensation and lasing where the $U(1)$ symmetry is spontaneously broken. This will not be the case under non-resonant excitation as we will see in the following pages.

2.3.3 Non-resonant excitation

Let us consider a different setting where the laser beam excites the sample at far higher energy than the cavity resonance, in vicinity of one of the DBR reflectivity minima (c.f. Fig. 2.3). This optical pump, creates electron-hole pairs which relax via phonon assisted processes toward the bottom (top) of the conduction (valence) bands and form bound exciton states. As some radiative exciton states are populated, they possibly enter the strong coupling regime with cavity photons. Notice that, due to the finite bandwidth of the DBR stop-band ($\Delta E \approx 90$ meV), most of the excitons which are injected, couple to leaky modes, i.e. the reflectivity minima outside the DBR photonic bandgap. These modes have extremely poor finesse thus do not enter the strong light-matter coupling regime. Assuming that $E_c(0) \approx E_x(0)$, and denoting k_0 the exciton wavevector which couples to the first leaky mode, satisfying $E_x(k_0) - E_x(0) = \Delta E$, one finds $k_0 \approx 7 \mu\text{m}^{-1}$. Given that the exciton radiative cutoff wavevector is $k_{rad} \approx 30 \mu\text{m}^{-1}$ (cf. Sec. 2.2.2), and assuming a uniform exciton density of stated (DOS) close to $E_x(0)$, the typical ratio of excitons entering the strong coupling regime is $k_0^2 / (k_{rad}^2 - k_0^2) \approx 0.09$. The remaining fraction of excitons forms a long-lived reservoir which can interact with polaritons via their excitonic component. In general this implies that the polariton field needs to be coupled to the exciton reservoir density via a system of dynamical rate equations see [34, 139, 140, 141] for details.

In a low density regime, where exciton-exciton interaction are negligible, the reservoir populates all the available polariton modes with a rate determined by the exciton relaxation and DOS at a given energy [139]. Once populated, each polariton mode emits radiatively via its photonic component, producing the microcavity luminescence. We schematize the off-resonant injection mechanism in Fig. 2.11-(a), where the y-axis represents the photon (polariton) energy. On the left part of the panel we plot the microcavity reflectivity profile, facing the polariton dispersion relations, traced in the

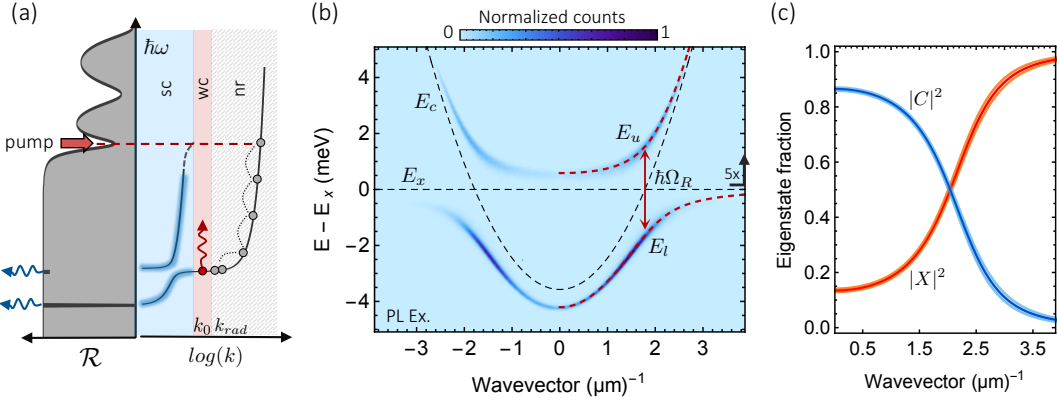


Figure 2.11: **Photoluminescence experiment** (a) Schematic representation of the off-resonant excitation scheme. The shaded gray profile is the microcavity reflectivity \mathcal{R} profile plotted against energy. The right part of the panel presents the polariton dispersion, wavevectors are log-scaled. (b) Measured angle-resolved photoluminescence. Dashed red lines represent a joint best fit of the polariton dispersion relations to the data $E_{u,l}$, dashed gray lines trace the corresponding bare cavity (E_c) and exciton (E_x) ones. For $E > E_x$ intensities are multiplied by a factor five. (c) Light-matter contents as a function of in-plane momentum for the lower polariton branch. Shaded areas correspond to the 95% confidence intervals.

right part of the panel. The shaded areas, for increasing k , correspond to the strong (sc), weak (wc) and non-radiative (nr) exciton-photon coupling regions. Dotted lines represent phonon-assisted scattering events. This excitation scheme offers a useful tool to characterize the eigenmodes of a planar microcavity structure with a simple photoluminescence (PL) experiment. Indeed, due to the in plane translational invariance of the microcavity, in plane momentum is conserved in the emission process. We can thus relate the in-plane momentum of polaritons \mathbf{k} to the energy and angle of the photon leaking outside the cavity as $|\mathbf{k}| = E \sin(\theta)/\hbar c$. A high numerical aperture objective collects the cavity emission and images it with a Fourier-conjugate system of lenses to the slit of a spectrometer coupled to a CCD camera. This configuration, originally proposed in [142], allows to simultaneously resolve in angle and energy the emitted photons, that is, imaging the dispersion relation with a single-shot of the CCD. For the details on the setup and on the imaging scheme we refer to the next chapter, dedicated to the experimental techniques.

As an example we present in Fig. 2.11-(b) the angle and energy resolved photoluminescence of a microcavity with 28(32) DBR pairs in the top (bottom) mirror and embedding a 15 nm $\text{In}_{0.05}\text{Ga}_{0.95}\text{As}$ QW. Two bright bands can be observed, corresponding to the upper and lower polariton. Dashed red lines show the result of a joint fit

| | E_x (meV) | δ_{cx} (meV) | $\hbar\Omega_R$ (meV) | n_{eff} |
|-----|-------------|---------------------|-----------------------|-----------|
| Exp | 1453.45(2) | -3.57(3) | 3.34(4) | 3.42(4) |
| Th | 1449(2) | (*) | 3.36 | 3.37 |

Table 2.2: **Fit of the polariton dispersion relation:** Errors correspond to the standard deviation. The detuning (*) changes spatially over the sample (cf. Sec. 3.1.1).

of the dispersion relations (2.31) to each maxima of the spectrum for a given in-plane momentum (angle). Correspondingly, the two gray dashed lines in the plot trace the bare exciton E_x and cavity E_c dispersion relation. The parabolic dispersion relation for a free exciton in the QW [Eq. (2.16)] looks flat because the exciton effective mass is four orders of magnitude larger than the one of a cavity photon. The results of the fit are summarized in Tab. 2.3.3. Importantly, if we compare the results of this fit to the parameters extracted in Sec. 2.1-2.2, an excellent overall agreement is found. The observed intensity profile as a function of energy depends on the different relaxation rates of polaritons and on the excitation power: it is a rather complicated problem to model, see [139, 143] for further details. In Fig. 2.11-(c) we calculate the Hopfield coefficients C, X as a function of the in plane momentum from the dispersion fit parameters.

In this manuscript we will not investigate thoroughly the high polariton density regime under non-resonant excitation. However, we want to qualitatively summarize the rich phenomenology characterizing it.

The first possibility when increasing the pump power, is that phase-space filling and the screening of Coulomb interaction leads to the dissociation of excitons in an electron-hole plasma before anything else happens. As a result, the system transitions from the strong to the weak-coupling regime around a critical density $n_0 \sim a_B^{-2}$. Even in the weak-coupling regime, for a density of carriers $n > n_{\text{thr}}$, stimulated emission in the electron-hole plasma may overcome cavity losses, resulting in a lasing action of the microcavity. At this stage the structure can be regarded as an optically-pumped vertical surface emitting laser (VCSEL). This will be the case for the experiments detailed in Chapter 4.

Let us now consider a different case where the saturation density n_0 is pushed to higher values. This can be experimentally achieved by embedding multiple QWs at each cavity antinode, thus lowering the average exciton density per QW. Then, since polaritons are composite bosons, if a state has an occupation larger than unity, bosonic stimulation sets in [33, 144]. Provided that the pump power required to have $\langle \hat{p}_{\mathbf{k}}^\dagger \hat{p}_{\mathbf{k}} \rangle > 1$ is still significantly smaller than the saturation density (n_0), the stimulation effect leads to a macroscopically occupied state, i.e. a polariton laser [33, 141, 36]. Furthermore if the carrier relaxation rate is significantly faster than any other loss mechanism in the cavity, bosonic stimulation is stronger for the lowest-energy state of the polariton branch. The macroscopically occupied state is therefore a (non-equilibrium) polariton condensate, see [145, 144]. Bose-Einstein condensation of exciton-polaritons was first reported by the group of B. Deveaud and L.S. Dang using CdTe microcavities [35]. Soon after, working with organic materials with tightly bound excitons, different groups achieved condensation at room temperature, see for instance [146, 147].

The condensation of polaritons is intrinsically out of equilibrium due to the constant injection of high energy carriers and optical losses in the cavity. For this reason, especially in the early works, the use of the word "Bose-Einstein condensate" has been strongly criticized, since it implies that the two phenomena belong to the same (equilibrium) universality class. Moreover the exciton reservoir can result in additional dynamical effects (modulational instabilities) further steering away from equilibrium the condensate [148, 149, 150, 151]. More recently, with the development of ultra-high quality factor cavities, two groups claimed to achieve equilibrium condensation both for a polariton system at 4K [152] and for microcavity photons at room temperature [153]. They argue that in their system, the relaxation rate τ_R is much faster than the

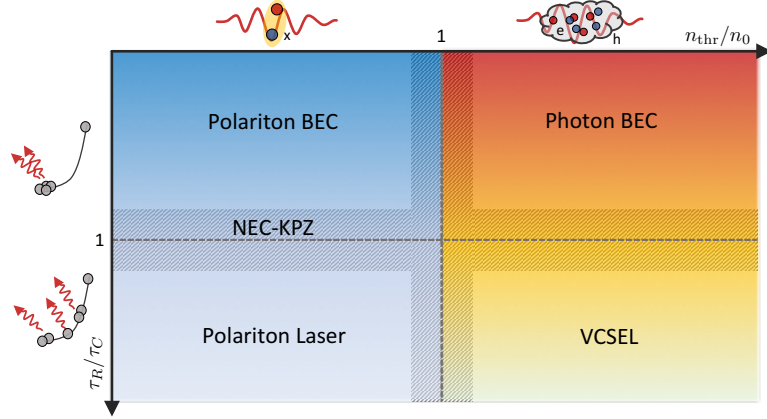


Figure 2.12: **Microcavity stimulated emission phenomenology under non resonant pumping.** Two order parameters rule the diagram: (1) the ratio between the bosonic stimulation threshold n_{thr} and exciton dissociation density n_0 and (2) the ratio between the relaxation time of excitations τ_R and their lifetime τ_C . Gray areas around $n_{thr}/n_0 \sim 1$ and $\tau_R/\tau_C \sim 1$ display a non-universal, hybrid phenomenology.

cavity decay rate τ_C , thus allowing effectively an equilibrium description. In Fig. 2.12 we tentatively chart the expected stimulated emission phenomenology of a semiconductor microcavity optically excited far from resonance. We organize the behavior on the basis of the ratio between the stimulated emission threshold density n_{thr} and the exciton dissociation density n_0 and relaxation time order parameters, dividing the diagram in four zones: weak vs strong coupling and equilibrium condensation vs lasing regimes. This distinctions of course allow significant intermediate areas where the behavior of the system is more complicated. Interestingly, in the gray area where the equilibrium description of polariton condensation fails, an interesting mapping between the Kardar-Parisi-Zhang (KPZ) equation modeling the growth of interfaces [154], and a non-equilibrium polariton condensate has been recently proposed [155, 156]. The location of a microcavity structure in this diagram depends both on the QW(s) design (e.g. material and number) and on the cavity finesse. Notice that since the relaxation rate depends on the pump power, a single microstructure may explore more than one region of the diagram.

In summary, we can use low power non-resonant excitation experiments as a tool to probe the polariton dispersion trough its spontaneous photoluminescence. The illustrative experiment presented in Fig. 2.11, supports the theoretical results presented in Sec. 2.1-2.2-2.3.1. For high excitation powers either condensation or lasing can be observed both in the weak and strong coupling regime of excitons and cavity photons depending on the specific sample design and choice of materials.

2.3.4 Polariton linewidth

In Sec. 2.3.1 we included losses at a semiclassical level in the polariton hamiltonian, see Eq. (2.40). Correspondingly, we defined the polariton decay-rate γ , without further commenting on its origin. In this section we theoretically address the dependence of the polariton lifetime τ_p on the bare cavity photon and exciton properties. This analysis is important to pinpoint the main limiting factors to the improvement of τ_p , a necessary

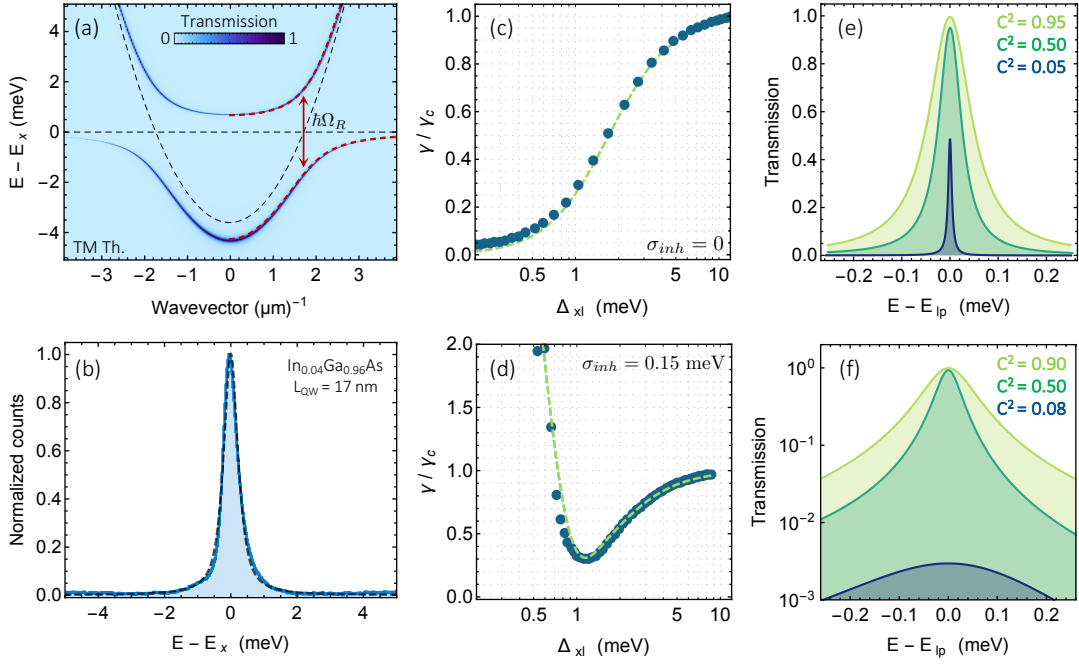


Figure 2.13: **Scaling of the polariton linewidth** (a) Transfer-matrix simulation of the microcavity transmission as a function of the incident in-plane wavevector and energy. Dashed line: nominal polariton dispersion relation [Eq. (2.31)]. (b) Typical PL spectrum of a shallow InGaAs QW, the dashed line is pseudo-Voigt profile fit. (c,d) Scaling of the polariton linewidth as a function of the exciton-lower polariton detuning $\Delta_{xl} = (E_x - E_l)$ for a radiatively limited exciton transition (c), or including a gaussian inhomogeneous broadening (d). (e,f) Representative examples of transmission spectra corresponding to panels (c,d), respectively.

step for the observation of strongly correlated quantum phases with polariton platforms [51, 157, 158, 159, 52]. As anticipated in Sec. 2.3.2, a low-power resonant spectroscopy experiment allows the precise determination of the resonant energy and the linewidth of polariton modes. In the simplest implementation of the experiment, a collimated laser beam illuminates the sample; the transmitted intensity is recorded as a function of the angle of incidence and wavelength of the pump beam, allowing to reconstruct the dispersion relation of the sample. Here we model such experiment using a transfer matrix method, where the QW optical response is included as a thin layer with a dielectric constant given by Eq. (2.21).

In figure 2.13-(a), we simulate the angle-resolved transmission spectrum of a symmetric microcavity formed by 20(24) DBRs pairs in the top(bottom) mirror and embedding a 17 nm thick $\text{In}_{0.04}\text{Ga}_{0.96}\text{As}$ QW for a bare exciton cavity detuning of $\hbar\delta_{cx} = -3.6$ meV. Converting the angle of incidence to in-plane wavevector, we obtain the microcavity dispersion relation. The dashed-red curve is the polariton dispersion relation derived in Sec. 2.3.1, plotted for the nominal microcavity parameters (cf. Tab. 2.3.3). The fair agreement of the two models in the linear regime is again not surprising [160], but validates the use of the transfer matrix method, which naturally includes cavity losses. As mentioned in Sec. 2.3.1, polaritons are linear superpositions of the bare exciton and cavity eigenmodes thus, we can expect their linewidth to depend on the decay mechanisms of both elementary components. For the lower polariton $\hat{p}_{\mathbf{k}} = C_{\mathbf{k}}\hat{a}_{\mathbf{k}} + X_{\mathbf{k}}\hat{b}_{\mathbf{k}}$,

superposition of an exciton (\hat{b}) characterized by a non-radiative decay γ_{nr} , and a cavity photon (\hat{a}) with a linewidth determined both by losses and absorption. Quite intuitively, one finds [37, 160]

$$\gamma = |C|^2\gamma_c + |X|^2\gamma_{nr} \quad (2.44)$$

The mechanism originating the non-radiative exciton decay channel is a complex compound of microscopic processes (Auger, phonon or trap-mediated recombination, just to name a few) and can be hardly estimated a priori. Concerning the cavity linewidth, the main limitation does not come from radiative decay, which could be made (in principle) arbitrarily small by adding more layer pairs to the DBRs, but due to residual absorption in the cavity. Absorption has two main origins, the first being the residual (Urbach) absorption tails of GaAs at the QW exciton resonance, the second due to deep traps created by residual doping in the spacer material [73]. In the samples fabricated at C2N, the linewidth of bare λ cavities is typically (20 – 30) μeV for (860 – 840) nm central wavelengths.

Residual absorption tails could be systematically avoided by red-shifting the QW resonance as far as possible from the bulk GaAs band-edge by increasing the In content in the QW (cf. Fig. 2.6). However, a higher In content is usually associated to larger alloy fluctuations in the material which, in the case of wide QWs, are mainly responsible for the inhomogeneous broadening of the exciton transition. For instance, Fig. 2.13-(b) shows a typical photoluminescence spectrum of 17 nm thick $\text{In}_{0.04}\text{Ga}_{0.96}\text{As}$ QW embedded in a GaAs matrix. A pseudo Voigt profile fit allowed to extract the peak energy $E_x = 1475.9$ meV and the full-width at half maximum of the spectrum 0.49(1) meV. From sample to sample we observed fluctuations of this value in the range (0.4 – 0.7) meV, much larger than the expected radiative exciton linewidth $\Gamma_x \approx 0.04$ meV. As first pointed out in [161], inhomogeneous broadening also contributes to the polariton linewidth. Indeed, if one thinks of the QW as an ensemble of emitters coupled to a cavity mode, the polariton states correspond to the bright linear superpositions of the cavity mode with the fully-symmetrical matter state [162]. All the other states, provided that all the emitters are identical, form orthogonal linear combinations which remain decoupled, thus are dark. Instead, if the emitters transition energy forms a continuum, distributed according to a spectral density $\rho(\omega)$, the dark states have slightly different energies, leading to progressive dephasing of Rabi oscillations [163].

Inhomogeneous broadening can be included within the transfer-matrix formalism by convoluting the QW dielectric constant $\epsilon(\omega)$ [Eq. (2.21)] with $\rho(\omega)$. To quantify the influence on the linewidth, we study two different situations. In the first one, a radiatively limited exciton transition is considered $\rho(\omega) = \delta(\omega - \omega_x)$. Fig. 2.13-(c) shows the linewidth of the $k = 0$ mode of the microcavity as a function of the bare exciton to lower polariton detuning $\Delta_{xl} = (E_x - E_l)$. Since non radiative mechanisms are not included in the transfer-matrix method, the data points are fairly interpolated by Eq. (2.45) with $\gamma_{nr} = 0$ (dashed green line). Then, we consider a gaussian $\rho(\omega)$, with standard deviation $\sigma_{inh} = 0.15$ meV, corresponding to the normal part of the Voigt profile of Fig. 2.13-(b). When this contribution is included, the scaling of the polariton linewidth with Δ_{xl} differs significantly, see Fig. 2.13-(d). For large values of the exciton-lower polariton detuning, the linewidth decreases as $\gamma/\gamma_c \approx |C|^2$, but as soon as $\Delta_{xl} \lesssim 1$ meV, an abrupt increase can be observed. The dependence of the polariton linewidth on the inhomogeneous broadening of the matter transition, was

first derived within a semiclassical description in [163]

$$\gamma = |C|^2\gamma_c + |X|^2(\gamma_{nr} + \pi\Delta_{xl}^2\rho(\Delta_{xl})) \quad (2.45)$$

being proportional to the second cumulant of spectral density at the polariton resonant frequency (assuming $\sigma_{inh} \ll \hbar\Omega_R$). A dashed curve traces this relation (no adjustable parameters) in Fig. 2.13-(d), fairly interpolating the results of the transfer-matrix analysis. In Fig. 2.13-(e,f), we show transmission spectra for three representative values of $|C|^2$ both in the case of $\sigma_{inh} = 0$ and $\sigma_{inh} = 0.15$ meV. In absence of inhomogeneous broadening the spectra have a Lorentzian profile, whereas for $\sigma_{inh} \neq 0$ they become skewed and the peak transmittance decreases much faster than in the $\sigma_{inh} = 0$ case. Interestingly, if $\gamma_{nr} < \gamma_c$ we observe both for Fig. 2.13-(c) and (d) that $\gamma < \gamma_c$, an effect sometimes referred as cavity protection [163, 164, 165]. It shall be emphasized that the radiative exciton decay Γ_x does not contribute to the polariton linewidth since its coupled only via higher order contribution to outer free-space modes [70, 160]. For this reason, the recent demonstration of atomically thin MoSe₂ mirrors, supporting excitonic modes which are radiatively limited [166], motivated proposals for novel polariton-blockade schemes [167, 168].

In summary, our analysis suggests that for small detunings of the polariton mode relative to the exciton, the main limiting factor for reducing the polariton linewidth is the inhomogeneous broadening of the exciton transition, which is still roughly an order of magnitude larger than the exciton radiative decay rate $\Gamma_x \approx 0.04$ meV. With the idea of contextually maximizing polariton interactions, scaling with the square of the exciton fraction [cf. Eq. (2.34)], it will be of outmost importance in the future to improve the fabrication technology, pushing it towards the limit of radiatively limited exciton transitions.

2.4 Polariton mode engineering

After having analyzed the properties of planar microcavities in the strong coupling regime, we want to discuss how to tailor the transverse modes of the system. One of the notable advantages stemming from the hybrid light-matter nature of microcavity excitations is the wide variety of mechanisms one can exploit to spatially engineer an effective potential for polaritons. We briefly review the mechanisms already demonstrated in literature, before focusing on the technique originally developed at C2N.

The general idea is to induce a position-dependent energy shift on either of the excitonic or photonic constituents. One possible approach, since the bandgap of a semiconductor is partly related to the lattice constants in the material, is the application of mechanical stress, which locally changes the exciton energy. This strategy was used for instance in [169] to realize a trap for a polariton condensate. Similarly, the excitonic energetic landscape can be patterned using the strain field produced by surface acoustic waves (SAW); one or two trains of surface acoustic have been used to implement 1D and 2D lattices [170, 171].

Another widely used mechanism exploits the fact that the off-resonant injection of excitons creates a reservoir which has essentially the same profile of the pump (cf. Sec. 2.3.3). Under the pump spot, exciton-exciton interactions induce a local blueshift of the exciton energy, acting as a repulsive potential for polaritons [44, 172, 41, 173].

The main advantage of this all-optical technique is the possibility to engineer almost any arbitrary pattern in a tunable and reversible fashion, using commercially available spatial light modulators. Recently, the constant refinement of this technique allowed to implement a classical XY -Hamiltonian in a lattice of polariton condensates [47], an important opening towards the analog simulation of complex systems.

Alternatively, one can engineer the refractive index landscape of the microcavity, thus spatially modifying its optical properties; this can be generally done in four different ways.

- Depositing on the top mirror a thin metallic film which induces a local blueshift of the cavity resonance [174]. This technique is versatile but the energy-shift produced is limited as the metal modifies only the evanescent tails of the cavity field. A variant of this method consists in overlaying a sub-wavelength grating on the top mirror [175].
- Another strategy to shift the cavity energy is to modify locally the cavity thickness. This can be done during the fabrication process, by etching selectively the spacer above the QW before growing the top DBR [176]. In the regions where the cavity spacer is thicker the cavity modes are locally redshifted. Also this method is versatile and allows the creation of nearly arbitrary patterns. However, the discontinuities at the spacer-top DBR interface tend to be the source for additional unwanted losses in the cavity.
- Open microcavities, where bottom DBR and spacer, grown on a planar substrate are separated from the top $\text{SiO}_2/\text{Ta}_2\text{O}_5$ DBR mirror. The top DBR is sputtered on a surface presenting a depression, e.g. a laser-ablated dimple on a fiber tip, thus forming a concave mirror [177]. This approach recently allowed to reach quality factors as high as $Q \sim 5 \cdot 10^5$ for a $1.4\lambda^3$ mode volume [178]. Moreover, an accurate design of the depression profile allows to engineer coupled arrays of microcavities [46]. The main limitation of this approach is that the radius of curvature of the depression R is directly related to the energy of the confined modes: fabrication imperfections $\delta R/\langle R \rangle \sim 10^{-3}$ lead to a fluctuation on the order of $(1 - 2)$ meV of the fundamental mode energy. This disorder tends to prevent the formation of extended states over several microcavities. Nevertheless open-access microcavities have the advantage of allowing the exploration of light-matter coupling with any active material, such as transition metal dichalcogenides (TMDs) [179, 180].
- Deep etching of the microcavity structure down to the substrate. In this approach the large refractive index contrast between semiconductor and air allows tightly confining the optical modes inside the structure by total internal refraction. This method was originally developed in parallel in our group [181] and by M.Bayer & collaborators [182].

Technical details can be found in the next chapter, here we focus on the result of this fabrication procedure and discuss how it can be used to implement an analog photonic emulator of lattice hamiltonians [183].

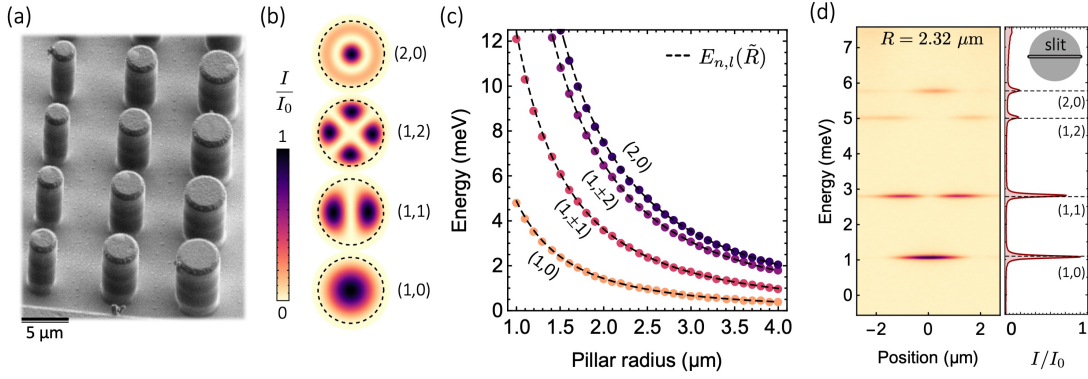


Figure 2.14: **Micropillars:** (a) SEM image of circular microcavities obtained by deep-etching a planar heterostructure. (b) Calculated intensity profile of the micropillar eigenmodes labeled by their principal and angular quantum numbers (n, l) . The dashed line represents the microstructure edge. (c) Finite element calculation of the energy of the lowest six eigenmodes as a function of the pillar radius (see App. 2.6 for details). Dashed lines are the predictions of Eq. (2.46) including the evanescent tails of the optical field ($\delta R \approx 0.05 \mu\text{m}$). (d) Spatially resolved PL spectrum measured on a pillar with nominal radius of $R = 2.32 \mu\text{m}$. Inset: position of the spectrometer slit; Dashed line: predictions of Eq. (2.46).

2.4.1 Micropillar cavities

The fundamental building block of our system are single, μm -sized pillars shown in Fig. 2.14-(a). The combination of the planar cavity DBRs with a lateral confinement due to the large refractive index mismatch between air and the heterostructure material, results in the discretization of the optical modes of the microcavity. For a pillar radius significantly larger than the confined mode wavelength, the stationary optical field in the microcavity can be factored in its longitudinal and transverse components. If the planar cavity TE-TM effects can be neglected, the longitudinal field profile can be found with a transfer-matrix method (cf. Sec. 2.1.2). This leaves out only the transverse field components to be determined by solving the Maxwell equations for an infinite dielectric waveguide, having a polarization-independent refractive index n_{eff} and a section corresponding to the structure transverse profile. TE-TM effects are also present for the transverse field components, however, in most experimental situations, light polarization can be controlled in excitation and selected in detection. The eigenmodes of the system can thus be found by solving a scalar Helmholtz equation for the infinite waveguide, which can be equivalently mapped to an optical Schrödinger equation within the paraxial approximation [184].

We plot in Fig. 2.14-(b) the spatial intensity profile of the four lowest eigenmodes of a cylindrical waveguide with $n_{\text{eff}} = 3.42$ (cf. Tab. 2.3.3). The cylindrical symmetry of the problem ensures that the angular momentum is a good quantum number, accordingly, we label all the confined eigenmodes with a principal and angular quantum number (n, l) , determining the number of radial and azimuthal nodes in the intensity profile. Notice that eigenvalues with the same absolute values of $l \neq 0$ are twice degenerate. The evanescent tails of the EM field outside the cavity decay on a short distance $\delta R \approx 0.05 \mu\text{m}$ which can be accounted for in the definition the radius of an equivalent infinite circular potential well of radius $\tilde{R} = R + \delta R$. The solution of this problem is a

known result of quantum mechanics [185]

$$E_{n,l} = \frac{\hbar^2}{2m_l^* \bar{R}^2} \mathcal{B}_0^2(n, l) \quad (2.46)$$

here, $\mathcal{B}_0^2(n, l)$ are the n -th zeroes of the l -th order Bessel function, $m_l^* \approx m_c/|C|^2$ the effective cavity photon mass and $|C|^2$ is the (energy dependent) polariton photonic fraction. Fig. 2.14-(d) shows the dependence of the calculated energies of bare microcavity photon $|C|^2 = 1$ as a function of the pillar radius R , dashed lines correspond to Eq. (2.46). Similar arguments can be applied to describe the eigenmodes of square and rectangular pillars. Notice that whenever the pillar circular symmetry is broken (i.e. due to a slight ellipticity) the degeneracy of eigenmodes with an equal $|l|$ is lifted.

As an illustrative example, we perform a low-power off-resonant excitation experiment on a circular micropillar with $R = 2.3 \mu\text{m}$ radius. The spatially and spectrally resolved emission of a pillar is shown in Fig. 2.14-(c). Energies are stated with respect to the planar cavity $k = 0$ mode (here $E_0 \approx 1445 \text{ meV}$). In this experiment the spatial coordinate corresponds to the spectrometer slit position, aligned along the center of the pillar as shown in the inset. The emission is filtered with a film-polarizer having an axis parallel to the slit. The four discrete levels observed, have profiles (energies) in fair agreement with the theoretical predictions, see Fig. 2.11-(b) and the (dashed lines). This is both telling us that the paraxial approximation is accurate, and that the fabrication technique is fairly reproducing the target structure.

In the perspective of implementing a lattice hamiltonian emulator, micropillars play the role of lattice sites, whose energies can be controlled via their radius (more generally their area), and where multiple orbital symmetries can be accessed. For instance $(n, 0)$ modes can be pictured as s -type hydrogen orbitals, $(1, \pm 1)$ as $p_x \pm ip_y$ orbitals and so on. Of course these modes do not share the exact same profile as hydrogen orbitals, since they are solution of a different, two dimensional Schrödinger equation. However, it can be useful to visualize them as atomic orbitals to use both Linear Combination of Atomic Orbitals (LCAO) and symmetry arguments to intuitively guess the optical modes of coupled pillar lattices [186, 187, 188, 50].

2.4.2 Coupling the micropillars

In order to understand the optical modes of microstructures composed by a large number of overlapping micropillars, we can start with the minimalistic case of two equal cylindrical microcavities with radius R , separated by a center-to-center distance CC' , see Fig. 2.15-(a). For $CC' < 2R$ the cylindrical symmetry of the bare pillar problem is broken and the solution of the associated optical Schrödinger equation does not admit exact analytic solutions. Even if the bare pillar eigenmodes $|\psi_{L,R}\rangle$ are not anymore a good basis, provided that the overlap between the two pillars is small, we can expect that it only introduces a perturbative effect with respect to the uncoupled problem. At lowest order in the perturbation theory, we can therefore expand the coupled eigenmodes as linear superpositions of $|\psi_{L,R}\rangle$ modes, in the spirit of a LCAO approach. If now we consider just the lowest (s -type) mode of each identical micropillar, the parity operator ($|\psi_L\rangle \rightleftharpoons |\psi_R\rangle$) commutes with the total (uncoupled) hamiltonian. Since this spatial symmetry is preserved in the coupled system, the linear possible LCAO superposition must obey $(|\psi_L\rangle \pm |\psi_R\rangle)/\sqrt{2}$. The total hamiltonian in this basis is

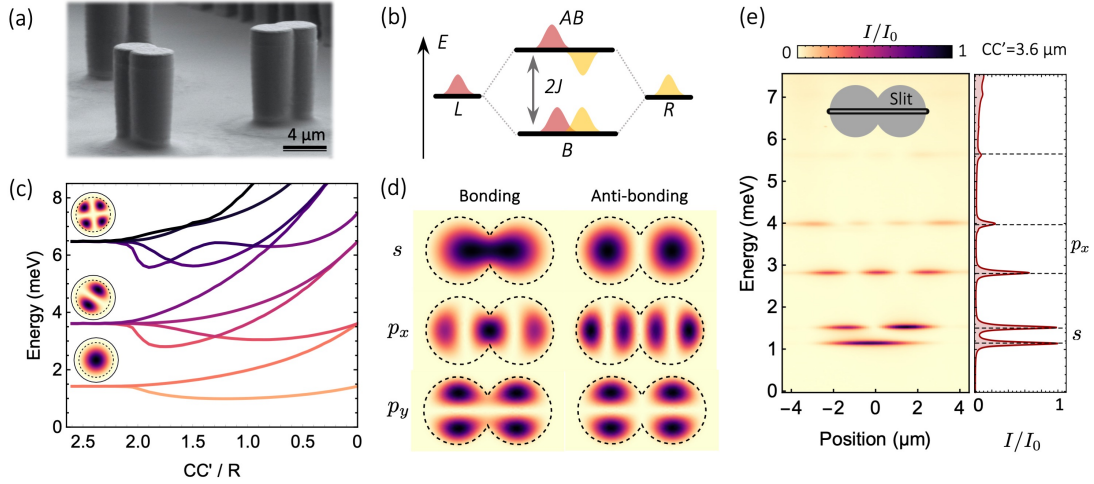


Figure 2.15: **Dimeric photonic molecules** (a) SEM image of overlapping microcavities forming a photonic dimer molecule. (b) Schematic representation of the hybridization of the two lowest bare pillar modes into molecular bonding (B) and anti-bonding (AB) photonic orbitals. (c) Finite elements calculation of the energy of lowest ten eigenmodes of two $R = 2 \mu\text{m}$ pillars as a function of their center-to-center distance CC' (cf. App. 2.6 for details). (d) The intensity profiles of the lowest six eigenmodes for $CC' = 3.6 \mu\text{m}$ can be classified based on the bare pillar mode and hybridization symmetry. (e) Spatially resolved PL spectrum measured on a dimer molecule with $R = 2.0 \mu\text{m}$ and $CC' = 3.6 \mu\text{m}$. Inset: position of the spectrometer slit. Dashed line: finite element predictions for the nominal structure.

$$\mathcal{H} = E_0(|\psi_L\rangle\langle\psi_L| + |\psi_R\rangle\langle\psi_R|) - J(|\psi_L\rangle\langle\psi_R| + |\psi_R\rangle\langle\psi_L|) \quad (2.47)$$

where \mathcal{H}_0 is the bare microcavity hamiltonian and -at first order- $J = \langle\psi_L|\mathcal{H}_0|\psi_R\rangle = J^*$, real due to the exchange symmetry. This coupled mode hamiltonian can be easily diagonalized yielding the energies $E = E_0 \pm J$. In analogy with a LCAO theory for molecular hydrogen the symmetric and anti-symmetric superposition of $|\psi_{L,R}\rangle$ are often referred as bonding (B) and anti-bonding (AB) modes, respectively. The level hybridization diagram is summarized in Fig. 2.15-(b) for $J > 0$. Since J is related to the overlap integral of the bare pillar eigenmodes, we can expect it to increase as CC' is made smaller. Indeed, in a second quantization picture, J/\hbar corresponds to the rate at which single excitations are transferred from one mode to the other. Of course this approximation is only valid when $J/E_0 \ll 1$, otherwise the overlap term cannot be decoupled by its effect on the on-site energy, i.e. $|\psi_{L,R}\rangle$ is not a normal basis anymore. Practically speaking, since the area of the single pillars determines E_0 , the approximation holds as long as the overlap produces a small change of the total area. The determination of an appropriate Wannier basis for the LCAO ansatz, eventually including inter-orbital couplings is beyond the scope of the manuscript, we thus refer to [189]. In Fig. 2.15-(c) we used finite element simulations to calculate the energy of the first ten modes of the coupled pillar structure as a function of CC'/R for a pillar radius of $2 \mu\text{m}$. Inspecting the s -orbital modes we can see that the splitting of the B and AB modes is non symmetric about $E_0 \propto A$, signaling the non-orthogonality of the $|\psi_{L,R}\rangle$ basis. For two modes, one can anyway call B and AB the solutions of the numerical calculation and define an effective coupling strength J by dividing their energy splitting

by two. When considering 1D and 2D lattices however the effect of non-orthogonality must be generally taken in account in order to fit the dispersion relation [189].

Even if the energy levels indicate a deviation from the $J/E_0 \ll 1$ case, the mode profiles calculated for molecular orbitals are always in agreement with the LCAO prediction. Indeed geometric arguments are extremely robust with respect to perturbations, provided that the generator of the transformation (here controlled by CC') does not break underlying symmetry considerations. In Fig. 2.15-(d) we show calculated intensity profiles for the first six eigenmodes for $R = 2.0 \mu\text{m}$ and $CC' = 3.6 \mu\text{m}$. We can see that all of them can be intuitively classified on the basis of the symmetry of the originating bare pillar eigenmodes and of their parity (nodes in the intensity signal a π phase jump). Finally, the spatially and spectrally resolved emission of a dimer molecule formed by pillars with $2.0 \mu\text{m}$ radius and $3.6 \mu\text{m}$ distance is shown in Fig. 2.11-(c). The spatial coordinate corresponds to the spectrometer slit position, as indicated in the inset and the emission polarization has been filtered along the slit axis. Notice that the eigenmodes corresponding to the hybridization of p_y orbitals are not visible with the present choice of the slit position. Dashed lines in the right-most panel of Fig. 2.11-(e) correspond to the predictions of finite element calculations for the nominal structure with no adjustable parameter.

2.4.3 Emulation of lattice hamiltonians

In the previous pages we discussed the discrete optical modes of micropillar structures and how a spatial overlap between them can be effectively mapped into a hopping term for the excitations of each microcavity. The extension to the case of multiple pillars is intuitive since these two elements are the essence of any tight-binding lattice model with nearest-neighbor couplings between the sites. We have shown that the energy of each bare micropillar eigenmode can be controlled via its radius and that the coupling can be controlled via their relative distance. The design of the spatial arrangement and size of the pillar thus allow to fully engineer the polariton dispersion relation in a lattice.

For instance, in the right panel of Fig. 2.16 a SEM image shows a honeycomb lattice of micropillars, where Dirac cones were directly observed with photoluminescence experiments [49, 190]. Moreover inter-orbital couplings can be also engineered by alternating smaller and larger pillars, in order to match the s -type and p -type eigenmode energies. It is worth mentioning that given a known tight-binding hamiltonian, the inverse design problem of determining the pillar size and arrangement is not straightforward, especially in the case where multiple values of the coupling constants J are needed within a unit cell (e.g. [48]). Indeed as we pointed out in the previous section changing CC' also renormalizes the "on-site" energy due to the non-orthogonality of the bare pillar eigenmodes. The development of inverse design methods not relying on brute force 2D finite elements is an important direction for future works.

Interestingly, since polaritons interact via their excitonic component, our system can also emulate (weakly) interacting bosons on arbitrary lattices, such as the celebrated Bose-Hubbard model. For values of the coupling strength J and a total interaction energy much smaller than the energy separation between the bare pillar eigenmodes ($E_{1,1} - E_{1,2}$), one can study only the modes deriving from the hybridization of $|\psi_{1,0}\rangle$ [37]. In a second quantization picture, denoting J the effective inter pillar coupling

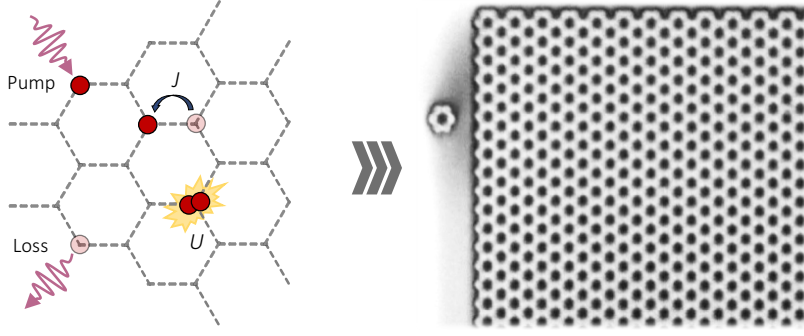


Figure 2.16: **A photonic platform for analog simulation:** (Left) schematic representation of a honeycomb lattice for interacting bosons subject to pump and losses. (Right) SEM image of the corresponding analog implementation with coupled microcavities, image adapted from [190].

strength and $U = U/\mathcal{A}$ the two-polariton interaction divided by the modal area $\mathcal{A}^{-1} = \int d^2\mathbf{r} |\psi_{1,1}|^4$, the polariton hamiltonian on a lattice is

$$\mathcal{H}_{BH} = \sum_i \hbar\omega_i \hat{p}_i^\dagger \hat{p}_i + \frac{U}{2} \sum_i \hat{p}_i^\dagger \hat{p}_i^\dagger \hat{p}_i \hat{p}_i - \sum_{\langle i,j \rangle} J_{(i,j)} (\hat{p}_i^\dagger \hat{p}_j + c.c.) \quad (2.48)$$

where \hat{p}^\dagger, \hat{p} are the creation-annihilation operators of a lower polariton in the discrete mode $|\psi_{1,1}\rangle$ with energy $\hbar\omega_i$. The brackets in the summation indices of the right-most term, indicate that nearest-neighbor coupling only are taken in account. In absence of dissipative processes ($\gamma \ll \hbar\omega, U, J$), the groundstate of this hamiltonian undergoes the superfluid to Mott insulator transition as the order parameter U/J becomes much larger than the lattice coordination number [191, 192].

In our system the losses can be made significantly smaller than the coupling strength, however even in state of the art samples $U \ll \gamma$, thus the dissipative processes cannot be adiabatically eliminated from the dynamics of the system. The possibility to coherently excite the system can be exploited to drive (prepare) it into any arbitrary steady-state [28, 37]. A coherent drive with frequency ω can be included as a time dependent on-site contribution to the total hamiltonian (cf. Sec. 2.3.2)

$$\mathcal{H}_D = i\eta \sum_i \mathcal{F}_i (\hat{p}_i^\dagger e^{i\omega t} - \hat{p}_i e^{-i\omega t}) \quad (2.49)$$

where η is proportional to the input coupling rate and \mathcal{F}_i is the complex amplitude of the pump on every site. Finally, single particle (polariton) losses can be included at the semiclassical level via an additional non-hermitian Hamiltonian $\mathcal{H}_{Loss} = -i \sum_j (\gamma_j/2) \langle \hat{p}_j^\dagger \hat{p}_j \rangle$ where γ_j is the on-site polariton decay rate at the frequency $\hbar\omega_j$ (cf. Sec. 2.3.1-2.3.4). Additional terms associated to a full quantum treatment of dissipation will be reviewed in the next section.

In summary, we have shown in the previous pages how to emulate lattice hamiltonians starting from micropillar cavities where polaritons are tightly confined in all spatial directions, thus defining the lattice sites. A finite spatial overlap between neighboring pillars can be mapped to a coherent coupling between the discrete polariton modes of the uncoupled microcavities. By tailoring the arrangement of the overlapping micropillars one can implement different 1D and 2D lattice models [49, 50, 188]. Furthermore,

the presence of polariton-polariton interactions allows exploring the physics of (weakly) interacting bosons on a lattice additionally featuring of one-body losses and a coherent drive term [48]. The combination of these ingredients puts forward microcavity polaritons as a versatile photonic platform for the emulation of the driven-dissipative Bose-Hubbard (DDBH) model. The development of such an analog emulator would allow the experimental investigation of dissipative phase-transitions in a scalable photonic platform [53, 193, 194, 195, 196, 197].

2.4.4 Master equation

In this section we want to write the equations ruling the dynamics of a quantum system subject to dissipative processes within a second quantization picture. As we will see, in most cases, polaritons can be accurately described with semiclassical models leaving aside an operatorial description of the observables. However, it is worth discussing the most general theoretical framework, both because it will be relevant for Chapter 6 and to clarify the physical meaning of the approximations introduced from time to time.

The problem of describing energy exchanges between an object and its surrounding environment, faced in the early 19th century by Thermodynamics, has been somehow extended to the quantum formalism only 50 years ago [198, 199, 200]. To tackle the problem, the idea is the following: consider an "universe" system (U), sum of an object (O) and of the surrounding environment (E), globally described as an isolated system obeying some known dynamical equations. Then, assuming that the environment is much larger than the object, allows neglecting the effect of the dynamics of the system on the dynamic of the bath. A summation over all the possible micro-states of the bath, supposed to be at equilibrium, allows marginalizing the bath and keep a description dependent only on the microscopic properties of the system, where the presence of a bath enters only via intensive quantities, such as its temperature. In the same spirit, if we consider the Hilbert space of the universe system $H_U = H_S \otimes H_B$, a pure state vector $|\psi\rangle$ in H_U will follow the Heisenberg equation of motion. Practically, preparing the state of the system is possible, but it is impossible to prepare the environment in a pure state. For this reason it is convenient to work with density matrices $\rho = \mathbb{E}[|\psi\rangle\langle\psi|]$, encoding in a statistical mixture of pure states our ignorance about the state of the environment. The hamiltonian of the total system can be decomposed as

$$\mathcal{H}_U = \mathcal{H}_S \otimes \mathbb{I}_B + \mathbb{I}_S \otimes \mathcal{H}_B + (\mathcal{H}_{SB} + c.c.) \quad (2.50)$$

where $\mathcal{H}_{S,B}$ are the terms acting only on the system or on the environment (bath) and \mathcal{H}_{SB} couples the two. Assume the effect of \mathcal{H}_{SB} to be perturbative both on the system and on the bath dynamics, i.e. a slow dissipation rate compared to the characteristic time of the system and no influence on the "infinitely" large bath (Born approximation). Then, one can also reasonably assume that the system is too small to perturb the environment, provided that the bath is at equilibrium, this implies a time independent density matrix for the bath degrees of freedom. This absence of memory in the bath (Markovianity) allows writing the universe density matrix as $\rho_U(t) = \rho_S(t) \otimes \rho_B$. Using the fact that ρ_B is time independent, the evolution of the object density matrix can be formally written by tracing out the bath degrees of freedom ($\hbar = 1$)

$$i\dot{\rho}_S(t) = \text{Tr}_B[[\mathcal{H}_U, \rho_U(t)]] = [\mathcal{H}_S, \rho_S(t)] + \text{Tr}_B[[\mathcal{H}_{SB}, \rho_S(t) \otimes \rho_B]] \quad (2.51)$$

thanks to the Born approximation, the hamiltonian \mathcal{H}_{SB} can also be expressed as a sum over all the possible system-bath interaction channels (ch) for tensor products of operators belonging to either the system or bath subspaces $\mathcal{H}_{SB} = \sum_k^{ch} J_{S,k} \otimes J_{B,k}$. Using this relation, completeness and neglecting within a secular approximation counter-rotating terms in the system-bath coupling [201] one finally can write the dynamical equation for the reduced matrix of the system:

$$\dot{\rho}_S = -i[\mathcal{H}_S, \rho_S] + \frac{1}{2} \sum_k^{ch} \gamma_k \left(2J_{S,k} \rho_S J_{S,k}^\dagger - \{J_{S,k}^\dagger J_{S,k}, \rho_S\} \right) \quad (2.52)$$

here γ_k is the rate of the k th interaction channel with the environment $\{\cdot, \cdot\}$ indicates an anticommutator and the operators $J_{S,k}$ are often called jump-operators and depend on the nature of the dissipative process. An alternative derivation relying on dynamical semigroups can be found in [199]. Hereafter we will drop the "S" subscript implicitly assuming that all the quantities refer only to the system, unless otherwise stated. For a bosonic system subject only to single-particle losses and in contact with a bath at an equilibrium temperature T , we have $J = a$ where a is the annihilation operator of an excitation in the system. Denoting $\mathcal{D}[\rho] = 2a\rho a^\dagger - \{a^\dagger a, \rho\}$, Eq. (2.52) becomes

$$\dot{\rho} = -i[\mathcal{H}, \rho] + \frac{\gamma}{2} \left((n_{th} + 1)\mathcal{D}[\rho] + n_{th}\mathcal{D}^\dagger[\rho] \right) \quad (2.53)$$

the two terms in the right-most part correspond respectively to the emission and absorption of an excitation in the bath, with n_{th} the average number of thermal excitations at the energy of the system eigenmodes. At optical frequencies $E \sim 1.45$ eV and liquid helium temperatures, since $k_B T \sim 0.4$ meV, one can always take $n_{th} = 0$ as a very good approximation due to the exponential damping in the Boltzmann factor. Furthermore, if \mathcal{H} is allowed to be non-hermitian, the right most term in Eq. (2.52) can be incorporated therein by defining

$$\mathcal{H}_{NH} = \mathcal{H} - i\frac{\gamma}{2} a^\dagger a \quad (2.54)$$

resulting in a non-unitary evolution of the state vectors of the system. Notice that this is exactly the phenomenological term included in Sec. 2.3.1 to the polariton hamiltonian in order to take in account the finite lifetime of the system. On the contrary, the term $2a\rho a^\dagger$ cannot be reabsorbed in the hamiltonian, thus preventing the simplification of Eq. (2.53) into an expression involving only pure states of the system. Interestingly, if we use the definition of expectation value of an observable $\langle \mathcal{O} \rangle = \text{Tr}[\rho \mathcal{O}]$, the linearity and cyclic property of the trace and the fact that $\text{Tr}[\dot{\rho}] = 0$, the time evolution of the expectation of the polariton field annihilation operator $\alpha = \langle a \rangle$ can be derived from Eq. (2.53). For a single mode of the polariton field we get ($\hbar = 1$)

$$i\dot{\alpha} = \left(-\Delta - i\frac{\gamma}{2} + U|\alpha|^2 \right) \alpha + i\sqrt{\gamma/2}\mathcal{F} \quad (2.55)$$

where $\Delta = (\omega_l - \omega_0)$ is the laser detuning relative to polariton eigenmode frequency ω_0 , and we moved to the frame rotating at the laser frequency. Remarkably, the above equation corresponds to the driven-dissipative Gross-Pitaevskii equation derived for a single mode of the polariton field in Sec. (2.3.2). As anticipated in Sec. 2.3.1, this indicates that we can understand the DDGPE as a classical approximation ruling the dynamics of the expectation values of the polariton field. Since quantum fluctuations and non-commutativity of the operators are dropped, this approximation is exact only for bilinear terms in the polariton operators. Instead, for the nonlinear term one has $\langle a^\dagger a a \rangle \rightarrow |\langle a \rangle|^2 \langle a \rangle$, i.e. correlations are dropped. This approximation thus fairly describes only the coherent states of the polariton field with large occupation numbers, i.e. when $1/\sqrt{n} \ll 1$ ensuring symmetrically distributed fluctuations about α . A more refined semiclassical treatment including the effect of fluctuations at the leading order will be discussed in Sec. 3.3.2.

Finally, we can conveniently rewrite Eq. (2.52) in the form $\dot{\rho} = \mathcal{L}[\rho]$ where \mathcal{L} is often called Liouvillian superoperator and is the infinitesimal generator of the quantum map $\rho(t + dt) = \Phi(\rho(t))$. The steady state density matrix of the system is therefore determined by $\mathcal{L}[\rho_{ss}] = 0$. Using a truncated Fock basis for the excitation Hilbert space, \mathcal{L} can be conveniently expressed in a matrix form [201, 202]. However the Liouvillian is not Hermitian, thus its eigenvectors are in general not orthogonal, or equivalently, left and right eigenvalues do not coincide [201, 202]. Excluding the exceptional points of the Hamiltonian parameter space or at the onset of a dissipative phase transition it can however be proved that \mathcal{L} can be diagonalized [203, 204]. Therefore \mathcal{L} admits a spectral decomposition

$$\rho(t) = \rho_{ss} + \sum_{k \neq 0} c_k(0) e^{-\lambda_k t} \rho_k \quad (2.56)$$

where λ_k (ρ_k) are the eigenvalues (eigenvectors) of the Liouvillian superoperator and $c_k(0) = \text{Tr}[\rho(0)\rho_k]$ are the projections of the initial density matrix. Notice that within a matrix representation of \mathcal{L} , if N is the Fock-state basis cutoff in the Hilbert space, the size of \mathcal{L} is $N^2 \times N^2$, thus making the diagonalization a tremendously hard problem as soon as N is large or when several modes of the polariton field need to be included in the calculation. The matrix representation of \mathcal{L} will be detailed among the numerical methods in Sec. 3.3.3.

In short, under suitable assumptions, we can describe a dissipative system via a master equation ruling the evolution of its density matrix. The action of the environment can be generally separated in two terms. Considering only single particle losses, the first one amounts to an additional non-hermitian term in the hamiltonian of the system, exponentially damping the average number of excitations over time. The interplay of this term with the coherent pumping determines the non-equilibrium steady-state of the microcavity. The second term, tends to mix the pure eigenstates of the system, and can be effectively seen as the back-action of the environment on the system [201]. Finally, we show that the driven-dissipative GPE is an approximate equation ruling the dynamics of the expectation values of the polariton field.

2.5 Summary

Sec. 2.1 discussed the properties of dielectric multilayer stacks and how they can be engineered to present photonic band-gaps. This feature can be used to create extremely high quality microcavities with a few-micron effective cavity length. Absorption is the main limiting factor for the cavity finesse in our samples. Furthermore the non-trivial polarization dependence of the photonic dispersion relation can be used in these cavities to observe optical analogues of the Spin-Hall effect [74, 76, 77].

In Sec. 2.2 the properties of Bulk and QW excitons are summarized. An iterative method for the determination of their properties in the delicate case of shallow QWs is presented, allowing a precise determination of the exciton binding energy, Bohr radius and oscillator strength. The latter allows estimating the optical response of the QW within a Lorenz-Drude model. Optical selection rules and exciton-exciton interactions were briefly discussed.

In Sec. 2.3 we have shown the different regimes of light matter coupling and their consequences on the properties of the fundamental excitations of the system. The hamiltonian description of exciton-polaritons is presented and benchmarked against a measurement of the polariton dispersion. An excellent agreement is found between the theoretical predictions based on the results of Sec. 2.1-2.2 and the experiment. Two optical excitation schemes, namely the quasi- and non-resonant excitation of microcavities are reviewed, along with the diverse phenomenologies arising in the high-polariton density regime. Finally, the dependence of the polariton lifetime on the parameters of the system is theoretically addressed: inhomogeneous broadening of the exciton transition appears as the main limiting factor for state of the art samples.

Sec. 2.4 surveys the most relevant strategies developed over the years to engineer polariton transverse modes. Focusing on the technique developed in C2N, that is deep etching of a preexisting planar heterostructure, we discuss how to implement an analog platform for the emulation of lattice hamiltonians. The fundamental building block of the lattice are micropillar cavities presenting discrete optical modes. A small spatial overlap between the pillars can be used to mimic a coupling term. The measured scaling of the couplings and of the on site energies is in excellent agreement with theory. The limitations of a tight-binding (LCAO) description are presented as well as the inverse design problem. Lastly, we presented a formal description of the microcavity polariton dynamics within the framework of master equations for open quantum systems.

2.6 Appendix A: Finite element simulations

In this section we briefly discuss how to use finite element methods to determine the optical modes of arbitrarily shaped micropillar structures. As mentioned in the introduction to Sec. 2.4.1, provided the characteristic lateral size of a microstructure is significantly larger than the wavelength of its confined modes, one can work in the paraxial approximation where the longitudinal and transverse electromagnetic field components are decoupled [184]. The longitudinal field profile can be determined using a transfer matrix method for the dielectric layer stacks forming the Fabry-Perot cavity. The longitudinal field profile is then used to determine the effective refractive index of the structure ($n_{eff} \approx 3.4$, cf Sec. 2.1.2). After this step the microcavity can be thought as an homogeneous infinite waveguide along the longitudinal direction sharing the same cross-section. We discuss hereafter three decreasing degrees of approximation which can be used to determine the transverse components of electromagnetic field within the "equivalent waveguide" picture. In absence of sources and charges, we can start by considering the vector-wave equation for the electric field vector \mathbf{E} in the waveguide structure

$$\nabla \times \nabla \times \mathbf{E} - (\omega/c)^2 \epsilon_r \mathbf{E} = 0 \quad (2.57)$$

where ω is the carrier wave frequency, c is the speed of light in vacuum and ϵ_r is the (spatially dependent) relative permittivity. We consider the waveguide axis to be oriented along z , and denote Ω its cross-section in the (xy) plane. Assuming a perfect dielectric, $\epsilon_r(x, y)$ is a step function returning n_{eff}^2 for $(x, y) \in \Omega$ and 1 otherwise. Using the relation $\nabla \times \nabla \times \mathbf{E} = \nabla(\nabla \cdot \mathbf{E}) - \nabla^2 \mathbf{E}$ and the charge-free condition $\nabla \cdot (\epsilon_0 \epsilon_r \mathbf{E}) = 0$ to rewrite $\nabla \cdot \mathbf{E} = -\epsilon^{-1}(\nabla \epsilon \cdot \mathbf{E})$, Eq. 2.57 becomes

$$\begin{aligned} 0 &= \nabla^2 \mathbf{E} + (\omega/c)^2 \epsilon_r \mathbf{E} - \nabla(\mathbf{E} \cdot \nabla \log \epsilon_r) \\ &= \nabla^2 \mathbf{E} + (\omega/c)^2 [\epsilon_r \mathbf{E} - (c^2/\omega^2) \nabla(\epsilon^{-1}(\nabla \epsilon \cdot \mathbf{E}))] \end{aligned} \quad (2.58)$$

whereas the first term within square brackets has order of magnitude $\mathcal{O}(n_{eff}^2) \mathbf{E}$, the second is $\mathcal{O}(n_{eff}^2/kl) \mathbf{E}$ with $k = 2\pi/\lambda$ is the vacuum wavevector and l is the characteristic length over which the electric field changes appreciably [205]. If we consider as an example the fundamental guided mode of a micropillar (i.e. modeled as circular waveguide) with radius $R \sim 2\mu\text{m}$ and resonant wavelength $\lambda_0 \sim 850\text{ nm}$, we get $kl \sim 2\pi R/\lambda_0 \sim 15^1$. Therefore, within a first order approximation, we can neglect the second term in the square brackets. This brings us to the first approximation:

OPTICAL SHRÖDINGER EQUATION: in absence of the $\nabla(\epsilon^{-1}(\nabla \epsilon \cdot \mathbf{E}))$ terms, each component of Eq. (2.58) decouples. We can then write a transverse wave in the form $\mathbf{E} = u(\mathbf{r}) \mathbf{e}_p$ for each polarization vector \mathbf{e}_p . Eq. (2.58) becomes then a scalar wave equation for the slowly varying envelope $u(\mathbf{r})$. For guided modes we have $u(\mathbf{r}) = u(x, y) e^{i\beta_n z}$ where β_n is the propagation constant of the n th-mode. Eq. (2.58) yields

$$\begin{aligned} (\nabla_{xy}^2 + n^2(x, y) k^2) u(x, y) &= \beta_n^2 u(x, y) \\ [(\hbar c)^2 \nabla_{xy}^2 + E_0^2 n^2(x, y)] u(x, y) &= n_{eff}^2 (E_0 + \delta E_n)^2 u(x, y) \end{aligned} \quad (2.59)$$

¹Notice that higher order modes present smaller spatial features, thus smaller l values.

In the last passage we have multiplied both sides for $(\hbar c)^2$, used $E_0 = \hbar c k$ and introduced $\delta E_n = \hbar c \delta k_n$, where δk_n represents the wavevector shift along z for the guided mode. For typical micropillar sizes $\lambda_0/n_{eff}R \ll 1$ thus $\delta E/E_0 = \mathcal{O}(\hbar c/E_0 n_{eff}R)^2 = \mathcal{O}(\lambda_0/n_{eff}R)^2 \lll 1^2$. Then we can safely drop the $\mathcal{O}(\delta E^2)$ terms in in Eq. (2.59), subtract to both sides $n_{eff}^2 E_0^2$ and divide both sides by $2E_0 n_{eff}^2$; we end up with the following eigenvalue problem

$$\left[-\frac{\hbar^2 c^2}{2E_0 n_{eff}^2} \nabla_{xy}^2 + \frac{E_0}{2} \frac{n_{eff}^2 - n^2(x, y)}{n_{eff}^2} \right] u(x, y) = \delta E u(x, y). \quad (2.60)$$

Noticing that $E_0 n_{eff}^2/c^2 = m_c^*$ is the effective mass of a photon in a planar microcavity (cf. Sec. 2.1.2), we recognize in the above equation the familiar two-dimensional Shrodinger problem for a single particle in the step potential $V(x, y) \approx E_0 \Theta(\Omega)/2$ where $\Theta(\Omega) = 0$ if $(x, y) \in \Omega$ and 1 otherwise. For this reason Eq. (2.60) is often referred as the optical Shrödinger equation³ [184]. Eq. (2.60) can be solved numerically by finite element methods, imposing homogeneous Dirichlet boundary conditions on a curve $\partial\Omega'$ enclosing Ω , such that $\min\|\partial\Omega' - \partial\Omega\| \gg d_0$ with d_0 being the decay length of evanescent tails outside the waveguide. Since a rough estimate of d_0 is given by $\lambda_0/2\pi(n_{eff}^2 - 1)^{1/2} \sim 40$ nm, it is safe to choose the outer discretization boundary $\partial\Omega'$ just 1 μm apart from any edge of the waveguide. For Mathematica users, this can be simply implemented via the built-in function NDEigensolve: specifying an Arnoldi iterative method for the eigenvalue problem and a Delaunay mesh with a maximal cell area of $10^{-2} \mu\text{m}^2$ yields in few seconds satisfactory results over a 100 μm^2 region.

Solving the optical Shrödinger equation allows determining the the scalar mode structure and radiation pattern for any coupled micropillar arrangement. This is relevant both for experiments where the TE-TM splitting is much smaller than the cavity linewidth but also for experiments where one excites (or post-selects) only a particular polarization component of the microcavity emission. Some examples are the spatial mode profiles presented in Sec. 2.4.1 and 2.4.2 for single and coupled micropillar structures. Of course, the far-field radiation patterns $\tilde{u}_n(k_x, k_y)$ can be obtained as the FFT of $u_n(x, y)$.

OPTICAL PAULI EQUATION: dealing with dielectric Fabry-Perot entails that the effective refractive index (related to photon effective mass) can be different TE and TM modes. Such effect vanishes for a cavity spacer whose optical thickness perfectly matches the central wavelength of the DBR, but in general is non-zero leading to an effective coupling of the pseudo-spin components of the optical field, see Sec. 2.1.2 for details. Additionally, when the transverse size of a microstructure is progressively reduced, due to the different interface continuity relations, the TE and TM waves may couple at the boundary of the structure. For micron-sized structures, these polarization-dependent effects are typically second order in the perturbations, as discussed in the previous paragraph. However, in high-finesse microcavities, the linewidth may become sufficiently narrow to reveal the fine structure of the optical modes. Introducing the spinor wavefunction $\psi_\sigma(x, y) = u(x, y)\mathbf{e}_\sigma$ with $\mathbf{e}_{+1} = (1, 0)^T$ and $\mathbf{e}_{-1} = (0, 1)^T$ representing the photon circular polarizations, the coupling of TE-TM modes can be included by taking the position representation of the effective spin-orbit coupling hamiltonian

²The scaling analysis is based on Eq. (2.46).

³The same equation can be equivalently derived starting from the paraxial Helmholtz equation and identifying the z coordinate with time by introducing the rescaled variable $t = z/c$.

Eq. (2.8) [74, 79]. Introducing the average effective refractive index for the TE and TM modes $\tilde{n} = (n_{eff}^{TE} + n_{eff}^{TM})/2$ some calculation yields

$$\begin{pmatrix} -\frac{\hbar^2 c^2 \nabla^2}{2E_0 \tilde{n}^2} + V(x, y) & \Delta_{so}(\partial_x - i\partial_y)^2 \\ \Delta_{so}(\partial_x + i\partial_y)^2 & -\frac{\hbar^2 c^2 \nabla^2}{2E_0 \tilde{n}^2} + V(x, y) \end{pmatrix} \psi_\sigma(x, y) = \delta E \psi_\sigma(x, y) \quad (2.61)$$

where Δ_{so} is the polarization coupling strength and can be decomposed in the sum of two terms. The first one relates to the different effective refractive indices for the TE and TM modes; denoting $\delta n = (n_{eff}^{TE} - n_{eff}^{TM})$ we have

$$\Delta'_{so} = \frac{\hbar^2}{2} \left(\frac{1}{m_{TE}^*} - \frac{1}{m_{TM}^*} \right) = \frac{(\hbar c)^2}{E_0 \tilde{n}^2} \frac{\delta n}{\tilde{n}} + \mathcal{O} \left(\frac{\delta n}{\tilde{n}} \right)^3. \quad (2.62)$$

Notice that δn can be both positive or negative. The second term, Δ''_{so} , comes from the boundary conditions, depends on the geometry of the microstructure and can be generally deduced from experiments. Again, the solutions of Eq. (2.61) can be found using finite element methods: one example is given in Chap. 4-Fig. 4.4 where we present the intensity patterns of the first twelve eigenmodes of an hexagonal arrangement of micropillars.

VECTOR WAVE EQUATIONS: if the properties of coupled micropillar structures needs to be finely engineered a priori, it is also possible to directly solve the vector-wave equations. In absence of charges and for a perfect dielectric we have that the \mathbf{E} field components satisfy Eq. (2.58) and the \mathbf{H} field obeys

$$0 = [\nabla^2 + (\omega/c)^2 \epsilon_r] \mathbf{H} - (\nabla \times \mathbf{H}) \times (\nabla \log \epsilon_r) \quad (2.63)$$

when modeling the microstructures as an equivalent waveguide, we can use the translational invariance along z to use the following ansatz: $\mathbf{E} = \sum_j E_j(x, y) \mathbf{e}_j e^{i\beta z}$ where \mathbf{e}_j denote the unit vectors of the cartesian coordinate basis (and similarly for \mathbf{H}). Solving for the TE(TM) waves one can additionally require $E_z = 0$ ($H_z = 0$) and developing β for small deviations around $n_{eff} k_0$, allows deriving from Eq. (2.58) and (2.63) two eigenvalue problems for the transverse components of \mathbf{E} and \mathbf{H} [206]. Assuming a step discontinuity in the refractive index profile at the waveguide boundary $\partial\Omega$, one needs to impose the interface continuity relations for E and H . Alternatively, one can artificially smooth ϵ_r in a narrow region about $\delta\Omega$, thus ensuring the continuity of the fields [207]. Implementing a hyperbolic tangent smoothing over a characteristic length of 50 nm, supported by a local refinement of the discretization mesh (cell area $\sim 20 \text{ nm}^2$) around the boundary $\partial\Omega$ allows reaching fairly accurate results. If we denote with ϵ_n the eigenvalues of the vector wave equations and denote $E_0 = \hbar c k_0$ the resonance at normal incidence of the planar cavity, we can express the energy blueshift of the microstructure eigenmodes with respect to E_0 as $\delta E_n = \hbar c \epsilon_n / (\epsilon_n / 2 - 2k_0 n_{eff}^2)$. We also stress that, upon choosing correctly the phenomenological TE-TM coupling Δ''_{so} , the results Eq. (2.61) and Eqs. (2.58)-(2.63) yield, present excellent agreement.

PERIODIC MICROPILLAR ARRANGEMENTS: in Sec. 2.4 we have described how to understand the collective modes of any pillar arrangement based on an intuitive tight-binding picture. This approximation often yields qualitative predictions however, in

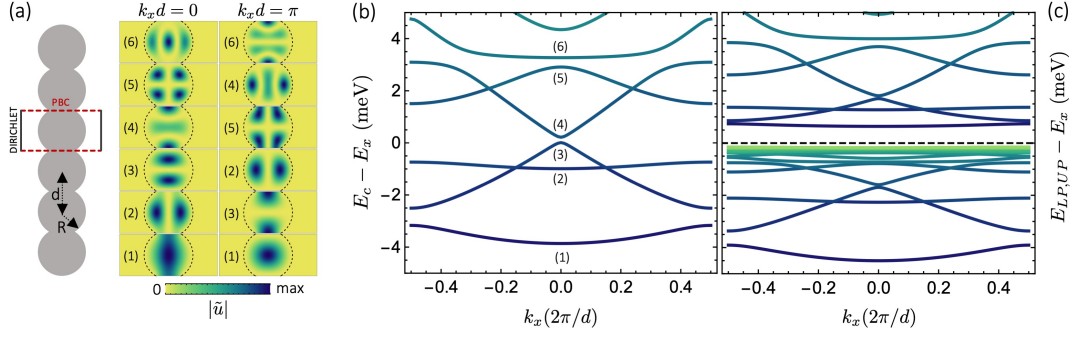


Figure 2.17: **Bandstructure of a 1D micropillar lattice:** (a) Illustration of the finite element boundary conditions (left) and envelopes of the first six Bloch modes deduced via Eq. 2.64 at $k_x d = (0, \pi)$ (right). Other parameters are $n_{eff} = 3.38$, $d = 3.4 \mu\text{m}$ and $R = 2 \mu\text{m}$. (b) Photonic bandstructure of the 1D lattice of micropillars; here the bare planar cavity exciton-photon detuning is $\delta_{cx} = -5 \text{ meV}$. (c) Lower and upper polariton dispersion relation corresponding to panel (b).

some situations (e.g. large pillar overlap), it may become inaccurate as the bare eigenmodes of each resonator are not anymore a good orthonormal basis (cf. Sec. 2.4.2). If a more quantitative model is needed, finite elements offer a rather accurate and efficient solution. One relevant question is to determine the polariton dispersion relation in a given microresonator lattice. As an example, we consider a basic problem: determining the scalar bandstructure of a periodic 1D arrangement of micropillars. We denote R the pillar radius and d the center-to-center distance, as Fig. 2.17-(a) illustrates. Exploiting the discrete translational symmetry of the lattice it is convenient to set up periodic boundary conditions on the finite element cell. Then, the Bloch theorem suggest us that the solution of Eq. (2.60) must be in the form $u(x, y) = \tilde{u}(x, y)e^{ik_x x}$. Inserting this relation in Eq. (2.60), we find the modified eigenvalue problem for the Bloch-wave envelopes

$$\left[-\frac{\hbar^2}{2m_c^*} (\nabla_{xy}^2 + 2ik_x \partial_x - k_x^2) + V_{eff}(x, y) \right] \tilde{u}_n(x, y) = \delta E_n(k_x) \tilde{u}_n(x, y). \quad (2.64)$$

Sampling the first n eigenvalues $\delta E_n(k_x)$ as a function of $k_x \in (-\pi/d, \pi/d)$ allows reconstructing the first n bands of the photon dispersion relation in the microcavity lattice. Finally, to convert the photonic bands into the polariton dispersion relation suffices using Eq. (2.31). In Fig. 2.17 we summarize the results of this calculation. These arguments can be straightforwardly generalized to 2D lattices by considering appropriate periodic boundary condition, as well as to each component of Eq. (2.61) to include polarization dependent effects.

Experimental and numerical techniques

These pages survey the experimental and theoretical tools which will be routinely used in the remaining part of the manuscript; the informations are organized in three sections. In Sec. 3.1, we describe the sample design criteria and fabrication protocol, highlighting the rational behind the choice of each parameter and some important details for the installation of the sample in the cryostat. Section 3.2, presents the experimental setup and two prototypical experiments. In the first, we characterize the magnification properties of the confocal microscope used for imaging the emission of the microstructure. In the second, we use a resonant excitation scheme to investigate the spectral properties of a discrete mode in a single micropillar cavity. Finally, Sec. 3.3 illustrates three possible approaches to calculate the steady-state properties and the dynamics of a system of coupled microcavities. The three approaches correspond to different levels of approximation: mean-field, truncated-Wigner and the quantum master equation.

3.1 Sample preparation

In this manuscript we focused mostly on two samples, both of them were originally conceived to study the nonlinear phenomena arising in micropillar structures where polaritons are tightly confined. In these experiments one is interested working with a quasi-resonant excitation scheme (cf. Sec. 2.3.2), which is possible both in a reflection or transmission geometry. The latter configuration however, has the significant advantage that one does not need to filter out the portion of light which is not coupled to the microstructure, allowing cleaner and technically easier experiments. For this reason, we decided to work with shallow $\text{In}_p\text{Ga}_{1-p}\text{As}$ QWs ($p = 0.04 - 0.05$) which are characterized by excitonic optical transitions well below the gap of any AlGaAs alloy forming the rest of the microstructure (cf. Sec. 2.2). Moreover, in order to maximize the strength of polariton-polariton interactions we work with a single quantum well, as excitons belonging to spatially separated quantum wells do not feel each other. Notice that, if we were interested in high-power off-resonant excitation experiments, e.g. to

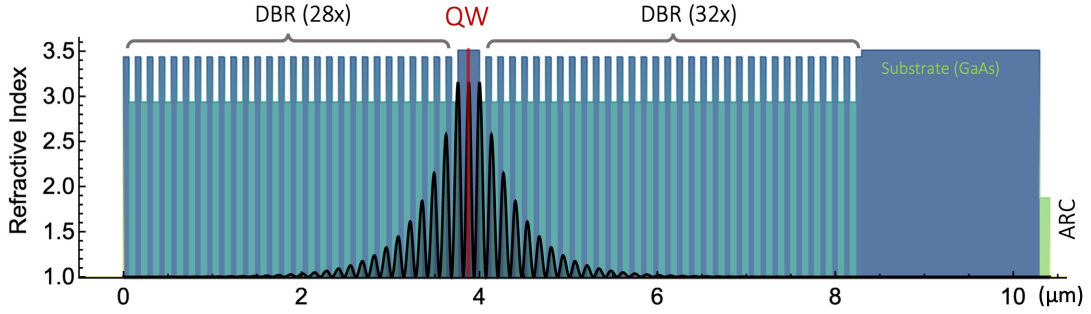
investigate polariton condensation and lasing, it would be instead desirable to have a large number of quantum wells to increase the power threshold for the exciton saturation density n_0 . Indeed for N quantum wells equally coupled to the cavity field, the resonant polariton interaction scales as $\sim N^{-1}$, the Rabi splitting as $\sim \sqrt{N}$ and the saturation density as $\sim N^{-3/2}$ [34, 108]. Having this general idea in mind, we illustrate the sample design criteria.

3.1.1 Design

The quality of InGaAs QWs is higher when GaAs is chosen as embedding matrix, thus being the natural choice for the cavity spacer material. GaAs has the highest refractive index among the AlGaAs alloys forming the rest of the heterostructure, meaning we have to work with a guiding-type cavity. In order to maximize the light-matter coupling strength, we have to position the QW at an antinode of the cavity field, using the smallest possible cavity length, in this case $L_c = \lambda_c$, where λ_c is the central wavelength of the Bragg mirrors. In our samples, residual absorption in the cavity spacer is the most important limiting factor of the cavity finesse \mathcal{F} . As already pointed out in section 2.1, some absorption mechanisms are due to the fabrication process (residual doping, interface roughness) and some are inherent to the material properties (Urbach tails). In order to minimize the latter, one needs to work with polariton modes as far as possible from the GaAs bandgap edge.

To do so, one can increase the Indium content: for 15 nm wide $\text{In}_p\text{Ga}_{1-p}\text{As}$ QWs the exciton optical transition wavelength redshifts with a linear slope $\Delta\lambda = 7.6(6) \cdot 10^2 p$ nm for $p < 0.15$. However, an increased Indium content typically leads to stronger alloy-fluctuations in the QW, resulting in an inhomogeneous broadening of the exciton emission spectrum. For the best QWs we observed a nearly constant inhomogeneous broadening up to $p = 0.05$ then increasing with a slope $(p - 0.05) \cdot 11(2)$ meV. This effect is detrimental for the polariton linewidth as Sec. 2.3.4 demonstrated. Another contribution to the inhomogeneous broadening of the exciton transition is due to thickness fluctuations of the QW layer, which can be minimized by working with wide and shallow QWs. In principle, one may want to work with extremely wide QWs to minimize this effect. However, this might result in a reduction of the light-matter coupling constant and in an enhanced strain within the QW layer because the lattice constants of InAs is roughly 7% larger than GaAs.

The best compromise we found between the reduction of the absorption in the cavity while minimizing the inhomogeneous broadening and strain effects are (15 – 20) nm wide $p = (0.04 - 0.05)$ $\text{In}_p\text{Ga}_{1-p}\text{As}$ QWs. We concluded that any further improvement of the planar heterostructure design should aim at reducing the GaAs layer thickness and inhomogeneous broadening for a $p = 0.05(1)$, for instance exploiting adiabatic cavity designs [208, 209, 210] and strain-releasing superlattices [178]. Regarding the $\text{Al}_x\text{Ga}_{1-x}\text{As}$ alloys chosen for the two DBR layers, common practice is to pick AlAs and GaAs in order to maximize the DBR stop-band [Eq. (2.7)]. However GaAs introduces additional absorption in the DBR layers close to the cavity spacer and AlAs tends to oxidize quickly in ambient pressure conditions, being potentially detrimental for microstructures with a large surface to volume ratio. A good compromise is the pair of Aluminum fractions $x = (0.1, 0.95)$. With these considerations in mind, we designed two planar heterostructures, that were used for all the experiment presented in this manuscript. Specifications are detailed in Tab. 3.1.1.



| | DESIGN 1 | δz (nm) | $n(\lambda_0)$ | N_{It} | DESIGN 2 | δz (nm) | $n(\lambda_0)$ | N_{It} |
|------------------|--|------------------|----------------|----------|--|------------------|----------------|----------|
| DBR ₁ | Al _{0.10} Ga _{0.90} As | 60.9 | 3.44 | 32 | Al _{0.10} Ga _{0.90} As | 62.0 | 3.43 | 28 |
| DBR ₂ | Al _{0.95} Ga _{0.05} As | 71.5 | 2.94 | 32 | Al _{0.95} Ga _{0.05} As | 72.6 | 2.93 | 28 |
| SP | GaAs | 110.8 | 3.52 | 1 | GaAs | 113.6 | 3.51 | 1 |
| QW | In _{0.04} Ga _{0.96} As | 17.0 | 3.52 | 1 | In _{0.05} Ga _{0.95} As | 15.0 | 3.51 | 1 |
| SP | GaAs | 110.8 | 3.52 | 1 | GaAs | 113.6 | 3.51 | 1 |
| DBR ₂ | Al _{0.95} Ga _{0.05} As | 71.5 | 2.94 | 36 | Al _{0.95} Ga _{0.05} As | 72.6 | 2.93 | 32 |
| DBR ₁ | Al _{0.10} Ga _{0.90} As | 60.9 | 3.44 | 36 | Al _{0.10} Ga _{0.90} As | 62.0 | 3.43 | 32 |
| SUB | GaAs | $3.5 \cdot 10^5$ | 3.52 | 1 | GaAs | $3.5 \cdot 10^5$ | 3.51 | 1 |
| ARC | SiO _{0.18} N _{1.22} | 111.9 | 1.88 | 1 | SiO _{0.18} N _{1.22} | 113.5 | 1.88 | 1 |

Table 3.1: **Sample design parameters:** Nominal parameters used for the growth of the two planar heterostructures. Design 1 and 2 target a central cavity wavelength λ_0 of 840 nm and 852 nm, respectively. Abbreviations: (DBR_{1,2}) quarter wave stacks forming dielectric mirrors, SP spacer layer, QW quantum well, (SUB) substrate wafer, (ARC) anti-reflective coating, δz is the layer thickness, $n(\lambda_0)$ is the refractive index of the alloy evaluated at λ_0 and N_{It} is the number of repetitions of each layer. The stoichiometric indexes in the Silicon Oxynitride layer are referred with respect to the Si abundance.

Notice that in all designs the bottom mirror has four more pairs than the top one. This is because the reflectivity of the bottom DBR is reduced due to the high refractive index of the substrate: the condition $N_{\text{bot}} = N_{\text{top}} + 4$ allows to balance this effect and work in a symmetric cavity configuration. Notice that in the conception of the first design we underestimated the absorption in the cavity, as it fluctuates from sample to sample and therefore we included too many mirror pairs. As a result, the transmission at resonance was pretty poor ($\mathcal{T}_0 \sim 0.1$). After a thorough characterization of different samples, we concluded that on average the second design gives the best compromise between the achievable linewidth (including absorption) $\gamma \approx 20 \mu\text{eV}$ and a transmission at resonance of $\mathcal{T}_0 \approx 0.65$ (see Fig. 2.3).

Indeed, if we consider for simplicity an empty cavity, we have two competing loss mechanisms: the radiative losses and absorption, with associated rates γ_c and γ_a , respectively. Using a classical oscillator model to describe the cavity field dynamics, one easily finds that the cavity transmission spectrum is Lorentzian with a linewidth $\Gamma = \gamma_c + \gamma_a$ and peak transmission coefficient $\mathcal{T}_0 = (\gamma_c/\Gamma)^2$ [70]. Whereas γ_c can be in principle made arbitrarily small by increasing the number of pairs in the DBRs, γ_a is constant, as it depends only on the residual absorption coefficient at a given wavelength. Therefore, once $\gamma_c \sim \gamma_a$, further increasing the DBR pairs is counter-productive as the cavity linewidth quickly saturates to its absorption-limited value while one loses all the transmitted power. Having in mind to probe dynamical phenomena

in a few-polariton excitation regime, keeping a collection efficiency as large as possible is extremely important.

3.1.2 Fabrication

Figure 3.1-(a) summarizes the main sample processing steps. (1) We use an undoped double-polished two inch GaAs wafer with a nominal thickness of 350 μm . (2) The wafer is introduced in a Molecular beam epitaxy (MBE) reactor [211], where the designed heterostructure is grown atomic layer by atomic layer. Since the growth process elapses up to 12h, a careful calibration of the Knudsen cell heaters flux is preliminarily done, and corrected for drifts due to cell emptying. For the calibration a Reflection High-Energy Electron Diffraction (RHEED) technique is used. Importantly, the molecular beams are not perfectly collimated and arrive with an angle on the substrate wafer, thus creating a deposition rate spatial gradient, which can be eventually minimized by rotating the wafer. This effect can be advantageously used to obtain a spatial gradient of the cavity central wavelength over the sample, allowing to change the relative detuning with respect to the QW exciton transition. In absence of rotation the detuning gradient is typically $\delta\Delta_{cx} \sim 6.5$ meV/mm but can be otherwise progressively reduced down to $\delta\Delta_{cx} \sim 0.1$ meV/mm. According to an atomic force microscopy (AFM) characterization, rotating the sample is beneficial for the surface reconstruction quality (~ 1 nm rms over 100 μm^2) whereas, without rotation, dense point and line defects have been observed possibly limiting the cavity finesse.

Once the growth of the planar heterostructure is complete, we proceed to characterize the cavity mode gradient in order to select a useful portion of the sample for the following steps of the fabrication process. Figure 3.1-(b) shows an example of a reflectivity spectrum of the planar cavity measured by Fourier-transform infrared spectroscopy (FTIR) at room temperature and in proximity of the wafer center. From the stop-band shoulders we deduce the cavity central wavelength, and by repeating the measurement for ~ 120 regularly spaced positions across the wafer we reconstruct a spatial map of the cavity resonance. Since the exciton energy is known from previous calibrations, we can build an exciton-photon detuning map Δ_{cx} , as shown in Fig. 3.1-(b). Notice that since the reflectivity measurements were taken at room temperature the resonance wavelength needs to be corrected for the cavity effective refractive index shift between 4 K and room temperature. The black rectangle in Fig. 3.1-(b) corresponds to a (15 \times 6) mm portion of the wafer selected as a sample. To isolate this piece we inscribe with a diamond tip cleaving grooves on the substrate side and propagate them applying a gentle pressure. The sample is then carefully cleaned from dust and washed in a bath of acetone followed by optical grade purity isopropanol to remove any residue on the surfaces, mild sonication can also be used, finally a nitrogen blower is used to quickly dry the solvents on the surface.

(3) In order to suppress spurious Fabry-Perot effects between the bottom DBR and the end facet of the substrate we also deposit a Silicon Oxynitride quarter-wavelength anti reflective coating (ARC). The quarter-wavelength ARC refractive index must be the square root of the one of Gallium Arsenide; given the refractive index around 850 nm for SiO_2 ($n = 1.45$) and Si_3N_4 ($n = 2.02$) a stoichiometry relative to Silicon of 0.18 for Oxygen and 1.22 for Nitrogen, allows us obtaining the desired dielectric coating ($n = 1.88$). In Fig. 3.1-(c) we show a measurement of the substrate reflectivity before (gray) and after (red) the deposition of the ARC layer. In a 25 nm wide region

centered at 845 nm the reflectivity is suppressed by four orders of magnitude, dropping below the noise floor of the apparatus, testifying the effectiveness of the ARC. Notice that the central wavelength of the ARC in Fig. 3.1-(c) is intentionally blue-shifted with respect to the ≈ 852 nm target to compensate for the temperature-dependent refractive index shift. We also point out that Silicon Oxynitride is a ceramic type material with very poor thermal conduction properties. This is an important point to remember when designing the thermal anchorage of the sample to the cold finger of the cryostat. Afterwards, plasma-enhanced chemical vapor deposition (PECVD) is used to deposit a $2 \mu\text{m}$ Silicon Nitride layer on the epitaxial side.

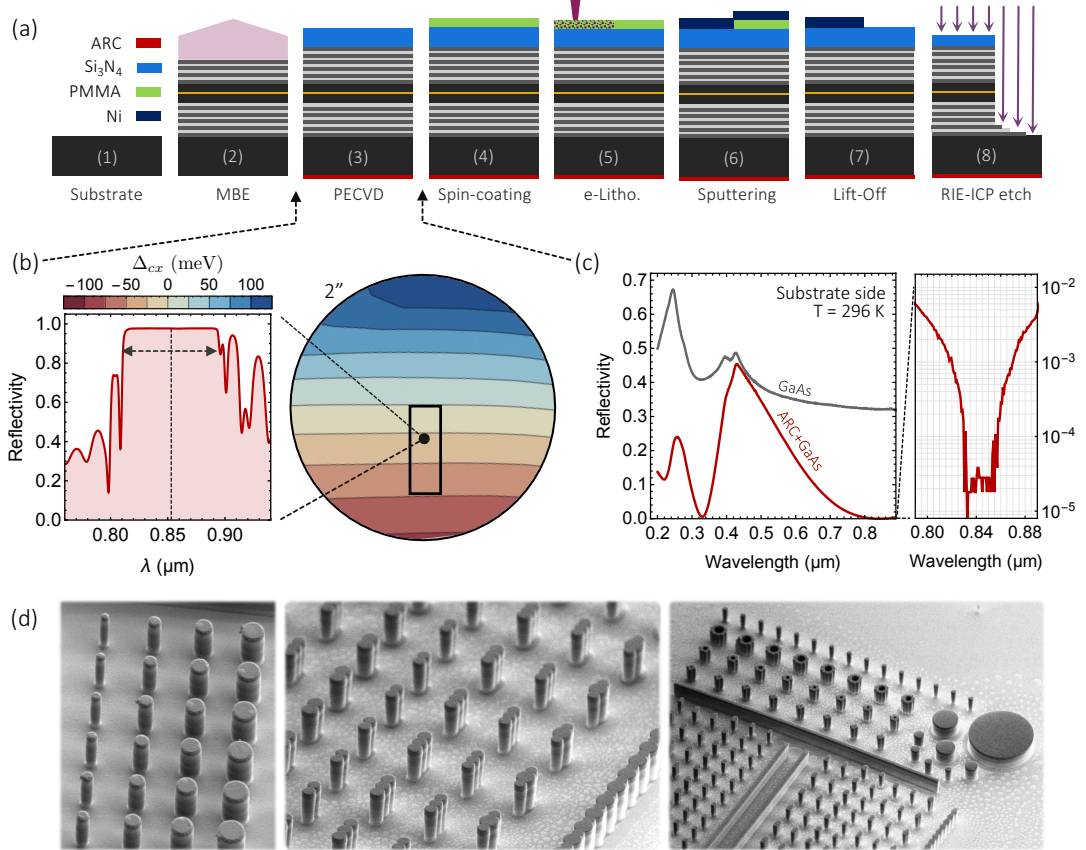


Figure 3.1: **Sample fabrication:** (a) Flow diagram of the sample fabrication (details in the main text). (b) Reflectivity spectra obtained by Fourier-transform infrared spectroscopy (FTIR) are used to map the cavity resonance across the two inch diameter planar heterostructure. Provided the energy of the exciton transition is known, this allows to derive an exciton-photon detuning map Δ_{cx} . Accordingly, a small piece of the wafer is selected for steps (3-8) of the fabrication (Black rectangle). (c) Reflectivity spectrum of the GaAs substrate before and after the anti reflective coating (ARC) deposition in step (3). The central wavelength of the ARC can be tuned with the layer thickness. (d) Representative SEM images of the microstructures fabricated with the process (1-8).

(4) Spin-coating is used to spread a drop of a Polymethyl methacrylate (PMMA) in solution, the resulting ~ 40 nm film is baked in an oven through the glass transition temperature. (5) Electron-beam lithography is used to imprint on the polymer the microstructure pattern, causing localized de-cross-linking within the PMMA. After

chemical development the PMMA layer is left only on the negative of the imprinted mask. To avoid proximity effects we keep a $\sim 20 \mu\text{m}$ minimal distance between the edge of neighboring structures. (6) A metallization reactor is used to deposit 60 nm of Nickel. (7) A sonicated bath in acetone lifts off the negative PMMA mask with the Ni layer. (8) Finally, a reactive ion etching (RIE) followed by a selective Inductively-coupled plasma (ICP) etching step is used to retain the positive of the sample mask. In Fig. 3.1 we show some SEM images of the different microstructures fabricated with this process.

3.2 Experimental Setup

In Fig. 3.2 we show a schematic representation of the core elements of the setup which has been used in all the experiments presented in this manuscript. From time to time, small adaptation of the setup have been implemented and will be detailed later on. The setup is organized in two main parts, the first one is devoted to the preparation and control of the laser beam properties, the second allows to collect the sample emission both in reflection and transmission geometries. Two laser sources are installed in the setup to ensure the possibility of using both continuous-wave (CW) and pulsed excitation schemes. The CW laser source is a tunable Ti:Sapphire oscillator (SolsTIS-PSX-R pumped by a 10W Millennia Xs) with a measured sub-MHz linewidth. The wavelength of the CW laser is constantly monitored via a high-finesse wave-meter and can be locked in frequency using a feedback loop. In absence of feedback loop (passive cavity) the wavelength drift is typically 0.4 pm over 10 minutes, mostly due to the temperature/humidity variations in the laboratory. When the feedback is activated, the wavelength is locked with a rms fluctuation of 0.02 pm. Above 100 Hz the laser power spectral density is shot noise-limited. The MSquared bowtie cavity produces an output beam with a 0.30(2) mm internal waist and a 1.4 mrad half-angle divergence. The pulsed laser is a mode-locked tunable Ti:Sapphire laser (Tsunami pumped by a 10W Millennia Xs) producing 2.6 ps wave-packets at a 81.16 MHz repetition rate. The (external) beam waist was 0.81(2) mm with a half angle divergence of 0.57 mrad.

The CW laser beam is collimated by a 500 mm focal length achromatic doublet (L_1) and is epurated from the small unconverted 532 nm pump beam residue using a low-pass filter. The average power of each laser beam can be roughly adjusted independently using a HWP facing the PBS where the two are combined. A telescope with a 2/3 magnification (T_1) in the pulsed laser arm has been used to mode-match the two beams having a common waist in the plane of the quarter-wave plate (QWP) preceding the electro-optical modulator (EOM). The free-space amplitude EOM has a bandwidth of 100 MHz and a full-wave modulation voltage of 270 V at 850 nm; a high-voltage amplifier (Falco systems) allowed full modulation in a DC to 5 MHz bandwidth. A beam expander (T_2 , 3/2 magnification) in combination with a 11 mm focal length aspheric lens has been used to launch the two beams into a single-mode polarization maintaining fiber. At the fiber output the beam is separated in two by a 50 : 50 beam-splitter: one of the arms goes to the experiment, the second is used to monitor the laser power via a photodiode (PD). The PD output is sent to a proportional-integral (PI) servo circuit feeding a 1 kHz bandwidth variable optical attenuator (VOA) coupled to the single mode fiber. When activated this feedback-loop allowed a stabilization of the relative DC power level to better than $3 \cdot 10^{-4}$. In combination with the EOM this

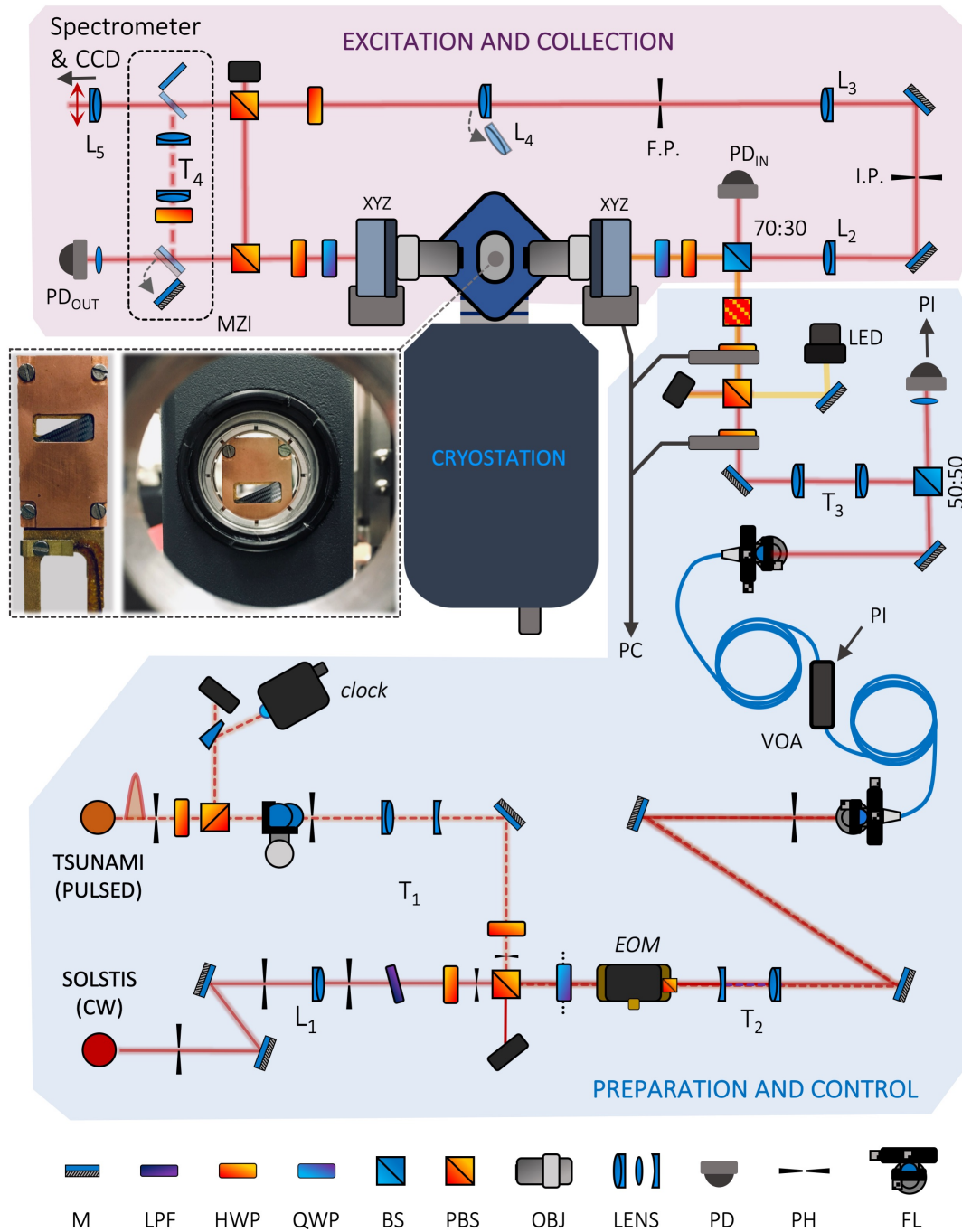


Figure 3.2: **Scheme of the setup.** Abbreviations: mirror (M), low-pass filter (LPF), half-wave plate (HWP), quarter-wave plate (QWP), beam-splitter (BS), polarizing beam-splitter (PBS), microscope objective lens (OBJ), photodiodes (PD), pinhole (PH), fiber launch stage (FL), electro-optical modulator (EOM), variable optical attenuator (VOA), proportional-integral servo controller (PI), light-emitting diode (LED), three-axis translation stage (XYZ), image plane (I.P.), Fourier-conjugate plane (F.P.), Mach-Zehnder interferometer (MZI). The inset shows an image of the transmission window of the cryostat and a detail of sample holder. See main text for details on the setup.

allows to have an extremely stable average power level while having the possibility of designing arbitrary modulation signals in the 1 kHz – 5 MHz band.

Two crossed PBSs preceded by HWPs mounted on motorized rotation stages allow to further attenuate up to a factor 10^6 the beam power. One of the PBS ports is used to couple the collimated emission of a light-emitting diode with 780 nm central wavelength serving sample illumination purposes. The beam is coupled with a 70 : 30 BS to a confocal microscope focussing it onto the sample with a long working-distance plan-APO microscope objective (OBJ_1). OBJ_1 has a nominal 0.55 numerical aperture (NA) and a 4 mm effective focal length. Precise positioning of OBJ_1 is ensured by a three stage piezo actuator. Moreover, the polarization state of the excitation beam is controlled by a HWP and a QWP while its divergence is tuned with a 2 : 1 beam expander (T_3) allowing to control the excitation spot beam waist. The sample emission is collected in reflection and imaged with a set of lenses $L_{2,3,5}$ on the entrance slit of a spectrometer coupled to a high-sensitivity (16-bit) CCD camera (Andor iKon-M 934 series). The lens L_4 , mounted on a flip-flop mount, allows to image the reciprocal space emission (see Sec. 3.2.1). Two pinholes in the image plane (I.P.) and Fourier plane (F.P) can be used for filtering purposes. The sample emission can be also collected in transmission geometry by a second microscope objective (OBJ_2) with a nominal 0.42 NA and a 10 mm effective focal length held by a three stage micro-positioner (20 nm accuracy). A QWP-HWP pair allows to control the collected beam polarization state, later analyzed with a PBS: the reflected component is injected to the imaging beam path while the transmitted component is sent onto an avalanche-photodiode (PD_{OUT}). Together with the photodiode PD_{IN} , this allows high-sensitivity input-output power measurements (down to ~ 1 nW) with a 50 MHz bandwidth. Finally, a mirror and a film BS mounted on removable magnetic mounts eventually form a Mach-Zehnder interferometer (MZI) in the transmission beam path which has been used for phase-resolving measurements. The telescope T_4 has a $1\times$ to $5\times$ variable magnification and is used to create a reference phase in one of the interferometer arms.

In the inset of Fig. 3.2 we show a picture of the cryostat window where the sample (grayish color) and its copper holder are visible. The patterns visible on the sample surface are ~ 120 repetitions of a microstructure motif, whose top portion is shown in the rightmost panel of Fig. 3.2-(d). A detail of the holder is shown on the left portion of the inset: it consists of a gold-plated support presenting a 10×2.5 mm transmission window and contacted with the cold finger of the cryostat and of a capping copper plate. The two plates sandwich the sample and apply a homogeneous pressure over the sample; a veil of specific vacuum grease (Apiezon-L) ensures good thermal contact between the components. The thermal anchoring of the epitaxial side of the sample is essential because the ceramic ARC deposited on the back of the substrate suppresses substantially the thermal conductance of the back contact. The holder is mounted on a two axis piezo stage allowing a precise relative positioning of the sample with respect to the excitation spot. The alignment of the excitation spot is done by shining both the laser beam and LED illumination onto the sample and imaging the reflected light on the CCD. Fine tuning of the input coupling can be done by acting on the excitation XYZ piezo actuators.

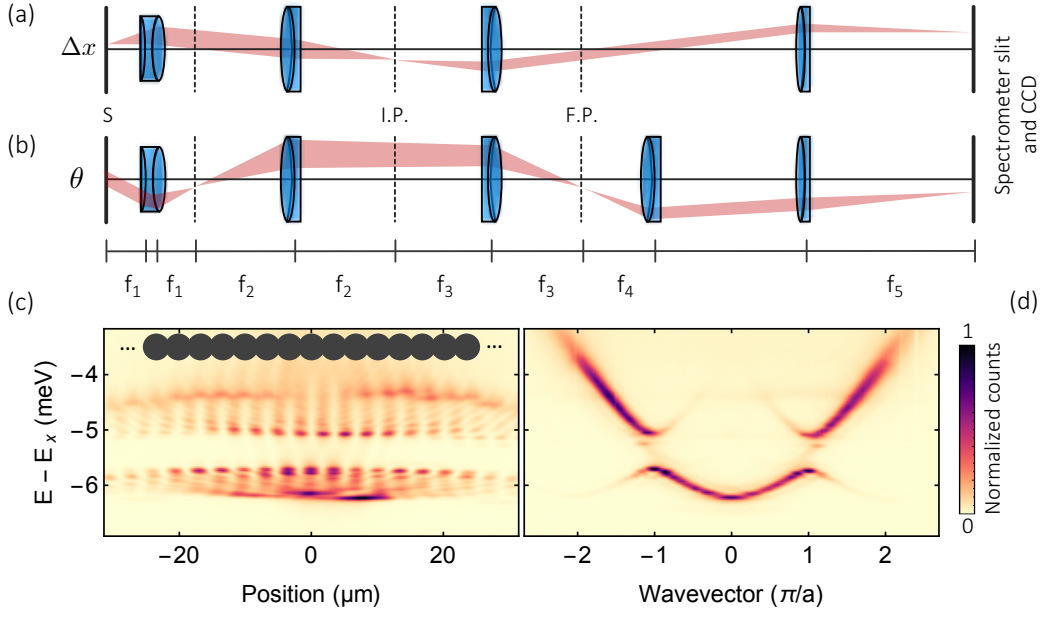


Figure 3.3: **Imaging techniques:** (a) Real space imaging: a point source in the sample plane (S) at a distance Δx from the optical axis is mapped to a point at a distance $\Delta x' \approx (f_2 f_5)/(f_1 f_3) \Delta x$ in the spectrometer entrance slit. (b) Momentum space imaging: the sample emission at an angle θ with respect to the optical axis is mapped to a point at a distance $\Delta x' \approx (f_3 f_5 / f_2 f_4) f_1 \tan \theta$ in the spectrometer entrance slit. The intermediate image plane (I.P.) and Fourier plane (F.P.) can be used for filtering purposes. (c,d) Examples of position (c) and momentum (d) resolved emission spectra of a 1D lattice formed by circular micropillars with radius $R = 2.0 \mu\text{m}$ and center-to-center distance $a = 3.4 \mu\text{m}$; $E_x \approx 1453.5 \text{ meV}$ is the exciton energy.

3.2.1 Real and momentum space imaging

The in plane momentum of polaritons is preserved in radiative processes as a consequence of the translational invariance of the system. As a result, an imaging system coupled to a dispersive optical element -for instance a spectrometer grating- allows to retrieve a complete information on the modes of the system [142]. In Sec. 2.3.3 we have used this idea to measure the polariton dispersion relation in a planar microcavity. In this section we want to use a non-resonant excitation scheme to image both in direct and reciprocal space the spectrally resolved emission of a one-dimensional lattice of coupled micropillars. Knowing the nominal period of the lattice, will allow us to precisely calibrate the magnification of the confocal microscope.

For real-space imaging we combined a $4f$ imaging system with a magnifying telescope, schematized in Fig. 3.3-(a). With simple ray optics arguments one can show that such arrangement of lenses sends rays emitted by a point source onto the sample plane (S), at a distance Δx from the optical axis, to a point at a distance $\Delta x' = \mathcal{M} \Delta x$ in the image plane. A small portion of the emission cone is shaded in red in Fig 3.3-(a). The magnification of the optical system, adopting the approximations of the lens-maker equation, amounts to $\mathcal{M} = (f_2 f_4)/(f_1 f_3)$. Depending on the focal length of the last lens adopted in the microscope $f_5 = 300(750) \text{ mm}$ we have $\mathcal{M} \approx 46.9(117.2)$, given the $13 \times 13 \mu\text{m}$ size of the CCD pixels this corresponds to 3.6(9.0) pix/ μm conversion.

| OBJ ₁ | L ₂ | L ₃ | L ₄ | L ₅ |
|------------------|----------------|----------------|----------------|-----------------|
| 4 mm | 250 mm | 400 mm | 300 mm | 300 mm – 750 mm |

Table 3.2: **Confocal microscope:** nominal effective focal length of the lenses employed for the imaging system. $L_{2,5}$ are achromatic doublets to avoid large spectral shifts of the focusing condition. Lens identification subscript refers to Fig. 3.2.

As pointed out earlier, there is a one-to-one relation between the in-plane wavevector of a polariton and the angle of emission of the photon resulting from its radiative decay in the free-space modes. An angle-resolved image of the emission of a microstructure is therefore enough to access reciprocal space. This can be done by imaging the focal plane of the lens L_3 as shown in Fig. 3.3-(b). Indeed, rays emitted at different positions in the sample plane, but with the same angle θ with respect to the optical axis, are focused in the Fourier conjugate plane (F.P.). That is $L_{2,3}$ form a $4f$ lens system targeting the objective back-focal plane. The telescope formed by L_4 and L_5 then images the F.P. to the spectrometer entrance slit. Using the lens-maker equation one can show that the angle-displacement relation is $\Delta x' \approx (f_3 f_5 / f_2 f_4) f_1 \tan \theta$. Considering a small-angle approximation and $f_5 = 300$ mm this yields a 0.5 pix/mrad conversion.

As an example, in Fig. 3.3-(c,d), we excite off-resonantly (cf. Sec. 2.3.3) a one dimensional lattice of circular micropillars and resolve the luminescence of the structure along the spectrometer slit in real and momentum space, respectively. The first diffraction order of the 1200 gr/mm grating lodged in the spectrometer is imaged onto the CCD, granting a 59.76(2) pix/nm chromatic dispersion along the axis orthogonal to the slit. In this way, Fig. 3.3-(c) gives the energy-position resolved emission where spatially extended modes can be observed. The lowest energy band corresponds to the hybridization of the s -type fundamental modes of each micropillar, the second lowest to p orbitals. Remarkably, the in-phase oscillation of the low k eigenmodes of the s -band can be directly inferred from the homogeneous intensity maxima spreading across several pillars (see the inset as a reference). Instead, on top of the s -band, the alternating phase of the intracavity field between neighboring pillars leads to zeroes in the intensity profile at each interface between the lattice sites. In Fig.3.3-(d) we inserted on the path the Fourier lens L_4 , thus imaging the reciprocal space: the bandstructure of the 1D lattice is directly revealed on the CCD.

The 1D lattice presented in Fig. 3.3-(c,d) is formed by 2 μm radius circular pillars with lattice parameter (inter-pillar distance) $a = 3.4 \mu\text{m}$. These values are rather precise (≈ 50 nm systematic error) and can be used to independently calibrate both the direct space and reciprocal space images. The former, using the distance between the intensity maxima measured on the top of the s -band, the latter by fitting the dispersion maxima at the end of the first Brillouin zone. These calibrations yield microscope magnification values consistent with the ones obtained by ray optics calculations with a relative error better than 5%. Notice that, in principle, the lens-maker equation does not apply to thick high-NA lenses, however the infinity-corrected microscope objective seem to be optimized to yield results in fair agreement with ray optics, due to the correction of all the aberrations.

The calibration of the spectrometer chromatic dispersion (not shown) was obtained by shining a small portion of the single-mode laser beam onto the spectrometer entrance slit. The maxima of the spectral peak was recorded for a set of equally-spaced wavelengths and fitted with a linear regression curve. Systematic deviations from the

linear regression due to aberrations are less than 1 pixel across the full CCD area. By fitting with a pseudo-Voigt profile (convolution of a Lorentian and a Gaussian distribution) the spectra at a fixed wavelength we obtained $32(3)\mu\text{eV}$ FWHM for the spectrometer point-spread function yielding the spectrometer resolution. Notice that both the Gaussian and Lorentian profiles are stable distributions, meaning a convolution of two Gaussian (Lorentian) profiles yields a Gaussian (Lorentian) profile. This fact combined with the associativity and commutativity of the convolution operation, can be used to readily deconvolve the spectral width of any measured Pseudo-Voigt spectral line from the spectrometer point-spread. This does not change the resolving power of the spectrometer but allows to measure spectral line-widths below the resolution limit upon careful data analysis. Finally, we point out that this technique can be intuitively extended to phase-sensitive schemes following an interferometric approach [35], or employing a Shack–Hartmann wavefront sensor [212].

3.2.2 Scaling of the microcavity linewidth

In this section we perform an experiment on circular micropillars. These structures present discrete modes whose linewidth can be precisely probed in resonant spectroscopy experiments. We can therefore use them to characterize the dependence of the linewidth of the microcavity as a function of the detuning of the lower polariton relative to the exciton. This information will be crucial to obtain a consistent input-output theory describing resonant experiments with microcavity polaritons.

In Sec. 2.3.4 we have shown that we can group the different polariton decay channel according to three contributions: the bare cavity linewidth including the radiative losses through the mirrors and absorption (γ_c), the non-radiative exciton decay rate (γ_{nr}) and the contribution due to the inhomogeneous broadening of the exciton. The first term is related to the photonic component of the polariton, the latter two are associated to the matter component, and are therefore weighted by the corresponding Hopfield coefficients. These considerations resulted in Eq. (2.45), which we rewrite here for simplicity

$$\Gamma = |C|^2\gamma_c + |X|^2(\gamma_{nr} + 2\pi\Delta_{xl}^2\rho(\Delta_{xl})) \quad (3.1)$$

where $|X|^2$ and $|C|^2$ are the exciton and photon fractions, $\Delta_{xl} = \hbar(\omega_x - \omega_l)$ is the detuning of the polariton mode with respect to the exciton transition and $\rho(\Delta_{xl})$ is the spectral density describing the inhomogeneous broadening of the exciton. For the derivation of the right most term in the above equation we refer to [163]. In order to avoid introducing too many parameters in the model we assume a gaussian distribution for $\rho(\Delta_{xl})$ with a standard deviation σ_{inh} . Notice that the Hopfield coefficients [Eq. (2.29)] depend on the cavity to exciton detuning $\Delta_{cx} = \hbar(\omega_c - \omega_x)$, related to the lower polariton detuning trough

$$\Delta_{cx} = \frac{(\hbar\Omega_R)^2 - 4\Delta_{xl}^2}{4\Delta_{xl}^2} \quad (3.2)$$

where $\hbar\Omega_R \approx 3.4$ meV is the Rabi splitting extracted from the fit of the polariton dispersion relation (cf. Sec. 2.3.3). Inserting this relation in the definition of the Hopfield coefficients yields an expression for Γ depending only on Δ_{lx} . We will use

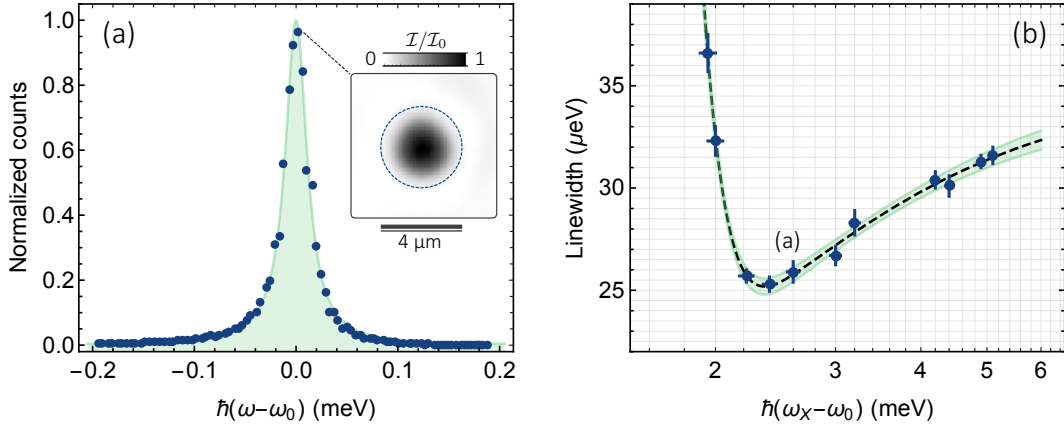


Figure 3.4: **Scaling of the polariton linewidth:** (a) Typical transmission spectrum of a circular micropillar with a $2.0 \mu\text{m}$ radius measured by resonant spectroscopy. Inset: emission profile at resonance (ω_0), here $\hbar(\omega_x - \omega_0) = 2.60(5) \text{ meV}$, the fit is a lorentian profile yielding the polariton linewidth $\Gamma = 25.9(5) \mu\text{eV}$. (b) Scaling of the measured polariton linewidth as a function of the detuning of the resonance with respect to the exciton transition (symbols). The dashed line is a fit with Eq. (3.1), the shaded areas correspond to the 95% confidence level of the fit.

this model to estimate the different contributions to the polariton linewidth from the scaling relation of the polariton linewidth with Δ_{lx} .

To this aim, we characterized a dozen of single micropillar structures with an equal nominal radius $R = 2.0 \mu\text{m}$ but presenting different detuning values Δ_{lx} of the lowest energy mode. For each pillar we performed a resonant spectroscopy experiment. The measurement protocol is the following; first, we approximatively determine the energies of the micropillar modes using a non-resonant excitation scheme while spectrally resolving the emission of the micropillar. Then, we tune the laser onto the lowest energy mode and maximize the input coupling of the laser beam. Finally, we collect the transmitted intensity as a function of the laser detuning. These measurement allowed retrieving the linear transmission spectrum of each pillar; we show a representative example in Fig. 3.4-(a). The inset presents an imaging of the transmitted light when driving resonantly the lowest energy mode. The absence of stray light outside the pillar edge (dashed line) suggests that the excitation spot has been efficiently coupled to the pillar mode. The experimental data points are then fitted using a Lorentian profile allowing to precisely retrieve the polariton linewidth; here $\Gamma = 25.9(5) \mu\text{eV}$ in Fig. 3.4-(a). From the mode profile at resonance we could also extract the modal area $\mathcal{A} \approx 6.1 \mu\text{m}^2$ (finite element calculations for the nominal structure yield $\mathcal{A} \approx 6.0 \mu\text{m}^2$). From the resonance energy and having previously calibrated the exciton energy as a function of the position of each pillar of the sample we could associate a detuning value Δ_{xl} to each pillar.

The results of this analysis are summarized in Fig 3.4-(b). Finally, we used Eq. 3.1 to fit the experimental data points: the result is traced as a dashed line in Fig 3.4-(b). From the fit we could extract the following values

| γ_c (μeV) | γ_{nr} (μeV) | σ_{inh} (meV) |
|-------------------------------|----------------------------------|----------------------|
| 35.1(7) | 16(1) | 0.53(1) |

Furthermore, from a measurement of the peak transmission (recall $\mathcal{T}_0 = (\gamma_c/\Gamma)^2$) for a large detuning (~ 10 meV), we could estimate that the absorption contribution to γ_c is roughly $10 - 15$ μeV . We also notice that the FWHM of the inhomogeneous distribution is roughly $2.35\sigma_{inh} = 1.2$ meV, which is roughly two times the typical one observed in simple QW structures embedded in a GaAs matrix (cf. Fig. 2.11). This might be due to a degradation of the surface reconstruction quality after having deposited the bottom DBR. To mitigate this effect the growth of a strain releasing superlattice before the DBR seems a relevant option, see the supplementary material of Ref. [213].

3.3 Modeling quasi-resonant experiments

In this section we want to review the two main approximations used for the description of the dynamics of a system of coupled micropillars cavities under a coherent pumping. We need them because the full description in terms of a Lindblad master equation for the density matrix of the system (cf. Sec. 2.4.4) is often unnecessary and becomes computationally unbearable already for a few coupled pillars and a few photons cutoff. Indeed, using a truncated Fock basis with $n \leq n_c$ for the Hilbert space of a microcavity, the Liouvillian superoperator admits a matrix representation with size $n_c^2 \times n_c^2$, becoming $n_c^{2N} \times n_c^{2N}$ for N coupled microcavities. Thus, a "brute force" solution of the Liouvillian zero-eigenvalue problem determining the steady-state density matrix is either time consuming or unfeasible. Moreover, considering the fact that we operate in a regime where the two-polariton interactions are still significantly smaller than the linewidth $U/\gamma \ll 1$, nonlinear effects sets in only when the cavity occupation is large, making a semiclassical or mean-field description of the dynamics rather accurate. In the following we discuss: (1) the Mean-field approximation; (2) a semiclassical method for the unravelling of the master equation; (3) how to find the steady state of the system within the master equation description in the case of a single resonator.

3.3.1 Mean-field equations

In a field theory, the mean-field or saddle-point approximation consists in finding the trial field which minimizes the action of the system. A well-known result is that the trial solutions must satisfy the classical Euler-Lagrange equation of motion. Indeed, in a path-integral picture, finding the extremal of the action means to move along the most probable trajectory at each point in phase-space, i.e. the trial function corresponds to the expectation values of the field. This is just a formalization of one consequence of the Ehrenfest theorem: to lowest order in the expansion around the expectation values of system observables (i.e. dropping quantum fluctuation), position and momentum follow the classical Hamilton equations. This kind of approximation is made for instance when using the Hartree ansatz for the matter field describing the condensate fraction of a diluted gas of neutral atoms [124], or in nonlinear optics whenever one expands the polarization of a medium in powers of the electric field and nonlinear susceptibilities [214]. In our case this boils down to study the dynamics of the cavity field expectation value, whose evolution can be derived by substituting the creation and annihilation operators \hat{p} (\hat{p}^\dagger) with the complex valued fields $\alpha^{(*)} = \langle \hat{p}^{(\dagger)} \rangle$ in the master equation for the reduced density matrix of the system (cf. Sec. 2.4.4) [37].

The resulting equations of motion are exact for quadratic and bilinear hamiltonians in $(\hat{p}, \hat{p}^\dagger)$ since higher than second order variations of the action are vanishing. This is not the case when including the contact interaction term in the polariton hamiltonian. Indeed, we are factorizing third (and eventually higher) order correlation terms when setting $\langle \hat{p}^\dagger \hat{p} \hat{p} \rangle \approx \langle \hat{p}^\dagger \rangle \langle \hat{p} \rangle \langle \hat{p} \rangle$ in the Heisenberg evolution of $\langle p \rangle$ [37, 214]. Considering a single-mode of the polariton field (e.g. one of the s-type eigenmodes of a single pillar) subject to a coherent monochromatic drive, the mean-field (MF) equation for the cavity field amplitude $\alpha \in \mathbb{C}$ yields ($\hbar = 1$)

$$\begin{aligned} i\dot{\alpha} &= \left(\omega_0 - i\frac{\gamma}{2} + U|\alpha|^2 \right) \alpha + i\sqrt{\gamma/2}\mathcal{F}e^{i\omega t} \\ &= \left(-\Delta - i\frac{\gamma}{2} + U|\alpha|^2 \right) \alpha + i\sqrt{\gamma/2}\mathcal{F} \end{aligned} \quad (3.3)$$

where ω_0 is the frequency of the mode, γ is the polariton linewidth, U is the two-body interaction strength and \mathcal{F} the complex drive amplitude with frequency ω and $\dot{\alpha} = d\alpha/dt$. In the second line, we moved to the frame rotating at the pump frequency by inserting the ansatz $\alpha = \alpha(t)e^{i\omega t}$ and defining the detuning $\Delta = \omega - \omega_0$. This ansatz is valid as long as $|\Delta| \ll \Omega_R$. Within the Heisenberg picture, generalizing Eq. (3.3) to a network of cavities coupled by resonant hopping terms with Hamiltonian $\mathcal{H} = -\sum_{i,j} J_{i,j}(\hat{p}_i^\dagger \hat{p}_j + c.c.)$ is straightforward. For the k-th resonator, one finds

$$i\dot{\alpha}_k = \left(-\Delta_k - i\frac{\gamma_k}{2} + U_k|\alpha_k|^2 \right) \alpha_k - \sum_j J_{k,j}\alpha_j + i\sqrt{\gamma_k/2}\mathcal{F}_k \quad (3.4)$$

The time evolution of this system of coupled ordinary differential equations (ODEs) can then be approached with standard numerical techniques. Notice that due to the nonlinear term, Eq. (3.4) can display stiff behaviors producing large discretization errors when using explicit (e.g. Runge-Kutta) numerical integration methods. Therefore semi-implicit or adaptive methods, readily implemented in commercial numerical suites, are necessary to avoid computational overheads; we refer to [215] for the theoretical background.

A problem relevant to this manuscript, will be the determination of the steady-state value $\tilde{\alpha}_k = \lim_{t \rightarrow \infty} \alpha(t)$ of the intracavity field once the parameter set $(\Delta, \gamma, U, J, \mathcal{F})_k$ is known. One way of doing this is to compute the long term evolution of the equation set (3.4), after adiabatically ramping from zero to its steady-state value each on-site drive amplitude $\tilde{\mathcal{F}}_k$. This method scales well with the number of modes α_k , but has a serious drawback: it is well-known that nonlinear ODEs often display a multistable behavior, that is, they admit a collection of inequivalent solutions $\{\tilde{\alpha}_k\}$ for the same parameter set, depending on the history of the drive terms. If one intends to simulate a specific experimental protocol, this generally does not constitute a problem. However, if one is interested a priori to know all the $\tilde{\alpha}_k$ values, choosing the right speed and overall history of each on-site drive ramp, calls for specific and often computationally intensive solutions.

Just to have an idea, we can try to give an upper bound to the number of solutions in the case of N resonators forming a linear chain with nearest-neighbor hopping and only $\mathcal{F}_1 \neq 0$. Since each steady state solution $\tilde{\alpha}$ must satisfy the condition $\dot{\alpha}|_{\tilde{\alpha}_k} = 0 \forall k$, Eq. (3.4) becomes a set of algebraic complex polynomial equation for which we know the number of (possibly degenerate) solutions equals its degree. Indeed for our specific

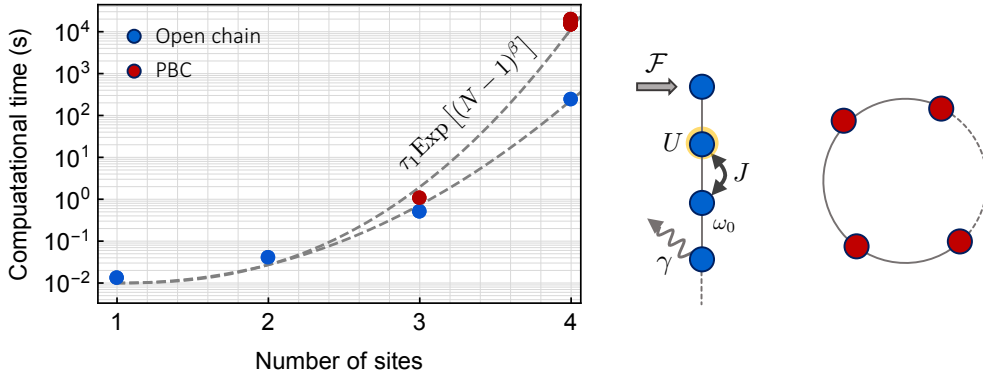


Figure 3.5: **Searching for the MF steady state - a heavy toll:** Scaling of the single-core computational time spent to find a complete set of steady-state solutions for Eq. (3.4) as a function of the number N of resonators in the lattice. Nearest-neighbor hopping only is considered both in the case of an open chain (blue markers) and imposing periodic boundary conditions (red markers). If τ_1 is the single resonator time, the scaling with N has the empirical form shown in the inset. The exponent β is 2.1(1) and 2.4(1) for the open and periodic boundaries, respectively. For each value of N we simulated 5 different values of $\mathcal{F}_1 \sim \sqrt{\Delta/\gamma U}$, that is deep in the multistable portion of parameter space. We consider identical resonators with $(\Delta, J) = 3\gamma$ and $U/\gamma = 10^{-2}$. For the computation we used a customized homotopy method implemented using the libraries of Mathematica running on 3.2 GHz processor.

cavity network, the N -th equation depends linearly on $\tilde{\alpha}_{N-1}$, we can express $\tilde{\alpha}_{N-1}$ as a cubic polynomial in $\tilde{\alpha}_N$ and substitute it in the $k = (N - 1)$ remaining equations. Iterating this procedure, one ends up with an equation in $\tilde{\alpha}_N$ of degree 3^N , equivalent to the number of roots of the algebraic system of equations.

The numerical search for these roots can be done with commercial softwares (e.g. Mathematica) implementing quasi-exact Homotopy methods. It is however striking to plot the scaling of the computational cost against N . In Fig. 3.5 we present the computational time needed to find the complete set of solutions $\{\tilde{\alpha}_k\}$ of the algebraic system encoding the steady-state of Eq. (3.4) as a function of the number N of resonators. We study a linear resonator chain both in the case of open and periodic boundary conditions (PBC), while considering only nearest neighbor couplings (details in the caption). Depending on the boundary conditions, between $N = 1$ and $N = 4$ there are four to six orders of magnitude increase in the computational overhead, with a dramatic super-exponential scaling. The higher toll observed in the case of PBC is due to the failure of a symbolic simplification by chain-substitution operated when possible by the software and aiming at reducing the dimensionality of the problem.

Using the symmetries of the system and drive schemes imposing a specific phase-pattern over a larger number of resonators can significantly reduce the number of inequivalent solutions. Even in this case the solution of this problem is quite challenging for large values of N . For this reason, coupled optical Kerr resonators, where the intensity and phase of each lattice site can be monitored with standard interferometric techniques, represent an implementation of a classical analog simulator encoding a remarkable degree of complexity.

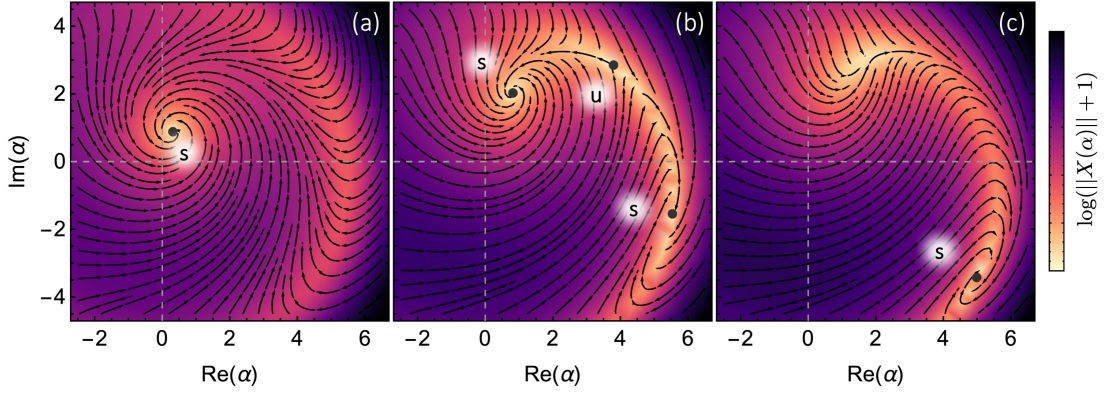


Figure 3.6: **Phase-space portrait for one Kerr resonator:** Streamlines showing the local direction of the vector field $X = \dot{\alpha}$ describing the MF dynamics a single Kerr resonator [Eq. (3.3)] for $\mathcal{F}^2/\gamma = (4, 18, 27)$ in panels (a,b,c) respectively. Other parameters are $\Delta/\gamma = 1.5$, $U/\gamma = 0.05$. Fixed-points ($X = 0$) are indicated by circular markers: both stable (s) and unstable (u) ones can be observed, as clearly indicated by the absence (presence) of outward pointing streamlines. The colormap encodes the scaled log-norm of the vector field indicating the local magnitude of the $\dot{\alpha}$. Panel (b) evidences the optical bistability phenomenon [214, 216].

At this point, it is important to introduce a second concept: the linear stability of the steady-state solutions. Indeed, not every steady-state solutions found with the algebraic method is physically relevant: the unstable ones for $t \rightarrow \infty$ cannot be observed since any technical or intrinsic fluctuation of the intracavity fields drive the system away from them. The right-hand side of Eq. (3.4) defines a vector field $X(\alpha_k) : \mathbb{C}^N \rightarrow \mathbb{C}^N$ prescribing at each point in phase-space $\dot{\alpha}_k$. Provided some analyticity conditions are met, one can imagine the field lines in \mathbb{C}^N as the gradient of a scalar potential presenting several "hills" and "valleys" in the complex phase-space. At the summit (bottom) of each of these loci $\dot{\alpha}_k$ simultaneously vanish, thus corresponding to steady-state solutions of Eq. (3.4). However, only the "valley" solutions are convex about $\tilde{\alpha}$, with any displacement $\delta\tilde{\alpha}_k$ being counteracted by a vector field component pointing towards $\tilde{\alpha}$. These fixed-points are thus generally called stable solutions or attractors. Conversely in "hill" solutions any $\delta\tilde{\alpha}_k$ is amplified over time by the outward-pointing components of $\delta\tilde{\alpha}_k$; for this reason these fixed-points are called unstable solutions. As an example, in Fig. 3.6 we show the streamlines generated in phase-space by the vector field $X(\alpha)$ in the single resonator case ($N = 1$), for three representative values of the coherent drive amplitude. This plot intuitively reveals the presence of stable (s) and unstable (u) solutions just by inspection of the direction of the vector field lines in vicinity of a fixed-point¹ (markers). The scaled log norm $\log(\|X\| + 1)$, plotted in color, indicating locally the magnitude of the velocity $\dot{\alpha}$. Light regions in the map indicate the vicinity to a fixed point, where $\|X\| = 0$. Remarkably, in Fig. 3.6-(b) three distinct fixed points are visible: two of them are stable $\tilde{\alpha}_{1,3}$ (optical bistability), presenting inward spiraling streamlines, the middle one, $\tilde{\alpha}_2$ shows instead an outward pointing line along the $\min|\dot{\alpha}|$ curve connecting $\tilde{\alpha}_2$ to $\tilde{\alpha}_{1,3}$, thus is unstable (saddle).

¹Since we highlighted that some of the roots of the algebraic set of equations are not physical steady-states we prefer to refer to them as "fixed-points".

More generally, for higher dimensions ($N > 1$) the analysis of these stream-plots becomes extremely difficult to visualize and one has to resort to a spectral analysis of the field generators in vicinity of the fixed-point. Indeed, the (linear) stability of each $\tilde{\alpha}$ can be addressed by studying the eigenvalues of the Jacobian of the vector field, evaluated at each fixed-point $\tilde{\mathcal{J}} = \mathcal{J}(X(\alpha))|_{\alpha=\tilde{\alpha}}$ [217, 218]. Notice that due to the presence of the square modulus $|\alpha_k|^2 = \alpha^* \alpha$, each component of the vector field is analytic but not holomorphic, thus the Wirtinger derivative $\partial_{\alpha^*} \neq 0$. For this reason one also has to consider the conjugate evolution of $\dot{\alpha}^*$ and $\mathcal{J}(X)_{i,j} = (\partial/\partial\alpha_i, \partial/\partial\alpha_i^*)^\dagger (X_j(\alpha, \alpha^*), X_j^*(\alpha, \alpha^*))$ has dimension $2N \times 2N$. If we call $E_{\tilde{\alpha},k}$ with $k = 1, \dots, 2N$, the complex eigenvalues of $\tilde{\mathcal{J}}$, three scenarios are possible:

1. If $\text{Im}(E_{\tilde{\alpha},k}) < 0 \forall k$, then any small fluctuation around the fixed point is damped over time: $\tilde{\alpha}$ is stable.
2. If $\exists k | \text{Im}(E_{\tilde{\alpha},k}) > 0$, fluctuations around $\tilde{\alpha}$ are amplified over time indicating an instability. The real part of the unstable eigenvalue(s) determines the monotonous (single-mode, $\text{Re}(E_{\tilde{\alpha},k}) = 0$) or oscillating ($\text{Re}(E_{\tilde{\alpha},k}) \neq 0$) character of the amplifying perturbation.
3. If $\exists k | \text{Im}(E_{\tilde{\alpha},k}) = 0$, a center subspace is found. The slow-dynamics around these solutions is generally complicated to predict and the forecasts of the above linearized spectral theory fails².

Notice that in the case of $\text{Re}(E_{\tilde{\alpha},k}) \neq 0$ instabilities, the long-term dynamics of the system may deviate from the predictions of a linearized theory. For instance, growing oscillations can stabilize the formation of limit cycles, which are stable attractor manifolds even if $\dot{\alpha} \neq 0$ for $t \rightarrow \infty$. The study of such cases and of central-subspaces forms a large body of literature still presenting several open questions [217]. As a practical example we consider the $N = 1$ case (a single Kerr resonator) described by Eq. (3.3) and compute the linear stability matrix $\tilde{\mathcal{J}}$.

$$\tilde{\mathcal{J}} = \begin{pmatrix} \partial_{\alpha} X & \partial_{\alpha^*} X \\ \partial_{\alpha} X^* & \partial_{\alpha^*} X^* \end{pmatrix}_{\tilde{\alpha}} = \begin{pmatrix} -\Delta - i\frac{\gamma}{2} + 2U|\tilde{\alpha}|^2 & U\tilde{\alpha}^2 \\ -U(\tilde{\alpha}^*)^2 & \Delta - i\frac{\gamma}{2} - 2U|\tilde{\alpha}|^2 \end{pmatrix} \quad (3.5)$$

denoting $n = |\alpha|^2$, some simple algebra yields:

$$E_{\tilde{\alpha}} = -i\gamma/2 \pm \sqrt{(\Delta - 3U\tilde{n})(\Delta - U\tilde{n})} \quad (3.6)$$

Evaluating the above expressions for the fixed points shown in Fig. 3.6 one can check that they convey the same information indicated by the streamlines of the vector field. The corresponding eigenvectors indicate, in vicinity of $\tilde{\alpha}$ the leading directions for the growth (decay) of the perturbations. Notice that this formal treatment is equivalent to consider a small perturbation ansatz $\alpha_k(t) = \tilde{\alpha}_k + \delta\alpha_k(t)$, plug it into the equations of motion (3.4) and linearize them by dropping any term $\mathcal{O}(\delta\alpha^2)$ or higher in the perturbations. Assuming the time evolution $\delta\alpha_k(t) = u_k e^{i\omega t} + v_k^* e^{i\omega^* t}$ for the excitation frequencies ω and amplitudes $\psi_k = (u, v)_k$, one gets the secular equation $(\tilde{\mathcal{J}}\psi - \omega\psi) = 0$. This second description assumes more the language of a Bogolyubov theory which, for instance, successfully describes the spectrum of small perturbation on top of a condensate wavefunction [124].

²The Grobman-Hartman theorem is valid only for hyperbolic fixed points (i.e. $\text{Im}(E) \neq 0$).

3.3.2 Truncated Wigner approximation

In this section we want to review a semiclassical approximation for a stochastic unraveling of the dynamics of the system in phase-space. The heart of this class of methods is the optical equivalence theorem, asserting that the expectation value of an operator in the Hilbert space equals the expectation value of its associated function in phase-space formulation, when computed with respect to a quasi-probability distribution describing the quantum state [219, 220]. In general, given the density matrix $\hat{\rho}$ of a system and an observable \hat{O}

$$\text{Tr}(\hat{\rho}\hat{O}) = \langle \hat{O} \rangle_{\mathcal{H}} = \langle O \rangle_{\mathcal{P}} = \int d\alpha d\alpha^* \mathcal{P}_s(\alpha, \alpha^*) O_s(\alpha, \alpha^*) \quad (3.7)$$

In the right-most term $O_s(\alpha, \alpha^*)$ is the phase-space representation of the operator \hat{O} and $\mathcal{P}_s(\alpha, \alpha^*)$ is a quasi-probability distribution in phase-space, satisfying the normalization condition $\int \mathcal{P}_s d\alpha d\alpha^* = 1$. The subscript $s = 0, \pm 1$ indicates the fact that there are different phase-space representations: choosing s affects both the definition of \mathcal{P}_s and the ordering of the operators when evaluating the phase-space average (3.7). Three celebrated representations are: $s = 1$ (Glauber-Sudarshan P) where observables are normally ordered, $s = -1$ (Husimi Q) with anti-normal ordering and $s = 0$ (Wigner) with symmetric ordering [219, 221, 222]. Here we focus on the Wigner representation for a single bosonic mode with ladder operators $(\hat{a}^\dagger, \hat{a})$

$$\mathcal{P}_0(\alpha, \alpha^*) = \frac{1}{\pi^2} \int d\beta d\beta^* \text{Tr}(\hat{\rho} e^{(\beta\hat{a}^\dagger - \beta^*\hat{a})}) e^{(\alpha\beta^* - \alpha^*\beta)} \quad (3.8)$$

Notice that: (1) the states (α, α^*) are not orthogonal, (2) $\mathcal{P}_s \geq 0$ is not verified for all the quantum states (e.g. a cat state). Recall that in this representation the observables must be symmetrically (Weyl) ordered, for instance starting from normal ordered operators $\hat{a}^\dagger\hat{a} \rightarrow (\hat{a}^\dagger\hat{a} + \hat{a}\hat{a}^\dagger - 1)/2$ and for the nonlinear term in the hamiltonian (2.48) one can use the fact that $(\hat{a}^\dagger)^2(\hat{a})^2 = (\hat{a}^\dagger\hat{a})(\hat{a}^\dagger\hat{a} - 1)$ and iterate the symmetrization procedure. More generally

$$\begin{aligned} \langle : (\hat{a}^\dagger)^n (\hat{a})^m :_S \rangle &= \frac{\partial^n}{\partial \beta^n} \frac{\partial^m}{\partial (\beta^*)^m} \text{Tr}(\hat{\rho} e^{(\beta\hat{a}^\dagger - \beta^*\hat{a})})|_{\beta, \beta^*=0} \\ &= \int d\alpha d\alpha^* \mathcal{P}_0(\alpha, \alpha^*) (\alpha^*)^n \alpha^m \end{aligned} \quad (3.9)$$

where $: \cdot :_S$ denotes the symmetrical ordering. The remarkable advantage in using this formulation is that the master equation (2.53) ruling the dynamics of the system density matrix, can be cast in the form of a generalized Fokker-Plank equation involving the partial derivatives of the quasi-probability \mathcal{P}_0 [222]. Indeed, after lengthy calculations, detailed in [223, 222], the operatorial terms in the master equation can be expressed in terms of \mathcal{P}_0 and its Wirtinger derivatives. The substitution table is $\hat{\rho} \rightarrow \mathcal{P}_0(\alpha, \alpha^*)$ whereas for the left and right action over $\hat{\rho}$ of the bosonic ladder operators becomes

$$(\hat{a}\hat{\rho}, \hat{\rho}\hat{a}) \rightarrow \left(\alpha \pm \frac{1}{2} \frac{\partial}{\partial \alpha^*} \right) \mathcal{P}_0 \quad - \quad (\hat{a}^\dagger\hat{\rho}, \hat{\rho}\hat{a}^\dagger) \rightarrow \left(\alpha \pm \frac{1}{2} \frac{\partial}{\partial \alpha} \right) \mathcal{P}_0 \quad (3.10)$$

When this correspondence table is inserted in the master equation (2.53), one obtains the desired phase-space diffusion equation for \mathcal{P} (hereafter we drop the subscript 0). We focus on the case of a single resonator (single mode); the generalization to a lattice (many modes) is rather simple since each mode commutes with the others, thus making the extension of the relations (3.9)-(3.10) trivial [222]. Considering a zero temperature bath ($\langle n_{\text{th}} \rangle = 0$) in (2.53) one obtains

$$i\partial_t \mathcal{P} = - \left[\frac{\partial}{\partial \alpha} \mathcal{D}(\alpha, \alpha^*) + \frac{\partial}{\partial \alpha^*} \mathcal{D}^*(\alpha, \alpha^*) \right] \mathcal{P}(\alpha, \alpha^*) + \left[\frac{\gamma}{2} \frac{\partial}{\partial \alpha \partial \alpha^*} \right] \mathcal{P}(\alpha, \alpha^*) - \left[U \frac{\partial}{\partial \alpha \partial \alpha^*} \left(\frac{\partial}{\partial \alpha} \alpha - \frac{\partial}{\partial \alpha^*} \alpha^* \right) \right] \mathcal{P}(\alpha, \alpha^*) \quad (3.11)$$

here $\mathcal{D}(\alpha, \alpha^*)$ denotes the drift term

$$\mathcal{D}(\alpha, \alpha^*) = (\Delta + i\gamma/2 - U(\alpha^* \alpha - 1)) \alpha - i\sqrt{\gamma/2} \mathcal{F}. \quad (3.12)$$

The first line of Eq. (3.11) is in the form of a generalized Fokker-Plank equation for the quasi-probability \mathcal{P} . The quasi-probability current at each point in phase space (first term) is proportional to the gradient of the drift term \mathcal{D} , which closely resembles the vector field generating the mean field dynamics (3.3). The constant positive diagonal diffusion term is instead proportional to the mode linewidth, suggesting its dissipative origin. The last right-hand term in Eq. (3.11) is proportional to third order derivatives of the Wigner quasi-probability, and prevents the canonical mapping of Eq. (3.11) into a stochastic differential equation (SDE). This is desirable as it significantly reduces the computational complexity of the problem. Fortunately, it has been demonstrated that this term can be neglected in the case of small nonlinearities $U\gamma \ll 1$ [224, 37]. Within this truncated Wigner approximation (TWA) the evolution of \mathcal{P} described by Eq. (3.11) can be obtained from the ensemble dynamics of the trajectories generated using the associated SDE

$$i d\alpha(t) = -\mathcal{D}(\alpha, \alpha^*) dt + d\chi(t) \quad (3.13)$$

where $d\chi$ is a Wiener process with $\chi(t)$ being a complex-valued uncorrelated gaussian noise of variance $\langle \chi^*(t') \chi(t) \rangle = \delta(t-t') \gamma/2$. If $\{\alpha_t\}_k$ with $k = 1, \dots, N$ is a collection of independent trajectories, the expectation value of a symmetrized operator $:\hat{O}:_S$ can be computed at every time t from the trajectory ensemble as

$$\langle : \hat{O}(t) :_S \rangle = \int d\alpha d\alpha^* \mathcal{P}_0(t) O(\alpha, \alpha^*) = \frac{1}{N} \sum_k O(\alpha_t, \alpha_t^*) \quad (3.14)$$

Notice that the computational cost of a stochastic unraveling in terms of \mathbb{C} -fields scales roughly linearly with the number of modes involved in the calculation. This makes the TWA the only viable choice when dealing with large resonator lattices [195, 197]. As a practical example we consider a single Kerr resonator with parameters identical to the ones presented in Fig. 3.6. We compute the martingale α_t by implementing Eq. (3.13) with a Euler-Maruyama discretization scheme. After having adiabatically ramped the drive power to $\mathcal{F}^2/\gamma = 19.67$, we let the stochastic evolution continue for $t_f = 10^4 \gamma^{-1}$. The discretization step, $\delta t \gamma = 10^{-2}$ ensures four-digit (or better) precision on different benchmark estimates. The evolution is repeated for 10^3 trajectories yielding the set $\{\alpha_t\}_k$. For constant parameter values, provided the total length of the

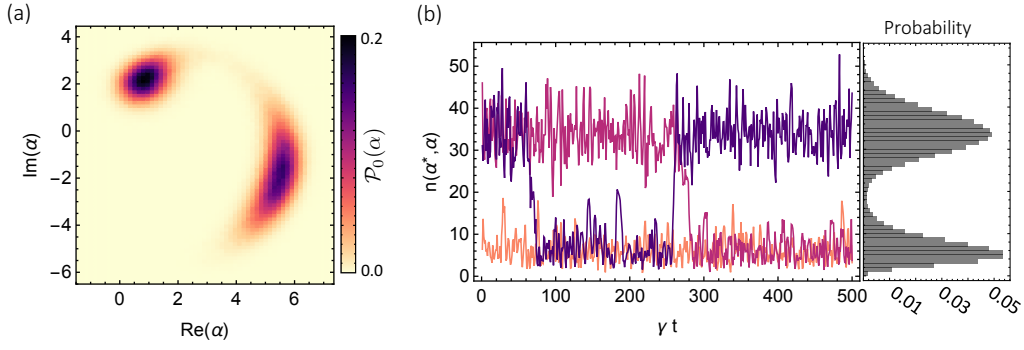


Figure 3.7: **Truncated Wigner approximation:** (a) Phase-portrait of $\mathcal{P}_0(\alpha, \alpha^*)$ describing a single Kerr resonator for the same parameters of Fig. 3.6-(b). To reconstruct P_0 we simulated 10^3 trajectories using Eq. (3.13), each one elapsing $10^4\gamma^{-1}$, with a $10^{-2}\gamma^{-1}$ discretization (Euler–Maruyama scheme). Recalling the Markovianity of the trajectories for $\delta t\gamma \gg 1$, one can assume ergodicity and obtain 10^6 independent values of α , then binned as function of their real and imaginary part. (b) Examples of the stochastic evolution of the number density operator in a phase-space representation ($n = \alpha^*\alpha - 1/2$). The frequency histogram of n shows bimodality underpinning the existence of mean-field bistable fixed-points, which are actually metastable due to quantum-activated switching between the two attractors in phase-space (see the abrupt jumps in the trajectories) [225, 226, 227].

trajectory is such that the values of α_t for $t = 0$ and t_f are completely uncorrelated and, using the Markovianity of the process, one can safely assume for $\delta t\gamma \gg 1$ independent samplings of α . In this way we obtain from $\{\alpha_t\}_k$ roughly 10^6 statistically independent samplings of the steady-state Wigner quasi-probability $P(\alpha)$, which we reconstruct with a binning procedure in Fig. 3.7-(a). Since the drift term in Eq. (3.13) is essentially equal to the MF vector field $X = \dot{\alpha}$ in Eq. (3.3), it is not surprising to observe when comparing Fig. 3.7-(a) and Fig. 3.6-(b) that $P(\alpha)$ is maximum where $\|X\| = 0$ that is, when the drift term vanishes. In other words, the maxima of $\mathcal{P}(\alpha)$ are in close vicinity of the MF solutions -as expected for consistency- and the bimodality of $\mathcal{P}(\alpha)$ indicates the existence of two stable fixed points in the MF. The diffusion term makes α explore the vicinity of the fixed points $\tilde{\alpha}$ with an exponentially suppressed probability in $\|X\|$. Sometimes the diffusion triggers abrupt switching events between the two lobes of \mathcal{P} , resulting in a metastable behavior of the steady state of the system [225, 226, 227, 203]. Fig. 3.7-(b) shows three samples of the trajectories described by the phase-space representation of the number operator $\hat{n} \rightarrow n(\alpha, \alpha^*) = \alpha^*\alpha - 1/2$ evidencing the jumps between the maxima of a bimodal distribution $\mathcal{P}(n)$. The study of such switching (or activation) time statistics and its effect on hysteresis experiments will be subject of the last chapter of the manuscript.

For intensive calculations we developed a fast-SDE solver implemented in C++ allowing to generate on a single core in a matter of few minutes $2.5 \cdot 10^{10}$ iteration steps, corresponding to 10 ms of real dynamics of a polariton microcavity with 40 ps lifetime. The most important bottleneck consists in the generation of pseudo-random gaussian-distributed numbers. Adaptive stochastic discretization schemes [228] would be an effective strategy to reduce the pseudo-random number generation overhead. Further numerical optimization schemes for lattices and disordered systems are summarized in [229].

3.3.3 Matrix representation of the Liouvillian

Although the semiclassical treatment presented in the previous section is capable of describing our system (where $U/\gamma = (0.05 - 0.001)$) faithfully, there are some cases where it is not the optimal solution in terms of computational time. Indeed, in vicinity of phase-transitions, dissipative systems are known to display a critical slowing down of the dynamics, with diverging temporal and spatial correlations [193, 230, 195, 231, 232]. In this case, the estimation of steady-state quantities becomes computationally intensive for trajectory based methods, requiring increasingly long temporal evolutions. However, for a single resonator, a representation of the Liouvillian superoperator $\hat{\mathcal{L}}$ (cf. Sec. 2.4.4) in a truncated Fock-space with cutoff $N_c \approx \eta(U\Delta/\gamma)$, is still possible in term of a matrix L of size $N_c^2 \times N_c^2$. Correspondingly, the density matrix becomes a vector $\hat{\rho} \rightarrow \rho_i$ with N_c^2 entries, while the master equation (2.53) can be written as $\dot{\rho} = L\rho$. The proportionality constant η sets the degree of approximation made in the truncation: $\eta = 2$ is typically sufficient to reach machine precision. Upon diagonalizing L one obtains the spectral decomposition of the master equation (cf. Sec. 2.4.4)

$$\hat{\rho}(t) = \hat{\rho}_{ss} + \sum_{k \neq 0} c_k(0) e^{-\lambda_k t} \hat{\rho}_k \quad (3.15)$$

where λ_k ($\hat{\rho}_k$) are the eigenvalues (eigenvectors) of the Liouvillian superoperator, $c_k(0) = \text{Tr}[\hat{\rho}(0)\hat{\rho}_k]$ are the projections of the initial density matrix and $\hat{\rho}_{ss}$ is the steady-state density matrix ($\lambda_k = 0$). Assuming an ordering $\lambda_1 < \lambda_2 < \dots$ of the L -eigenvalues, for a slowly evolving system, only the first λ_k matter for the long term dynamics. This is an important observation: since L is rather sparse, using an Arnoldi iterative method to determine the few smallest eigenvalues drastically changes the computational cost of the simulation. As a reference, for $N_c = 300$ (that is a 9000×9000 matrix), finding the first ten smallest eigenvalues requires 3.2 s on a 3.6 GHz single core. This offers a quite powerful tool to investigate the steady state of the system, even in vicinity of a dissipative phase transition.

In order to find the matrix representation of $\hat{\mathcal{L}}$, we need to start from the master equation (2.53) ($n_{th} = 0$), and use the expansion $\hat{\rho} = \sum_{nm} \rho^n_m |n\rangle\langle m|$ with $\rho^n_m = \langle n|\hat{\rho}|m\rangle$ in a truncated Fock basis with $m, n = 1, \dots, N_c$. Notice that we will use an Einstein summation convention and we distinguish covariant (lower) and contravariant (higher) indexes for later use.

$$\begin{aligned} \dot{\rho}^n_m &= -i(\tilde{\mathcal{H}}\rho - \rho\tilde{\mathcal{H}})^n_m + \gamma a^n_k \rho^k_l a^{\dagger l}_m \\ &= -i\left(\tilde{\mathcal{H}}^n_k \rho^k_m - \rho^n_k \tilde{\mathcal{H}}^k_m\right) + \gamma \left(a^n_k a^*_m{}^l\right) \rho^k_l \\ &= -i\left(\tilde{\mathcal{H}}^n_k \delta_m{}^l - \delta^n_k \tilde{\mathcal{H}}^T{}_m{}^l + i\gamma a^n_k a^*_m{}^l\right) \rho^k_l \\ &= -iL^n{}_m{}^l{}_k \rho^k_l \end{aligned} \quad (3.16)$$

where $\tilde{\mathcal{H}}$ is the effective non-hermitian hamiltonian (2.54), we denoted $a^{(\dagger)n}_m = \langle n|\hat{a}^{(\dagger)}|m\rangle$, used $a^{\dagger n}_m = a^*_m{}^n$ and δ^i_j denotes the Kronecker delta function. In Eq. (3.16), each component of the rank-2 tensor $\dot{\rho}^n_m$ is a linear combination of ρ^k_l elements with coefficients given by the rank-4 tensor $L^n{}_m{}^l{}_k$. In order to represent L as a matrix, we need to flatten $\hat{\rho}$ in a superspace where it becomes a vector, that is $|n\rangle\langle m| \rightarrow |n\rangle \otimes |m\rangle$. For a basis $(e^n)_m$ of a rank-2 vector space V and $(e_k)^l$ for its dual V^* , $e^n_{mk}{}^l$ is a basis of

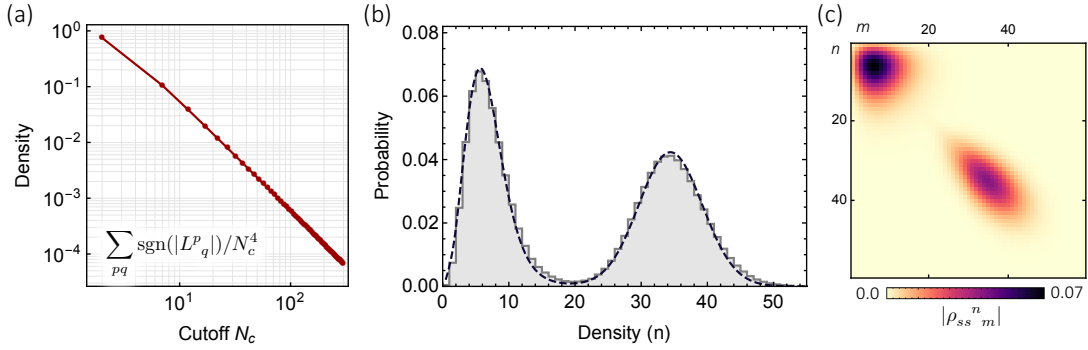


Figure 3.8: **Diagonalization of the Liouvillian:** (a) Density of the sparse matrix L representing the Liouvillian in the superspace $|n\rangle \otimes |m\rangle$ basis as a function of the Fock basis cutoff N_c ($\dim(L) = N_c^4$). (b) Comparison of the number density distribution obtained with the TWA (gray bars) and from the diagonal elements of the steady state density matrix ρ_{ss} , that is the $\lambda = 0$ eigenvector of L (dashed line). Parameters are the same as in Fig. 3.7. (c) Absolute value of the $\rho_{ss}^n_m$ entries.

$V^* \otimes V$, it is simple to recognize in the elements of L that the decomposition in the superspace can be written as

$$\dot{\rho}^p = -i(\tilde{\mathcal{H}} \otimes \mathbb{I} - \mathbb{I} \otimes \tilde{\mathcal{H}}^T + i\gamma a \otimes a)_q^p \rho^p \quad (3.17)$$

where $(p, q) = 1, \dots, N_c^2$ run on the superspace dimension $\dim(V^* \otimes V) = \dim(V)^2$ and we used the fact that the projections of \hat{a} in a Fock basis are real numbers. The tensor products can be easily implemented on a program using the Kronecker delta functions. As previously mentioned, this makes the representation of L in superspace rather sparse. In Fig. 3.8-(a) we quantify the density of non-zero elements of L , given by $\sum_{pq} \text{sgn}(|L_{pq}^p|)/N_c^4$, as a function of the Fock basis cutoff N_c . For $N_c \sim 2 \cdot 10^2$, which is a representative value of the cutoff for some of the experiments of the manuscript ($U\Delta/\gamma = 10^{-2}$), the Liouvillian has a density $\sim 10^{-4}$. Using a sparse matrix implementation paired with an Arnoldi iterative diagonalization method, allows a remarkable hundred-fold reduction of the computational time with respect to a full singular value decomposition, whose computational cost scales as $\mathcal{O}(N_c^6)$. Provided $N_c \approx 2(U\Delta/\gamma)$ the diagonalization of L gives an exact information on the system steady state density matrix ρ_{ss} (satisfying $L\rho_{ss} = 0$) and can thus be used to benchmark the results of the truncated Wigner approximation (TWA). Figure 3.8-(b) compares the TWA predictions of the number density distribution (gray bars), with the exact values given by $p(n) = \delta_{nm}^n \rho_{ss}^m_n$ (dashed line). A good overall agreement is found already for $U/\gamma = 0.05$ (the other parameters being as in Fig. 3.7). Finally, Fig. 3.8-(c) presents the absolute value of the steady-state density matrix entries ($n, m < 60$).

In summary we have surveyed three possible descriptions of the dynamical equations ruling the dynamics of coherently driven Kerr-resonators, modeling the physics of discrete polariton modes in micropillar cavities. The more general approach is based on the master equation for the system density matrix. The dimensionality of the matrix representation (L) of the Liouvillian superoperator ruling the density matrix evolution limits the applicability of this exact approach. Alternatively, since the ratio of the nonlinear constant to the cavity linewidth is small ($U/\gamma \ll 1$), we can rely on a

semiclassical approximation. We map the master equation to a generalized Fokker-Planck equation for the Wigner quasi-probability. Neglecting a term small in U/γ , we can sample the quasi-probability distribution using an unraveling in terms stochastic trajectories describing the cavity field dynamics in phase-space. This method greatly reduces the computational cost, as one only needs to compute the (stochastic) evolution of a \mathbb{C} number. We benchmarked the validity of this approximation against the exact master equation, obtaining a fair agreement. The deterministic (drift) term in the stochastic evolution, corresponds to the mean-field equations for the cavity field, which can therefore be understood as the non-diffusive limit of the truncated Wigner method. Concerning mean-field equations, we have illustrated how to get the steady-state intracavity field as the solution of a set of algebraic equations. We also discussed a general method to address the linear stability of the mean-field solutions.

Optically controlling the emission chirality of microlasers

ABSTRACT: Structured light beams presenting a twisted wavefront carry photons with a net orbital angular momentum (OAM). Contrary to the spin angular momentum (SAM) of photons, associated to their circular polarizations $\sigma = \pm\hbar$, the OAM is an unbounded degree of freedom $\ell \in \mathbb{Z}\hbar$. Especially for this reason, harnessing the OAM appears advantageous for increasing the information density of both classical and quantum information channels. Furthermore, the angular momentum of light can be used to address the rotational degrees of freedom of nanoscale optically levitated objects and to enhance sensing techniques.

So far, integrated sources of coherent light carrying an OAM are based on resonators whose design imposes a single, non-tailorable chirality of the wavefront (that is, clockwise or counter-clockwise vortices). Here we propose and demonstrate the realization of an integrated microlaser where the chirality of the wavefront can be optically controlled. The scheme relies on the interplay of two ingredients, namely, an analog spin-orbit coupling for photons in our dielectric microstructures and the spin-polarization of the gain medium. As a result, we are able to optically break time-reversal symmetry in the microlaser, which is essential for generating an emission carrying a net OAM. Furthermore, while investigating the saturation regime of such chiral microlasers, we demonstrated a bistable behavior involving two modes with distinct OAM ($\ell = 0$ and $|\ell| = 2$) and polarization patterns. Using a dynamical rate equations model, we understand the mechanism underlying the bistability in terms of a polarization-dependent saturation of the gain medium.

The proposed OAM control mechanism is rather general and can be readily extended to different laser architectures and injection schemes, thus paving the way to the realization of a new generation of OAM microlasers with tunable chirality. Moreover, the observed bistability phenomenon could be potentially used for implementing ultrafast OAM optical switches and for the exploration of dynamical processes involving phase and polarization vortices. The core results presented in this chapter are published in refs. [233, 234].

4.1 Introduction

The advent of laser light sources sparked the quest for controlling and harnessing the degrees of freedom of light [235]. Historically, a major flywheel for the development of novel light sources has been the synergy between the microelectronics and telecommunication industry. The first benefitted from the improvement of the UV optical lithography techniques, decreasing progressively the transistor footprint thus boosting the efficiency and computational power of micro-processors. In turn, this allowed the development of first-principle numerical tools helping researchers improving and conceiving new laser designs. The second lead to the development and miniaturization of fast optoelectronic modulators and receivers, allowing unprecedented control of the temporal and polarization properties of the optical field.

A lot of the early works were devoted to the control of the temporal (spectral) envelope of the laser emission. Continuous-wave lasers, characterized by a nearly monochromatic emission, are essential instruments for optical spectroscopy techniques or for the coherent excitation of matter transitions. On the opposite end, sources of ultrafast laser pulses, have reached few optical cycle envelopes. This control over the spectral density of the laser emission, lead to impressive advances in optical metrology, ranging from atomic-clocks [236], to frequency comb generation schemes [237, 238] and super-continuum sources [239]. Conversely, in the temporal domain, ultrashort pulses allowed the resolution of the electronic (or molecular) dynamics on attosecond timescales [240], while the generation of high-intensity ultrashort optical pulses [241], has been essential for medical applications and for the development of multi-photon microscopy in bio-sciences [242, 243]. The temporal and spectral envelopes of the laser emission constitute a Fourier conjugate pair of observables ultimately subject to uncertainty relations, as schematically illustrated in Fig. 4.1-(a). In order to modify the spectral density of the envelope, one can combine nonlinear effects (e.g. Kerr lensing and focusing) with dispersive optical elements (gratings, prisms, etc.) [244, 238, 241].

In parallel, the possibility of tailoring the polarization, intensity and phase pattern of the laser emission are, since the early days of laser sources, an important field of research [58]. The ability to structure the light beam properties first relied on bulk optical elements placed outside the optical cavity. For instance, the polarization of a paraxial beam can be controlled by using half- and quarter-wave plates. In the same way, a patterned neutral density filter or a glass substrate of varying thickness can be used to introduce an amplitude or phase modulation, respectively. These first approaches lacked of versatility, as each different pattern called for new custom optical elements. In this sense, the invention of spatial light modulators (SLMs) based either on liquid crystals or micro-mirror arrays represented a revolution. Indeed, these devices allow to shape the incident wavefront with high spatial resolution in a reconfigurable and fully controlled fashion [245, 246]. Having full access to the spatial properties of light constitutes a major advantage for the multiplexing of telecommunication channels [247]. Moreover it allows focusing light and imaging objects trough complex media [248], which is of crucial importance for in-vivo studies of biological tissues. As well, SLMs are the core technology for the storage of impressively dense 3D holographic images [249]. Rather than shaping or filtering the source emission, another approach is to insert amplitude or phase masks within the laser cavity, which thus emits directly in the desired mode, see [58, 250] for an overview. For instance, by inserting a metal wire crossing the axis of a confocal Fabry-Perot cavity, one increases the losses for the

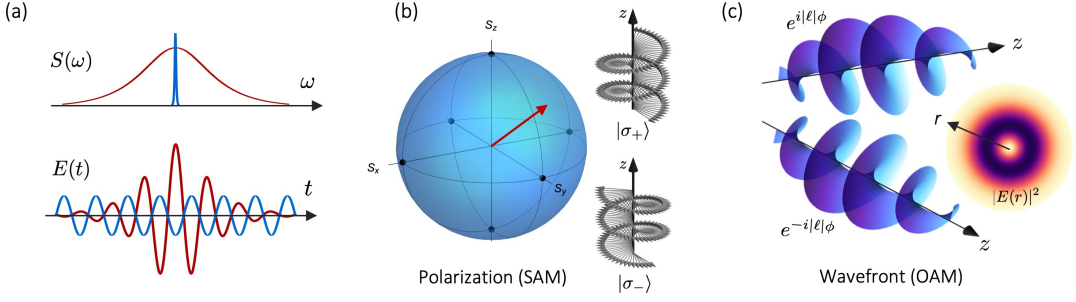


Figure 4.1: (a) Spectral and the conjugated temporal envelope of a coherent beam, in the limit of $S(\omega) \rightarrow \delta(\omega - \omega_0)$ one recovers monochromatic plane waves. (b) The pseudo-spin, polarization or spin angular momentum (SAM) of a photon can be represented on the Poincaré sphere. (c) Schematic representation of the wavefront of an optical pulse carrying an OAM $\ell = \pm 1$, that is a 2π clockwise or anti-clockwise phase vortex, respectively. The inset shows the radial intensity pattern of such beam, belonging to the LG_{01} (Laguerre-Gauss) class of solutions of the paraxial wave equation.

fundamental gaussian mode of the laser (TEM_{00}) and, as a result, mode competition is won by the Hermite-Gauss GH_{01} mode [251]. Alternatively, SLMs can be used to dynamically shape the resonant cavity mode, obtaining on-demand laser modes [252]. One advantage of this approach is that it is robust to imperfections: profiting from the stimulated nature of the laser operation, a slight imbalance on the gain/loss ratio for a given mode M_{in} of the resonator, results in an emitted beam M_{out} with extremely high purity $|\langle M_{out} | M_{in} \rangle|^2 \approx 1$. Instead, in the filtering/ wavefront shaping approach, the quality of the desired output beam is only determined by the precision and accuracy of our optical manipulation technique. As a concrete example, if we take a laser with an output gaussian mode and we shine it through a wire, the resulting beam profile would only qualitatively resemble HG_{10} , whereas putting the same wire inside the laser cavity, as previously mentioned, results in a nearly perfect HG_{10} emission [251]. This motivated us to pursue this second avenue in the development of the structured light source presented in this chapter.

For a transverse electromagnetic wave the polarization, intensity and phase patterns are related to the total angular momentum of light. This quantity, as we will later demonstrate, can be conveniently separated in two components: the spin angular momentum (SAM) and the orbital angular momentum of light (OAM). A third one, the external angular momentum, exists, but can always be gauged away with an appropriate choice of the system of coordinates for the paraxial light beams we are interested in [80]. The SAM is a manifestation of the fact that a photon is a massless spin-1 boson [253]: for transverse photons, the spin operator admits only the ± 1 S_z projections, thus any polarization state can be represented on a Poincaré sphere with poles corresponding to the circular polarization states σ_{\pm} , see Fig. 4.1-(b). Notice that in a paraxial beam the polarization spatial pattern is solely determined by the local phase relation between the transverse electric and magnetic field components, and is thus independent of the field spatial distribution. The OAM is instead related to the field spatial distribution, but not to its polarization [254, 255]. In the simpler case of a paraxial beam with an envelope presenting a cylindrical symmetry, the OAM describes the number of times (ℓ) the phase of the wavefront winds around the direction of propagation within an optical period, as Fig. 4.1-(c) illustrates [255, 256].

The most notable asset of the OAM is that, contrary to SAM, which is restricted to the values $\pm\hbar$, it is theoretically unbounded; for example, generation of light vortices carrying more than 10^4 quanta of OAM has recently been demonstrated [257]. Over the past decade, numerous proposals and demonstrations that take advantage of this unbounded Hilbert space have emerged. For instance, it has been acknowledged that these higher-dimensional quantum states could offer a drastically enhanced information density, both in classical [258, 259, 260, 261] and quantum [262, 263, 264, 265] communication channels, and they could also allow improvements to the resilience against noise and eavesdropping of quantum communication protocols [266, 267, 268]. Moreover, since the early works of J.H. Poynting [269], R. Beth [270] and later L. Allen and collaborators [255], it is known that light possessing a SAM or OAM can be used to exert an optical torque on absorbers or scattering bodies. The former, induces a rotation of the particle around its own center (spinning), the latter instead, will generate a revolution of the particle around the beam axis [271, 272]. Remarkably, this mechanical equivalence can be exploited to address the rotational degrees of freedom of optically levitated nanoscale objects [273, 256, 274, 275], or in the development of novel tools for optomechanics [276, 277]. From a fundamental point of view, generating and entangling quantum states with such arbitrarily large quantum numbers has been demonstrated to be a very promising avenue for investigating the foundations of quantum mechanics [278, 279, 278].

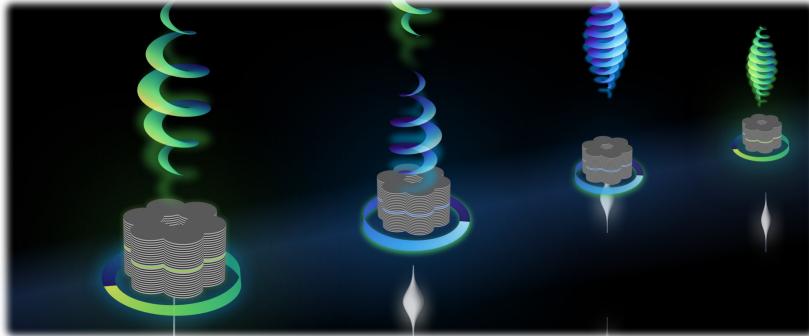
The growing interest for the OAM degree of freedom of light calls for the development of coherent sources carrying well-defined and tunable OAM. One possible strategy that has been extensively explored is to shape the phase front of paraxial beams using bulk optical elements such as spiral phase plates [280] or computer generated holograms presenting a pitchfork dislocation via a SLM [259, 260]. Although these approaches have the advantage of being extremely versatile, allowing the generation of high-order vortices, they typically suffer from low operation frequencies and remain extremely difficult to integrate on a chip. Another strategy relies on the fact that for a generic vector beam the polarization and spatial degrees of freedom are non-separable [58] thus, exploiting simultaneously anisotropic and inhomogeneous mediums, SAM to OAM conversion can be achieved [80, 281]. The conversion of circular polarization to OAM has been implemented both with nano-structured metasurfaces [282, 283, 284, 285], Q- and J-plates [286, 287, 288]. Remarkably, in these schemes the handedness of the polarization can be used to switch between two OAM values however, their full integration is challenging, as they rely on complex architectures involving several optical elements.

In the quest for the development of coherent laser sources, their miniaturization and eventual integration on a chip has driven a consistent amount of research with the long term goal of generating, routing, controlling and detecting light on the same chip. Semiconductor laser diodes, omnipresently used for telecom applications, were one of the first and most notable results of this effort [289, 290]. In this regard, direct gap semiconductors are excellent gain mediums which can be both optically and electrically pumped. Moreover, since the pioneering work of E. Yablonovitch [291], the idea that the periodic juxtaposition of material with different dielectric constants could be used to confine or tailor the dispersion relation of photons [63, 292], found a natural realization in semiconductor heterostructures growth and etching technologies (cf. Sec. 2.1). These elements, combined together suggest a viable path for the realization of integrated sources of structured light.

In this sense, recent demonstrations of integrated OAM lasers based on ring resonators [293, 294, 295] are very promising. However, it is very challenging in these integrated devices to break the mirror symmetry between clockwise (CW) and counter-clockwise (CCW) propagating modes, which is necessary to generate an emission carrying a net OAM. So far, this difficulty has been successfully overcome by engineering chiral resonators, for example by tuning the gain and loss around the resonator, but the scalability of this approach is strongly limited because the engineering of the devices imposes a given, non-tailorable chirality to the lasing mode: each device can generate only either a CW or a CCW vortex.

Here, we propose and demonstrate a novel scheme to achieve OAM lasing in a fully integrated device where the chirality of the emission (that is CW or CCW vortices) can be optically controlled. To do so we consider a hexagonal arrangement of micropillar cavities supporting optical modes displaying a discrete rotational symmetry [187]. Rather than relying on the engineering of a chiral resonator, our scheme is based on optically breaking time-reversal symmetry by spin-polarizing a gain medium with a circularly polarized optical pump. By taking advantage of the spin-orbit coupling of photons confined in planar microcavities with rotational symmetry [79, 80, 187], this allows us to generate a lasing emission that carries OAM with a chirality that can be controlled solely by tuning the polarization of the pump. Although the magnitude of the OAM ($|\ell|$) is not tunable in a single device, we show that this parameter can be accurately controlled during the fabrication process by tailoring appropriately the geometry of each microlaser. Furthermore, we demonstrate that this scheme could be extended to N -site ring arrays of cavities allowing the generation of large OAM values. We also experimentally test the robustness of the scheme with temperature and discuss possible avenues for achieving a room temperature operation. Finally, we investigate the gain saturation regime of the microlaser unveiling a bistable behavior involving two modes of the microlaser carrying distinct values of the OAM ($|\ell| = 2$ and $\ell = 0$).

The chapter is organized as follows: first, we discuss the optical modes of coupled microcavities arrays arranged in a ring geometry and the lasing mode selection mechanism in Sec. 4.2. Then, in Sec. 4.3, we experimentally characterize the emission intensity, spectral and spatial properties of three microlaser structures under non-resonant pumping and test the robustness of the scheme with temperature. Section 4.4 is dedicated to the OAM bistability experiments and the elucidation of the mechanism via a coupled-rate equation model. Lastly, in Sec. 4.3 we outline future research directions. For an interested reader, we derive the general expression for the angular momentum of light and apply it to the case of Bessel beams in the Appendix 4.6.



4.2 Ring-type photonic molecules

Based on the discussion on the engineering of the transverse modes of coupled microcavities of Sec. 2.4, we want to investigate the optical modes of N coupled microcavities arranged on the vertices of a regular polygon. As it will be the experimentally relevant case, we choose $N = 6$ and leave the general case for a later discussion. Also, in the beginning, we consider the case of degenerate polarization states; in such a way, we can work initially with scalar quantities.

The microstructures realized for the experiments presented in this chapter correspond to the first sample design detailed in Sec. 3.1.1. As previously mentioned, since a single QW is embedded in the cavity, under strong off-resonant pumping, the system loses the strong exciton-photon strong coupling regime due to phase-space filling effects (cf. Sec. 2.2.3-2.3.3). Simple calculations and experiments show that the lasing threshold in the microstructures occurs in the weak coupling regime [144, 233], which can therefore be considered as a vertical cavity surface emitting laser (VCSEL).

In figure 4.2-(a), we show an optical microscopy and scanning electron microscopy (SEM) image of an arrangement of six coupled micropillars. As discussed in detail in Sec. 2.4 this structure can be qualitatively pictured within a linear combination of atomic orbitals (LCAO) description as a photonic equivalent of a benzene molecule [187]. For this reason, we can start by considering a tight-binding model for each fundamental mode (s-type) of the pillars described by an amplitude $|\psi_j\rangle$. We recall that due to the s-type symmetry of the fundamental mode of each uncoupled pillar, $|\psi_j|^2$ closely resembles a gaussian profile. The hamiltonian reads

$$\mathcal{H} = \hbar\omega \sum_i |\psi_i\rangle\langle\psi_i| - \hbar t \sum_j (|\psi_{j+1}\rangle\langle\psi_j| + c.c.) \quad (4.1)$$

in terms of the energy $\hbar\omega_j = \hbar\omega$ ($j = 1, \dots, 6$) and tunneling matrix element t . We impose $N + 1 = 1$ as we consider periodic boundary conditions (PBC). To diagonalize the hamiltonian (4.1), it is convenient to work in a reciprocal space basis where $|\psi_\ell\rangle = N^{-1/2} \sum_j e^{i\ell a j} |\psi_j\rangle$ where $a = 2\pi/6$ for the PBCs. For $N = 6$ the quantum number $\ell = (0, \pm 1, \pm 2, 3)$ labels the six eigenmodes of (4.1) and corresponds to the number of times the phase of each mode winds after one round trip on the lattice sites, therefore corresponding to the eigenmode OAM (cf. Appendix 4.6). Correspondingly, the normal modes oscillate at a frequency $\omega_\ell = \omega - 2t \cos(a\ell)$. The $\ell = 0(3)$ eigenmode corresponds to in-phase (out-of-phase) oscillations of the amplitudes $|\psi_j\rangle$, whereas the $\ell = \pm 1$ and $\ell = \pm 2$ present a $\pm 2\pi$ and $\pm 4\pi$ phase vortex, and are therefore the interesting ones to generate an emission carrying a net OAM. Since the modes with equal $|\ell|$ but opposite sign (chirality) are degenerate in energy we refer to the couples $\pm|\ell|$ as an OAM manifold. The situation is schematically represented in Fig. 4.2-(b). The four modes presenting a phase circulation can be regarded as the aromatic orbitals stemming from the hybridization of the out of plane p_z orbitals of carbon atoms in the benzene molecule C_6H_6 [187].

Figure 4.2-(c) shows the angle and energy resolved photoluminescence of a benzene photonic molecule formed by pillars with center-to-center distance $d = 2.3 \mu\text{m}$ and radius $R = 1.6 \mu\text{m}$. The measurement is obtained by imaging the Fourier-conjugated plane of the microstructure emission on the entrance slit of a spectrometer; a weak

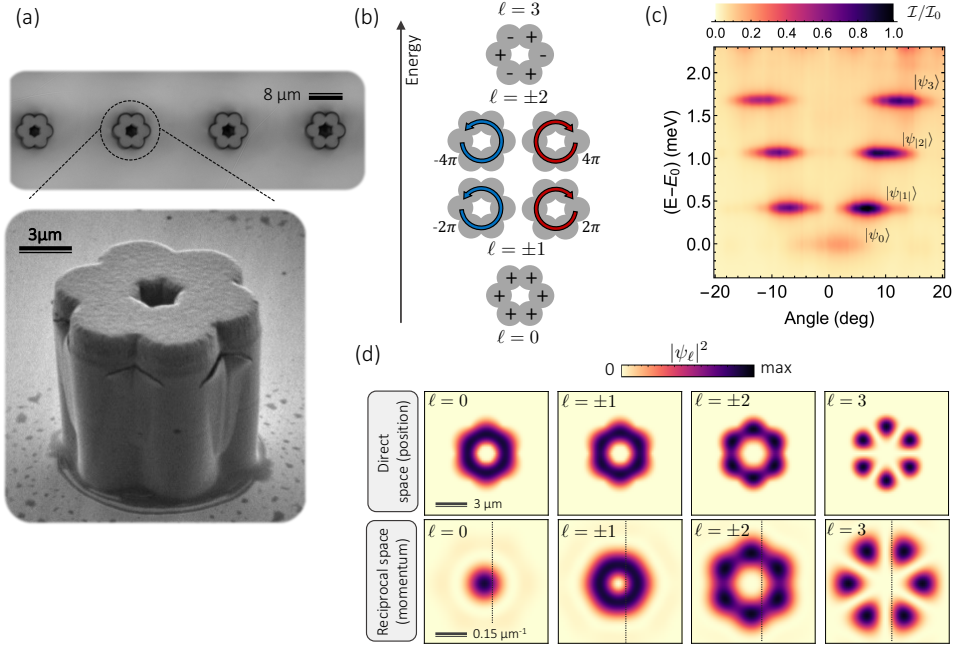


Figure 4.2: **Benzene photonic molecules:** (a) Top view optical microscopy and detail of the side view (SEM) of a coupled array formed by six overlapping micropillars with $R = 1.6 \mu\text{m}$ radius and variable inter-pillar distance. (b) Schematic representation of the scalar eigenmodes $|\psi_\ell\rangle$ of the structure; the phase relation between pillars is indicated. (c) Energy and angle-resolved photoluminescence of the microstructure below the lasing threshold, presenting the four OAM manifolds $\ell = (0, \pm 1, \pm 2, 3)$, $E_0 \approx 1470 \text{ meV}$. For comparison, panel (d) shows finite elements calculation of the $|\psi_\ell\rangle$ profile both in direct (position) and reciprocal (momentum) space (cf. App. 2.6). The dashed line corresponds to the position of the slit used for panel (c).

off-resonant pump ($\lambda_{\text{exc}} \sim 770 \text{ nm}$, $P_{\text{exc}} \sim 0.5 \mu\text{W}$) is used. For further details on the measurement technique we refer to Sec. 3.2.1. The energy axis of panel (c) is rescaled for the $\ell = 0$ mode energy $E_0 \approx 1470 \text{ meV}$ (or $\lambda_0 \sim 843.5 \text{ nm}$), which means the pump is roughly 130 meV above the emission, in correspondence with the first reflectivity dip of the DBR, thus ensuring a good injection efficiency. As it is not intuitive to guess the momentum (angle) resolved profile of the modes due to the non-trivial phase relation between pillars, we calculated both the real and reciprocal space emission for each $|\psi_j\rangle$ using finite elements method; the result is shown in Fig. 3.2.1-(d). For direct comparison with panel (c), we indicate the spectrometer slit position in the reciprocal space profiles $|\langle k|\psi_\ell\rangle|^2$ with a dashed line.

Unsurprisingly, all the intensity patterns have a doughnut-shaped spatial profile and the absence of zeroes in the $|\ell| = 1, 2$ modes is a first suggestion of the fact that they support a phase circulation. The intensity nodes in $|\langle r|\psi_3\rangle|^2$ correspond to the amplitude nodes between neighboring pillars oscillating with a π phase difference. When looking at reciprocal space, the $\ell = 0$ mode is the only one presenting a maximum at $k = 0$, whereas for $\ell \neq 0$ there is a clear zero. This happens because for $\ell \neq 0$, opposite pillars have the same amplitude and phase in modulus but opposite sign, as a consequence of the mirror symmetry of the hamiltonian (4.1), whose point group symmetry is $C_{6,v}$. As a result, close to the optical axis the emission from opposite pillars destructively

interfere; this effect is sometimes referred as the hole-burning effect for vortices.

For the moment, even if we found some optical modes carrying OAM, it is not possible to envisage a lasing scheme which would break the degeneracy between modes presenting a counter-propagating phase winding. Remarkably the polarization degree of freedom, which has not been taken in account up to now, can be exploited to overcome this issue.

4.2.1 Fine structure of the optical modes

In Section 2.1.2 and 2.4 we discussed two distinct effects that can lead to a polarization and in-plane momentum dependent energy splitting of the microstructure eigenmodes. The first one, originates from the different penetration depth of a transverse EM wave in the DBR mirrors depending on its angle of incidence and polarization [71, 74]. This effect is vanishing at normal incidence or if the cavity spacer optical thickness is matched to a multiple of the DBR central wavelength (see Fig. 2.4). This is a likely situation in this set of experiments, as we targeted the design of the planar structure to satisfy this condition in order to maximize the cavity finesse (cf. Sec. 3.1.1). The other polarization splitting effect arises in microstructures with a broken rotational symmetry due to the influence of boundary effects for the transverse EM field modes. This latter contribution becomes generally dominant when the lateral size of the microstructure becomes commensurate with the wavelength of the confined mode. Notice that these two different contributions to the polarization dependent energy splitting can both add or cancel, eventually resulting in complex polarization dependent patterns.

We focus now on the second mechanism, which is comprehensively characterized in the case of coupled micropillar structures in [296]. The result of the authors analysis is that the structure supports four linearly polarized modes: two at lower energy show a bonding (B) profile and orthogonal linear polarizations while the other two display an anti-bonding (AB) profile, (see Sec. 2.4.2 for details on the coupled pillar modes). Interestingly, the B and AB modes polarized along the axis linking the direction (x), present the largest energy splitting. In a tight-binding picture, where we decompose the bare pillar eigenmodes in the linear polarization basis $(l, n)_i$ with l_i the unit vector aligned with the link axis on the i th site, this corresponds to take a tunneling matrix element $t_l \sim \langle l_1 | l_2 \rangle > t_n$. This can be intuitively pictured as a larger penetration depth for the field polarized along l due to the boundary conditions at the constriction between the two pillars. The structures we will consider hereafter are composed of $R = 1.6 \mu\text{m}$ radius pillars with variable center-to-center distances $d = (2.3 - 2.6) \mu\text{m}$, for which $t_l > t_n$ and $\Delta t \sim (20 - 50) \mu\text{eV}$ are expected [296]. We schematically represent this situation in Fig. 4.3-(a).

The situation becomes even more interesting when moving to a ring arrangement of an even number N of coupled micropillars, illustrated in the case of $N = 6$ in Fig. 4.3-(a). Indeed, the axis linking the center of two consecutive pillars \vec{l}_i changes orientation while doing a round trip across the structure. As a result, a linearly polarized photon is subject to an azimuthally varying birefringent axis while traveling across the structure. This amounts to a coupling of the polarization to the in plane motion, which can thus be regarded as an analog spin-orbit coupling term [187].

In order to clarify this point we need to study the system hamiltonian including the polarization degree of freedom. We use a tight binding approach where we neglect

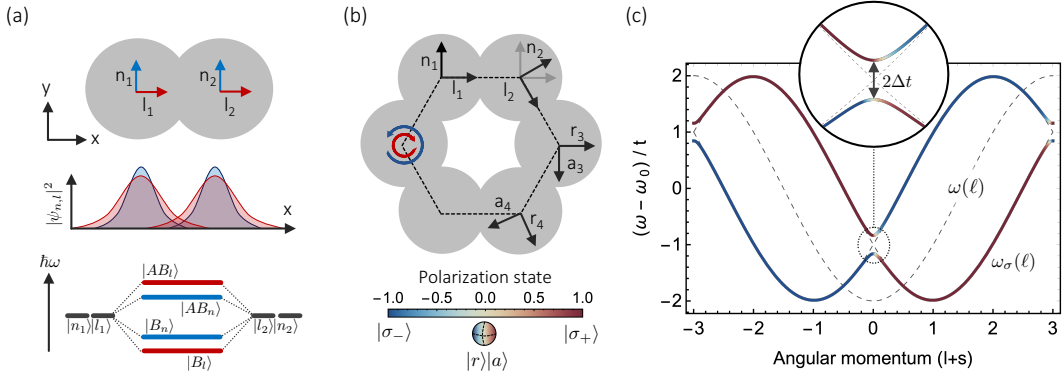


Figure 4.3: **Analog spin-orbit coupling:** (a) The modes linearly polarized along x ($\vec{l}_{1,2}$ basis) have a larger coupling than the ones polarized along y ($\vec{n}_{1,2}$ basis). In a tight-binding picture this corresponds to a larger overlap integral $t_l \sim \langle l_1 | l_2 \rangle > t_n$, where $|\psi^i\rangle$ are the bare pillar modes. This results in a splitting of the bonding (B) and anti-bonding (AB) modes in the level hybridization diagram. In benzene photonic molecules, as the link direction \vec{l}_i changes from pillar to pillar this creates an azimuthally varying birefringent axis for the linearly polarized photons (c), corresponding to an analog spin (polarization) orbit coupling [187]. (d) The eigenmodes of a ring arrangement of microcavities can be classified based on the total angular momentum $J = \ell + \sigma$, and follow the dispersion relation $\omega_\sigma(\ell)$ (here $N = 6$, details in the main text). When introducing a finite polarization splitting $\Delta t = (t_l - t_n) > 0$, the modes written in a circular polarization basis $\sigma = \pm 1$ (SAM) hybridize at $j = 0, 3$, lifting the degeneracy of the $|\ell| = 1, 2$ multiplets.

the non-orthogonality of the bare pillar eigenmodes [189]. Although non-orthogonality becomes significant for values $d/R < 1.5$, this approach has been proven to yield satisfactory results in our experiments (for an alternative approach based on an analysis of the point symmetry group of the hamiltonian see Appendix 4.8). The starting point is to introduce the linearly polarized bare pillar eigenmodes in the $(\vec{n}_i, \vec{l}_i)_i$ basis, labeled $(|n_i\rangle, |l_i\rangle)$. Also, a second linear polarization basis $(\vec{r}_i, \vec{a}_i)_i$, is useful to allow a finite energy splitting $\Delta E = (E_r - E_a)/2$ between radially and azimuthally polarized modes. This splitting can be phenomenologically understood noticing that azimuthally polarized photons on site i , experience a reduced transverse confinement due to a larger penetration depth expected along the $\vec{l}_{i-1, i+1}$ directions; we thus expect $\Delta E > 0$. In particular, for N sites, as Δt is proportional to the difference between the penetration depth of $|l, t\rangle$, we expect $\Delta E \sim \Delta t [\cos(\theta_N/2) - \sin(\theta_N/2)]$, where $\theta_N = 2\pi/N$. We can consider a single excitation in the tight-binding hamiltonian \mathcal{H} of the system, denote $-t_{(n,l)} = \langle (n, l)_j | \mathcal{H} | (n, l)_{j+1} \rangle$ ($\hbar = 1$ units) and rescale all the on-site energies for the offset $\omega_0 = (\omega_r + \omega_a)/2$. Since we consider only nearest-neighbor hopping, \mathcal{H} has a 2×2 block structure, this suggest to group the on-site basis using the compact notation $|\psi_i\rangle = |r_i, a_i\rangle$. The block elements of the Hamiltonian in this basis are

$$\mathcal{A} = \mathcal{H}|\psi_i\rangle\langle\psi_i| = \Delta E \begin{pmatrix} 1 & 0 \\ 0 & -1 \end{pmatrix} \quad (4.2)$$

For the tunneling matrix elements one can show with simple trigonometric relations and recalling the rotation matrix definition and properties that

$$\mathcal{B} = \mathcal{H}|\psi_i\rangle\langle\psi_{i+1}| = \mathcal{R}(\theta_N) \begin{pmatrix} -t_n & 0 \\ 0 & -t_l \end{pmatrix} \mathcal{R}^T(\theta_N) \quad (4.3)$$

where $\mathcal{R}(\theta_N)$ is the counter-clockwise rotation matrix by an angle $\theta_N = 2\pi/N$. In order to explicitly write the hamiltonian in a spin (polarization) and angular momentum (phase-winding) basis, we can transform it to the on-site circular polarization basis $|\sigma_j\rangle = \mathcal{C}_j|\psi_j\rangle$, determined by the block elements

$$\mathcal{C}_j = \frac{1}{\sqrt{2}} \begin{pmatrix} 1 & i \\ 1 & -i \end{pmatrix} [\mathcal{R}(\theta_N)]^j \quad (4.4)$$

with $j = 0, \dots, N-1$ and $[\mathcal{R}(\theta_N)]^j$ taking in account the extra phase due to the rotation of the $(r, a)_j$ frame. In the circular polarization basis the hamiltonian has a tridiagonal 2×2 block form: if we define the block elements in the circular polarization basis $(\tilde{\mathcal{A}}, \tilde{\mathcal{B}})_j = \mathcal{C}_j(\mathcal{A}, \mathcal{B})\mathcal{C}_j^\dagger$, it can be easily diagonalized using the properties of circulant matrixes. Indeed, the normalized eigenvectors u_ℓ and eigenvalues ϵ_ℓ of such a (tridiagonal) matrix read

$$\begin{aligned} v_\ell &= (1, \omega_\ell, \omega_\ell^2, \dots, \omega_\ell^{(N-1)})/\sqrt{N} \\ \epsilon_\ell &= \tilde{\mathcal{A}}_\ell + \tilde{\mathcal{B}}_\ell e^{-i\theta_N} + \tilde{\mathcal{B}}_\ell^T e^{i\theta_N} \end{aligned} \quad (4.5)$$

where $\omega_\ell = e^{i\theta_N \ell}$ and $\ell = 0, \dots, N-1$ or equivalently $|\ell| = 0, \dots, N/2$ because of the modulo 2π freedom. The linear transformation that block-diagonalizes the hamiltonian, is thus change of basis $|\ell\rangle = \sum_j^N e^{i\theta_N j \ell} |\sigma_j\rangle$ with $|\ell| = 0, \dots, N/2$. This is telling us that each block element is labeled by the orbital angular momentum number, and for a given ℓ the entries of the block are the projections on the circular polarization basis $|\sigma\rangle$. If we introduce the total angular momentum $k = \ell + \sigma$, and define $\tilde{t} = (t_l + t_n)/2$, the block elements in the $|\ell, \sigma\rangle$ basis are

$$\mathcal{J}_{\ell, \sigma} = -2\tilde{t} \cos(\theta_N k) \delta_{(\sigma, \sigma')} + [\Delta t \cos(\theta_N k) - \Delta E] e^{-2i\theta_N \sigma} \delta_{(\sigma, \sigma')} \quad (4.6)$$

where δ indicates the Kronecker delta. Remarkably, the eigenvalues can be classified using only the quantum numbers (k, σ) . In absence of spin orbit coupling $\Delta t = 0$ and assuming for simplicity $\Delta E = 0$, the eigenvalues correspond to the scalar ($\sigma = 0$) dispersion relation $\omega(\ell) = -2t \cos(\theta_N \ell)$ shifted by $\sigma = \pm 1$ on the discrete k axis, see dashed lines in Fig. 4.3-(c) ($N = 6$). The off-diagonal elements, when increasing Δt , hybridize the circularly polarized bands in vicinity of their crossings for $|k| = (0, N/2)$. Figure 4.3-(c) shows the dispersion relations $\omega_\sigma(\ell)$ plotted as a function of k for $\Delta t/\tilde{t} = 0.25$ displaying a clear level anti-crossing for $|k| = (0, N/2)$. The degree of circular polarization deduced from the eigenvectors of $\mathcal{J}_{\ell, \sigma}$ is color-coded along $\omega_\sigma(\ell)$. Each vertical cut trough the dispersion relation $\omega_{\pm 1}(k)$ for an integer k value, defines the fine structure eigenfrequencies of a N (even) ring arrangement of micropillars.

As we are interested in the OAM of the modes, we conveniently label each eigenstate using an $|\ell, \sigma\rangle$ basis. Interestingly, we observe that the eigenmodes $|\ell| \neq (1, N/2 - 1)$ are eigenstates of the circular polarization operator (σ_z). On the contrary, for $|\ell| = (1, N/2 - 1)$ two modes (labeled $\psi_{2,3}$) are degenerate in energy and have well defined but opposite circular polarizations. The other two (labeled $\psi_{1,4}$) are split in energy by $\approx 2\Delta t \sin(2\theta_N)$ and present some linearly polarized pattern [inset in Fig. 4.3-(c)]. More

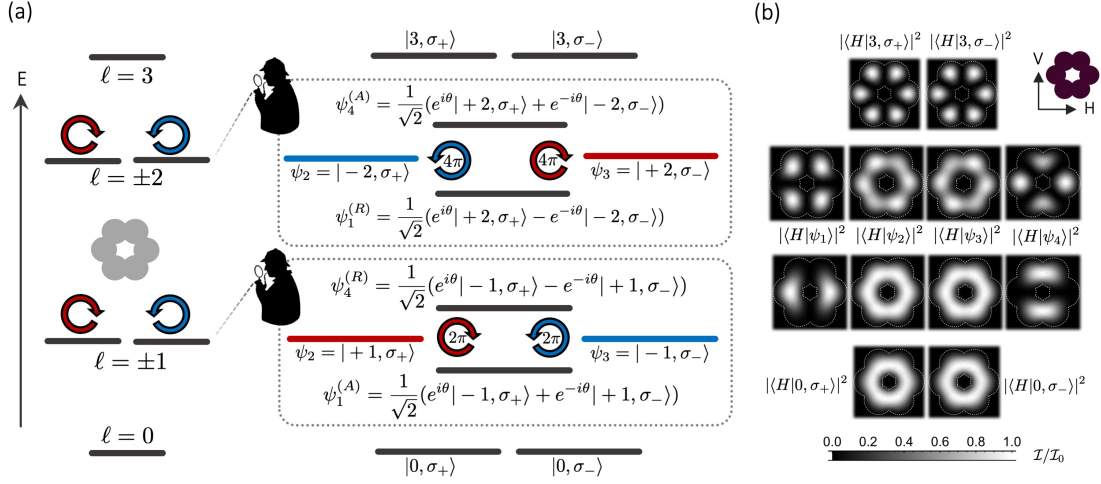


Figure 4.4: **Fine structure modes:** (a) Schematic illustration of the energy ladder for $N = 6$ both for the scalar model and when including a finite spin-orbit coupling Δt . Each level eigenmode is classified according to a SAM-OAM basis decomposition. (b) Normalized spatial intensity patterns obtained by finite element methods upon projecting the electric field along the x axis (H), see App. 2.6 for details. In the V polarization basis all the patterns remain unchanged, except for $\psi_{1,4}(\ell)$ satisfying the relation $|\langle H|\psi_{(1,4)}\rangle| = |\langle V|\psi_{(4,1)}\rangle|$.

specifically, Fig. 4.4-(a) illustrates the fine-structure modes decomposed in a $|\ell, \sigma\rangle$ basis for the $N = 6$ case. From this decomposition we see that the $\psi_{1,4}$ modes correspond to the symmetric or anti-symmetric superpositions of the rotated states $e^{\pm i\theta_N}|\ell, \pm 1\rangle$ thus yielding, respectively, an azimuthally or radially polarized emission pattern. In particular, the (linear) polarization axis of $\psi_{1,4}(\ell)$ modes winds $|\ell|$ times upon encircling the structure. This latter observation will turn out to be useful in experiments, as we will be able to discriminate the $\psi_{1,4}$ from the $\psi_{2,3}$ based on their emission pattern. Although a linear polarizer does not affect the circularly polarized pattern of $\psi_{2,3}$, it creates intensity nodes for radial (or azimuthal) patterns in correspondence of the regions where the polarization of the emission and of the analyzer are crossed. As an example, in 4.4-(b), we show calculations of the spatial emission patterns of each mode in the fine structure when analyzed in the horizontal (H) linear polarization basis.

The fact that the modes $\psi_{2,3}(\ell)$ are degenerate in energy but present opposite SAM and OAM is the first key ingredient we will capitalize on for the implementation of our laser scheme.

4.2.2 A spin polarized gain medium

The starting point of this experimental project was actually an unexpected result we obtained while looking at the data obtained in a polarization tomography of the emission of a single micropillar cavity under a weak non-resonant excitation. In this experiment we excited both with a linearly and a circularly polarized optical pump at 770 nm a single pillar. When analyzing the spectrally resolved photoluminescence (PL) of the microstructure in the circular polarization basis the two excitations gave different results. Under a linearly polarized pump the σ_{\pm} components of the PL spectra have

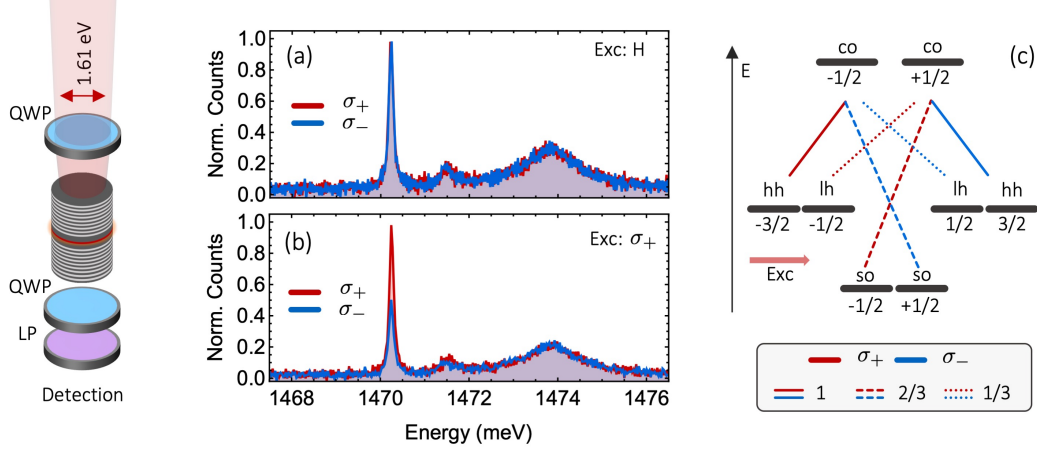


Figure 4.5: **Optical polarization of the gain:** (a,b) Energy resolved emission of a $1.8 \mu\text{m}$ radius pillar under a linearly and σ_+ circularly polarized off-resonant pump, respectively. The emission is analyzed in the circular polarization components, a small fraction of the pump circular polarization is preserved ($\eta \approx 0.06$) in panel (b). Illustration of the GaAs Γ -point polarization and relative intensity of the optical dipole matrix elements, adapted from [86]. Notice that the pump energy ($E_p = 1.61 \text{ eV}$) is well below the split-off band transition ($E_{so} = 1.86 \text{ eV}$, cf. Sec. 2.2).

precisely the same magnitude, see Fig. 4.5-(a). On the contrary, under a σ_{\pm} polarized pump the emission keeps a finite degree of circular polarization, see Fig. 4.5-(b). In particular the emission is preferentially circularly co-polarized with the pump, with a measured degree of circular polarization of $\eta = (I_{\pm} - I_{\mp}) / (I_{\pm} + I_{\mp}) \approx 0.06$.

To understand this observation we need to recall the Γ -point optical selection rules for bulk GaAs. In Fig. 4.5-(c) we summarize the polarization and relative magnitude of the non-zero dipole matrix elements between the heavy-hole (hh), light-hole (lh) and split-off (so) band towards the conduction band [86]. It is quite clear that any linearly polarized excitation, will promote a globally neutral population of carriers which, upon relaxation, will produce PL emission with $\eta = 0$. Similarly, using circularly polarized light with an excitation energy greater than the so-band ($E_{so} = 1.86 \text{ eV}$) all the transitions balance out, yielding again an unpolarized carrier population. On the contrary, if the excitation energy is below the so-band transition, like in our experiments, the carriers should have $\eta = -2/3$ degree of circular polarization with respect to the pump, which means an $\eta = 2/3$ co-circularly polarized emission upon recombination.

The reason why this result was quite surprising for us is that in between the creation of carriers at 1.61 eV and the microcavity emission at 1.47 eV , one needs phonon-mediated relaxation processes to bring the carriers to the bottom of the conduction band. Although phonons are spinless excitations of the lattice, there are a number of coupling mechanisms ultimately leading to random spin-flips over short timescales; we refer to [75, 297, 298, 299] for an overview. Our measurements suggest that for high quality samples at low temperatures (4K), the relaxation rate is fast enough when compared with the spin relaxation mechanisms, thus allowing to partially keep a fraction of the spin polarization imprinted to the carriers.

If now we consider partially spin-polarized photo-generated carriers, the imbalance is transferred to the optical gain. In the limiting case of a fully polarized medium

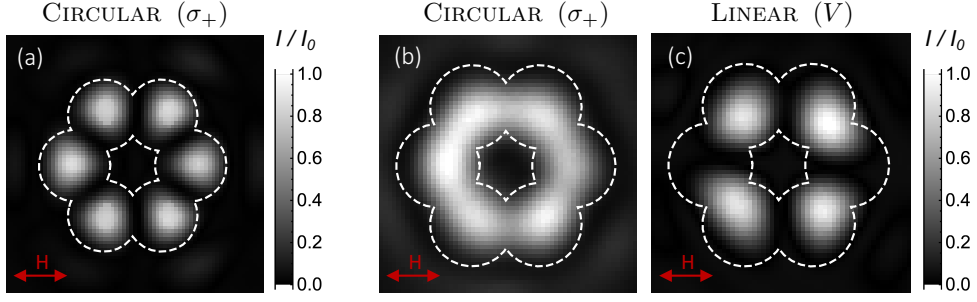


Figure 4.6: **First hints:** Imaging of the microlaser emission above the lasing threshold for a $d = 2.6 \mu\text{m}$ (a) and $d = 2.4 \mu\text{m}$ (b,c) microstructure. The pump polarization is circularly (σ_+) polarized in (a,b) and vertically polarized in (c); all the three emission patterns were analyzed with a polarizer in the H basis (see arrow). These patterns can be directly compared with the calculations presented in Fig. 4.4-(b).

the gain is twice as large for ψ_2 or ψ_3 (depending on the polarization) than for the radially or azimuthally polarized modes ψ_1 or ψ_4 , because these latter modes exhibit a reduced overlap with the polarized reservoir stemming from the $1/\sqrt{2}$ coefficients in their wavefunction, see Fig. 4.4-(a). Therefore, we expect such an imbalance of the gain within each manifold to result in a single-mode lasing in either of the chiral modes $\psi_{2,3}$ by injecting spin-polarized carriers in the device. This optical breaking of time-reversal symmetry would allow ultrafast switching times limited only by the relaxation of carriers ($\sim \text{ps}$) [300, 301].

In a series of preliminary experiments, we used a circularly (σ_+) polarized pump to trigger lasing in benzene photonic molecules with $1.6 \mu\text{m}$ radius and different inter-pillar distance $d = (3.1 - 2.3) \mu\text{m}$. For $d > 2.5 \mu\text{m}$ we have observed the six lobes of the $\ell = 3$ mode in all the emission patterns, see Fig. 4.6-(a) corresponding to the emission of a microlaser with $d = 2.6 \mu\text{m}$ (no spectral filtering). Interestingly, for $d = 2.4 \mu\text{m}$, the pattern changed to a homogenous doughnut-shaped profile [Fig. 4.6-(b)], since we analyzed the emission in the H basis this suggested we were lasing as expected in the circularly polarized ψ_2 mode. Indeed, as we changed the pump polarization to linear (V), the linearly polarized $\psi_{1,4}$ modes are favored by the gain, resulting in the appearance of a four-leaf clover pattern shown in Fig. 4.6-(c). This patterns can be directly compared with the finite element calculation of the polarization resolved mode profile presented in Fig. 4.4-(b), suggesting that lasing occurred with the $|\ell| = 2$ OAM manifold in either $\psi_{2,3}$ and ψ_1 under a σ_+ and V polarized pump, respectively.

4.3 Demonstration of the OAM control scheme

To demonstrate the optical control the microlaser emission chirality, we investigated two different devices. We consider two photonic molecules formed by six $3.2\ \mu\text{m}$ -diameter micropillars with an inter-pillar distance of $2.3\ \mu\text{m}$ (molecule M1) or $2.4\ \mu\text{m}$ (molecule M2). The variation of the inter-pillar distance modifies the relative gain/loss ratio of the photonic modes (details in the next section), allowing to select a precise $|\ell|$ manifold in which lasing occurs: for the molecule M1 (M2), lasing occurs in the $|\ell| = 1$ ($|\ell| = 2$).

In order to minimize the lasing power threshold, we operate with molecules whose optical modes are slightly red-detuned ($5 - 3$) meV from the exciton transition ($E_x = 1475.10(5)$ meV). The measured finesse of the cavity is $\mathcal{F} \approx 4 \cdot 10^4$ mainly limited by residual absorption. The relative detuning can be adjusted by moving on the sample thanks to the cavity thickness spatial gradient implemented during the growth (cf. Sec 3.1.1). Here the microstructures were held at 4K and optically pumped by a laser tuned in vicinity of one reflectivity minima of the DBRs (1.61 eV). For details on the setup we refer to Sec. 3.2, with a slight modification being that the excitation objective had been substituted with a 100 mm focal lens producing a $20\ \mu\text{m}$ (FWHM) spot providing an homogeneous illumination of the microstructure. The emission of the microstructure has been collected in transmission geometry, in this way the residual of the pump beam is absorbed in the GaAs substrate, allowing to avoid any further spectral filtering.

Figure 4.7 presents the results for molecule M1 when exciting the device with a circularly polarized (σ_+) off-resonant pump. A nonlinear increase of the integrated emission intensity (red markers) can be observed in Fig. 4.7-(b) above a threshold power density of $P_{\text{thr}} = 0.4\ \text{kW}/\text{cm}^2$; correspondingly, the linewidth of the $|\ell| = 1$ manifold peak (black markers) narrows below the spectrometer resolution (dot dashed line). Examples of the emission spectra for excitation powers above, around and below this threshold are respectively presented in Fig. 4.7-(b,c,d). Above threshold, we observe a single mode emission from the $|\ell| = 1$ manifold.

At low excitation power -see Fig. 4.7-(d)- the emission presents a small but non-negligible degree of circular polarization ($\eta \sim 5\%$), demonstrating that the spin polarization of photo-generated carriers is significantly preserved during their relaxation in the gain medium. In the lasing regime, η is greatly enhanced reaching almost unity ($\eta > 90\%$), thanks to the stimulated nature of the emission, see Fig. 4.7-(b). Real space images of the device emission (without any spectral filtering) under co- and cross-polarized detection evidence that the entire emission presents this strong degree of polarization, as Fig. 4.7-(e,f) respectively show. This indicates that the spin-polarized pump indeed triggers lasing in a circularly polarized mode, that is either ψ_2 or ψ_3 .

When considering the second device (M2), we now observe that a σ_+ polarized pump triggers lasing in the $|\ell| = 2$ manifold, see Fig. 4.8-(a-d). As in M1, the degree of circular polarization of the emission in the lasing regime is very strong ($P > 95\%$) and is dictated by the polarization of the pump, as the spectra [Fig. 4.8-(b)] and emission pattern [Fig. 4.8-(e,f)] demonstrate.

In order to evidence the phase vortex associated to the lasing modes of M1 and M2, we interfere the beam with a magnified image of the emission from one of the molecule pillars, which acts as a phase reference, as schematized in Fig. 4.9-(a). The resulting

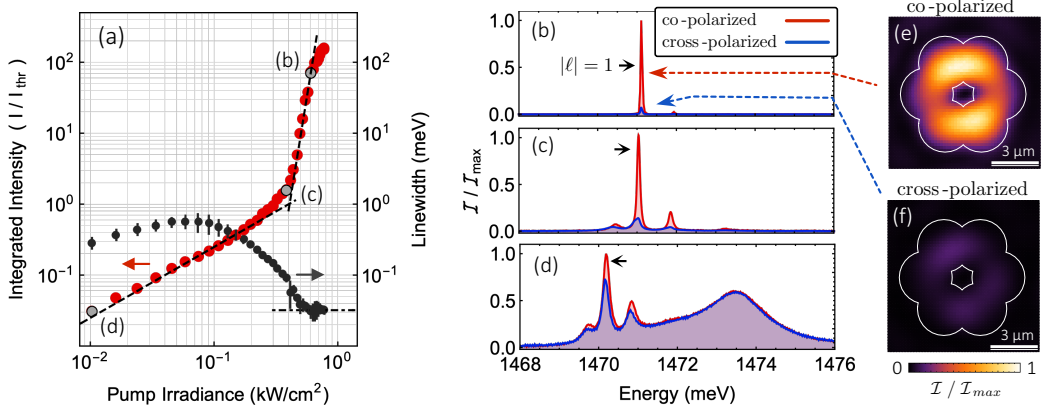


Figure 4.7: **M1 microlaser.** (a) Integrated output intensity and linewidth of the $|\ell| = 1$ emission measured as a function of incident pump power; the lasing threshold is at $P_{\text{thr}} \sim 0.4 \text{ kW}/\text{cm}^2$. Dashed lines: I-P curve power law fits; Dot-dashed line: spectrometer resolution. (b-d) Polarization and energy resolved emission spectra under σ_+ polarized pump above (b), at (c) and below (d) the lasing threshold. Red and blue curves correspond to (σ_+) co- and (σ_-) cross-polarized emission with respect to the polarization of the pump. (e,f) Co- and cross-polarized real space images of the emission under a σ_+ polarized pump without any spectral filtering.

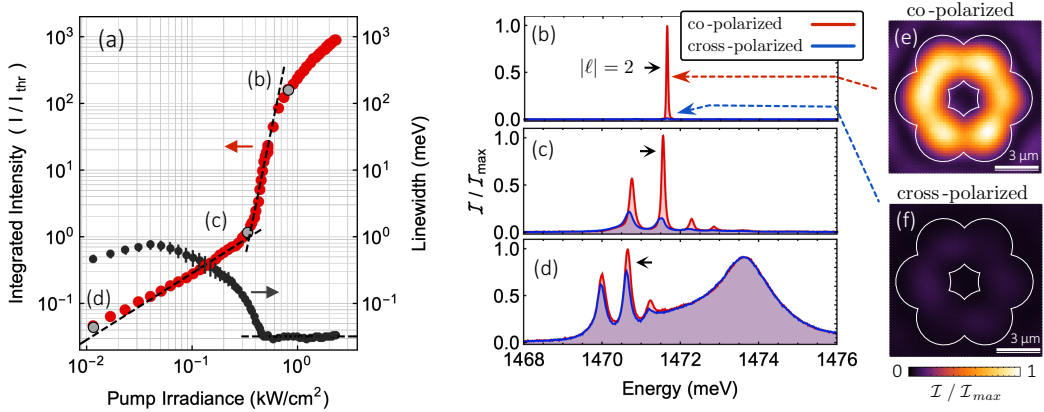


Figure 4.8: **M2 microlaser.** (a) Integrated output intensity and linewidth of the $|\ell| = 2$ emission measured as a function of incident pump power; the lasing threshold is at $P_{\text{thr}} \sim 0.3 \text{ kW}/\text{cm}^2$. Dashed lines: I-P curve power law fits; Dot-dashed line: spectrometer resolution. (b-d) Polarization and energy resolved emission spectra under σ_+ polarized pump above (b), at (c) and below (d) the lasing threshold. Red and blue curves correspond to (σ_+) co- and (σ_-) cross-polarized emission with respect to the polarization of the pump. (e,f) Co- and cross-polarized real space images of the emission under a σ_+ polarized pump without any spectral filtering.

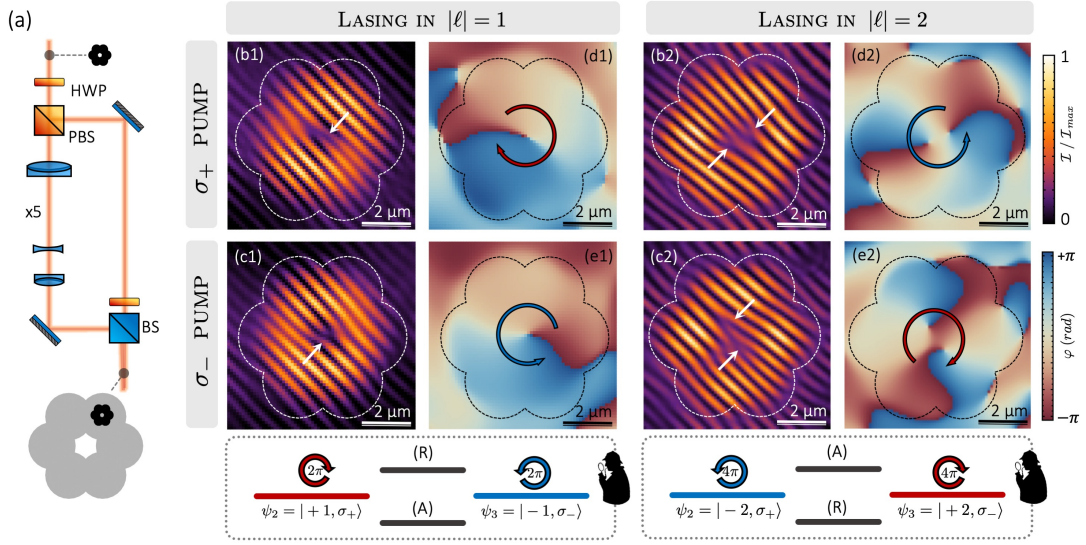


Figure 4.9: **Measuring the wavefront twist.** (a) Illustration of the modified Mach-Zehnder arrangement used for the OAM measurement, the relative intensity, magnification and polarization of the two arms can be adjusted. (b1,c1) Measured interference patterns for the device M1 at $P = 0.6 \text{ kW/cm}^2$, corresponding to Fig. 4.7-(d), for a σ_+ and σ_- polarized pump, respectively. (d1,e1) Corresponding phase maps showing 2π CW (CCW) vortex under σ_+ (σ_-) pump. (b2-e2) Same for the M2 device, here $P = 0.8 \text{ kW/cm}^2$ and the presence of a double pitchfork dislocation indicates a 4π CCW (CW) vortex under σ_+ (σ_-) pump. Bottom: fine structure of the $|\ell| = 1, 2$ manifolds.

interferogram for M1 under a σ_+ excitation, taken without spectral nor circular polarization filtering, is shown in Fig. 4.9-(b1). The corresponding phase map, obtained with a standard off-diagonal Fourier filtering technique (details in Appendix 4.7), is presented in Fig. 4.9-(d1). The pitchfork in the interferogram (marked by a white arrow) and the vortex in the phase map evidence a 2π winding of the phase around the molecule, showing that the laser mode presents an OAM of $\ell = +1$. This OAM value corresponds to the ψ_2 mode of the $|\ell| = 1$ fine structure (see bottom of 4.9). Remarkably, when changing the excitation polarization to σ_- , the polarization of the gain medium is inverted, and the lasing mode, fully σ_- polarized, now evidences opposite chirality, corresponding to $\ell = -1$ (ψ_3). This is evidenced by the interferogram and corresponding phase map presented in 4.9-(c1) and (e1) showing respectively an inversion of the pitchfork dislocation and of the circulation of the phase. This demonstrates the ability to optically break time-reversal symmetry and control the chirality of the lasing mode.

When considering the second device (M2) under a σ_+ polarized illumination, we obtain the interferogram presented in Fig. 4.9-(b2). Now, two pitchforks dislocations appear in the interferogram (white arrows), thus corresponding to a 4π CCW vortex as indicated by the associated phase map shown in 4.9-(d2). This clearly shows that the emission presents an OAM of $\ell = -2$. Then, by changing the polarization of the pump to σ_- , the chirality of the emission is inverted to $\ell = +2$ (4π CW vortex), as the interferogram and phase map presented in 4.9-(c2) and (e2) demonstrate, respectively.

The phase circulation inversion observed between the $\psi_{2,3}$ modes of the $|\ell| = 1$ and $|\ell| = 2$ OAM microlaser matches the predictions of the minimal tight-binding model presented in Sec. 4.2.1, see the bottom insets of Fig. 4.9.

Importantly, the high degree of circular polarization of the emission above threshold ($\sim 95\%$), associated to a rather clean single-mode operation, largely exceeds the degree of polarization of the gain medium below the lasing threshold ($\sim 5\%$). This indicates that our lasing scheme provides a strongly enhanced resilience against depolarization of the excitation, in comparison to optical devices that convert directly circular polarization to OAM (e.g. q-plates or metasurfaces). As we pointed out in the introduction of this chapter, this is one of the main motivations for the development of active components directly emitting structured light.

4.3.1 Selection of the OAM lasing manifold

In experiments we noticed that, for a given negative detuning $\delta = \omega_\ell - \omega_x$ of the optical modes with respect to the exciton energy, the larger the inter-pillar distance d , the larger the OAM of the lasing mode. In particular, for $\delta \sim -10$ meV only the $\ell = 3$ modes were lasing, regardless of d . For more moderate detuning values, as in the previous section, we observed that for $R = 1.6 \mu\text{m}$ and $d = (2.6, 2.4, 2.3) \mu\text{m}$ the lasing OAM manifold was $|\ell| = (3, 2, 1)$, respectively. We will refer to these structures as M3¹, M2 and M1. In this section we provide an explanation of this observation based on a simple model which uses a minimal number of parameters to describe how it is possible to tune the relative gain/loss ratio of each OAM manifold.

The fact that for very negative detuning the lasing mode is independent of d , can be simply understood in terms of the spectral dependence of the gain. Indeed, for QW lasers, the position of the maximum of the differential gain is in vicinity of the exciton transition ($E_x = 1475.10(5)$ meV) and has a typical spectral bandwidth of $\sim (20 - 50)$ meV depending on the details of the heterostructure [302, 303]. If the optical modes are significantly red-shifted from the maximum, the slope of the spectral gain curve is significant even over the $(1.5 - 2)$ meV spanned by the OAM modes, thus favoring the highest energy one ($\ell = 3$). On the contrary, in vicinity of E_x , the spectral dependence of the gain can be essentially neglected, see the sketch in Fig. 4.10-(a). Moreover, as the structure was evenly illuminated, we can as well consider that the spatial overlap between the gain medium and every mode is nearly identical. This suggest that, as a first approximation, we can consider equal gain for of each of the scalar modes, as any spectral or spatial dependence of the gain can be disregarded.

Thus, for moderate detunings, we expect the selection of the lasing manifold to be solely determined by the relative losses associated to each manifold. In our microcavities, losses associated to photons leaking through the mirrors (i.e. the radiative lifetime) are identical for each mode. However, the dry etching process creates near the pillar edges a high density of scattering or non-radiative recombination centers (RCs): these RCs represent the main contribution to the variation of losses from one mode to the other, as each mode overlaps differently with the edge of the structure.

An estimate of the relative contribution of these non-radiative losses can be obtained by computing the overlap integral of each eigenmode with the RCs density profile. For

¹The emission of the $d = 2.6 \mu\text{m}$ microlaser is shown in Fig. 4.6-(a)

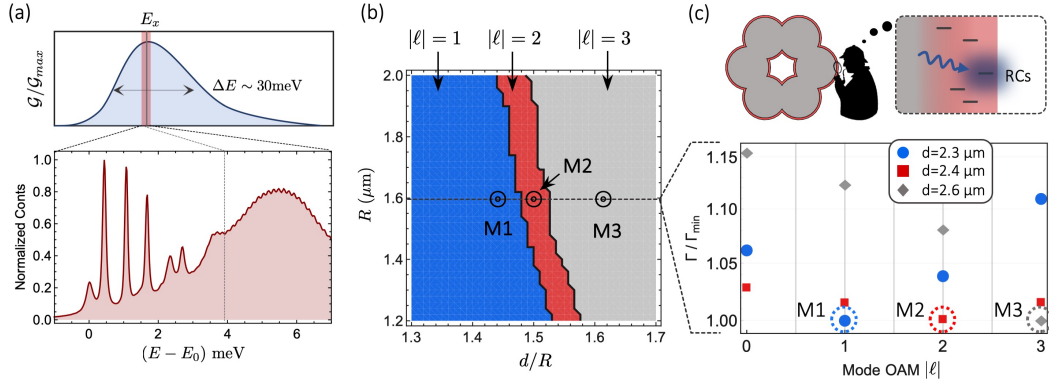


Figure 4.10: **Mode selection mechanisms.** (a) Comparison between the normalized differential gain spectrum and the low power PL spectrum of a $d = 2.3 \mu\text{m}$ microstructure. (b) Mapping of the manifold with the lowest non-radiative loss as a function of the inter-pillar distance d and pillar radius R . Black circles correspond to the experimental results obtained for the devices M1, M2 and M3. (c) Relative non-radiative losses associated to each scalar eigenmode ($\Gamma_{\min} = \min_{\ell} \Gamma_{\ell}$). Blue circles, red squares and grey diamonds nominally correspond to M1, M2 and M3. Inset: schematic illustration of the recombination region (RC) along the device perimeter (in red).

simplicity, we assume the latter to be uniform over a thickness δR along the edges of the structure, as sketched in the inset of Fig. 4.10-(c). For the calculation of the overlap integral, we calculated the scalar eigenmodes profile with finite element methods using the infinite waveguide approximation described in Sec. 2.4. The refractive index of the waveguide, whose transverse profile matches the cross-section of the microstructure, was chosen to match the effective refractive index of the vertical cavity ($n_{\text{eff}} \approx 3.42$ cf. Sec. 2.3.3).

The result of these calculations is summarized in Fig. 4.10-(b), identifying the mode with lowest non-radiative contribution as a function of the micropillar radius R and inter-pillar distance d . In the plot, red, blue and gray areas correspond to $|\ell| = (1, 2, 3)$ respectively. We see that for sufficiently small inter-pillar distance the smallest overlap with the RC region is always for $|\ell| = 1$ whereas large d/R values favour $\ell = 3$; in-between these two regions, when $d/R \sim 3/2$, the $|\ell| = 2$ modes present the lowest non-radiative loss. This behaviour stems from the competition between two different mechanisms. On the one hand, modes with increasing $|\ell|$ have a profile that peaks at larger values of the radial coordinate (cf. Fig. 4.2), thus having a greater overlap with the outer edge of the microstructure. On the other hand, modes with a smaller $|\ell|$ present a larger overlap with inter-pillar regions where the density of RC is the largest; this second effect is more pronounced as d increases.

The exact range of inter-pillar distances d/R , where the $|\ell| = 2$ mode is favored, depends on the thickness of the non-radiative recombination region considered. In order to match the experimental observations (black circles), we had to set $\delta R \approx 80$ nm, which is a reasonable value. Finally, in Fig. 4.10-(c), we plot the relative non-radiative linewidth as a function of $|\ell|$ for three structures nominally identical to M1, M2 and M3. Although the relative change of the RC-induced losses changes only by a few percents between modes with different OAM, we always observed² an increasing OAM

²over dozens characterizations of different structures

of the lasing manifold when increasing d for a fixed detuning. This is the same general behavior illustrated by the calculation in Fig. 4.10-(b,c).

More complex nonlinear contributions to the balance of population dynamics such as gain saturation, spectral and spatial hole burning or band gap renormalization are neglected. Indeed, although the proposed model is minimalist, it has been sufficient to properly reproduce, for all excitation powers, the dependence of the lasing manifold on the device shape without more complex contributions. Notice that in this section we refer only to the OAM manifold, rather than the specific fine structure, where mode competition is essentially dictated by the degree of polarization of the gain medium, as anticipated in Sec. 4.2.2. Interestingly, in Sec. 4.4, we will see that nonlinear effects, such as saturation, do not change $|\ell|$ but lead to a bistable behavior of the microlaser involving distinct OAM fine structure modes.

4.3.2 Temperature robustness

Intuitively, the possibility to control the chirality of the emission only requires that the spin-dependence of the gain within one OAM manifold dominates all other possible contributions, e.g. spectral dependence of the gain, asymmetry of the structure, etc. This condition can be undermined by the onset of thermally activated spin-relaxation processes. In order to evaluate the robustness of our devices against these processes, we measured the degree of circular polarization of the photoluminescence from a single quantum well (without the cavity) as a function of temperature.

Figure 4.11-(a) illustrates the measurement setup. We used a few μW excitation laser at 1.61 eV (as in the OAM microlaser experiments) to excite the microstructure; its initial linear polarization (V) could be changed to circular by using an achromatic quarter wave-plate (QWP). When the fast axis of the QWP is aligned along the V polarization axis, a couple of PBS in the collection path allows spatially separating along the H and V components of the QW emission. Similarly, when the QWP is rotated to produce a σ_+ excitation, the σ_{\pm} components of the counter-propagating QW emission are mapped into the H, V linear basis and separated by the PBS. We use a $\lambda/2$ and linear film polarizer (P) to compensate for the slightly different losses in the two collection paths. This is done by balancing the signals under a linear excitation used as a reference for zeroing the apparatus. For each temperature, we acquired two images corresponding to the (V, σ_+) excitations; each of them includes two spots, whose integrated intensities yield the relative weight of the two polarization components along the axis of the Poincaré sphere parallel to the excitation. As an example, Fig. 4.11-(b) shows the CCD frame acquired at $T = 10.0(1)$ K under a σ_+ pump, the visible asymmetry between the left and right parts of the panel testifies a finite degree of circular polarization of the emission ($\eta \approx 0.17$). To ease the comparison, we integrate the image along the vertical direction and compare the resulting normalized profile (red) with the one obtained under a linear excitation (dashed).

In Fig. 4.11-(c) we present the result of these measurements as a function of temperature. Interestingly, the degree of polarization remains non-negligible ($\sim 10\%$) up to $T = 80$ K, while above 100 K, it slowly vanishes below 5%. Thanks to this temperature resilience of the degree of spin-polarization of the QW, we were able to implement our scheme above liquid nitrogen temperatures. Figure 4.11-(d-k) presents a full characterization of the lasing properties of the device M2 at 80K. In panel (d) we show the

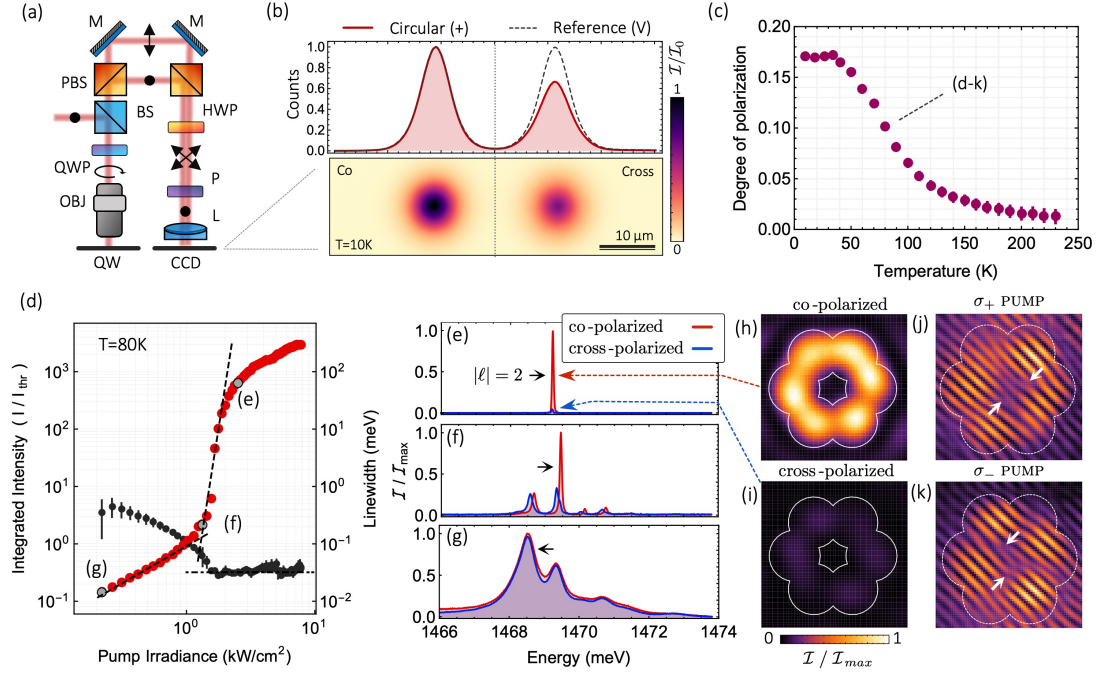


Figure 4.11: **Probing the temperature robustness of the scheme.** (a) Schematic of the degree of polarization measurement apparatus (details in the main text). (b) Example of the detected signal under a circular (σ_+) excitation at 10K; left and right sides of the panel correspond to the co- and cross-circularly polarized components of the QW emission, respectively. Top: normalized vertical binning of the image, the dashed line shows the corresponding profile acquired under a linear excitation (V). (c) Measured degree of circular polarizations as a function of temperature; error bars correspond to two standard deviations. (d-k) Characterization of the M2 device at 80K. (d) Intensity and linewidth dependence with pump power under a σ_+ excitation. (e-g) Polarization resolved emission above, at and below the lasing threshold ($P_{\text{thr}} \approx 1.1 \text{ kWcm}^{-2}$), respectively. (h-i) Co- and cross-circularly polarized emission pattern in the lasing regime corresponding to (e). (j,i) Interferograms under a σ_+ and σ_- polarized excitation, respectively. The inversion in the pitchfork dislocations between panel (j) and (k) signals that the 4π vortex helicity is switched.

I-P curve and linewidth of the emission as a function of the power of a σ_+ polarized pump. Again, a clear threshold is signaled by the abrupt increase in the output power with the simultaneous narrowing of the emission linewidth below the spectrometer resolution. The lasing threshold is roughly 4 times higher than at 4K due to the increased absorption across the whole microstructure. From panels (e,h,i) we can see that above threshold the emission is still single mode and strongly co-circularly polarized with the pump. Finally, panels (j,k) show that exciting device M2 at 80K with opposite circular polarizations, still allows optically controlling the chirality of the ($|\ell| = 2$) emission. Above this temperature, the lasing mode approaches the GaAs band gap [68], thus drastically enhancing light absorption and increasing significantly the threshold power. This technical limitation prevents us from exploring the lasing regime of our structure at higher temperatures. Nevertheless, by using a pulsed excitation instead of a CW and an appropriate heterostructure design, we expect to extend the range of operation of the microlaser up to room temperature [300].

4.4 OAM bistability

In semiconductor lasers, when the pump power is much larger than threshold, one enters the gain saturation regime. In this regime a variety of nonlinear effects -such as spectral and spatial hole burning and bandgap renormalization- sets in, eventually resulting in mode hopping or in bistable behavior [304]. In this section, we show that the interplay of a nonlinear gain dependence with the fine structure of the optical modes leads to bistable regime. Here, the bistability involves modes presenting distinct values of the OAM ($\ell = 0$ and $|\ell| = +2$) and different polarization textures, due to spin-orbit coupling in the microstructure.

We will focus on the device M2, whose emission in the lasing regime (before gain saturation) has been presented in Fig 4.8. As we already demonstrated the ability to control the emission chirality with the circular polarization of the pump (see Fig 4.9), we will restrict to the case of a σ_+ excitation. All the measurements in this section have been acquired with linear (H) polarization filtering, as it provides a complementary tool to identify the lasing mode (cf. Sec. 4.2.2). In Fig 4.12-(a) we recall the fine structure of the $|\ell| = 2$ manifold, and the calculated emission pattern of each mode upon projecting along H the electric field ($|\langle H|\psi_i\rangle|^2$). The evolution of the emission intensity as a function of pumping power [Fig. 4.12-(b)] shows a lasing threshold around $P_{\text{thr}} \approx 0.33 \text{ kW cm}^{-2}$ while the saturation regime starts around $P_{\text{sat}} \approx 0.75 \text{ kW cm}^{-2}$.

In the following we investigate the power region $(1 - 3)P_{\text{sat}}$ to test the nonlinear response of the microlaser. In a first experiment we imaged the emission pattern and measured the spectrum as a function of power both for an increasing and decreasing ramp. The results are summarized in Fig. 4.12-(c): the black (red) dots track the maximum of emission energy when the power is ramped up (down), error bars correspond to one standard deviation. When ramping up the excitation power, the emission energy exhibits an abrupt jump ($\Delta E \approx 20 \text{ } \mu\text{eV}$) around $5.6 P_{\text{thr}}$ (1.85 kW cm^{-2}). Correspondingly, the spatial profile of the beam changes from a homogeneous doughnut shape (lower-right inset) to a four-lobe profile (upper-left inset), persisting for higher incident powers. Upon decreasing the excitation intensity [red dots, Fig. 4.12-(c)], we observe an abrupt lowering of the peak energy at $4.0 P_{\text{thr}}$ (1.30 kW cm^{-2}) back to its initial value, thus defining a hysteretic cycle. Notice that the mode profile throughout the two branches of the cycle is constant and corresponds to the patterns shown in the insets. Moreover, throughout the bistability region, the emission of each branch remains single mode with a typical sideband suppression of 25 dB, see Fig. 4.12-(d,e).

Comparing the emission pattern and the spectral shift of the emission with the fine structure calculations presented in Fig. 4.12-(a), we conclude that the bistability involves the ψ_2 and ψ_4 modes, presenting distinct OAM values ($\ell = -2$ and $\langle \ell \rangle = 0$) and distinct polarization patterns, i.e. circular (σ_+) and linear (azimuthal). To further enforce these observations, we show a self-interferometry of the beam for a pump power $4.8 P_{\text{thr}}$ (1.65 kW cm^{-2}), both in the lower and upper branch of the bistability and presented in Fig. 4.12-(h,f), respectively. In the lower branch, a double pitchfork dislocation indicates a 4π CCW vortex beam (i.e. $\ell = -2$) as confirmed by the associated phase-map [Fig. 4.12-(i)]. When measured in the upper branch, the phase map presents four abrupt jumps between $\pi/2$ and $-\pi/2$, see Fig. 4.12-(g)]. Such a phase profile describes well the standing wave that characterizes ψ_4 as a result of the linear combination of counter-propagating components $\ell = \pm 2$: the phase jumps

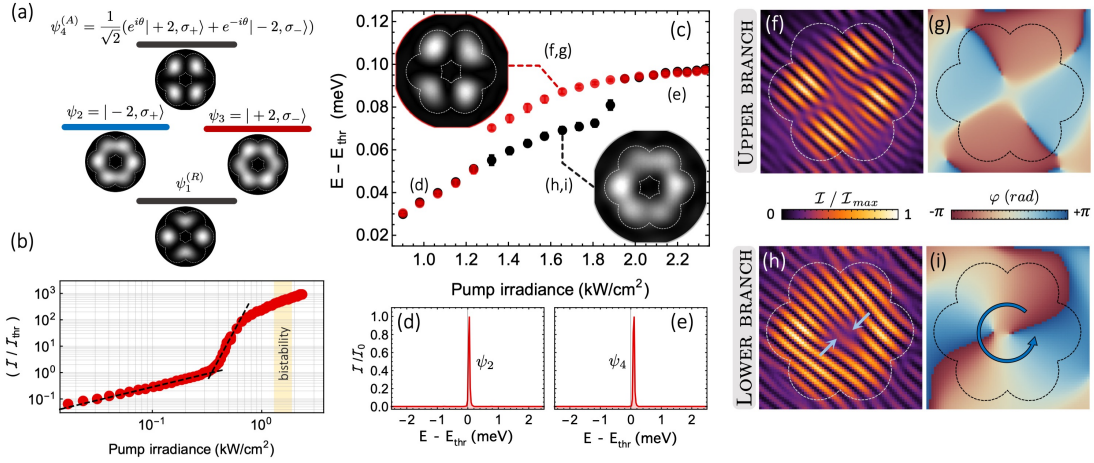


Figure 4.12: **OAM bistability - data.** (a) Illustration of the modes in the M2 lasing manifold ($|\ell| = 2$) fine structure. The calculated the emission patterns for each mode is filtered in the H polarization basis. (b) Measured I-P curve, no hysteretic behaviour can be appreciated in the intensity. (c) Energy of the emission peak as a function of excitation power, when the power is ramped up (black dots) and down (red dots). The insets show real space images of the beam below and above the bistability. (d,e) Normalized emission spectra for $P = (1.0, 2.2)$ kWcm⁻², respectively. (f,h) self-interferometry patterns and (g,i) corresponding phase maps measured in the (f,g) lower and (h,i) upper branches of the bistability, for the same pump power. All images are taken with a horizontal polarization filtering.

correspond to the nodes of this standing wave.

Importantly, we want to point out that this bistable regime occurs at relatively low pump power and therefore, is not due to heating effects in the microstructure which, for increasing powers, tend to redshift rather than blueshift the microlaser emission. Anyway, to rule out this possibility, we repeated the scan using a pulsed excitation with a duty cycle of 0.1% and a frequency of 1 kHz in order to drastically mitigate thermal effects: the upward abrupt jump could still be observed for the same peak power. Notice that even if the lasing mode presents an hysteretic behavior, the total emitted intensity does not present discontinuities [see Fig. 4.12-(b)], thus suggesting that the overall gain/loss in the device evolves smoothly with power and that the bistability must be related to a competition mechanism between the spin-polarized and unpolarized population reservoirs in the gain medium. This confluence of optical bistability and spin-orbit coupling of light is particularly interesting for the exploration of dynamical processes involving distinct phase and polarization vortices [305].

4.4.1 Dynamical rate equations

In order to address the phenomenological origin of this bistable regime, we used a dynamical system of rate equations. Since the measured emission spectrum in the lasing regime always presented a single, strongly dominant spectral component, either ψ_2 or ψ_4 , we considered only these two optical modes in the model. Since each carrier in the gain has spin, with a possibly non zero average, while the modes $\psi_{2,4}$ have different overlaps with the σ_{\pm} polarized optical transitions, we need to split the reservoir in two

separate equations for each spin component. We can describe the system using the following set of rate equations for the modes and gain populations:

$$\begin{aligned}
 \dot{I}_1 &= (g_1 N_+ - \Gamma_c) I_1 + N_+ \Gamma_r \\
 \dot{I}_2 &= (g_2 N_{tot}/2 - \Gamma_c) I_2 + N_{tot} \Gamma_r / 2 \\
 \dot{N}_+ &= P(1 + \eta) - (g_1 I_1 + g_2 I_2 / 2 + \beta \Gamma_r) N_+ \\
 \dot{N}_- &= P(1 - \eta) - (g_2 I_2 / 2 + \beta \Gamma_r) N_-
 \end{aligned} \tag{4.7}$$

Here, $I_{1,2}$ are the occupation of the modes $\psi_{2,4}$ of the fine structure; N_{\pm} is the number of σ_{\pm} polarized excitations in the gain; $g_{1,2}$ are the gain coefficients of each mode; Γ_c is the radiative decay rate; Γ_r is the recombination rate in each mode³; β is the spontaneous emission factor; P is the injection rate of carriers and η is the degree of polarization of the carriers after relaxation (cf. Sec. 4.3.2). Since both modes involved in the bistability belong to the same OAM manifold, we consider the non-radiative loss contribution to be identical for $I_{1,2}$ and is thus included in Γ_c .

Since we are interested on the behavior on timescales much longer than $\Gamma_c \sim 25 \text{ ps}^{-1}$ or $\Gamma_r \sim 100 \text{ ps}^{-1}$, we find the steady-state solution of the system by setting the time derivatives of $I_{1,2}$ and N_{\pm} to zero. With some calculations one can show that the resulting system of algebraic equation admits a unique solution (i.e. no bistability) for any value of P ⁴. Indeed, many studies on bimodal lasers attribute the existence of a bistable regime to nonlinear gain contributions [306, 307, 308]. To account for such effects, we express the gain coefficients as

$$g_{1,2} = g_0(1 - \epsilon_{1,2}^s I_{1,2} - \epsilon_{1,2}^c I_{2,1}) \tag{4.8}$$

where g_0 is the unsaturated gain coefficient -identical for the two modes- and $\epsilon_{1,2}^s$ and $\epsilon_{1,2}^c$ are the self- and cross-saturation coefficients of $I_{1,2}$. For two-mode lasers coupled to a single reservoir, the general requirement for bistability is that $\epsilon_1^s \epsilon_2^s < \epsilon_1^c \epsilon_2^c$ [306].

Here, the situation is more complex as the two modes couple to two distinct reservoirs, namely, σ_+ and σ_- polarized carriers. Moreover, due to their different polarization, they couple differently to each reservoir: I_2 (linearly polarized) couples identically to N_+ and N_- , whereas I_1 (circularly polarized) couples only to N_+ . With the inclusion of the nonlinear gain terms, we could not find an explicit closed solution for (4.7). To study the problem, we solved numerically the steady-state equations associated to (4.7) yielding a set of N solutions $\{\tilde{I}_{1,2}, \tilde{N}_{1,2}\}_{j=1, \dots, N}$ for each set of parameters. As discussed in detail in Sec. 3.3.1, for a set of first order nonlinear ODEs not all the stationary solutions are physical, that is, asymptotically stable. Therefore, for each steady state solution we computed the eigenvalues λ_i of the linear stability matrix (the Jacobian of 3.3.1 evaluated at $\{\tilde{\cdot}\}_j$) and kept only the solutions with $\lambda_i < 0 \forall i$ (cf. Sec. 3.3.1, assuming real valued variables). In the rate equation model, the specific value of the saturation coefficients is rather difficult to estimate, as it depends on a variety of microscopic phenomena. Although we could not prove it rigorously, a systematic exploration of the $\epsilon^{s,c}$ parameter space suggest that to observe bistability we

³We consider $\Gamma_{r,1} = \Gamma_{r,2}$ in virtue of the fact that the two modes: 1) present an energy separation ($\sim 20 \mu\text{eV}$) which is orders of magnitude smaller than the gain spectral dependence ($\sim 20 \text{ meV}$); 2) present nearly identical spatial profiles, i.e. overlap with the gain medium.

⁴The system is bilinear in the variables, thus the equation set admits a Smith normal form, where the solutions are given in terms of a system of quadratic equations. Uniqueness follows from the fact that all variables are positive real numbers.

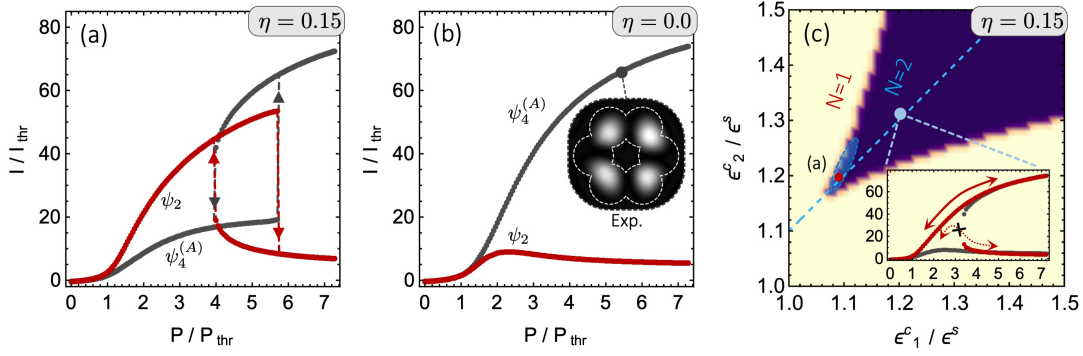


Figure 4.13: **OAM bistability - model.** (a) Calculated intensity of the photonic modes ψ_2 and ψ_4 under a (a) circularly and (b) linearly polarized excitation. Under a circular excitation, a bistability region can be observed, the arrows indicating the scanning history. Simulation parameters: $g_0 = 0.55 \mu\text{s}^{-1}$, $\epsilon_{1,2}^s = \epsilon^s = 5.0 \cdot 10^{-5}$, $\epsilon_1^c/\epsilon^s = 1.09$, $\epsilon_1^c/\epsilon^s = 1.20$, $\beta\Gamma_r = 1.05 \text{ ps}^{-1}$, $\Gamma_c = 4\Gamma_r = 25 \text{ ps}^{-1}$. (c) Number of stable steady-state solutions for $P = 5P_{\text{thr}}$ in the cross saturation parameter space; panel (a) corresponds to the red dot. The elliptic shaded area encompasses the region where modal hysteresis can be observed for an adiabatic power ramp. Outside of it, two solutions exist but one of them can be followed continuously explored for any pump power. The other one can thus be reached only with an appropriate non-adiabatic pump protocol [218], see the inset for an example.

need to impose $\epsilon_1^c > \epsilon_2^c$; this is possibly related to the asymmetric coupling of the modes to the nonlinear dynamics of the gain.

Figure 4.13-(a) shows the (stable) steady-state occupation for the modes I_1 (ψ_2 , in red) and I_2 (ψ_4 , in gray) as a function of power for a gain spin-polarized fraction of $\eta = 0.15$. While estimates for the cavity lifetime, carrier relaxation time and unsaturated gain can be deduced from the characterizations of the sample and from literature [309, 310], the beta factor and saturation coefficients were defined in order to obtain a lasing threshold and bistability region at similar powers as those observed experimentally (see caption). For the same parameters, but setting $\eta = 0$ i.e. a linearly polarized pump, we do not observe any bistability [Fig. 4.13-(b)] and the emission is now dominated by ψ_4 for the whole power range explored (inset: measured emission pattern at $5.4 P_{\text{thr}}$). The calculated relative intensities do not match the measured ones, as the minimalistic model we developed aims at providing a phenomenological understanding of the origin of the bistability, rather than a quantitative description of the relative populations.

Finally, we present in Fig. 4.13-(c) a mapping of the number of stable steady-state solutions of (4.7) for $P = 5 P_{\text{thr}}$ (within in the hysteresis cycle) when changing the cross saturation coefficients $\epsilon_{1,2}^s$. Interestingly, a wide bistability region ($N = 2$) can be observed (purple area); However, by further requiring a single mode behavior above $P = 6.5 P_{\text{thr}}$ (as in the experiment), the relevant parameter space collapses to the small blue ellipse [the red dot corresponds to Fig. 4.13-(a)]. Outside of this ellipse, two stable solutions always exist for $P \geq 5 P_{\text{thr}}$, but one of them can be adiabatically followed for all the P values, see the inset of Fig. 4.13-(c). Therefore, under a slow power ramp protocol (when compared to Γ_c and Γ_r), the second solution above $P \geq 5 P_{\text{thr}}$ is never explored. Nevertheless, these solutions may become relevant when implementing non-adiabatic ramps or quenches of the pump power.

4.5 Summary and Perspectives

Profiting from the versatility of our semiconductor-based platform in determining exotic coupled microcavity geometries, we investigated the possibility of designing novel integrated sources of structured light. Among them, vortex beam emitters deliver photons carrying a non zero OAM, an unbounded degree of freedom which control is desirable for fundamental studies while being a technologically relevant candidate for the multiplexing of telecom channels.

To this aim we considered coupled microlaser arrangements presenting a discrete rotational symmetry. Thanks to an analog photonic spin-orbit interaction the optical modes of these structures present a fine structure where some modes, while degenerate in energy, present opposite sign OAM charge and opposite circular polarizations. In combination with the possibility to spin-polarize the gain medium (here a QW) via the pump polarization, we propose a fully-optical scheme to break time reversal symmetry in such microstructures, deterministically lasing in an optical mode carrying a net orbital angular momentum.

We demonstrate the scheme in a benzene-like photonic molecule ($N = 6$), showing the ability to control the sign of the OAM-pure emission with the helicity of the off resonant pump. To our knowledge this was the first demonstration of an OAM microlaser with a tunable chirality. We expect this mechanism to be compatible with ultrashort control timescales, limited only by the relaxation times of carriers. It is important to point out that the scheme we demonstrate here is not restricted to benzene-like molecules, but can be implemented in any N-pillar ring molecules with an even $N \geq 4$. When considering N pillars, the $|\ell| = 1$ and $|\ell| = N/2 - 1$ manifolds present the adequate fine structure allowing in principle the implementation of microlasers generating arbitrarily large values of OAM.

Investigating the robustness of the lasing scheme with temperature, as the spin relaxation of carriers is expected to be faster for higher temperatures, we demonstrate the ability of controlling the laser emission chirality up to 80 K under CW excitation. We expect a significative improvement of this result with a new heterostructure design and using a pulsed excitation scheme. We believe that our design could be readily transposed to other laser architectures, because the underlying concepts (that is spin-orbit coupling of photons and spin-polarization of the gain medium) are ubiquitous. Also, combining the present design with ferromagnetic electrodes [311] could open the possibility to fabricate OAM microlasers with electrical injection.

Furthermore, following an unexpected experimental observation, we elucidate how nonlinear effects in OAM microlasers lead to an optical bistability involving two modes with distinct OAM values $|\ell| = (2, 0)$ and polarization textures. We qualitatively explained the phenomenon using dynamical rate equations, indicating the origin of the bistability in the confluence of co- and cross-saturation contributions to the gain. As the switching mechanism is expected to be limited by the relaxation of photo-generated carriers, it appears very interesting for implementing optical switches based on the OAM of light, as well as for exploring dynamical processes between phase and polarization vortices exhibiting distinct topological charges.

Finally, from a more fundamental point of view, our results could be extended beyond the field of OAM lasers, for example in optomechanics by coherently transferring

photonic angular momentum to chiral torsional modes of the microstructures [312, 313]. Furthermore, by embedding a quantum emitter (for example, a quantum dot or semiconductor defects) in the resonator instead of a quantum well, it would be possible to generate single photons with a controllable OAM [314]. Also, by lifting the degeneracy of the σ_{\pm} transitions of an ensemble of emitters via a transverse magnetic field, one could imagine to study how does a chiral coupling to the optical modes of a cavity affects the collective super (sub) radiant modes [315].

4.6 Appendix A: The angular momentum of light

In this appendix we want to derive the expression of the total angular momentum carried by electromagnetic waves. To do so, an elegant way is to use the Noether theorem to study the conserved currents associated to the continuous Poincaré symmetry group of the electromagnetic field action [254, 316]. We will use extensively the Einstein summation convention ($x_1y^1 + x_2y^2 + \dots \equiv x_iy^i$) and a tensor notation for the fields as it ensures automatically the covariance of the expressions. We recall that upper case indexes denote contravariant (vector) objects while lower case indexes denote covariant (dual) objects with respect to a change of basis. For instance, a vector with components v^i transforms under the change of basis described by the matrix M as $v'^i = M^i_j v^j$, whereas the covector v_i transforms as $v'_i = \tilde{M}_i^j v_j$, where $\tilde{M}_i^j = g_{ik} M^k_l g^{lj}$ and g_{ij} is the metric tensor. In the case of special relativity, g is the Minkowski metric $\text{diag}(1, -1, -1, -1)$, which can be used to raise and lower the indexes of mixed tensors $M^i_j = M^{ik} g_{kj}$. Greek letter indexes will correspond to the four entries of the space-time coordinates $x^\mu = (x^0, x^1, x^2, x^3)$ where c is the speed of light and will be hereafter set to unity, $x^0 = ct$ corresponds to time and $\mu = 1, 2, 3$ refers to the spatial coordinates, which will be labeled in a compact form with regular characters. We start by considering the Lagrangian of the electromagnetic (EM) field in vacuum

$$\mathcal{L} = -\frac{1}{4} F^{\mu\nu} F_{\mu\nu} = \frac{1}{2} (E^2 - B^2) \quad (4.9)$$

where E and B are, respectively, the electric and magnetic field and

$$F^{\mu\nu} = \partial^\mu A^\nu - \partial^\nu A^\mu \quad (4.10)$$

is the covariant expression for the EM field associated to the gauge field $A^\mu = (\phi, \vec{A})$ expressed in terms of the electric (ϕ) and vector potential (\vec{A}) of the electromagnetic field. We recall for later use that $E^i = -\partial^i A_0 - \partial_0 A^i$ and $B^i = \nabla \times \vec{A} = \epsilon^{ijk} \partial_j A_k$. Notice that \mathcal{L} is a scalar, thus is invariant under transformations belonging to the Poincaré group: the spacetime isometries including translations, rotations and boosts. The action functional for the EM field is

$$\mathcal{S}[A_\mu] = \int d^4x \mathcal{L}(A_\mu(x), \partial_\mu A_\nu(x)) \quad (4.11)$$

and its variations $\delta\mathcal{S}[A_\mu]$ are minimized for a field A^μ satisfying the Euler-Lagrange (EL) equations

$$\partial_\mu \frac{\partial \mathcal{L}}{\partial(\partial_\mu A_\nu)} - \frac{\partial \mathcal{L}}{\partial A_\nu} = 0 \quad (4.12)$$

for the free electromagnetic field Lagrangian (4.9), these Euler-Lagrange equation yields $\partial_\mu F^{\mu\nu} = 0$; which simplifies in the Lorentz gauge ($\partial_\mu A^\mu = 0$) to $\square A^\nu = 0$, whose components can be easily related to the Maxwell equations, since $\square = \partial_t^2 - \nabla^2$. Electromagnetic waves thus satisfy the EL equations for (4.9), thus we can apply the Noether theorem to characterize the conserved quantities associated to the Poincaré symmetry group. To do so, we first need the general form of the infinitesimal generators of the

group, which we divide in the generators of rotations and boosts (Lorentz group) and in affine spacetime translations. The former will be described by the elements of a rank-two tensor (matrix) $\Lambda^\mu{}_\nu$, the latter by a translation vector a^μ . It can be shown that Λ has Lie generator given by an antisymmetric matrix ω such that $\Lambda = e^\omega$. If $\beta = v/c$ is the generic speed of a boost and (\vec{n}, φ) are the axis and angle of rotation, $\omega_{00} = 0$, $\omega_{i0} = -\omega_{0i} = \beta_i$ and $\omega_{ij} = \varphi \epsilon_{ijk} n^k$ [316]. Since we are interested in infinitesimal transformation, we can expand Λ as $e^\omega = \delta^\mu{}_\nu + \omega^\mu{}_\nu + \dots$ where δ indicates the Kronecker delta. An infinitesimal change of coordinates under the Poincaré symmetry group has therefore the form

$$\delta x^\mu = x'^\mu - x^\mu = (\delta^\mu{}_\nu + \omega^\mu{}_\nu) x^\nu + a^\mu - x^\mu = a^\mu + \omega^\mu{}_\nu x^\nu \quad (4.13)$$

In a similar way we have that the field A^μ transforms as $A'^\mu(x') = \Lambda^\mu{}_\nu A^\nu(x)$; notice that we can define for this rank-one tensor two types of variation, the first is total $\bar{\delta}A^\mu = A'^\mu(x') - A^\mu(x)$, whereas the second one depends only on the field $\delta A^\mu = A'^\mu(x) - A^\mu(x)$, thus referred as "form" variation. We can explicitly write the former as $\bar{\delta}A^\mu = \omega^\mu{}_\nu A^\nu$, while for the form variation

$$\begin{aligned} \delta A^\mu &= A'^\mu(x) - A^\mu(x) = A'^\mu(x) - A'^\mu(x') + A'^\mu(x') - A^\mu(x) \\ &= A'^\mu(x) - A'^\mu(x + \delta x) + \bar{\delta}A^\mu = -\delta x^\nu \partial_\nu A'^\mu(x) + \bar{\delta}A^\mu \\ &= -\delta x^\nu \partial_\nu A^\mu(x) + \bar{\delta}A^\mu \end{aligned} \quad (4.14)$$

and we used in the last step the fact that the difference between A'^μ and A^μ depends to first order in the symmetry generators a^μ and $\omega^\mu{}_\nu$. Now, since the Lagrangian of the EM field is invariant under the Poincaré symmetry group, its infinitesimal variation must vanish

$$\begin{aligned} 0 &= \delta \mathcal{L}(A(x), \partial A(x), x) = \frac{\delta \mathcal{L}}{\delta x^\mu} \delta x^\mu + \frac{\delta \mathcal{L}}{\delta A^\mu} \delta A^\mu \\ &= \delta x^\mu \partial_\mu \mathcal{L} + \delta A_\mu \frac{\partial \mathcal{L}}{\partial A_\mu} + (\partial_\mu \delta A_\nu) \frac{\partial \mathcal{L}}{\partial (\partial_\mu A_\nu)} \\ &= \partial_\mu (\delta x^\mu \mathcal{L}) + \delta A_\nu \left(\frac{\partial \mathcal{L}}{\partial A_\nu} - \partial_\mu \frac{\partial \mathcal{L}}{\partial (\partial_\mu A_\nu)} \right) + \partial_\mu \left(\delta A_\nu \frac{\partial \mathcal{L}}{\partial (\partial_\mu A_\nu)} \right) \\ &= \partial_\mu (\delta x^\mu \mathcal{L} + \delta A_\nu \Pi^{\mu\nu}) \end{aligned} \quad (4.15)$$

Notice that in the third line we used the fact that $\delta_\mu \delta x^\mu = g_{\mu\nu} \omega^{\mu\nu} = 0$, in virtue of the fact that ω is antisymmetric and g is diagonal and we used the chain rule on the right most term. Moreover, in the last line, we used the fact that A^μ satisfies the EL equation (4.12) and defined the conjugated moments

$$\Pi^{\mu\nu} = \frac{\partial \mathcal{L}}{\partial (\partial_\mu A_\nu)} = -F^{\mu\nu} \quad (4.16)$$

The last line of Eq. (4.15) defines the conserved quantities under the Poincaré symmetry group via the continuity equation $\partial_\mu j^\mu = 0$, that is $\partial_t j^0 = \nabla \cdot \vec{j}$ associated to the four-vector $j^\mu = (\delta x^\mu \mathcal{L} + \delta A_\nu \Pi^{\mu\nu})$. Substituting in j^μ the explicit forms of δA_ν , δx^μ , of the free EM field Lagrangian (4.9) and working down some algebra, one finds

$$j^\mu = -a_\nu T^{\mu\nu} + \frac{1}{2} \omega_{\alpha\beta} J^{\mu\alpha\beta} \quad (4.17)$$

where the two quantities $T^{\mu\nu}$ and $J^{\mu\alpha\beta}$ are a compact notation for

$$\begin{aligned} T^{\mu\nu} &= \partial^\mu A^\alpha F^\nu{}_\alpha - \frac{1}{4} g^{\mu\nu} F^{\alpha\beta} F_{\alpha\beta} \\ J^{\mu\alpha\beta} &= (x^\alpha T^{\mu\beta} - x^\beta T^{\mu\alpha}) + (F^{\alpha\mu} A^\beta - F^{\beta\mu} A^\alpha) = L^{\mu\alpha\beta} + S^{\mu\alpha\beta} \end{aligned} \quad (4.18)$$

which are separately conserved quantities since $\partial_\mu j^\mu = 0$ holds for any a^μ and $\omega^\mu{}_\nu$. Remarkably, if we inspect j^μ we can see that the tensor $T^{\mu\nu}$ is associated to the generator of spacetime translations, with four associated conserved charges given by $p^\mu = \int d^3x T^{0\mu}$. Since $T^{00} = (E^2 + B^2)/2$ and $T^{0i} = \epsilon^{ijk} E_j B_k$, this corresponds to the conservation of the energy and linear momentum density for the EM field in absence of sources. Instead, $J^{\mu\alpha\beta}$ is associated to the generator of infinitesimal spacetime rotations ω , and thus corresponds to the canonic angular momentum tensor, generating six conserved quantities, due to the asymmetry of the contracted indexes (α, β) . Importantly we can see that two terms $J^{\mu\alpha\beta}$ do not depend explicitly on the choice of coordinates thus we group them in a term $S^{\mu\alpha\beta}$, associated to the helicity of the vector field A^μ while the other two terms are proportional to x^μ and are grouped in a tensor $L^{\mu\alpha\beta}$ associated to the angular momentum of the EM field [316]. Let us see which are the conserved charges associated to the continuity equation $\partial_\mu J^{\mu\alpha\beta} = 0$, recalling that the charges are associated to the spatial integral of the $\mu = 0$ component and that (α, β) are antisymmetric indexes we can associate to the spatial components of the charges $Q^{\alpha\beta} = \int d^3x J^{0\alpha\beta}$ a vector

$$J^i = \frac{1}{2} \epsilon^{ijk} \int d^3x J^{0jk} = \frac{1}{2} \int d^3x \epsilon^{ijk} (L^{0jk} + S^{0jk}) = L^i + S^i \quad (4.19)$$

We now want to evaluate separately the components of S_i and L_i ; working in the Coulomb gauge ($A^0 = 0, \partial_i A^i = 0$) in this case is convenient. Notice however that $J^{\mu\alpha\beta}$ is not gauge invariant, thus the values of J^i may change: a discussion of this apparent paradox can be found in [316]. Since the metric tensor g is diagonal

$$L^i = \int d^3x \epsilon^{ijk} x^j \partial^k A^\mu F^\mu{}_\mu = \int d^3x \epsilon^{ijk} x^j \partial^k A^l E_l \quad (4.20)$$

using for the second passage the Coulomb gauge and that $F^0{}_i = E_i$. Similarly, the spin angular momentum yields

$$S^i = \int d^3x \epsilon^{ijk} F^{j0} A^k = \int d^3x \epsilon^{ijk} E^j A^k \quad (4.21)$$

Or equivalently, in vector notation

$$\mathbf{J} = \mathbf{L} + \mathbf{S} = \sum_{i=1}^3 \int d^3x E_i (\mathbf{r} \times \nabla) A_i + \int d^3x (\mathbf{E} \times \mathbf{A}) \quad (4.22)$$

and it is again possible to demonstrate that these are separately conserved quantities. Let's now consider a light beam within the paraxial approximation and consider a monochromatic wave propagating along z with a transverse electric field $E(\mathbf{r}, t) = \text{Re}(E(\mathbf{r})e^{-i(\omega t - kz)})$. Since we are working in the Coulomb gauge, $E^i = F^{i0} = \partial^i A^0 - \partial^0 A^i = -\partial^0 A^i$ therefore we have $E(\mathbf{r}, t) = i\omega A(\mathbf{r}, t)$. We can now represent in Fourier space the spatial coordinates

$$E(\mathbf{r}, t) = \int \frac{d^3k}{(\sqrt{2\pi})^3} \left[E(k)e^{-i(\omega t - kz)} + E(k)^*e^{i(\omega t - kz)} \right] \quad (4.23)$$

upon inserting this relation, and using $E(\mathbf{r}, t) = i\omega A(\mathbf{r}, t)$ in the expression for the spin part of the angular momentum one finds

$$\mathbf{S} = \int d^3x (\mathbf{E} \times \mathbf{A}) = \frac{2}{i\omega} \int d^3k (\mathbf{E}^*(k) \times \mathbf{E}(k)) \quad (4.24)$$

using a Jones vector representation of the complex electric field, where the spatial components are encoded in a form $\vec{E}(k) = \vec{\epsilon} \mathcal{E} u(k)$ where $\epsilon = [1(0), 0(1), 0]^T$ denotes the vector for of the horizontal (H) and vertical (V) linear polarizations, respectively and \mathcal{E} is the modulus of the of the electric field and $u(k)$ is a normalized envelope function in momentum space. Inserting this expression in the above relation, one finally gets

$$\mathbf{S} = \hat{z} \left(\frac{\mathcal{E}^2}{\omega} \Omega \right) \eta \quad (4.25)$$

where Ω is the volume of integration, \hat{z} is unit vector along z and $|\eta|^2$ is the degree of circular polarization of the wave, given by the difference between the projections $\eta = |\vec{\epsilon} \cdot \vec{\epsilon}_R|^2 - |\vec{\epsilon} \cdot \vec{\epsilon}_L|^2$ with $\vec{\epsilon}_{L,R} = (1, \pm i, 0)/\sqrt{2}$. The term in the parenthesis yields \hbar for a single excitation of the electromagnetic field, that is circularly polarized photons carry a spin angular momentum with z projection $\pm\hbar$. This relation is valid within the paraxial approximation and for each spectral components of a wave, thus for an arbitrary linear combination of monochromatic waves, e.g. a light pulse.

Finally we can focus on the orbital part of the angular momentum, we consider again the case of paraxial waves and we assume that the spatial envelope of the wave presents a cylindrical symmetry about the propagation axis z . It is in this situation convenient to exploit this assumption to express

$$(\mathbf{r} \times \nabla) = (-(z/\rho)\partial_\phi, (z/\rho)\partial_\rho\rho - \rho\partial_z, \partial_\phi)^T \quad (4.26)$$

(ρ, ϕ, z) parametrize the cylindrical degrees of freedom. Now, using the coulomb Gauge for a paraxial wave, it is clear that the electric field and vector potential do not have components along the propagation direction (we neglect them). The summation in the expression of \mathbf{L} can be thus rewritten using a complex notation for the fields in the cylindrical coordinate system

$$\begin{aligned} \sum_i E_i(\mathbf{r} \times \nabla)A &\approx \frac{1}{2}(E_i^*(\mathbf{r} \times \nabla)_z A^i + c.c.) \\ &= \frac{1}{2i\omega}(E_\rho^* \partial_\phi E_\rho + E_\phi^* \partial_\phi E_\phi + c.c.) \end{aligned} \quad (4.27)$$

If we further require that E_ρ does not change with the angle, that is the envelope of E is constant in modulus with ϕ (e.g. for a Bessel-beam) and that $E_\phi \propto e^{-i\ell\phi}$ with $\ell \in \mathbb{Z}$, some simple algebra yields

$$\mathbf{L} = \hat{z} \left(\frac{\mathcal{E}^2}{\omega} \Omega \right) \ell \quad (4.28)$$

again we find that for a single photon with a wavefront characterized by a phase winding ℓ times in an optical period, the orbital angular momentum is $\ell\hbar$. A more general calculation of \mathbf{L} and \mathbf{S} in the case of Bessel- and Hermite-type solutions of the paraxial wave-equation can be found in [255]. Interestingly the term $E^* \partial_\phi E \equiv \langle E | \partial_\phi | E \rangle$ recalls the definition of the Pancharatnam-Berry phase: this analogy has been investigated in [317]. An important consequence of this fact is that a smooth transformation of the wavefront cannot modify the quanta of OAM carried by the beam, which essentially counts the number and order of phase vortices present in the beam. For this reason OAM is believed to be an eavesdropping-resilient degree of freedom useful for free-space telecommunication.

Notice that for an arbitrary vector fields, where the dependence of the vertical and horizontal components of the transverse wave is not constant over the spatial coordinates, the decomposition of the total angular momentum is not always separable in its spin and angular components [58]. A discussion of this specific case, can be found in [318], where the authors describe the angular momentum of strongly focussed beams using a multipole expansion of the EM field.

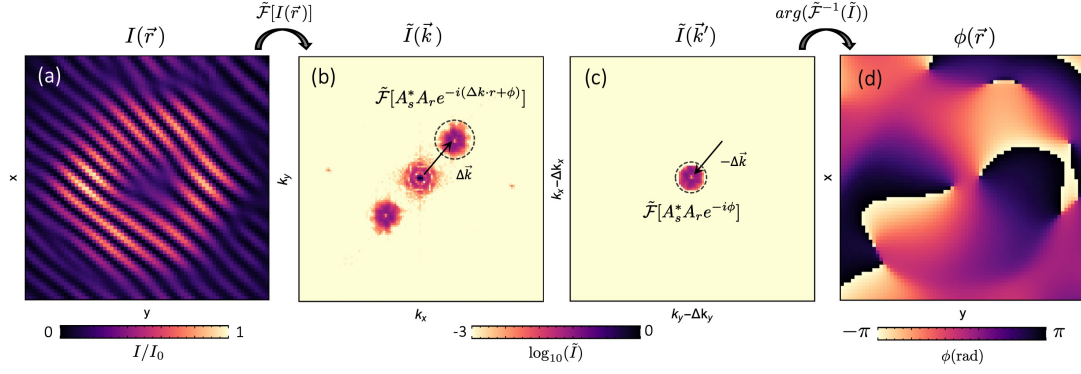


Figure 4.14: **Retrieving the wavefront phase:** (a)-Typical interference pattern for the $|-2, \sigma_+\rangle$ mode, produced by interfering the emission and reference arm with an in-plane wavevector difference $\Delta\mathbf{k}$. (b) Log-scale absolute value of the CCD image fast Fourier transform (FFT). (c) After a rigid translation of the FFT by $-\Delta\mathbf{k}$ we apply a radial low-pass filter. (d) Real space image of the emission phase $\phi(r)$, obtained as the argument of the inverse FFT.

4.7 Appendix B: Retrieving the phase maps

Along the chapter we presented several interferograms and associated to each of them a phase map. In order to extract these maps we have used a spatial Fourier filtering technique, which we schematically illustrate in Fig. 4.14. The idea is that if the signal and reference beams are described by the complex field amplitudes:

$$\begin{aligned} \mathcal{A}_s &= A_s(\mathbf{r})e^{-i(\omega t - \mathbf{k}_s \cdot \mathbf{r} + \phi)} \\ \mathcal{A}_r &= A_r(\mathbf{r})e^{-i(\omega t - \mathbf{k}_r \cdot \mathbf{r})}, \end{aligned} \quad (4.29)$$

thus the fringe pattern produced at the spectrometer entrance plane ($z = 0$) is:

$$\begin{aligned} I(\mathbf{r}) &= |\mathcal{A}_s + \mathcal{A}_r|^2 \\ &= |A_s|^2 + |A_r|^2 + \left(A_s A_r^* e^{-i(\Delta\mathbf{k} \cdot \mathbf{r} + \phi)} + c.c. \right) \end{aligned} \quad (4.30)$$

where $\Delta\mathbf{k}$ is the in-plane wavevector difference between the signal and reference beams. One example of these fringe patterns is provided in Fig. 4.14-(a). If we Fourier-transform the fringe pattern $\tilde{I}(\mathbf{k}) = \tilde{\mathcal{F}}[I]$, the first two terms in equation (4.30) produce a peak centered at the reciprocal space origin, whereas the third and fourth term correspond to two satellite peaks translated by $\pm\Delta\mathbf{k}$ with respect to the origin. In Fig. 4.14-(b) we color code the log-scaled modulus of the fringe pattern in reciprocal space. The satellite peaks carry the information on the wavefront phase, which can be retrieved by operating a rigid translation of the reciprocal space by $\pm\Delta\mathbf{k}$ and filtering-out all the other peaks [Fig. 4.14-(c)]. The remaining signal corresponds to $\tilde{\mathcal{F}}[A_s A_r^* e^{-i\phi}]$. Then, by taking the argument of inverse Fourier transform of this complex amplitude, we can extract the phase pattern [Fig. 4.14-(d)] associated to the initial interference pattern [Fig. 4.14-(a)]. Remarkably, the phase singularity present in the fringe pattern, is manifest also in reciprocal space, where it shows as a dark spot in the middle of the side-peaks.

4.8 Appendix C: Eigenmodes via a group theory approach

The discrete rotational symmetry of a ring arrangement of n coupled micropillars allows defining a quantum number ℓ associated to the OAM of eigenmodes, i.e. to the phase-relation between the field in neighboring pillars. In Sec. 4.2.1 we have shown by studying an effective tight-binding hamiltonian associated to the system, that the presence of an analog spin-orbit coupling in these structures produces a fine structure necessary to implement our lasing scheme in the $|\ell| = (1, n/2 - 1)$ manifolds.

In this section we want to show an alternative way to understand and characterize the eigenmodes in such photonic structures. To this aim we will study the irreducible representations of the symmetry group associated to the Hamiltonian. Although this approach is not able to predict the specific energy of each mode but only their spectral ordering, it has the advantage to work irrespectively of the microscopic details of the Hamiltonian, i.e. it could be straightforwardly extended to different resonators sharing the same symmetry of our microstructures.

The group of all symmetry operations for of a ring arrangement of n coupled micropillars is C_{nv} . The character table of C_{nv} with n even (odd) is presented in Table 4.1 (Table 4.2). There, A_i and B_i are unidimensional irreducible representations (irreps) of the group. E_i are two-dimensional irreps; E (identity), C_n ($2\pi/n$ rotations) and σ_v (σ_d) (reflections across vertical planes that cross two opposite pillars) are the symmetry operations of the group [319]. One possible basis for the scalar wave-functions of the coupled cavities (i.e. without considering the spin) is given by the fundamental mode of each pillar (ψ_i); the eigenmodes of the systems can thus be expressed in the form of a vector $\Psi = (\psi_1, \dots, \psi_n)^T$. One can then identify a set of matrices that describe how this vector transforms under each symmetry operation of the group.

Since the Hamiltonian of the system commutes with every symmetry operator, this set of matrices forms a reducible representation of the group (Γ_n^s). The trace (character) of each of these matrices is given in the bottom line of Table 4.1 (4.2) for n even (odd). The decomposition in irreps can be found by looking for the minimal set of elements of the group whose summed characters equal the ones of Γ_n^s . For even $n > 4$ one finds

$$\Gamma_{\text{even}}^s = A_1 \oplus B_1 \oplus E_1 \oplus E_2 \oplus E_3 \oplus \dots \oplus E_{n/2-1}. \quad (4.31)$$

Similarly, for a molecule presenting an odd number of pillars, the representation associated to scalar modes is decomposed in irreps as:

$$\Gamma_{\text{odd}}^s = A_1 \oplus E_1 \oplus E_2 \oplus E_3 \oplus \dots \oplus E_{(n-1)/2} \quad (4.32)$$

The Γ_{even}^s decomposition indicates that the spectrum of the scalar system is formed of $n - 2$ energy levels: 2 non-degenerate states transforming according to A_1 and B_1 and $n/2 - 1$ degenerate doublets transforming as E_i with $i = 1, \dots, n/2 - 1$. Inspecting the characters associated to the eigenmodes transforming as A_1 and B_1 shows that they are respectively, symmetric under all symmetry operations of the group (i.e. $\ell = 0$) and anti-symmetric under $2\pi/n$ rotations (i.e. $\ell = n/2 - 1$). The doublets transforming as E_i correspond instead $|\ell| = i$ manifolds: the OAM is extracted directly from the wave-function of each mode, determined by expanding the generators of each irrep [319]. It is possible to spectrally order all the modes as their energy scales with the phase gradient

4. Optically controlling the emission chirality of microlasers

| $ \ell $ | C_{nv} | E | $2C_n$ | $2C_n^2$ | ... | $C_n^{n/2}$ | $3\sigma_v$ | $3\sigma_d$ |
|-------------------|-------------------|-----|----------------------------------|------------------------|-----|---|-------------|-------------|
| 0 | A_1 | 1 | 1 | 1 | ... | 1 | 1 | 1 |
| | A_2 | 1 | 1 | 1 | ... | 1 | -1 | -1 |
| $n/2$ | B_1 | 1 | -1 | 1 | ... | -1 | 1 | -1 |
| | B_2 | 1 | -1 | 1 | ... | -1 | -1 | 1 |
| 1 | E_1 | 2 | $2\cos(\theta)$ | $2\cos(2\theta)$ | ... | $2\cos(\frac{n}{2}\theta)$ | 0 | 0 |
| 2 | E_2 | 2 | $2\cos(2\theta)$ | $2\cos(4\theta)$ | ... | $2\cos(n\theta)$ | 0 | 0 |
| ... | ... | ... | ... | ... | ... | ... | ... | ... |
| $\frac{n}{2} - 1$ | $E_{n/2-1}$ | 2 | $2\cos((\frac{n}{2} - 1)\theta)$ | $2\cos((n - 2)\theta)$ | ... | $2\cos(\frac{n}{2}(\frac{n}{2} - 1)\theta)$ | 0 | 0 |
| | Γ_{even}^s | n | 0 | 0 | ... | 0 | 2 | 0 |

Table 4.1: **Character table for C_{nv} (even n)**: the bottom line corresponds to the characters of the reducible representation associated to the scalar modes ($\theta = 2\pi/n$).

| $ \ell $ | C_{nv} | E | $2C_n$ | $2C_n^2$ | ... | $C_n^{(n-1)/2}$ | $3\sigma_v$ | $3\sigma_d$ |
|-----------------|------------------|-----|------------------------------|----------------------|-----|----------------------------------|-------------|-------------|
| 0 | A_1 | 1 | 1 | 1 | ... | 1 | 1 | 1 |
| | A_2 | 1 | 1 | 1 | ... | 1 | -1 | -1 |
| 1 | E_1 | 2 | $2\cos(\theta)$ | $2\cos(2\theta)$ | ... | $2\cos(\frac{n-1}{2}\theta)$ | 0 | 0 |
| 2 | E_2 | 2 | $2\cos(2\theta)$ | $2\cos(4\theta)$ | ... | $2\cos((n-1)\theta)$ | 0 | 0 |
| ... | ... | ... | ... | ... | ... | ... | ... | ... |
| $\frac{n-1}{2}$ | $E_{(n-1)/2}$ | 2 | $2\cos(\frac{n-1}{2}\theta)$ | $2\cos((n-1)\theta)$ | ... | $2\cos((\frac{n-1}{2})^2\theta)$ | 0 | 0 |
| | Γ_{odd}^s | n | 0 | 0 | ... | 0 | 2 | 0 |

Table 4.2: **Character table for C_{nv} (odd n)**: the bottom line corresponds to the characters of the reducible representation associated to the scalar modes ($\theta = 2\pi/n$).

associated to the angular momentum ($A_1 - E_1 - \dots - E_{n/2-1} - B_1$). For Γ_{odd}^s , we have instead only one non-degenerate state transforming according to A_1 and $(n-1)/2$ degenerate doublets transforming as E_i with $i = 1, \dots, (n-1)/2$. The main difference with the case of even n is the absence of B_1 states, as the two possible antisymmetric states presenting a π phase shift between neighboring pillars are inequivalent and the spectral ordering reads ($A_1 - E_1 - \dots - E_{(n-1)/2}$).

In order to take into account the spin of photons, one needs to identify the irreps that transform identically as this spin moment: for the C_{nv} symmetry groups, $\ell = \pm 1$ angular momenta transform as E_1 . Then, to retrieve the energy levels of our benzene molecule in the presence of spin-orbit coupling, we need to consider the tensor product between E_1 and Γ_n^s :

$$\begin{aligned}
E_1 \otimes \Gamma_{even}^s &= E_1 \otimes (A_1 \oplus B_1 \oplus E_1 \oplus E_2 \oplus E_3 \oplus \dots \oplus E_{n/2-1}) \\
&= \underbrace{E_1}_{\ell=0} \oplus \underbrace{E_{n/2-1}}_{\ell=n/2} \oplus \underbrace{A_1 \oplus A_2 \oplus E_2}_{|\ell|=1} \oplus \underbrace{E_1 \oplus E_3}_{|\ell|=2} \oplus \underbrace{E_2 \oplus E_4}_{|\ell|=3} \\
&\quad \oplus \dots \oplus \underbrace{E_{n/2-3} \oplus E_{n/2-1}}_{|\ell|=n/2-2} \oplus \underbrace{B_1 \oplus B_2 \oplus E_{n/2-2}}_{|\ell|=n/2-1}.
\end{aligned} \tag{4.33}$$

Similarly, the odd scalar modes composition with polarization yields

$$\begin{aligned}
 E_1 \otimes \Gamma_{\text{odd}}^{\text{s}} &= E_1 \otimes (A_1 \oplus E_1 \oplus E_2 \oplus E_3 \oplus \dots \oplus E_{(n-1)/2}) \\
 &= \underbrace{E_1}_{\ell=0} \oplus \underbrace{A_1 \oplus A_2 \oplus E_2}_{|\ell|=1} \oplus \underbrace{E_1 \oplus E_3}_{|\ell|=2} \oplus \underbrace{E_2 \oplus E_4}_{|\ell|=3} \oplus \dots \\
 &\quad \dots \oplus \underbrace{E_{(n-3)/2} \oplus E_{(n-1)/2}}_{|\ell|=(n-1)/2}.
 \end{aligned} \tag{4.34}$$

Focusing first on the even n case, we see that in the spin-coupled basis, the $\ell = 0$ and $\ell = n/2$ states become two-fold degenerate (spin degeneracy), and transform respectively as the E_1 and $E_{n/2-1}$ irreps. More importantly, the $|\ell| = 1$ ($|\ell| = n/2 - 1$) manifolds split to form a three-level fine structure formed by two non-degenerate states transforming as $A_{1,2}$ for $|\ell| = 1$ ($B_{1,2}$ for $|\ell| = n/2 - 1$), doublets transforming as E_2 ($E_{n/2-2}$). By inspection of the symmetry of every eigenstate of the fine structure, it is possible to retrieve explicitly the wave-functions of each of these states. For the $\ell = 1$ manifold, states that transform as $A_{1,2}$ are symmetric under $2\pi/n$ rotations, indicating that they carry a total angular momentum $j = (\ell + \sigma) = 0$; furthermore, A_1 (A_2) is symmetric (anti-symmetric) under reflections $\sigma_{v,d}$. Therefore, the associated wave-functions (in the $|j, \sigma\rangle$ basis) are:

$$\psi(A_{1,2}) = \frac{1}{\sqrt{2}}(e^{i\theta} |0, \sigma_+\rangle \pm e^{-i\theta} |0, \sigma_-\rangle) \tag{4.35}$$

Here, the phase $\theta = 2\pi/n$ accounts for the n -fold rotational symmetry of the wave-function. Eigenmodes associated to the E_2 doublet form conjugated partners with a total angular momentum $|j| = 2$, but opposite chirality (E_j is associated to modes presenting j AM quanta)

$$\psi_{\pm}(E_2) = |\pm 2, \sigma_{\pm}\rangle \tag{4.36}$$

In the $|\ell| = n/2 - 1$ manifold, states that transform according to $B_{1,2}$ are anti-symmetric under $2\pi/n$ rotations, indicating modes with total angular momentum $J = n/2$; furthermore, B_1 is symmetric (anti-symmetric) under σ_v (σ_d) reflections (vice-versa for B_2). Therefore, the associated wave-functions are

$$\psi(B_{1,2}) = \frac{1}{\sqrt{2}}(e^{i\theta} |-n/2, \sigma_+\rangle \pm e^{-i\theta} |n/2, \sigma_-\rangle) \tag{4.37}$$

Wave-functions associated to the $E_{n/2-2}$ doublet form conjugated partners with a total angular momentum $|j| = n/2 - 2$, thus

$$\psi_{\pm}(E_{n/2-2}) = |\pm n/2 - 2, \sigma_{\mp}\rangle \tag{4.38}$$

Importantly, each three-level fine structure presents the followings necessary assets for our lasing scheme: (1) only one state is entirely polarized σ_+ and only one is entirely polarized σ_- , so that these states present the highest gain when spin-polarizing the gain medium, and (2) these σ_{\pm} -polarized states present opposite OAM (i.e. $\pm\ell$). This is indeed the case for the states forming the E_1 and E_2 doublets.

The other manifolds of the spectrum ($2 \leq |\ell| \leq n/2 - 2$) split in pairs of doublets transforming as $E_{|\ell-1}$ and $E_{|\ell+1}$. The associated wave-functions (with corresponding OAM) can be written as:

$$\begin{aligned}
 \psi_{\pm}(E_{|\ell-1}) &= |j = \pm(|\ell| + 1), \sigma_{\mp}\rangle \rightarrow \text{OAM} = \pm|\ell| \\
 \psi_{\pm}(E_{|\ell+1}) &= |j = \pm(|\ell| - 1), \sigma_{\pm}\rangle \rightarrow \text{OAM} = \pm|\ell|.
 \end{aligned} \tag{4.39}$$

Consequently, none of these manifolds offer an appropriate fine structure to implement our lasing scheme. Indeed, although all the states are circularly polarized, the polarization (σ_{\pm}) is not linked to a single chirality, thus preventing triggering lasing in a mode carrying a net OAM when spin-polarizing the gain medium.

A similar analysis can be done for the case of an odd number of coupled cavities, with the main difference being the absence of the second interesting fine structure ($B_1 \otimes B_2 \otimes E_{n/2-2}$) which, in principle, is the one allowing to implement of our lasing scheme for arbitrarily large values of the OAM.

General guidelines related to the symmetry of the device

Following the above group theory arguments, the general guideline for designing a structure is that it must exhibit both circular symmetry (in order for angular momentum to be a conserved quantity of the system) *and* mirror symmetry (in order for the system to lase as well in CW and CCW propagating modes); the confluence of these two symmetries corresponds to C_{nv} symmetry groups.

Furthermore, a structure presenting a C_{nv} (with $n > 4$) symmetry will present the appropriate fine structure for the $|\ell| = 1$ manifold and, for n even, for the $|\ell| = n/2 - 1$ manifold. The physical reason why only these two manifolds can present the appropriate fine structure is related to the fact that photon polarization can only take values of $\pm\hbar$; therefore, due to the combined requirement of angular momentum and energy conservation, spin-orbit coupling can only mix together states $\ell = \pm 1$ (and $\ell = \pm n/2 - 1$, considering the periodic nature of a structure with an even number of pillars).

Parametric instabilities in coupled nonlinear microcavities

ABSTRACT: Nonlinear photonic systems, being inherently lossy, have been proposed as a natural playground for the exploration of out-of-equilibrium lattice models [157, 51]. One example is the driven dissipative Bose-Hubbard (DDBH) model, describing interacting bosons hopping on a lattice in presence of pump and loss. A minimal realization of this model is represented by two coupled nonlinear Kerr-type resonators. Despite its apparent simplicity, this paradigmatic system presents a rich phenomenology including spontaneous symmetry breaking [320], self-trapping and Josephson oscillations [321], periodic squeezing [322] and a nonlinear hopping phase [323].

Moreover, fluctuations and nonlinearities are known to conspire in strongly driven oscillators, eventually resulting in the self-modulation of an internal parameter of the system, feeding self-pulsing instabilities [218, 324, 325], which can be exploited to realize efficient integrated optical parametric oscillators [326, 238, 327, 328, 329]. Although the presence of such parametric instabilities had been predicted for a DDBH-dimer [330], it has not been observed yet. In this chapter we report its observation with coupled microcavities hosting polariton excitations.

The mechanism responsible for the instability relates to the opening of a resonant scattering channel from the pump toward two modes as their energy gets renormalized by the nonlinearity. Imaging the emission pattern of signal and idler modes in the instability regime, we evidence opposite spatial symmetries. This feature is reminiscent of the bonding and anti-bonding linear modes from which they originate, supporting the description of the instability mechanism proposed in [330]. We comprehensively model our findings combining a linear stability analysis with semiclassical calculations of the cavity field dynamics via Langevin equations.

The inherent scalability of our semiconductor platform, enriched with a strong Kerr nonlinearity, is promising for the realization of integrated optical parametric oscillator networks operating in a few-photon regime. The core results presented in this chapter can be found in this preprint [331].

5.1 Introduction

Understanding strongly correlated phases of matter is a formidable task as the excitations of the system display long-range collective behaviors which are often intractable both analytically and with numerical techniques. One possible solution is to condense the essential elements of the problem in a minimal many-body hamiltonian model depending on few parameters. Upon implementing the model in a controlled experimental setting, direct measurements allow to gather information on the original problem.

Among others, the Bose-Hubbard model is particularly relevant for solid-state physics. It consists of interacting bosons in a lattice with nearest neighbor hopping (cf. Sec. 2.4.3). Because it considers only contact-type interactions, that is $\sim \hat{a}^\dagger \hat{a}^\dagger \hat{a} \hat{a}$ on site terms, it is naturally implemented in a variety of systems, ranging from Rydberg atoms to Kerr resonators [332]. Remarkably, this model describes the superfluid to Mott insulator transition as the order parameter given by the ratio of the hopping to interaction strength U/J becomes larger than the coordination number of the lattice [191, 192].

If one allows the Bose-Hubbard hamiltonian to include interaction with the environment with a coupling rate comparable with interactions or to the kinetic energy, the system enters a non-equilibrium regime where energy can flow from and towards the system. With the inclusion of particle loss, pumping and eventually decoherence, the many-body hamiltonian is usually referred to as a driven-dissipative Bose-Hubbard (DDBH) model. Not only its phase diagram is still largely unexplored except for the case of very strong or weak interactions [52, 195, 196], but the possibility to coherently drive the system offers a useful tool for preparing and stabilizing exotic states of matter, which are not necessarily in the hamiltonian ground state [333, 334, 335].

As photonic systems are inherently lossy, engineered arrays of coupled cavities endowed with a strong Kerr nonlinearity have been proposed as a natural implementation of the DDBH model [157, 51, 158, 159]. In this sense, semiconductor microcavities hosting polariton excitations are a promising platform (cf. Sec. 2.4.3). Although the magnitude of two-polariton interaction (U) is still small when compared to the dissipation rate ($U/\gamma \lesssim 0.1$), limiting the exploration of strongly quantum-correlated phases [336, 53], recent works implementing dipolar interaction for indirect exciton-polaritons [56] and polaron-polaritons in the fractional-quantum hall regime [337] are promising avenues. A minimal yet phenomenologically rich realization of the DDBH hamiltonian consists on two coupled Kerr resonators (CKRs) where all the ingredients of the model, namely nonlinearities, coherent exchange of population, losses and site-selective driving are present.

Even in the weak interaction regime CKRs have shown to display a variety of behaviors including spontaneous symmetry breaking [320], self-trapping and Josephson oscillations [321, 338, 339], periodic squeezing [322] a nonlinear hopping phase [323] and the emission of quantum correlated photons [340]. Interestingly, the production of entanglement in a spatial-symmetry-breaking phase transition [341] and the presence of a parametric instability [330] have been predicted but, so far, have not been experimentally addressed. In this chapter we report the observation of a parametric instability characterizing the non-equilibrium steady state of coherently driven coupled micropillar cavities.

Parametric instabilities are ubiquitous both in linear systems as a result of the

periodic modulation of an internal degree of freedom (e.g. the resonance frequency of an oscillator [342]) and in nonlinear systems driven out-of-equilibrium [218]. In dissipative systems, provided the instability growth rate is larger than any competing damping mechanism, any perturbation of the system about its steady-state is amplified often resulting in a self-pulsing behavior (parametric oscillation) or in spatial pattern formation [343]. One interesting feature already pointed out in early works on vibrating bodies [344, 342, 345] is that these resonances do not necessarily occur at one of the natural frequencies of the system. One everyday example is the fact that a kid standing on a swing need to duck two times per period in order to increase the amplitude of the oscillations [346]. In the context of optical parametric oscillators (OPO), this has been exploited since the 60s for coherent frequency conversion purposes [347]. Indeed, for a second (third) order nonlinearity, photons at the pump frequency ω_p are converted via the parametric process into signal and idler photons at frequencies ω_s and ω_i satisfying energy $\omega_p = \omega_s + \omega_i$ ($2\omega_p = \omega_s + \omega_i$) and momentum $\mathbf{k}_p = \mathbf{k}_s + \mathbf{k}_i$ ($2\mathbf{k}_p = \mathbf{k}_s + \mathbf{k}_i$) conservation.

One of the main drives of the research on parametric processes is their technological relevance: for instance, close to oscillation threshold, that is when the instability growth rate and losses are comparable, parametric oscillators can be used to build narrowband ultralow-noise amplifiers [348, 349, 350]. In ring resonators presenting hundreds of equally spaced modes, parametric processes generate octave-spanning frequency combs [351, 352], a key resource for metrological studies [353]. As well, squeezing [354, 355, 356] and non-classical correlations characterize the fields generated by parametric processes [357, 358, 359], which are key resources for the implementation of quantum information protocols in the continuous variable domain. Combining these features with the impressive refinement of nano-fabrication techniques, on-chip structured quantum light sources have been recently demonstrated [360]. In this sense, the versatility of our semiconductor platform is extremely promising.

If now we consider a lattice of coupled microresonators endowed with a third order (Kerr) nonlinearity, as the one present in polariton microcavities (cf. Sec. 2.3), the process associated to the parametric generation of signal and idler can be modeled with the on-site four-wave mixing (SFWM) hamiltonian [214, 360]

$$\mathcal{H}_{SFWM} = \eta \sum_m (\hat{a}_{m,i}^\dagger \hat{a}_{m,s}^\dagger \hat{a}_{m,p} \hat{a}_{m,p} - \hat{a}_{m,p}^\dagger \hat{a}_{m,p}^\dagger \hat{a}_{m,i} \hat{a}_{m,s}) \quad (5.1)$$

where $\hat{a}_{p,s,i}$ are the ladder operators acting respectively on the pump, signal and idler modes and the index m runs over the lattice sites (micropillars cavities). The coefficient η is proportional to the polariton-polariton scattering rate times the overlap integral of the spectral and spatial distribution of the modes involved in the four wave mixing processes $(p,p) \rightleftharpoons (s,i)$. The second term in Eq. (5.1) is typically small when compared to the first one as the population of the sideband (signal and idler) modes is typically much smaller than the one at the drive frequency. Within this approximation, the SFWM hamiltonian corresponds up to a multiplicative factor to the resonant polariton-polariton interaction term (cf. Sec. 2.4). Parametric oscillation has indeed been extensively studied in planar polariton microcavities [131, 128, 132, 136], and micropillars [361]. All these realizations operated in a triply resonant condition, that is, both the pump and the sidebands are resonant with a polariton mode; this will not be the case for the experiments presented in this chapter. The difference and advantages

of the two schemes will be discussed at a later stage.

Let us now focus on how to identify the presence of a parametric instability in the non-equilibrium steady state of a driven-dissipative system. Importantly, for weak nonlinearities, the presence of dynamical instabilities can be addressed already at the semiclassical level inspecting the spectrum of small fluctuations around the fixed points of the dynamics. As discussed in Sec. 3.3.1, this is equivalent to studying the eigenvalues λ_i of the linear stability matrix.

Parametric instabilities are associated to steady-state solutions whose stability matrix has at least one eigenvalue with a positive imaginary part (gain) and a non zero real part (i.e. an oscillating character). For instance, if we consider only the lowest energy mode (with resonance frequency ω_0) of a single pillar, driven by a monochromatic pump oscillating at ω_p , the eigenvalues of the stability matrix read $\lambda_{\tilde{\alpha}} = -i\gamma/2 \pm \sqrt{(\Delta - 3U\tilde{n})(\Delta - U\tilde{n})}$ ($\hbar = 1$), see Sec. 3.3.1. Here $\Delta = (\omega_p - \omega_0)$ is the laser detuning, U is the interaction constant, γ is the linewidth and $\tilde{n} = |\tilde{\alpha}|^2$ is the cavity steady-state occupation. Clearly, the square root can yield either a purely real or imaginary contribution, thus the parametric instability conditions are never met. This does not mean that the four-wave mixing processes do not occur but just that they are not amplified. This is not the case for two (or more) coupled cavities, as we show in the following.

5.1.1 Semiclassical coupled mode model

The dynamics of the lowest-energy mode of two coupled micropillars (CKRs) is captured at the level of a truncated Wigner approximation by a set of two stochastic differential equations for the complex amplitudes $\alpha_{1,2}$ of the polariton fields in each micropillar¹. In the frame rotating at the pump frequency and setting $\hbar = 1$, one has

$$\begin{aligned} id\alpha_{1,2} &= -(\mathcal{D}(\alpha_i, \alpha_i^*) + J\alpha_{2,1}) dt + d\chi_{1,2}(t) \\ \mathcal{D}(\alpha_j, \alpha_j^*) &= (\Delta + i\Gamma/2 - U(\alpha_j^*\alpha_j - 1)) \alpha_j - i\sqrt{\Gamma/2}\mathcal{F}. \end{aligned} \quad (5.2)$$

Here Δ is the laser detuning relative to the bare cavity resonance (we take $\omega_1 = \omega_2$), F_j the on-site drive amplitude, Γ is the polariton linewidth, U the Kerr nonlinearity, J the coupling constant and $\chi_j(t)$ is a complex-valued gaussian noise of variance $\langle \chi_j^*(t)\chi_{j'}(t') \rangle = \delta_{j,j'}\delta(t-t')\Gamma/2$. In the following we pump only the site $j = 1$, to avoid imposing the phase relation between the two coupled modes [330, 113, 341], thus $F \equiv (F_1, 0)$ can be taken real, without loss of generality. These equations yield correctly normalized input-output relations only in the case of an equal reflectivity of the top and bottom microcavity mirrors and in absence of absorption and non-radiative processes. A description of the linear eigenvalues of this model ($U = 0$) can be found in Section 2.4.2.

In order to find eventual parametric instabilities in the CKRs parameter space, we can follow a two step procedure. First, we determine the mean-field steady-state values $\tilde{\alpha}_j$ for each given parameter set. To do so, we solve numerically the set of algebraic equations associated to the right hand side of (5.2) neglecting phase-space diffusion

¹see Section 3.3.2 and refs [37, 362, 222] for the details

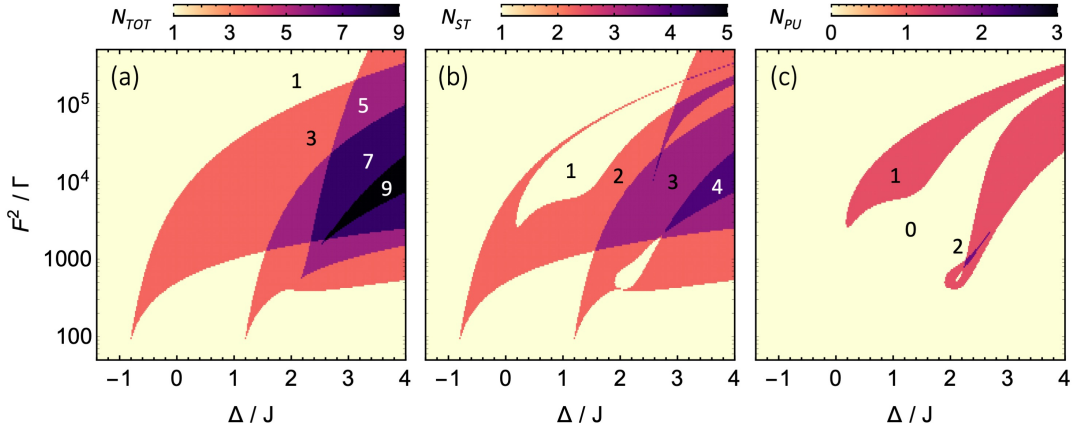


Figure 5.1: **Phase diagram of the CKRs:** (a) Total number of steady state solutions as a function of the drive detuning Δ and power F^2/Γ . (b) Number of stable solutions; bistability occurs for $\Delta > -J + \sqrt{3}/2\Gamma$, multistability for $\Delta/J > 1.56$. (c) Number of parametrically unstable solutions, $N \geq 1$ if $\Delta > \Gamma$. Single mode unstable solutions can be deduced subtracting panel (b,c) to panel (a). Other parameters: $U/\Gamma = 0.01$ and $J/\gamma = 5$.

(i.e. the stochastic terms $d\chi_j$). Then, we address the linear stability of the solutions encoded in the eigenvalues of the Jacobian matrix (cf. Sec. 3.3.2)

$$\tilde{\mathcal{J}} = \begin{pmatrix} -\tilde{\Delta}_1 & U\tilde{\alpha}_1^2 & -J & 0 \\ -U(\tilde{\alpha}_1^*)^2 & \tilde{\Delta}_1^* & 0 & J \\ -J & 0 & -\tilde{\Delta}_2 & U\tilde{\alpha}_2^2 \\ 0 & J & -U(\tilde{\alpha}_2^*)^2 & \tilde{\Delta}_2^* \end{pmatrix} \quad (5.3)$$

where the effective complex detuning reads $\tilde{\Delta}_j = \Delta + i\Gamma/2 - 2U(\alpha_j^*\alpha_j - 1)$. If a given solution is found to be parametrically unstable, any fluctuation around the steady-state solution due to the fluctuation term $d\chi_j(t)$ is exponentially amplified eventually leading to the onset of a self-pulsing behavior [325]. Such genuinely non-equilibrium steady-state has been reported with coherently excited two-level atoms [324] and molecules [363] in optical cavities. Importantly, the stability matrix gives a sufficient condition for the parametric process to be amplified, however it does not predict whether the oscillation will stabilize or grow uncontrollably leading the system to the closest stable solution. Indeed as the perturbation grows in amplitude the linearization hypothesis used for the derivation of the stability matrix is no longer valid; a full calculation of the dynamics is typically necessary.

As an example, in Fig. 5.1, we considered a strongly-coupled regime ($J/\Gamma = 5$) of the CKRs with $U/\Gamma = 0.01$ and explored the detuning and pump power (Δ, F^2) parameter space. Figure 5.1-(a) shows the total number of steady-state solutions $\tilde{\alpha}$ as a function of the driving conditions. For a given pump power and detuning up to nine roots of the algebraic equation system can be found. Indeed, as anticipated in Sec. 3.3.1, when driving only the first out of N CKRs, a chain substitution allows to express the equation set as a polynomial of degree 3^N in some $\tilde{\alpha}_N$, which admits up to 3^N complex valued solutions (i.e. 9 for the dimer). In Fig. 5.1-(b,c) we address the stability of each solution and count the number of stable and parametrically unstable solutions,

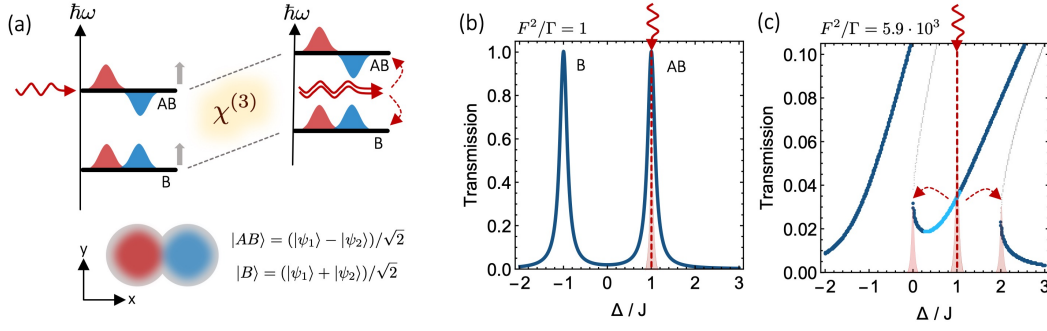


Figure 5.2: **Parametric instability - underlying mechanism:** (a) The opening of a resonant scattering channel from the pump toward two modes as their energy gets renormalized by interactions is at the origin of the parametric instability; adapted from [330]. In the simplest scenario, the sidebands corresponds to the nonlinear bonding (B) and anti-bonding modes (AB), corresponding to the symmetric and anti-symmetric superposition of the bare pillar eigenmodes (cf. Sec. 2.4.2). Calculated transmission spectra in the linear (b) and parametric instability regime (c). In panel (c) blue, cyan and gray dots correspond respectively to stable (S), parametrically unstable (PU) and (single-mode) unstable (U) solutions. A possible resonant parametric scattering process for a $\Delta = J$ detuned pump is shown in panel (c). Simulation parameters: $U/\Gamma = 0.01$ and $J/\gamma = 5$ (same as figure 5.1).

respectively. From panel (b) we can see that bistability occurs for $\Delta > -J + \sqrt{3}/2\Gamma$ while multistability sets in for $\Delta/J > 1.56$. Interestingly for $\Delta > \Gamma$ a tongue of parametrically unstable solutions can be observed, see Fig. 5.1-(c).

In ref. [330], D. Sarchi and collaborators suggested an intuitive picture to understand the origin of the parametric instability region. In order to illustrate the idea, let us consider a specific situation where a coherent drive excites at $\Delta = J$ the coupled microcavities, see Fig. 5.2-(a). In the linear regime, this corresponds to drive resonantly the anti-bonding (AB) mode of the system². If one increases the pump power, the net effect of a Kerr nonlinearity ($U > 0$) is to blueshift the resonances associated to the nonlinear eigenmodes by an amount proportional to $U n_{tot}$ where $n_{tot} = n_1 + n_2$ is the total number of polariton excitations in the two microcavities. If $\Delta > 0$, there will always exist a drive power for which the average energy of the nonlinear B and AB modes corresponds to the energy of the pump. In the specific case under consideration, since $\Delta = J$, this will happen for $U n_{tot} \approx J$, as Fig. 5.2-(a) illustrates. Then, a resonant scattering channel from the pump towards the two nonlinear modes is opened, eventually allowing four wave mixing processes to set in. Additionally, if the scattering is stimulated, the system possibly enters a self-pulsing regime, which can be seen as the result of the coherent beating of the pump with the sideband modes [330].

To support this qualitative picture, we plot the transmission spectrum of the coupled microcavities in the linear regime ($UF^2/\Gamma \ll 1$) and for a representative value of the drive power within the parametric instability region ($F^2/\Gamma = 5.9 \cdot 10^3$), see Fig. 5.2-(b) and (c), respectively. Stable, parametrically-unstable and (single-mode) unstable solutions are colored in blue, cyan and gray, respectively. The transmission coefficient

²The bonding (B) and anti-bonding (AB) modes corresponds to the in- and out-of-phase superpositions of the bare pillar eigenmodes $|\psi_{1,2}\rangle$, that is $|B, AB\rangle = (|\psi_1\rangle \pm |\psi_2\rangle)/\sqrt{2}$ at frequencies $\Delta_{B,AB} = \mp J$ see Sec. 2.4.2 for details.

of the coupled microcavities is calculated as $\mathcal{T} = \Gamma n_{\text{tot}}/2F^2$, depends on the stationary values of the intracavity fields ($\tilde{\alpha}_j$) and is possibly multivalued in the nonlinear regime. Unsurprisingly, in Fig. 5.2-(b), two sharp resonances corresponding to the linear B and AB modes appear for $\Delta = \pm J$. In Fig. 5.2-(c) we can see that the transmission spectra bend towards larger energies due to the Kerr nonlinearity. For this drive power the system is parametrically unstable at $\Delta = J$, simultaneously, at the the frequency of the nonlinear B and AB modes ($\Delta \approx 0, 2J$) solutions are stable and the transmission is large. Now, the parametric gain is roughly equal to the initial state occupation times the two-polariton interaction constant $\eta \sim Un_{\text{tot}}$ [330]; since $\eta/\Gamma \sim 2U\mathcal{T}\mathcal{F}^2/\Gamma^2 > 1$, the resonant scattering process is stimulated, resulting in an instability. This validates the intuitive picture presented in Fig. 5.2-(a). This mechanism applies in general for $\Delta > \Gamma$. Indeed, in order to have amplification $\eta/\Gamma > 1$, while $Un_{\text{tot}} \sim \Delta$ in order to have the opening of some resonant scattering channel from the pump toward the nonlinear modes, that is $\eta \sim \Delta > \Gamma$, in agreement with the predictions of Fig. 5.1-(c).

5.2 Experiments with coupled micropillar cavities

Inspired by the results of the calculations outlined in the previous section, we want to experimentally address the presence of a parametric instability in the nonlinear response of two coupled micropillar cavities. We will consider a sample derived from the heterostructure design number two (see Sec. 3.1.1), embedding a single 15 nm thick $\text{In}_{0.05}\text{Ga}_{0.95}\text{As}$ QW, with a heavy-hole exciton transition at $E_x = 1454(1)$ meV. In the sample the measured planar cavity finesse (prior to etching) is $\mathcal{F} \approx 7 \cdot 10^4$. Hereafter we consider two overlapping microresonators with radius $R = 2.0 \mu\text{m}$ and a center-to-center distance $d = 3.6 \mu\text{m}$.

In resonant excitation experiments, before entering the nonlinear regime, it is necessary to precisely characterize the linear properties of the coupled micropillar cavities. For this reason, we organize this section as follows: First, we extract the exciton and photon fraction of the microstructure discrete modes; Then, we use a quasi-resonant excitation experiment to characterize the linear transmission spectrum of structure; Finally, we investigate the nonlinear response of the microstructure.

5.2.1 Retrieving the eigenstate fractions

Estimating the bare cavity and exciton energy in microstructures presenting discrete optical modes is difficult. Indeed, even knowing Ω_R from a characterization of the planar cavity prior to etching, one needs to measure both the energy of the lower (LP) and upper polariton (UP) resonance to extract the exciton-cavity detuning. However, the UP modes are hardly visible in experiments as they are spectrally close to the exciton, thus experiencing an enhanced absorption (cf. Sec. 2.3.4).

To circumvent the problem, in each repetition of the microstructure pattern we leave large unetched areas ($120 \times 120 \mu\text{m}$). In these large portions of planar cavity, the confined modes effectively form a continuum which we use to measure the polariton dispersion relation (cf. Sec. 2.3.3). In Fig. 5.3-(a) we show a polariton dispersion relation measured in close vicinity of the coupled microcavity structures we will focus

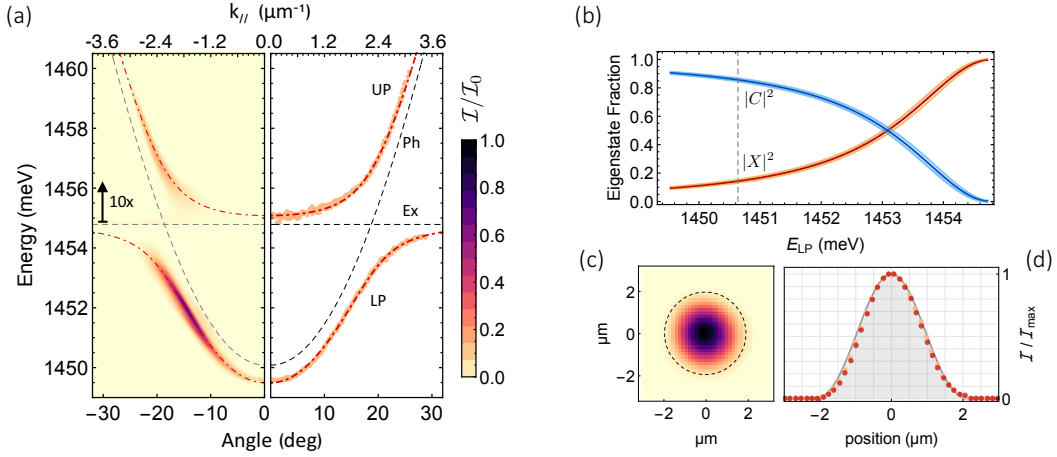


Figure 5.3: **Eigenstate fraction and mode volume:** (a) Energy and angle resolved photoluminescence of a square $120 \times 120 \mu\text{m}$ unetched portion of the sample (left) and corresponding fit with the polariton dispersion relation (right). (b) Eigenstate fraction as a function of the lower polariton energy, deduced from the fit of panel (a). (c) Measured emission pattern $|u(\mathbf{r})|^2$ of the lowest energy ($E_0 = 1450.61(1)$ meV) discrete mode of a $2 \mu\text{m}$ radius micropillar. (d) Cuts through the x and y axes of the measured mode profile (c) are compared with the predictions of a finite element model of the micropillar (cf. Sec. 2.4.1), allow extracting the modal area $\mathcal{A} \approx 6.0 \mu\text{m}^2$.

our resonant experiments in the following. As already mentioned in Sec. 2.3.3, a peak-finding algorithm is used to extract the energy and momentum doublets (right panel side) from the CCD image (left panel side). The resulting data points are simultaneously fitted using the polariton dispersion relations [eq. (2.31)]. From the fit we extract the bare exciton transition $E_x = 1454.78(3)$ meV, the $k = 0$ cavity mode resonance $E_c = 1450.08(2)$ meV and the Rabi splitting $2\hbar\Omega_R = 3.39(4)$ meV. The same procedure, repeated over all the large unetched areas allows to obtain an estimate of for E_c and E_x at any point in the sample.

Furthermore, using the relations between the exciton ($|X|^2$) and photon fraction ($|C|^2$) [eq. (2.29)] and $(E_{c,x}, \Omega_R)$, we deduce their dependence as a function of the lower polariton energy, as Fig. 5.3-(b) shows. Using this information we can relate the energy of any discrete lower polariton mode of a microstructure to the corresponding eigenstate fractions³.

As an example, we consider a single $2 \mu\text{m}$ radius micropillar cavity, the fundamental building block forming the couple microcavities investigated in the following. With an off-resonant spectroscopy experiment we measure the lowest energy resonance $E_0 = 1450.61(1)$ meV, deriving $|X|^2 = 0.14(1)$. In Fig. 5.3-(c) we show the measured spatial profile $u(\mathbf{r})$ of the mode and in Fig. 5.3-(d) we compare two orthogonal cuts through the profile maxima (markers) with the profile obtained with finite element calculations. We can use this profile to deduce the modal area $\mathcal{A} = (\int d^2\mathbf{r} |u(\mathbf{r})|^4)^{-1} \approx 6 \mu\text{m}^2$.

³This estimate may suffer from unpredictable systematic errors in small asymmetric ($\sim 2\mu\text{m}$) microstructures as strain-release effects can modify the exciton transition energy [364].

5.2.2 Resonant spectroscopy

To complete the characterization of the coupled microcavities we perform a resonant spectroscopy experiment allowing to precisely measure the linear response of the structure. In Fig. 5.4-(a) we show a representative SEM image of three dimer molecules. In these experiments we will probe the transmission of the dimer structures by shining a single-mode CW laser on one of the two micropillars, in order to equally couple to the B and AB modes (for details on the setup cf. Sec. 3.2). As resonant experiments are extremely sensitive to the excitation conditions, we summarize the protocol we have developed.

- As a first step, we roughly align the excitation spot on top of the structure while the sample is illuminated by a broadband LED light. Then we turn off the LED and tune the laser wavelength to ≈ 780 nm in order to off-resonantly excite the structure. The PL is collected in transmission geometry and dispersed in energy with the spectrometer. Once we identify a relevant resonance, say the bonding mode, we mark on the CCD the pixel of the resonance peak, then we tune the laser wavelength until the transmitted signal matches it. To ensure an operation in the linear regime we typically use (50 – 100) nW incident power.
- Once the laser is locked to one resonance we can directly image the transmitted pattern (without spectral selection): if the collection focus is correct, it usually resembles the mode profile encompassed by some stray light around it, as the input coupling is not optimal at this stage. To optimize the input coupling one can first act on the in-plane piezo positioning stage while trying to maximize the transmitted intensity, then act on the focus and repeat until convergence. One can further enhance the input coupling by matching the input beam waist to the effective waist of the pillar mode, to do so one needs to play simultaneously with the beam divergence and focus of the excitation objective lens.
- The final step is to match the polarization state of the excitation beam to one of the cavity modes. In the case of a dimer molecule, we have a doublet of orthogonal linearly polarized states both for the B and AB modes (see Sec. 4.2.1 and [365]). To excite only one of the two (B-AB) doublets, we first roughly align the linear polarization of the excitation to one of the dimer symmetry axes, and then cross-polarize the detection. Walking the excitation and detection polarization to maximize extinction, allows a precise determination of the polarization axes of the eigenmodes. Residual birefringence in the cryostat windows and DBRs can be finely corrected using quarter-wave plates.

Once these steps are completed, we record the transmitted emission pattern as a function of the weak excitation laser frequency. From each frame we compute the integrated intensity, yielding a signal proportional to the microcavity transmission spectrum; the result is shown in Fig. 5.4-(c). We can observe two sharp resonances corresponding to the bonding and anti-bonding modes of the structure, the transmission pattern measured at each resonance is shown in the insets. These patterns display an even (odd) spatial symmetry, confirming the bonding (anti-bonding) character of the modes. Notice that these are raw images, there is no post-processing to remove stray light thus indicating the effectiveness of the input coupling optimization protocol.

When driving a single site, the coupled mode theory presented in Sec. 5.1.1 predicts an equal relative height of the B and AB resonances ($Un_{\text{tot}} \ll 1$). However, in the

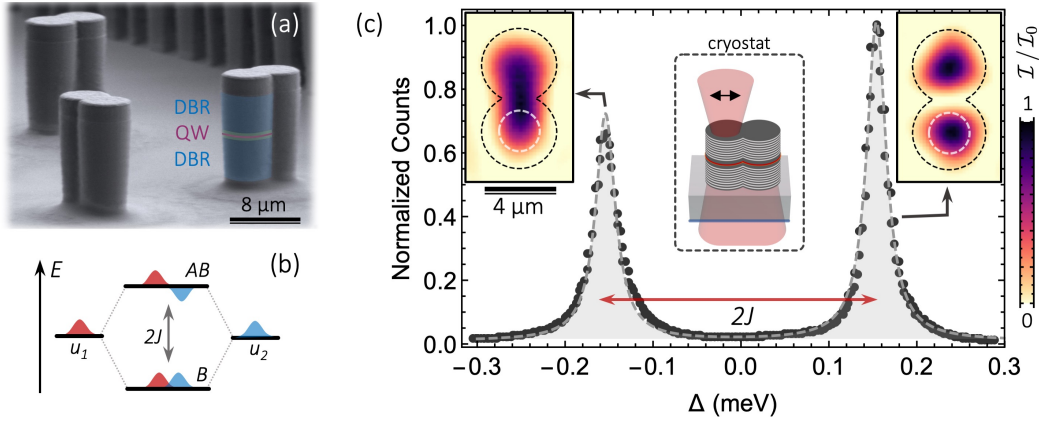


Figure 5.4: **Resonant spectroscopy:** (a) SEM image of the coupled micropillar cavities the DBRs, cavity spacer and quantum well (QW), are highlighted in false blue, green and purple false-colors, respectively. (b) Schematic representation of the hybridization of the two bare pillar modes into molecular bonding (B) and anti-bonding (AB) photonic modes. (c) Measured transmission (circles) as a function of the laser detuning relative to the uncoupled cavity resonance (Δ); the dashed line is a fit with Eq. (5.5). The left and right insets show the transmission pattern measured at each resonance. The dashed lines indicate the edge of the microstructure and the half maximum contour of the incident laser spot.

experiment, the B and AB modes have similar but unequal spatial profiles in the driven pillar, see the insets in Fig. 5.4(c). Consequently, the excitation spot (dashed white line) may couple differently to the B and AB mode. Of course, by translating the spot position towards the center of the structure one could balance the input coupling. Unfortunately, this means the tails of the excitation spot overlap more with the second pillar; simulations indicate this would be detrimental for the onset of a parametric instability. For this reason, we prefer to optimally couple to the AB mode and make sure that twice the waist of the excitation spot is smaller than the pillar diameter (slightly degrading the input coupling efficiency).

In order to fit the transmission spectrum, as we used an extremely weak laser drive, we can take the limit $U|\alpha_j|^2 \rightarrow 0$ in the set of Langevin equations (5.2). If now we solve for the steady-state expectation value, that is we set $d\alpha_j^{ss}/dt = 0$ and average over the stochastic variables $\tilde{\alpha}_j = \langle \alpha_j^{ss} \rangle$, using the linearity of the equations, we obtain

$$\begin{aligned} 0 &= (-\Delta - i\Gamma/2)\tilde{\alpha}_1 - J\tilde{\alpha}_2 + i\sqrt{\Gamma/2}F \cos(\eta) \\ 0 &= (-\Delta - i\Gamma/2)\tilde{\alpha}_2 - J\tilde{\alpha}_1 + i\sqrt{\Gamma/2}F \sin(\eta) \end{aligned} \quad (5.4)$$

where the coefficient η allows to model the different spatial overlap of the excitation spot to the B and AB modes (for $\eta = 0$ the pumps drives the two equally). We recall that (Γ, Δ, J) are, respectively, the polariton linewidth, the laser detuning relative to the bare micropillar resonance and the coupling strength. Solving for the $\tilde{\alpha}_j$ and using the definition of the transmission coefficient we get

$$\mathcal{T}(\Delta) = \frac{\Gamma^4 + 4\Gamma^2 (\Delta^2 + J^2 - 2\Delta J \sin(2\eta))}{(\Gamma^2 + 4\Delta^2)^2 + 16J^4 + 8J^2 (\Gamma^2 - 4\Delta^2)} \quad (5.5)$$

In Fig. 5.4-(c) we used the above relation to fit the experimental data, the result is traced with a dashed line showing an excellent overall agreement. From the fit we obtain the polariton linewidth $\Gamma = 27.4(8) \mu\text{eV}$, the coupling strength $J = 154.1(6) \mu\text{eV}$ and the fundamental mode energy $\hbar\omega_0 = 1450.64(1) \text{ meV}$. Using the calibration of the exciton fraction as a function of the lower polariton energy discussed in the previous section, we can convert this latter fit parameter to $|X^2| = 0.14(1)$. Recalling that the modal area of each pillar is $\mathcal{A} \approx 6 \mu\text{m}^2$, and that $g_0^{exp} \sim 5 - 40 \mu\text{eV} \mu\text{m}^2$, we get a rough estimate of the expected interaction constant $U \sim 0.02 - 0.13 \mu\text{eV}$. Having characterized all the parameters of the coupled microcavities and shown that observations can be fairly reproduced using a coupled mode equations model, we move to the exploration of the high polariton density regime, where the onset of parametric instabilities is expected.

5.2.3 Nonlinear regime

To probe the nonlinear response of the coupled microcavities, we tune the frequency of the laser to the anti-bonding resonance ($\Delta = J$). At this value of the detuning, we expect to cross the instability region as we increase the pump power above some threshold power (see Fig. 5.1). We are interested in measuring the polariton population as a function of the input drive amplitude. To this aim we acquired a series of CCD images while synchronously changing the input laser power, which we monitored using a power meter. From each CCD frame the site-resolved polariton population was deduced by integrating the counts over a region of interest corresponding to each micropillar, see the inset of Fig. 5.5-(a). The count rates ($\Phi_{1,2}$) are corrected for detection efficiency and converted to a population using the relation $n_i = 2\tau|c_p|^2\Phi_i$ where $\tau \approx 24 \text{ ps}$ is the polariton lifetime and $|c_p|^2 = 0.86(1)$ is the polariton photonic fraction at the frequency ω_0 . In the collection efficiency one needs to include the substrate transmission $\mathcal{T}_{sub} \approx 0.62$, the losses induced by the collection optics $\mathcal{T}_{opt} \approx 0.69$ the spectrometer transmission $\mathcal{T}_s \approx 0.87$ and the quantum efficiency of the (front-illuminated) CCD $\mathcal{Q} \approx 0.34$. Notice that, in order to avoid dealing with the polarization dependent transmission coefficient of the spectrometer grating at the 0th order, we moved the turret to the metallic mirror stage instead.

To calibrate the input power we need to evaluate the radiative part of the cavity linewidth. According to the characterization presented in Sec. 3.2.2, in this experiment we can neglect the contribution to the polariton linewidth accounting for the inhomogeneous broadening of the exciton. Indeed, here, the polariton detuning relative to the exciton $\hbar(\omega_0 - \omega_x) \approx -4.14(3) \text{ meV}$ is much larger than the inhomogeneous broadening $\sigma_{inh} \sim 0.5 \text{ meV}$. This means we can write the polariton linewidth (Γ) in Eq. (5.2) as $\Gamma \approx [(\gamma_c + \gamma_a)|C|^2 + \gamma_{nr}|X|^2]$, where γ_c , γ_a and γ_{nr} denote the bare cavity radiative decay rate, the absorption and exciton non-radiative decay rate, respectively. Moreover, since the exciton fraction is small ($|X|^2 \sim 0.14$) and $\gamma_{nr} \sim \gamma_c/2$ according to the calibration in Sec. 3.2.2, we can neglect the $|X|^2\gamma_{nr}$ term at first order, thus $\Gamma = (\gamma_c + \gamma_a)|C|^2$. Using the input-output relations⁴ to define the reflection (\mathcal{R}) and transmission (\mathcal{T}) coefficients at resonance one easily finds that $\mathcal{T}_0 \approx (\gamma_c/\Gamma)^2$ and $\mathcal{R}_0 \approx (1 - \gamma_c/\Gamma)^2$. Then, by performing a simultaneous measurement of the reflected and transmitted light at resonance, we derived $\gamma_c = \Gamma\sqrt{\mathcal{T}_0} \approx 19 \mu\text{eV}$ and $\gamma_a \approx 13 \mu\text{eV}$.

⁴See for instance ref. [163].

From the difference between the expected reflection coefficient ($\mathcal{R}_0^{\text{th}} \approx 0.09$) and the measured one $\mathcal{R}_0^{\text{exp}} \approx 0.21$ one gets the input coupling efficiency $C_{eff} \approx 0.86$.

With these two calibrations we converted each CCD frames and power meter reading to polariton population and input power values; the result is presented in Fig. 5.5-(a,b). Hereafter, subscript 1 (2) refers to the driven (undriven) cavity. We observe that the coupled cavity population exhibits a hysteretic behavior as the pump power is cycled between $40 \mu\text{W}$ and $400 \mu\text{W}$. This is a consequence of the dispersive bistability induced by the Kerr nonlinearity of our microresonators, a well known phenomenon in the context of nonlinear optics [366, 216, 133]. The dashed lines in Fig. 5.5-(a,b) correspond to the steady-state mean-field predictions (i.e. neglecting noise terms and setting $\dot{\alpha}_i = 0$) derived from Eq. (5.2) with U being the only adjustable parameter. We find the best agreement between experiments and theory for $U \approx 0.1 \mu\text{eV}$, corresponding to an exciton-exciton interaction constant⁵ $g_0^{\text{exp}} \sim 30 \mu\text{eV}\mu\text{m}^2$. Importantly, for $P > 200 \mu\text{W}$, along the lower branch of the hysteresis, the predictions of a steady-state model are inaccurate. This is a hint of what we are looking for: the failure of steady-state predictions is a potential signature of the onset of dynamical features.

The left column of Fig. 5.5-(c) shows measured transmission patterns for five representative values of the pump power across the hysteresis cycle. At low power (1), since $\Delta = J$, the emission closely resembles the linear AB mode. Darkening of the driven cavity is observed in (2), due to an interference effect induced by the nonlinearity [323]. A small power increase (above $P_{\text{thr}} \approx 240 \mu\text{W}$) produces an abrupt jump in the driven cavity population, as shown in (3). By further increasing the pump power, we observe in (4) another jump in the transmitted intensity and a change to a bonding-type spatial profile, that persists throughout the upper branch of the hysteresis (5). The right column of figure 5.5-(c), presents the corresponding theoretical predictions obtained by time-averaging the long term dynamics of Eq. (5.2) after having adiabatically ramped the power to a specified value. Notice that in this simulations the effect of fluctuations of the intracavity field is included. The amplitudes $\langle \alpha_i \rangle_t$ are multiplied by a gaussian spatial profile approximating the uncoupled pillar modes. The resulting intensity maps are in excellent agreement with the experimental observations showing that, when including fluctuations, we can fully reproduce the data in Fig. 5.5-(a).

In Fig. 5.5-(d), we compute the total interaction energy $U(n_1 + n_2)$ as a function of pump power along the lower branch of the hysteresis. This quantity represents the eigenmode energy shift induced by the nonlinearity. Interestingly, when approaching the instability region around P_{thr} , the blue-shift becomes comparable with J within the mode linewidth. Thus, a resonant two-polariton scattering channel opens from the pump into the nonlinear bonding and anti-bonding modes, now symmetrically spaced in energy with respect to the pump. This suggests, within the intuitive picture proposed by D. Sarchi and collaborators [330], that a parametric instability is triggered above

⁵We stress that this value critically depends on the assumptions we used in the determination of the coupling efficiency and absorption coefficients which, apart from the standard errors, accounts a truncation of the term $|X|^2\gamma_x$ which we estimate to be order of $3 - 5 \mu\text{eV}$. Taking in account all the contributions we expect a relative error on the measured g_0 of the order of 25 %. Some authors also pointed out that in CW experiments Auger and phonon scattering might lead to the formation of a long-lived exciton reservoir, which artificially increases the measured interaction constant [367]. These effects, for large exciton-photon detunings (i.e. small $|X|^2$), and in the absence of a significant exciton density of states at the lower-polariton energy, should be strongly suppressed. To some extent, this is backed by the fact that the interaction constant we found is consistent with the one derived in recent weak polariton blockade experiments, which employed a pulsed excitation scheme [55, 54].

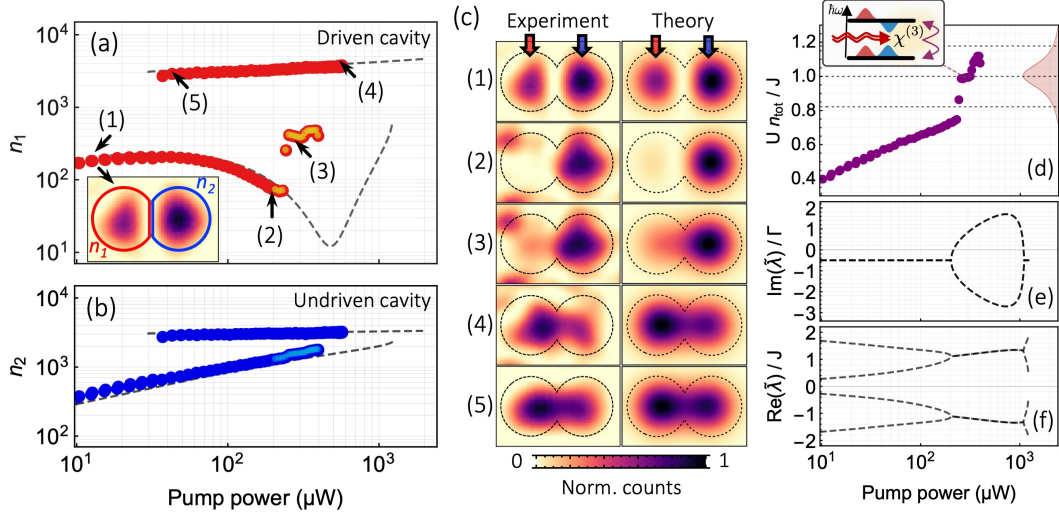


Figure 5.5: **Nonlinear response:** (a,b) Symbols: measured polariton occupation number of the (a) driven and (b) undriven cavity, as a function of pump power. Dashed line: steady-state prediction deduced from Eq. (5.2) with U being the only adjustable parameter. The best agreement is found for $U \approx 0.1 \mu\text{eV}$. (c) Left panels: intensity patterns measured at the five different pump powers indicated in panel (a). Right panels: calculated intensity patterns obtained as time-averaged solutions of Eq. (5.2), multiplied with a gaussian spatial profile, approximating the fundamental mode of each micropillar. (d) Total interaction energy $U(n_1 + n_2)$ deduced from the experiment as a function of the incident pump power along the lower bistability branch. Horizontal dashed lines correspond to $(J - \Gamma, J, J + \Gamma)$. Inset: schematics of the parametric instability mechanism occurring as $|Un_{\text{tot}} - \Delta| \approx 0$.

P_{thr} , eventually resulting in sustained oscillations of the intracavity field.

Figure 5.5-(e) and (f) presents, respectively, the imaginary and real parts of the eigenvalues of the stability matrix when evaluated along the lower branch of the bistability. Interestingly, for a moderate pump power of $\sim 200 \mu\text{W}$, the imaginary part of the eigenvalues bifurcates with two of them becoming positive for $P > P_{\text{thr}}$, i.e. when $Un_{\text{tot}} \approx J$, signaling the onset of an instability. Correspondingly, the real part of the eigenvalues collapses around $\pm J$ indicating an oscillating behavior of the perturbations: these are all characteristic features of a parametric instability (cf. Sec. 5.1.1). The region where the imaginary part of the eigenvalues bifurcates as a function of pump power thus corresponds to a vertical (constant detuning) cut through the parametric instability region in Fig. 5.1-(c). Experimental data points fulfilling this condition in figure 5.5-(a,b) are marked with a lighter dot.

5.2.4 Parametric Instability

Since all the criteria for the observation of the parametric instability are met and $Un_{\text{tot}} \approx \Delta > \Gamma$, we expect the instability to drive the system in a self-sustained oscillatory regime. If this is the case, the parametric excitation of signal and idler fields should be detected as clearly resolved sidebands in the coupled microcavity emission spectrum.

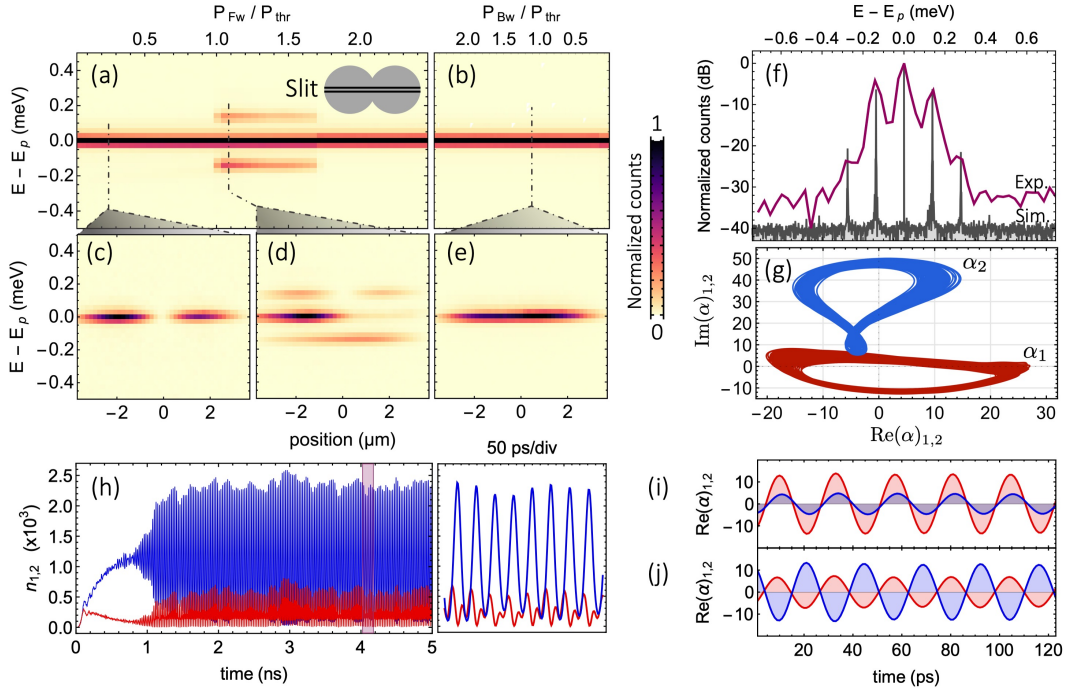


Figure 5.6: **Self-pulsing of the intracavity field** (a,b) Spectrally resolved emission of the microstructure measured while increasing (b), or decreasing (c) the pump power P_{Fw} (P_{Bw}), expressed in units of P_{thr} . (c,d,r) Position and energy resolved emission patterns (d) below, (e) within and (f) well above the instability region. As illustrated in the inset of panel (a), the spatial profile corresponds to a cut through the long symmetry axis of the structure. (f) Measured (purple) and simulated (gray) emission spectrum of the coupled cavities at $1.1P_{thr}$. (g) Calculated trajectories of the cavity field amplitudes $\alpha_{1,2}$ showing a limit cycle behavior in the instability region (4 ns evolution). (h) Left: temporal dynamics of the cavity occupations α_1 (red) and α_2 (blue). Right: zoom in spanning the 4.0 – 4.2 ns region. (i,j) Reconstruction of the cavity field dynamics obtained by band-pass filtering ($\Delta E = \Gamma/2$) the spectrum associated of the temporal dynamics shown in panel (h) around the signal and idler sidebands showing, respectively, an in-phase or out-of-phase oscillation of $\alpha_{1,2}$ as expected for a mode presenting a B or AB like spatial symmetry.

To this aim, we imaged the transmission of the structure on the entrance slit of the monochromator coupled to our CCD camera. The slit was aligned with the dimer axis as shown in the inset of Fig. 5.6-(a). Then, we recorded the resulting energy and position resolved patterns while scanning forward and backward the input power across the bistability. Figure 5.6-(a) and (b), present the normalized integrated spectra as a function of power along the increasing and decreasing power ramp, respectively. We present, in Fig. 5.6-(c-e), the spatially and spectrally resolved emission patterns (corresponding to a single click of the CCD), for three representative power values.

For a pump power below the instability region $P < P_{thr}$, the spectrum in Fig. 5.6-(a) is single toned. Since the pump is closer in energy to the anti-bonding resonance, it couples preferentially to this mode through its finite linewidth. Therefore, the corresponding spatial profile has an anti-bonding symmetry, clearly indicated by the intensity node at the center, see Fig. 5.6-(c). As soon as the pump power reaches P_{thr} , two well-

resolved sidebands displaced by $\pm 0.14(1)$ meV about the pump energy (E_p) appear. This is a clear signature of the sustained parametric oscillations triggered by the instability, with the pump coherently exciting signal and idler fields. The corresponding spatially resolved pattern in Fig. 5.6-(d) demonstrates that the lower (higher) energy sideband has a bonding (anti-bonding) symmetry, thus supporting the intuitive picture presented in Fig. 5.2-(a). When the input power exceeds $1.7 P_{\text{thr}}$, the microcavity mode switches to the upper branch of the bistability. Along this branch the emission is monochromatic, as evidenced by the measured spectra in the backward power scan [Fig. 5.6-(b)] and confirmed by a stability analysis of the upper branch solutions. The emission pattern is characterized by a bonding-type symmetry, shown in Fig. 5.6-(f).

Figure 5.6-(f) presents in log-scale the spatially integrated spectrum measured at $1.1 P_{\text{thr}}$. In addition to the bright signal and idler peaks, additional sidebands are clearly resolved arising from higher order four-wave mixing processes. The simulated spectrum (gray line), is the power spectral density of the cavity field dynamics and faithfully reproduces the sideband magnitudes. However, in order to match the spectral position of the peaks, we have to rescale the energy axis of the simulation by a factor 0.86. This discrepancy can be ascribed to the fact that the coupling strength J gets renormalized when increasing the pump power, since interactions modify the spatial profile of the modes, determining the coupling strength in a coupled mode picture [330]. Importantly, the energy fraction stored in the main sidebands is found to be as large as $I_{\text{sb}}/I_{\text{tot}} = 0.38$. Such efficient parametric process is possible despite the absence of a triply resonant condition in our experimental scheme, because the parametric gain ($\sim Un_{\text{tot}}$) at threshold, is more than five times larger than the losses, see Fig. 5.5-(d).

In the frame rotating at the pump frequency, the presence of sidebands implies that the cavity fields ($\alpha_{1,2}$) display a limit-cycle dynamics in phase space, as shown by simulations in Fig. 5.6-(g). The associated temporal evolution of the cavity population, shown in Fig. 5.6-(h), displays periodic oscillations modulated by a random envelope. The formation of such limit cycles in the dynamics of nonlinear coupled cavities was recently compared with the phenomenology of dissipative time crystals [368, 369], that is a dissipative quantum system whose observables display a discrete temporal translational invariance. However, we can see in Fig. 5.6-(g) that the limit cycle wanders in phase space as a consequence of the random fluctuations of the intracavity field. When increasing the interaction strength U , since the average number of polaritons at the oscillation threshold decreases, the relative amplitude of fluctuations increases. This effect may ultimately wash out the coherence of the oscillations resulting in the disappearance of the limit cycle [369]. In this sense, the possibility of realizing a time crystal in these dissipative systems seems to be limited to the classical limit $U \rightarrow 0$. Interestingly, the scaling of the coherence time of the sideband fields as a function of U could be easily accessed in our system using an interferometric scheme. We envisage this measurement as a short term follow up of this work.

Finally, in simulations, we extract the cavity field dynamics corresponding to the signal and idler fields using a spectral band-pass filter around the sidebands; the result is shown in Fig. 5.6-(i) and (j), respectively. The in-phase (out-of-phase) oscillation of α_1 and α_2 in the signal (idler) field is in agreement both with the experiment [5.6-(d)] and with the intuitive picture of the parametric oscillation discussed by [330].

5.3 Summary and Perspectives

In summary, we have demonstrated the onset of a multimode parametric instability within the hysteresis cycle of two coupled microresonators operating in the exciton-photon strong coupling regime. The spontaneous fluctuations of the intracavity field feeds the instability triggering sustained parametric oscillations. The coherent excitation of signal and idler fields is confirmed by the presence of well-resolved sidebands in the emission spectrum. All the observations have been comprehensively modeled combining the results of the dynamical coupled-mode equations for the intracavity fields (including vacuum fluctuations) with a linear stability analysis.

Unlike previously demonstrated triply resonant schemes involving microcavity polaritons [131, 128, 132, 136, 361], here the parametric process involves just two polariton modes, the pump not being in resonance with any of them. This configuration not only prevents dephasing of the pump mode in the cavity via parametric luminescence [370], but also ensures excellent spatial overlap of the modes participating to the process. As a result we observe remarkably contrasted sidebands, where roughly 38% of the total radiated energy is stored. Moreover, thanks to the hybrid light-matter nature of polariton excitations, the system is endowed with a strong Kerr nonlinearity allowing to observe the instability already at 240 μW threshold power. In this direction, recent works [55, 54, 56] seem encouraging for the investigation of optical parametric oscillators operating in the few photon regime [371].

The mechanism at the heart of the instability, namely the opening of a resonant scattering channel from the pump towards the bonding-like signal and the anti bonding-like idler modes, is experimentally confirmed by individually resolving their spatial profile while tracking the total interaction energy in the system. This interpretation, originally proposed in ref. [330], does not only apply to the dimer and, when generalized to lattices of microcavities, offers an intuitive way to predict and eventually engineer the presence of parametric instabilities. For instance, by changing the center to center distance between the microcavities, we could tune the energy separation between the sidebands. Profiting from the inherent scalability of a semiconductor platform, we envisage the observation of similar parametric instabilities in lattices of microcavities presenting modes with a macroscopic degeneracy [50, 48], or with nontrivial topological features [372, 60, 360].

A possible follow-up of this work could be to investigate in coupled microcavities the interplay between the parametric instability, the excitation polarization degree of freedom and the singlet exciton interaction channel. Indeed, when the number of modes participating to the process is increased, the instability may trigger a chaotic behavior of the intracavity field [373, 374]. Alternatively, chaotic oscillations were predicted for a single resonator subject to a two color drive scheme [375]. In the long run, when approaching the strong interaction limit $U/\Gamma > 1$, this would allow investigating the relation between chaos and ergodicity in open quantum systems [376].

Metastability in a driven Kerr resonator

ABSTRACT: Optical bistability is a characteristic phenomenon in driven nonlinear systems. Experimentally reported in a variety of experimental platforms, it is well described using a mean-field (MF) approximation of the electric polarizability [216]. However, a quantum treatment of the same problem predicts that the steady state of a nonlinear cavity is always unique [225]. This apparent contradiction is solved upon noticing that the two solutions predicted in the MF treatment, become metastable due to quantum fluctuations, triggering switching events between the two [377]. The average time between two switching events drastically diverges as the number of excitation in the system increases [226]. This slow dynamics is related to the emergence of a soft-mode and associated to the onset of a first-order phase transition [378, 379].

In this chapter we investigate the metastability regime using a single mode of a micropillar cavity. Following a recent theoretical proposal [380], we cycle the power of a coherent drive to perform dynamical hysteresis experiments. Using a scaling analysis of the hysteresis area as a function of the drive parameters, we characterize the critical exponents and infer the onset of a dissipative phase transition, occurring in the limit of an infinite intracavity population [230]. This work has been done in collaboration with the group of C. Ciuti (Université de Paris) and is condensed in [232].

Furthermore, we propose a mapping of the driven Kerr resonator onto a Logical Bit subject to stochastic bit-flip events. As we have access to the microcavity dynamics at a single trajectory level, we can describe the system within the framework stochastic-thermodynamics. Measuring the entropy production along the single trajectories, we test a non-equilibrium integral fluctuation theorem [381]. This preliminary measurements opens interesting perspectives for the exploration of non-equilibrium thermodynamics using nonlinear photonic platforms. This work is done in collaboration with the group of A. Auffeves from Institut Néel in Grenoble.

6.1 Introduction

In this chapter we consider one of the simplest, textbook models of a nonlinear driven-dissipative system: a single-mode Kerr-type resonator coherently excited by a laser. Firstly, we will investigate the steady-state properties of the model, comparing the predictions of a mean-field (MF) treatment with the exact quantum solution. The two approaches yield quantitatively different results. Whereas a MF treatment can support a bistable behavior, that is the existence of two stable states with different photon numbers for the same driving conditions, the exact solution is always unique.

Counterintuitively, experimental reports of optical bistability cannot be reproduced by the exact solution. In Sec. 6.1.1 we address the origin of this apparent contradiction investigating the role of quantum fluctuations, leading to a slow, metastable dynamics of the intracavity field. Then, in Sec. 6.1.2, we discuss the relation between the slowing down of the metastable dynamics in a suitably defined thermodynamic limit and the onset of a dissipative phase transition. In Sec. 6.2 we experimentally investigate the metastable dynamics of a micropillar cavity using dynamical hysteresis experiments, which we use to characterize the onset of a dissipative phase transition. Finally, in Sec. 6.3, we propose and experimentally test the possibility of interpreting the metastable dynamics of a driven Kerr resonator from the standpoint of stochastic thermodynamics.

6.1.1 An apparent contradiction

Let us consider the MF equation for a single Kerr resonator (cf. Sec. 3.3.1), in the frame rotating at the pump frequency ($\hbar = 1$), we have

$$i\dot{\alpha} = (-\Delta + U|\alpha|^2 - i\Gamma/2)\alpha + i\sqrt{\Gamma/2}\mathcal{F} \quad (6.1)$$

where $\Delta = (\omega - \omega_0)$ is the detuning of the pump (ω) with respect to the cavity resonance (ω_0), Γ is the cavity linewidth, U is the interaction constant and \mathcal{F} is the drive amplitude. We want to find the stationary solutions to this equation: imposing $\dot{\alpha} = 0$ for some $\tilde{\alpha}$ and multiplying the resulting algebraic equation for its complex conjugate yields

$$\mathcal{F}^2 = \frac{2}{\Gamma} [(\Delta - U\tilde{n})^2 + \Gamma^2/4] \tilde{n} \quad (6.2)$$

where $\tilde{n} = |\tilde{\alpha}|^2$ is the stationary occupation of the cavity. The above equation is telling us that we can express the input power ($\sim \mathcal{F}^2$) as a third order polynomial in \tilde{n} . For a given drive power, the stationary occupation \tilde{n} is multivalued if $\partial\mathcal{F}^2(\tilde{n})/\partial\tilde{n} = 0$ admits two distinct real and positive roots ($\tilde{n} \in \mathbb{R}^+$). The roots are parametrized by

$$\tilde{n}_{\pm} = \frac{2\Delta}{3U} \pm \frac{1}{6U} \sqrt{4\Delta^2 - 3\Gamma^2} \quad (6.3)$$

thus Eq. (6.2) is multivalued when $\Delta > \sqrt{3}\Gamma/2$ and $\mathcal{F}_+ \leq \mathcal{F} \leq \mathcal{F}_-$; \mathcal{F}_{\pm} are obtained by inserting Eq. (6.3) in Eq. (6.2). In Fig. 6.1-(a) we trace the region supporting multiple solutions for the cavity occupation in the detuning and input-power parameter space ($U/\Gamma = 0.05$). Although Eq. (6.2) admits three positive real solutions in the shaded

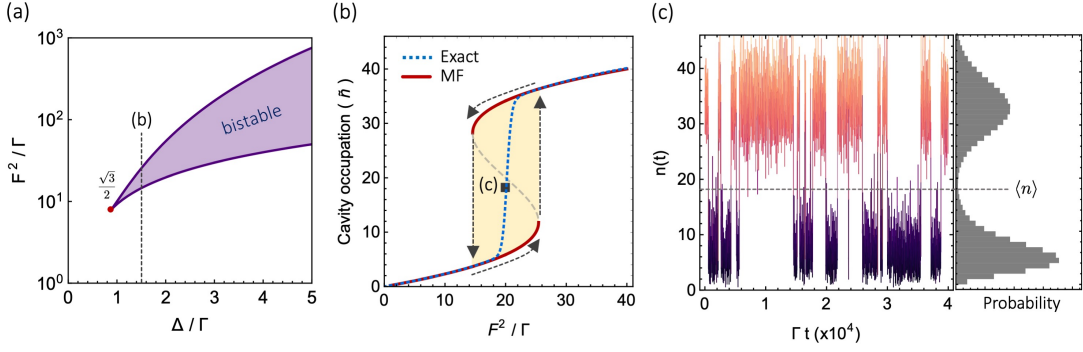


Figure 6.1: **Optical metastability:** (a) Region of the detuning versus input power parameter space supporting an optical bistability according to a mean field (MF) analysis. (b) Steady-state cavity occupation as a function of the input power for a detuning $\Delta/\Gamma = 1.5$. The predictions of both a MF and exact (quantum) treatment of the system dynamics are traced with solid (red) and dashed (blue) lines, respectively; the dashed gray line is an unstable MF solution branch. According to MF prediction, as the input power is swept forward and backward across the bistability region (shaded), an hysteretic behavior of the cavity occupation should be observed (arrows). On the contrary, the exact solution is single valued across at any value of the input power. (c) Calculation of the intracavity field dynamics including vacuum fluctuations for a fixed input power in the bistability region (cf. Sec. 3.3.2). The cavity field displays a slow metastable behavior about the two MF solutions. As $t \rightarrow \infty$, an averaged measurement the population tends to the exact solution. In all the calculations: $U/\Gamma = 0.05$; in panel (c) we set $F^2/\Gamma = 19.7$.

region, we speak of bistability as one of them, satisfying $\tilde{n}_- < \tilde{n} < \tilde{n}_+$ is found to be (single-mode) unstable according to a linear stability analysis (cf. Sec. 3.3.1). In Fig. 6.1-(b), we plot the steady-state cavity occupation (\tilde{n}) obtained from Eq. (6.2) as a function of the input photon rate \mathcal{F}^2/Γ for a constant value of the detuning $\Delta/\Gamma = 1.5$ and for $U/\Gamma = 0.05$. Stable solutions are traced with solid red lines, whereas the unstable one is dashed in gray. According to this MF analysis, for an input photon rate between 14Γ and 25Γ , we can observe the presence of a bistable behavior of the intracavity field. If we adiabatically increase the input power, the system can be continuously steered along the lower branch of the bistability, until the turning point $\tilde{n} = \tilde{n}_-$, where we cavity occupation abruptly jumps to the upper branch. Similarly, reversing the protocol, the system follows the upper branch until $\tilde{n} = \tilde{n}_+$ where it switches back to the lower branch. For the same drive power, the system can be either in the lower or upper branch, depending on the history of the drive protocol. Thus, upon cycling the input power across the bistability region, one observes an hysteretic behavior of the cavity field, see the arrows in Fig. 6.1-(b).

We want now to compare the MF results with the exact quantum solution of the problem. We start by considering the driven Kerr resonator hamiltonian. In the frame rotating at the pump frequency ($\Delta = \omega - \omega_0$)

$$\mathcal{H} = \Delta a^\dagger a + \frac{U}{2} a^\dagger a^\dagger a a + i\sqrt{\Gamma/2}\mathcal{F}(a^\dagger - a) \quad (6.4)$$

here, a^\dagger and a are the ladder operators creating or destroying an excitation in a mode

of the resonator and obey bosonic commutation rules. Losses couple the resonator to the environment, thus we need to describe the dissipative dynamics of the system via a Lindblad master equation. Since we will be interested in optical resonators operated at cryogenic temperatures ($k_B T \sim 0.4$ meV), we can neglect the number of thermal excitations at the resonance frequency ω_0 . We can therefore treat the environment as an (effectively) zero temperature bath, i.e. there is no flux of energy from the environment to the system, see Sec. 2.4.4 for details. Taking into account only single particle losses and denoting ρ the system density matrix, the Lindblad master equation reads

$$\partial_t \rho = \mathcal{L}\rho = -i[\mathcal{H}, \rho] + \frac{\Gamma}{2} \left(2a\rho a^\dagger - a^\dagger a \rho - \rho a^\dagger a \right) \quad (6.5)$$

where \mathcal{L} is the Liouvillian superoperator. The steady-state density matrix $\tilde{\rho}$ satisfies $\partial_t \rho|_{\tilde{\rho}} = 0$: we can write in a truncated Fock basis the right hand side of Eq. (6.5) in a matrix form (cf. Sec. 3.3.3), solve the eigenvalue problem $\mathcal{L}\rho = \lambda\rho$ and find the density matrix $\tilde{\rho}$ associated to the $\lambda = 0$ eigenvalue. Once $\tilde{\rho}$ is determined, the steady-state expectation values of an observable \mathcal{O} can be calculated as $\langle \mathcal{O} \rangle = \text{Tr}(\tilde{\rho}\mathcal{O})$. In Fig. 6.1-(b), we use this method to trace the expectation value of the cavity occupation as a function of the input power (dashed blue line): we can observe that this time $\langle \tilde{n} \rangle$ is unique at any value of \mathcal{F}^2 . Importantly, with a refined calculation Drummond and Walls obtained in 1980 an exact expression for the dissipative Kerr resonator model and demonstrated that the steady state is unique at any point in the parameter space [225], in stark contrast with the MF prediction.

A priori, one could assume that the (exact) quantum treatment yields the most accurate result when compared to experiments, since MF relies on some approximations. However, optical bistability has been reported in a variety of systems and configurations both in the dispersive and absorptive regime [382, 383, 384, 385, 386, 135].

In 1978 Bonifacio and Lugiato already speculated on this apparent contradiction, noticing that fluctuations of the intracavity field (quantum or classical), can render the mean-field steady states metastable [377, 387, 388], so that the unique steady-state corresponds to their average. In their analysis, the authors point out that the average time spent by the system in vicinity of one of the two metastable solutions may become astronomically long. Indeed, pioneering experiments in the 1980s with two-mode lasers, evidenced extremely long times between two consecutive switching events [226]. The timescale associated to the metastable dynamics was predicted to rapidly diverge for weak fluctuations and/or large photon numbers [378].

To illustrate the metastable behavior of the system, we plot in Fig. 6.1-(c) one realization of the intracavity field dynamics for a fixed value of the input power within the MF bistability region. In this calculation, we evolved the cavity field according to the Langevin equation associated to a truncated Wigner approximation (cf. Sec. 3.3.2). We can observe that the cavity occupation fluctuates over short timescales around one of the two MF steady state values; from time to time, over a much slower timescale we call τ_R , a switching event is triggered. Notice that here τ_R is of the order of 10^3 times the cavity lifetime, even if the average occupation number is comparable with the fluctuation amplitude ($\Delta/\Gamma = 1.5$, $U/\Gamma = 0.05$).

The observation of bistability and of a finite hysteresis area when sweeping the input power is therefore a matter of competing timescales. On the one hand, an averaged measurement of the cavity occupation over a timescale much longer than τ_{sw} yields a

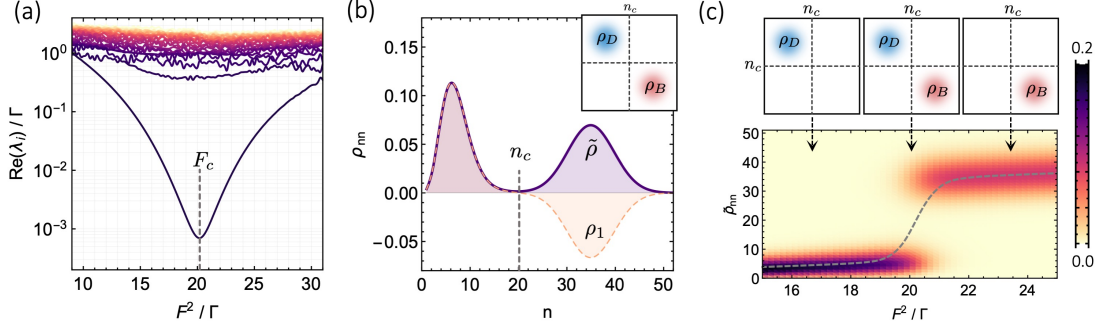


Figure 6.2: **Spectral properties of the Liouvillian:** (a) Real part of the first thirty eigenvalues of the liouvillian superoperator \mathcal{L} as a function of the drive amplitude F . (b) Diagonal elements of the steady-state density matrix $\tilde{\rho}$ and of ρ_1 , associated to the smallest non zero eigenvalue λ_1 of \mathcal{L} . Inset: illustration of the interpretation of the bimodality of $\tilde{\rho}$ as a statistical admixture of ρ_D and ρ_B related to the projections of ρ_1 on the subspaces $n < n_c$ and $n > n_c$, respectively. (c) Evolution of the stationary cavity occupation probability ($\tilde{\rho}_n n$) with the input power across the metastability region. Inset: illustration of the transition from the "dark" state (ρ_D) to the "bright" (ρ_B), trough a coexistence at the critical point $\mathcal{F} = \mathcal{F}_c$. Simulation parameters: $U/\Gamma = 0.05$, $\Delta/\Gamma = 1.5$, Fock-space cutoff $n_{cut} = 100$.

single value $\langle n \rangle$, irrespectively of the initial state, as predicted by the quantum solution. On the other hand, if τ_{sw} substantially exceeds the timescale over which we perform the experiment, the cavity population has not enough time to switch between the two metastable branches. In the latter case, the system effective behavior is bistable, displaying an hysteretic response when cycling the input power.

Risken, Vogel and collaborators first investigated this metastable dynamics for a dispersive Kerr nonlinearity in the late 1980s [227, 389, 390]. Their analysis relies on the spectral properties of the Liouvillian superoperator \mathcal{L} . Indeed, as we anticipated in Sec. 2.4.4, \mathcal{L} can be decomposed in terms of its eigenvalues $0 = \lambda_0 < \lambda_1 < \dots < \lambda_k$ and eigenvectors ρ_k as follows [227]

$$\rho(t) = \tilde{\rho} + \sum_{k \neq 0} c_k(0) e^{-\lambda_k t} \rho_k \quad (6.6)$$

where the coefficients $c_k(0) = \text{Tr}[\rho(0)\rho_k]$ are the projections of the initial density matrix. In their analysis, the authors noticed that in the region where the MF equation predicts a bistable behavior, the second smallest eigenvalue becomes real ($\lambda_1 = \lambda_1^*$) and extremely small, approaching zero for a specific ("critical") value of the drive amplitude, denoted \mathcal{F}_c . Correspondingly, the relaxation dynamics towards the steady state is extremely slow. Moreover, as $\lambda_1 \ll \lambda_2 < \dots < \lambda_k$ and $\lambda_k \sim \Gamma$ for $k \neq 0, 1$, after a few cavity lifetimes the relaxation is governed only by λ_1 , thus defining the asymptotic decay rate of the system. As an example, in Fig. 6.2-(a) we trace the real part of the smallest 30 eigenvalues of the Liouvillian as a function of input power ($\lambda_0 = 0$ is not shown) for the same parameters of Fig. 6.1-(b). When $\mathcal{F}^2 \rightarrow \mathcal{F}_c^2 \approx 20\Gamma$ we can observe that $\text{Re}(\lambda_1)/\Gamma \rightarrow 7 \cdot 10^{-4}$, meaning the inverse of the asymptotic decay rate exceeds by three orders of magnitude the cavity lifetime ($\tau = \hbar/\Gamma$). Interestingly, this value is comparable with the typical timescale of metastable dynamics presented in Fig. 6.1-(c).

This is not a coincidence, indeed in vicinity of \mathcal{F}_c , the separation of timescales allows to approximate Eq. (6.8) for $\Gamma t \gtrsim 1$ with

$$\rho(t) \approx \tilde{\rho} + c_1(0)e^{-\lambda_1 t} \rho_1 \quad (6.7)$$

furthermore, λ_1 is real implying that ρ_1 is hermitian [204]. Since the master equation (6.5) by construction preserves the trace of $\rho(t)$ at any time [199] and $\text{Tr}(\tilde{\rho}) = 1$, it follows $\text{Tr}(\rho_1) = 0$ which means that for some $n < n_c$ (respectively $n > n_c$) the diagonal elements of ρ_1 will assume positive (respectively negative) values, see Fig. 6.2-(b). This allows writing $\rho_1 \propto (\rho_D - \rho_B)$ as a superposition of density matrices representing the high density or "bright" (ρ_B) and low density or "dark" (ρ_D) branches of the metastability. We can rewrite Eq. (6.8) as [227, 204]

$$\rho(t) \approx \tilde{\rho} + e^{-\lambda_1 t} [p \rho_D - (1 - p) \rho_B] \quad (6.8)$$

where p corresponds to the inner product of ρ_D with the steady state density matrix. Expanding Eq. (6.8) for small time increments, one can equivalently cast it in terms of a two state rate equation for the probabilities of being in the "bright" (p_B) or "dark" (p_D) metastable branch [227, 391]

$$\begin{pmatrix} \dot{p}_D \\ \dot{p}_B \end{pmatrix} = \begin{pmatrix} -\Gamma_{D \rightarrow B} & \Gamma_{B \rightarrow D} \\ \Gamma_{D \rightarrow B} & -\Gamma_{B \rightarrow D} \end{pmatrix} \begin{pmatrix} p_D \\ p_B \end{pmatrix} \quad (6.9)$$

with $\Gamma_{i \rightarrow j} = 2\tilde{\lambda}_1 \tilde{p}_j$, $\tilde{p}_j = \text{Tr}(\rho_j \tilde{\rho})$ and $\tilde{\lambda}_1 = \lambda_1|_{\mathcal{F}_c}$. In Fig. 6.2-(c) we map the diagonal values of $\tilde{\rho}$ as a function of the input power across the MF bistability region. We observe that if $\mathcal{F} < \mathcal{F}_c$ one finds $\tilde{p}_D \approx 1$ (i.e. $\tilde{\rho} \approx \rho_D$) while $\tilde{p}_B \approx 1$ for $\mathcal{F} > \mathcal{F}_c$. At the critical drive amplitude ($\mathcal{F} = \mathcal{F}_c$) we have $\tilde{p}_D = \tilde{p}_B = 1/2$, $\Gamma_{i \rightarrow j} = \Gamma_{j \rightarrow i} = \tilde{\lambda}_1$ and we can interpret the bimodal $\tilde{\rho}$ as a statistical admixture of ρ_D and ρ_B .

6.1.2 The relation with dissipative phase transitions

The coexistence of two metastable states or "phases", in concurrence with a critical slowing down of the dynamics, has been related to the onset of a first-order phase transition since the early works on two-mode lasers [392, 378, 379]. One everyday example of a first order phase transition is the boiling of water: heating the liquid (phase 1) brings it to its critical temperature T_c , where it starts simmering and producing steam bubbles (phase 2) which coexist with the liquid. The liquid evaporates completely only after the system has received all the latent heat necessary for the phase transition and, during the coexistence of the phases, temperature is constant ($T \approx T_c$). As the two phases share the same symmetry (roto-translational invariance), the transition is first-order and the latent heat corresponds to the discontinuity in the derivative of the free entropy as a function of temperature, see Fig.6.3-(a) and [393, 394].

There are two significant differences in our system. First, the number of thermal excitations for a cavity operating at optical frequencies is negligible (cf. Sec. 2.4.4). In absence of thermal fluctuations, phase transitions are driven by quantum fluctuations. In this regime, the thermodynamics and dynamics of the system are inextricably mixed and phase transitions can be understood in terms of competing ground state phases

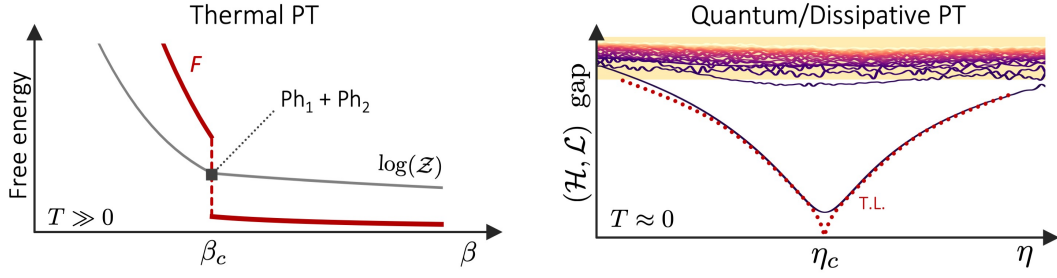


Figure 6.3: **Phase transitions classification:** (a) For a thermal system the equilibrium state is a Gibbs state minimizing the free energy. A non analytic behavior in one or all the moments of the generating function $\log(\mathcal{Z})$ (\mathcal{Z} is the canonic partition function) indicates the onset of a thermal phase transition (here, first order). (b) At zero temperature, quantum (dissipative) phase transitions are associated to the vanishing spectral gap between the groundstate (steady-state) and first excitation of the operator generating the dynamics of the observables. Here, η parametrizes some externally controlled parameter in \mathcal{H} or \mathcal{L} .

[395, 396, 397]. Second, the system dissipates energy/particles in the environment while, at the same time, it can be driven by some external source. The combination of these two competing mechanisms generally drives the system to a non-equilibrium steady-state. If such non-equilibrium steady-state suddenly changes after one parameter is smoothly modified, one speaks of a dissipative phase transition (DPT) [193, 196, 230, 398, 399].

Quantum phase transitions are revealed by clear spectral signatures either in the hamiltonian or liouvillian operator ruling the system dynamics. More specifically, for isolated systems, phase transitions are characterized by a vanishing of the energy gap (Δ) between the groundstate and some excited state as one parameter (η) of the system is adiabatically changed. Indeed, as long as the Hamiltonian (\mathcal{H}) of the system is gapped, any smooth change of η will leave the system in the groundstate, i.e. in the same phase. On the contrary, if Δ vanishes for some value of η , any perturbation or fluctuation in the system may drastically change its properties as two ground state phases compete [396]. For an open system the dynamics is governed by the Liouvillian superoperator \mathcal{L} . One can apply the same reasoning upon replacing \mathcal{H} with \mathcal{L} and the energy gap with the asymptotic decay rate (ADR). When the smallest non-zero eigenvalue of \mathcal{L} vanishes the ADR diverges and the dynamics is critically slowed down. The connivence of this "soft" excited mode with the steady-state gives then rise to a DPT [193, 230, 392]. We schematically illustrate this general picture in Fig. 6.3-(b). Notice that finite size effects, a reduced dimensionality and/or disorder can prevent the full closure of the gap [197, 229].

DPTs are much less explored than quantum phase transitions in isolated systems. Moreover the dissipative coupling to the environment offers the possibility of observing and stabilizing critical effects non-destructively [335, 400]. From the theoretical point of view, the development of a general framework for DPTs is an ongoing work. Analog photonic platforms, being inherently lossy, are especially suited for the exploration of DPTs: first reports for cavity systems endowed with a dispersive nonlinearity recently appeared [231, 401, 402].

In summary, through the last pages, we have seen that the two stable branches of solutions characterizing the optical bistability of a Kerr resonator, become metastable due to intrinsic fluctuations of the intracavity field. For specific driving conditions, the metastable dynamics becomes extremely slow; correspondingly, the density matrix of the system displays bimodality, describing the statistical admixture of two states. Then, we related these two features to the physics of dissipative phase transitions. More specifically, it has been shown that the driven Kerr resonator displays a first order dissipative phase transition when the cavity occupation at the critical driving condition (n_c) tends to infinity [230]. Although the $n_c \rightarrow \infty$ limit cannot be practically accessed, W. Casteels and coworkers proposed a protocol to retrieve the critical exponents of the DPT using dynamical hysteresis experiments [380]. In a nutshell, we concluded Sec. 6.1.1 observing that the measurement of a finite hysteresis area is conditioned by the competition between two timescales: the one of the metastable dynamics and the period of the power modulation protocol. The scaling of the hysteresis area as a function of the driving conditions can thus be used as a probe of the critical slowing down of the resonator dynamics. We pursue this proposal in the following.

6.2 Probing a dissipative phase transition

In this section, we present dynamical hysteresis experiments inspired by the theoretical proposal of W. Casteels and coworkers [380]. In these experiments we need to work with a single mode of the electromagnetic field. To this aim we consider a rectangular micropillar with $4.4 \mu\text{m}$ and $2.2 \mu\text{m}$ sides. In this structure the two lowest eigenmodes are *s*-type, well separated in energy and present orthogonal linear polarizations. The lowest energy one, called hereafter TE, is linearly polarized with an axis parallel the long side of the rectangular section, see inset in Fig. 6.4-(a). The other mode (TM) is higher in energy and its separation increases as the pillar size decreases.

6.2.1 Characterization of the microcavity

As a first step, we characterized the linear response of the microstructure with a resonant spectroscopy experiment. For the optimization of the excitation coupling and polarization we followed the protocol described in Sec. 5.2.2. In the experiment we scan the wavelength of a weak excitation laser ($P \sim 100 \text{ nW}$) while recording CCD images where the transmitted and reflected patterns are simultaneously imaged. Upon knowing the difference between the collection efficiency along the transmitted and reflected beam path, the measurement is self-calibrated. From the images, we retrieve the transmission \mathcal{T} and reflection \mathcal{R} coefficients as a function of the laser frequency; the result is shown in Fig. 6.4-(a). A joint fit with two Lorentian profiles allows retrieving the polariton linewidth $\Gamma = 32.3(4) \mu\text{eV}$, the resonance energy $E_0 = 1451.728(1) \text{ meV}$ and the peak transmission and reflection coefficients $\mathcal{T}_0 = 0.45(1)$ and $\mathcal{R}_0 = 0.21(1)$, respectively. With a similar measurement for the TM mode (not shown) we determined its energy separation relative to the TE mode $\Delta E \approx 0.11 \text{ meV}$, significantly larger than the linewidth of both resonances.

In Fig. 6.4-(b) we show the transmitted intensity pattern at resonance. The absence of stray light outside the pillar edge (dashed line) suggests that the excitation spot was efficiently coupled to the TE mode. From this pattern we can also extract the

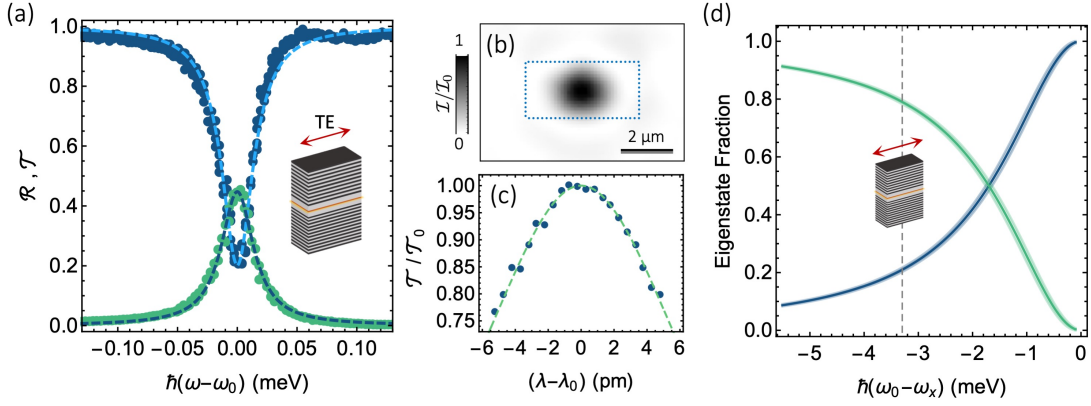


Figure 6.4: **Characterization:** (a) Reflection and transmission spectra of the lowest energy eigenmode of a $(4.4 \times 2.2) \mu\text{m}$ rectangular micropillar measured with a resonant spectroscopy experiment (symbols). Dashed lines: best fit with a Lorentzian profile, we obtain the linewidth $\Gamma = 32.3(4) \mu\text{eV}$, reflection $\mathcal{R}_0 = 0.21(1)$ and transmission $\mathcal{T}_0 = 0.45(1)$ coefficients at resonance. Inset: sketch of the microstructure, the arrow indicates the linear polarization of the excitation. (b) Transmitted intensity pattern at resonance; dashed line: edge of the microstructure. (c) Refinement of the transmission spectrum close to resonance, we get $\lambda_0 = 853.0651(2) \text{ nm}$. (d) Eigenstate fraction as a function of the detuning of the lower polariton relative to the exciton ($E_x = 1455.02(2) \text{ meV}$) determined from a fit of the polariton dispersion relation (cf. Sec. 5.2). From this calibration we obtain $|X|^2 = 0.21(1)$; confidence intervals (2σ) are shaded with lighter colors.

modal area $\mathcal{A} \approx 4.5 \mu\text{m}^2$ (finite element simulations for the nominal structure yield $\mathcal{A}^{th} = 4.4 \mu\text{m}^2$). A precise determination of the detuning of the driving field with respect to the TE resonance is important for nonlinear experiments. To this aim we refined the sampling of the resonant spectroscopy experiment in vicinity of E_0 , as shown in Fig. 6.4-(c) and determined the peak wavelength within better than 0.2 pm. In order to extract the exciton and photon fraction of the polariton mode, we measured the polariton dispersion in a neighboring unetched region following the protocol detailed in Sec. 5.2. From the fit of the polariton dispersion (not shown) we get the bare exciton energy $E_x = 1455.02(2) \text{ meV}$, the bare cavity energy $E_c = 1450.04(1) \text{ meV}$, and the normal mode splitting $\hbar\Omega_R = 3.40(4) \text{ meV}$. Using this information, in Fig. 6.4-(d) we plot the eigenstate fractions $|X|^2$ and $|C|^2$ as a function of the detuning of the lower polariton mode relative to the exciton $\Delta_{lx} = \hbar(\omega_0 - \omega_x)$. For the TE mode $\Delta_{lx} = -3.29(2) \text{ meV}$, which we use to infer the exciton and photon fractions $|X|^2 = 0.21(1)$ and $|C|^2 = 0.79(1)$, respectively. Using an exciton interaction constant $g_{xx} \sim 30 \mu\text{eV} \mu\text{m}^{-2}$ (cf. Sec. 5.2.3 and refs [55, 54]) we can roughly estimate the polariton-polariton interaction constant to be $U/\Gamma \sim 0.01$.

Finally, we can derive from the polariton linewidth Γ and \mathcal{T}_0 the relative weight of the radiative and non-radiative loss mechanisms. We can start from the characterization of Γ as a function of Δ_{lx} presented in Sec. 3.2.2. Using the best fit of Eq. (3.1) obtained with those experiments, we conclude that the contribution due to the inhomogeneous broadening of the exciton is negligible at the TE resonance. Therefore we can write $\Gamma = |C|^2(\gamma_a + \gamma_c) + |X|^2\gamma_{nr}$, where γ_c (γ_a) is the cavity radiative decay rate (absorption) and $\gamma_{nr} \approx 16 \mu\text{eV}$ represents the exciton non-radiative decay (see Sec. 3.2.2). Using

the relation $\mathcal{T}_0 = (\gamma_c/\Gamma)^2$ we can deduce $\gamma_c \approx 22 \mu\text{eV}$ and $\gamma_a \approx 15 \mu\text{eV}$. Using this information, one similarly has $\mathcal{R}_0 = (1 - \gamma_c/\Gamma)^2 \approx 0.11$, comparing this estimate with the measured value we get the input-coupling efficiency $C_{eff} \approx 0.89$.

6.2.2 Dynamical hysteresis experiments

To reveal any hysteretic behavior of the microcavity, we need to perform an input-output power measurement while the power of the excitation laser is cycled across the metastability region. Indeed, the transmitted optical power is proportional to the instantaneous cavity occupation $n(t)$, possibly assuming different values in the increasing and decreasing power ramps. If we denote n_F and n_B the average cavity occupation measured for the same power in the increasing and decreasing part of the power modulation cycle, a finite hysteresis is observed whenever $n_F \neq n_B$. Furthermore, we want to explore how the hysteresis area changes as a function of the speed of the input power modulation cycle.

The experimental arrangement is rather simple: we use a single mode CW laser to excite the micropillar cavity near resonance. The laser power can be modulated using an amplitude electro-optical modulator (EOM) driven by an arbitrary function generator. Part of the incident power and the transmitted intensity are monitored by two fast Silicon photodiodes, see Fig. 6.5-(a). The photodiodes have a 60 MHz bandwidth and a measured quantum efficiency $\mathcal{Q} \approx 0.76$. Given the estimated nonlinear constant is $U/\Gamma \sim 0.01$, we expect nonlinear effects to occur already with sub- μW output powers. For this reason the output detector operates in the avalanche regime with a multiplication factor $M = 43.6(8)$. By characterizing the losses along the excitation and collection beam paths, calibrating the photodiode preamplifier I-V characteristics, and using the input-output relations described in the previous section, we deduce the input photon rate \mathcal{F}^2 and the cavity occupation n as a function of time from the two PD readouts. The photodiodes and function generator signals were all readout using a Lecroy WavePro-7Zi oscilloscope. The three voltage traces were synced to better than 0.5 ns using a Lissajous method.

Fig. 6.5-(b) shows representative single-shot trajectories of the cavity occupation (n) acquired while ramping the pump power upward (FW) or downward (BW) following a triangular ramp with period $\tau_{Sw} = 0.5 \text{ ms}$ ¹. In this experiment, the power sweep is much slower than the asymptotic decay rate of the system, therefore we can clearly observe stochastic jump events between the "dark" and "bright" metastable states. As a result, when we average over many trajectories the hysteresis cycle is barely visible (dashed line).

Let us now consider an averaged measurement of the cavity occupation as a function of the input power for different values of the sweeping time τ_{Sw} and detuning Δ . In Figure 6.5-(c) we show a measurement of the hysteresis cycle experienced by the average cavity population when the triangle wave modulation period ranges between 0.03 ms and 0.86 ms, for a constant laser detuning $\Delta/\Gamma = 1.13$. For the faster sweeps (blue line) a finite hysteresis area can be observed, meaning that the switching rate between the metastability branches is comparable or slower than τ_{Sw} . Upon increasing

¹Notice that the input photon rate (\mathcal{F}^2/Γ) has been corrected for the coupling efficiency and absorption. This means that from the plots one can deduce the transmission coefficient of a corresponding absorption-less cavity by dividing the y -axis by twice the x -axis of the plots ($\mathcal{T} = \Gamma n/2\mathcal{F}^2$).

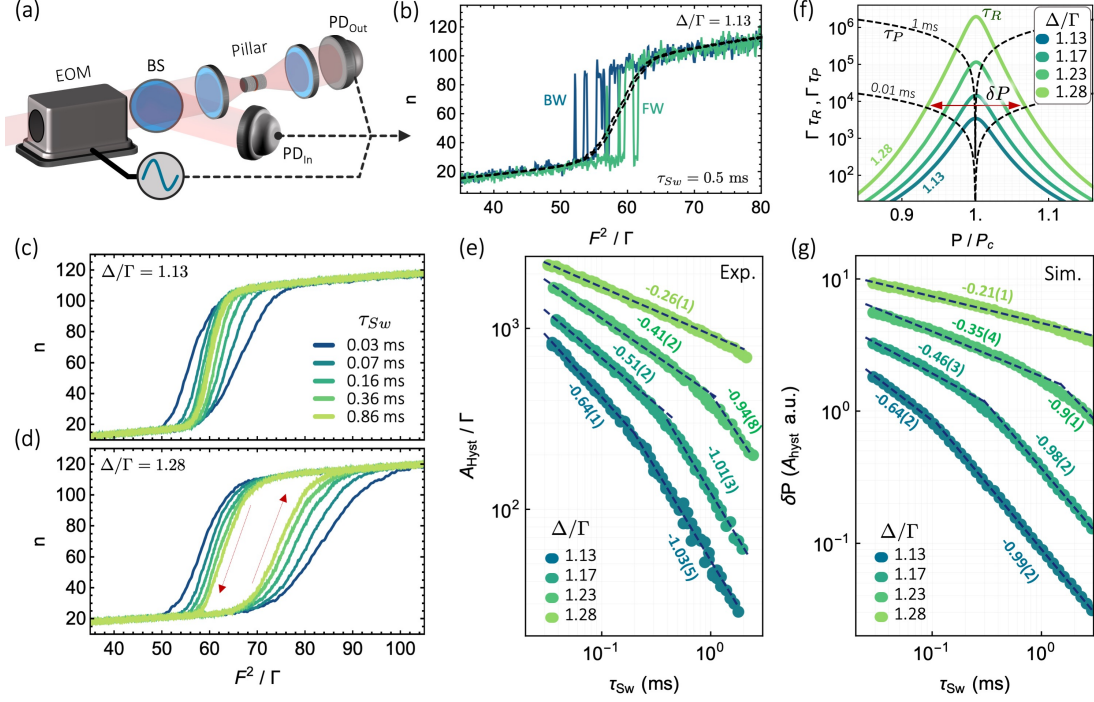


Figure 6.5: **Dynamical Hysteresis:** (a) Sketch of the experimental setup. (b) Example of single-shot (solid lines) and averaged (dashed line) trajectories of the cavity occupation (n) as a function of the input power (F^2/Γ). Here, the power is modulated with the EOM following a triangle-wave with period $\tau_{Sw} = 0.5$ ms. FW (BW) refers to the trajectory associated to an increasing (decreasing) side of the power ramp. (c,d) Hysteresis cycles obtained averaging over 10^3 trajectories as a function of the modulation period τ_{Sw} for two detuning values (see the inset). (e) Measured average hysteresis area as a function of the modulation period. Different colors correspond to different detuning values (see the inset). Dashed lines are power law fits whose exponents are reported along with 2σ confidence intervals. (f) Calculation of the relaxation (τ_R , solid lines) and modulation (τ_P , dashed lines) timescales: the intersection of τ_R with τ_P determines the non-adiabatic power region δP proportional to the hysteresis area (see main text). (g) Scaling of the calculated δP with τ_{Sw} for the same parameters of the experiments. Dashed lines are power-law fits.

τ_{Sw} the hysteresis cycle progressively vanishes. For the slowest sweep, the averaged cavity occupation trajectory closely resembles the steady-state prediction obtained via the quantum master equation (see Fig. 6.1-(b), dashed blue line). If we now repeat the experiment keeping the same power ramps, but we increase the laser detuning to $\Delta/\Gamma = 1.28$, the hysteresis area again decreases when increasing τ_{Sw} , but not as fast, see Fig. 6.5-(d). In particular, even for the slowest modulation time ($\tau_{Sw} = 0.86$ ms) the hysteresis area is non vanishing. Since the hysteresis area closes only in the limit where the modulation period τ_{Sw} is much slower than the metastability characteristic time τ_R , these measurements suggest that τ_R increases with detuning. From Fig. 6.5-(c,d) we can see that the hysteresis cycle shifts to larger input powers as Δ increases, so does average cavity occupation. The increase of τ_R with Δ is thus consistent with the fact that the stochastic jumps are triggered by fluctuations, whose relative amplitude is suppressed as the number of excitations in the system increases [227, 230]. We will

address the scaling of τ_R with Δ in the next section. Here we focus on a systematic characterization of the scaling properties of the average hysteresis area as a function of the modulation period. To this aim, we fed to the EOM a customized succession of triangle waves with constant amplitude and log-spaced periods ranging between 0.03 ms and 2.3 ms. The input and output power traces were averaged over $2 \cdot 10^3$ realizations. From each trace we can compute the hysteresis area using

$$A_{hyst} = \int_0^{\tau_{Sw}} n(t) \dot{P}(t) dt \quad (6.10)$$

where $P(t) \equiv \mathcal{F}^2(t)$ and used a Simpson rule to compute the integral over the digitized values of the trajectory. Figure 6.5-(e) presents the result of the analysis for four different detuning values (see the inset). For the smallest detuning ($\Delta/\Gamma = 1.13$) the hysteresis area scales with the modulation period τ_{Sw} following two distinct power laws, as predicted in refs. [380, 403]. A fit allows us to extract the exponents $\alpha = -0.64(1)$ for $\tau_{Sw} \lesssim 0.2$ ms and $\beta = -1.03(5)$ for $\tau_{Sw} \gtrsim 0.2$ ms. The latter exponent is in agreement with the -1 value predicted for the long-time decay of the hysteresis area, results from quantum fluctuations and is expected to be universal [230]. The first exponent (α) in general is not universal and depends on the specific driving conditions and cavity parameters. In particular, it is also present in the absence of fluctuations as it originates from the drag exerted by a rapid power sweep on the upward and downward edges of the MF bistability [404]. As we increase the detuning, we observe the onset the power-law with -1 exponent for larger and larger values of τ_{Sw} . For $\Delta/\Gamma = 1.28$, the -1 power law sets in beyond our observation window. In order to further elucidate the relation between the double power law-scaling of the hysteresis area and the characteristic timescale of the metastable dynamics, we want to model these results.

One possible approach could be to numerically integrate the stochastic evolution of the cavity occupation using the truncated Wigner equation described in Sec. 3.3.2. However, this is both computationally intensive² and does not give a very deep insight on the physics. We can alternatively use the scaling analysis proposed by W. Casteels and collaborators in ref. [380]. It relies on the determination of the region where the system response is non-adiabatic in the spirit of the Kibble-Zurek mechanism for dynamical phase transitions [405]. In this analysis, we compare the response time of the system (τ_R) with the timescale associated to the power modulation (τ_P). The former (τ_R), corresponds to the inverse of the lowest non-zero eigenvalue (λ_1) of the Liouvillian superoperator (\mathcal{L}), i.e. $\tau_R = \text{Re}(\lambda_1)^{-1}$. The latter (τ_P), is given by the inverse of the normalized sweep rate: $\tau_P = \tau_{Sw} |P - P_c| / 2\Delta P$, where P_c is the critical drive power and ΔP is the modulation amplitude. The region of input powers where $\tau_R > \tau_P$ determines the region where the system responds non-adiabatically to the modulation.

In Fig. 6.5-(f) we trace the relaxation timescale τ_R as a function of the input power for the four detuning values corresponding to the experiments in Fig. 6.5-(e). To calculate τ_R we diagonalize the Liouvillian in a truncated Fock basis (cf. Sec. 3.3.3) to get the second smallest eigenvalue λ_1 , whose inverse defines τ_R . The model parameters are fixed by the characterization presented in the previous section (Sec. 6.2.1). We observe

²Each trajectory is 50 ms long, or 10^9 polariton lifetimes. Then one needs $\sim 10^3$ realizations and, for numerical convergence, the integration time-step should be such that $\Gamma\delta t \sim 10^{-2}$. Putting these numbers together, one needs to generate 10^{14} integration steps: roughly a dozen hour computational overhead over a 32-node cluster with a high performance C++ routine.

that $\tau_{R,c}$ grows with Δ , consistent with the scaling properties of the hysteresis area. The dashed lines in Fig. 6.5-(f) correspond to the modulation timescale τ_P , evaluated for $\tau_{Sw} = (0.01, 1)$ ms: we denote δP the input power range where the diabatic condition ($\tau_R > \tau_P$) is met. Within this region, the system does not have time to relax, the metastable dynamics can be neglected, thus one effectively observes a bistable behavior of the cavity occupation. Then, one can show³ that $\delta P \propto A_{hyst}$. Figure 6.5-(g) shows calculations of δP for the same detuning and sweep times considered in the experiments. The calculated values of δP fairly reproduces the scaling of experimental results. The small discrepancy between the calculated and experimental α exponents can be ascribed to the relatively large uncertainty we have in the estimate of U . Indeed, as α appears to be non-universal, it may depend on specific values of the microcavity parameters.

Overall, Fig. 6.5 demonstrates that for a given detuning and nonlinear constant relative to the mode linewidth, one can define a response time for the system at each driving power. When performing a dynamical hysteresis experiment two limiting situations can be defined: 1) when the response time is much faster than the duration of the experiment, the system responds quasi-adiabatically. The hysteresis area becomes vanishingly small as it diminishes in proportion to the number of switching events between the metastable branches, occurring at a $\tau_R^{-1} \gg \tau_P^{-1}$ rate. 2) When the response time is much slower than the duration of the experiment, switching events are inhibited, the averaged hysteresis area is finite. The scaling of the hysteresis area with the period of the power modulation cycle (τ_{Sw}) follows double power law, whose critical exponents capture the dynamical properties of the systems in the above two limiting cases. In particular, when the response of the system is quasi-adiabatic one finds a universal exponent $\beta = -1$, whereas for diabatic modulation protocols one finds a non-universal exponent $\alpha > -1$.

We have also deduced from the scaling of the hysteresis area that τ_R grows rapidly with Δ . Indeed, already for a detuning as small as 1.28 cavity linewidths (~ 23 pm), we could not observe anymore the onset of the -1 power law exponent within our observation window: this entails $\tau_R \sim \tau_{Sw} \sim$ ms, exceeding by orders of magnitude the polariton lifetime ($\hbar/\Gamma \sim 20$ ps). Eventually, if one keeps increasing Δ , i.e. the average photon number within the hysteresis cycle, the relaxation time τ_R exceeds any experimentally accessible timescale. Then, the hysteresis area evolves towards a single power law decay irrespectively of fluctuations. In such "thermodynamic" limit of large photon numbers the metastable dynamics is completely frozen at the critical drive power, signaling the onset of a dissipative phase transition [193, 230]. Such dramatic slowing down of the dynamics has been recently reported in a variety of systems, including driven-dissipative Rydberg gases [406], polariton microcavities [407, 231] and with superconducting microwave resonators [401, 231]. In these first experimental reports the excitations of the system were either fully confined or their kinetic energy was negligible. By studying coupled microcavity arrays it could be interesting to investigate the interplay of an engineered dispersion relation with the metastable dynamics of each resonator.

³In absence of switching events between the metastable branches, the mean field predictions correctly yield the expectation value of the cavity occupation in the forward and backward drive ramp ($n_{F,B}$). If we define $\delta n = |n_B - n_F|$, since $\delta n = 0$ outside a δP -wide window centered around the critical power, the hysteresis area reads $A_{hyst} = \int_0^\infty \delta n(P) dP = \delta P \int_{P_c - \delta P/2}^{P_c + \delta P/2} (\delta n(P)/\delta P) dP = \delta P \langle \delta n \rangle_P$.

6.2.3 Scaling of the tunneling time

In the previous section we have shown that for the same modulation protocol, if we increase the laser detuning, the hysteresis area increases. We qualitatively understood this observation in terms of a slowing down of the metastable dynamics associated to the relaxation timescale τ_R . In this section we want to directly measure the scaling of τ_R with the pump detuning Δ . The idea motivating this analysis is the following: the Kibble-Zurek analysis we used to model the observations in the previous section suggests that the dynamical response of the microcavity is ruled only by a competition of timescales. Therefore, if we characterize the scaling of τ_R as a function of the other parameters $\eta = (U, \Delta)$, the decay of the hysteresis area with the rescaled modulation period $\tau_{Sw}/\tau_R(\eta)$ should collapse onto the same curve, regardless of the specific choice of η . If demonstrated, this kind of scaling analysis would be a useful tool to understand the coarse-grained behavior of DPTs in more elaborate systems, e.g. resonator lattices.

In order to measure the characteristic timescales of the metastable dynamics there are two main possibilities. The first is to directly look at the cavity occupation dynamics at a constant drive power, build a statistics of the time delay within consecutive switching events and then use Eq. (6.9) to deduce τ_R [226, 231]. This intuitive approach, relies on the possibility of having direct access to the cavity occupation dynamics at a single-shot trajectory level. This can be a limiting factor as it imposes a tradeoff between the number of excitations in the cavity and the detection readout bandwidth. A second approach, developed in the group of A. Imamoglu, is based on photon correlation ($g^{(2)}$) measurements [402]. In a nutshell, the detection of a photon correspond to the action of the collapse operator \hat{a} on the cavity, thus projecting the system out of its steady-state, described by the density matrix $\hat{\rho}_{ss}$, into some other state, described by the density matrix $\hat{\rho}'$. If the expectation values $\text{Tr}(\hat{a}^\dagger \hat{a} \hat{\rho}')$ and $\text{Tr}(\hat{a}^\dagger \hat{a} \hat{\rho}_{ss})$ differ, the conditional detection of a second photon can be used to probe the relaxational dynamics of $\hat{\rho}'$ towards $\hat{\rho}_{ss}$. The main advantage of this approach is that it can operate with extremely low photon count rates with a bandwidth limited only by the single photon detector response (typically ~ 50 ps).

In the following we adopt the first strategy as we dealt with manageable average power signals ($\sim 0.2 \mu\text{W}$)⁴. The basic idea of the measurement is that at the critical drive power P_c the stationary probability of finding the system in the dark and bright state are equal $\tilde{p}_D = \tilde{p}_B = 1/2$. Inserting this condition in the two mode model Eq. (6.9), we see that the transition rates between ρ_D and ρ_B are also equal, thus yielding the inverse of the tunneling time [227]. The requirement $\tilde{p}_D = \tilde{p}_B$ is extremely sensitive to power or input coupling fluctuations, therefore we had to elaborate a robust procedure to ensure this condition is met. The idea is simple: we continuously readout the photodiode signal on the oscilloscope and we condition the trigger for the acquisition of a trajectory with the requirement that the median and the average of the voltage signal are equal within a 10^{-2} relative error. A posteriori we could check that this protocol grants on average $\tilde{p}_D/\tilde{p}_B = 1.00(0.03)$ for our system parameters. We acquired (0.1 – 1) ms long trajectories in order to ensure an operation in the shot-noise limited region of the laser intensity power spectrum. Figure 6.6-(a) shows the stochastic dynamics of the microresonator over a 100 μs interval for 10^2 trajectories

⁴We use a the photodiode whose preamplifier bandwidth (BW) is 60 MHz. Since one needs at least three samplings of the signal to define the residential time, our estimate of τ_R^{-1} will be biased below one third of BW. See the gray dashed line in Fig. 6.6.

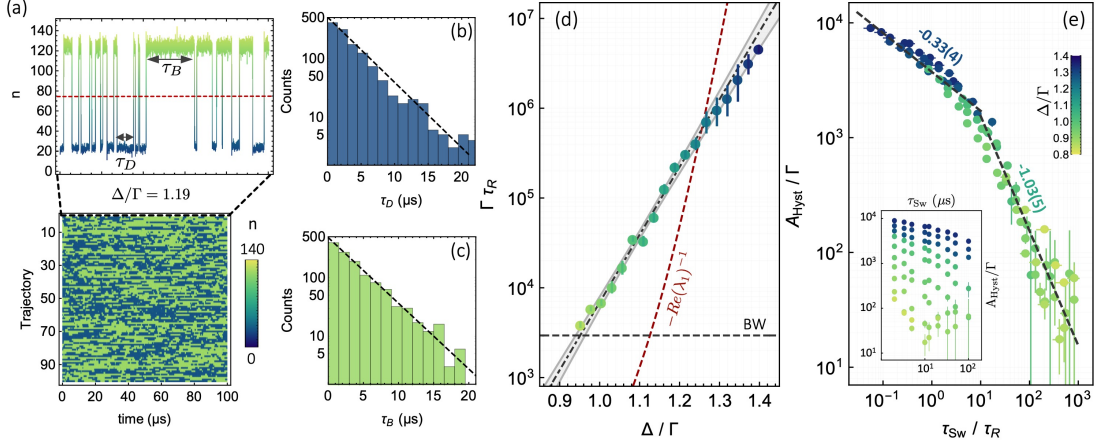


Figure 6.6: **A scaling analysis of the tunneling time:** (a) Stochastic evolution of the cavity occupation (n) as a function of time for a fixed input power $P = P_c$ and detuning $\Delta/\Gamma = 1.19$. The residence times in the dark (bright) metastable state is denoted τ_D (τ_B), the discrimination threshold is dashed in red. (b,c) Histograms of the residence times computed from the 10^2 trajectories elapsing $100 \mu\text{s}$ shown in panel (a). The dashed lines are exponential fits allowing us to retrieve τ_R (see main text and Eq. (6.9)). (d) scaling of the tunneling (or relaxation) time τ_R as a function of the laser detuning. Each data point has been obtained as the weighted average between five measurements as the one shown in panels (a-c). Dot-dashed line: best fit with an exponential, 2σ confidence interval are shaded. Dashed red line: inverse liouvillian gap for $U/\Gamma = 0.01$. (e) Measurement of the average hysteresis area for ten values of the detuning ranging between 0.83Γ and 1.34Γ . For each detuning we use a sine sweep of the input power $P(t) \approx P_c(1 + 0.4 \sin(2\pi t/\tau_{Sw}))$ for nine frequencies $\tau_{Sw}^{-1} = (10 - 500) \text{ kHz}$. All data points collapse onto the same double power law dependence upon rescaling τ_{Sw} for the corresponding tunneling time τ_R . Dashed lines are power law fits; for $\tau_{Sw}/\tau_R \gtrsim 10$ we consistently find the -1 universal exponent.

acquired with this procedure at a detuning $\Delta/\Gamma = 1.19$, the cavity occupation (n) is color coded. Overall, in this set of data, $\tilde{p}_D/\tilde{p}_B = 1.000(4)$. In the inset we show a representative trajectory from the ensemble displaying the characteristic telegraphic signal resulting from the metastability of the non-equilibrium steady state. We use the median between the expectation value of n in the two branches as a threshold to digitize the trajectory (dashed line). This allows defining the residential times $\tau_{D,B}$ for each of the metastable states. From each trajectory we extract $\tau_{D,B}$ and we collect them in two separate histograms, see Fig. 6.6-(b,c). From these histogram we can test two hypotheses. First, assuming a white noise spectrum of fluctuations for the intracavity field and the validity of a two-mode model, the residential time histograms must follow an exponential distribution [408, 409]. In Fig. 6.6-(b,c) the exponential best fits to the histogram (dashed lines) are in good agreement with the data, validating our assumptions. Second, if $\tilde{p}_D = \tilde{p}_B$ it follows from Eq. (6.9) that $\tau_D = \tau_B$, i.e. detailed balance holds at the critical point. From the exponential fits we get $\langle\tau_D\rangle = 3.9(2) \mu\text{s}$ and $\langle\tau_B\rangle = 3.87(6) \mu\text{s}$, thus supporting our hypothesis and the data acquisition protocol.

For each detuning we repeated the analysis presented in Fig. 6.6-(a-c) for five independent datasets. From each dataset we extracted the residential times and the associated statistical errors. We finally estimated a representative $\langle\tau_R\rangle$ as the weighted

average of these values⁵. Figure 6.6-(d) presents the results of this analysis repeated for different values of the laser detuning; error bars represent the weighted standard deviation between the five datasets. We can observe that the tunneling time increases by roughly three orders of magnitude within 0.4 linewidths (~ 8 pm). In Fig. 6.6-(d) we fit the dependence of τ_R as a function of $\tilde{\Delta} = \Delta/\Gamma$ using the empirical formula $\tau_R(\tilde{\Delta}) = \exp((\tilde{\Delta} - \tilde{\Delta}_0)/\beta)$. The best fit (dot-dashed line) is found for $\tilde{\Delta}_0 = 0.49(2)$ and $\beta = 17.4(5)$. From this scaling we can extrapolate that for $\Delta/\Gamma = 2$ the tunneling time becomes of the order of seconds while for $\Delta/\Gamma = 3$ becomes of the order of years. Considering the energy scales we are dealing with, yet for a the small number of excitations in the the microcavity ($\langle n_c \rangle \sim 80$), it not surprising that early works of optical bistability, often operating at $\Delta/\Gamma \gg 1$ and with $\langle n_c \rangle \gg 10^2$, never reported such metastable dynamics.

Although an exponential growth of τ_R with Δ/Γ fairly interpolates all the data points, it does not agree with the expected scaling of the smallest non-zero eigenvalue λ_1 of the Liouvillian superoperator (dashed red line). Some authors questioned the validity of the identification of λ_1 with the switching rate in the regime of small cavity damping ($U, \Delta \gg \Gamma$) [389, 390]. Unfortunately this not seem applicable to our case. Then, we allowed the Liouvillian dissipator to include a small number of thermal excitations (cf. Sec. 2.4.4): it did not improve the agreement with the experimental data. We can get some further physical insight noticing that λ_1^{-1} scales roughly as $\exp((\tilde{\Delta} - \tilde{\Delta}'_0)^2/\beta')$ for some $\tilde{\Delta}'_0$ and β' . The difference in the exponent (2 or 1) in the argument of the exponential is significative. Indeed, if we adopt the spirit of a Kramer's analysis of a brownian particle hopping between the minima of a double well potential (cf. ref [408, 409]), the hopping rate is exponentially suppressed when the ratio of the height of the potential barrier to the variance of thermal fluctuations is linearly increased. Inspecting the unraveling of the Lindblad master equation in terms of a Langevin equation (Eq. (3.13) in Sec. 3.3.2) we see that the noise terms on the field quadratures are additive with a constant variance $\Gamma/2$. Since this noise term produces the $\sim \exp(\tilde{\Delta}^2)$ dependence of λ^{-1} , we can wonder which kind of term would produce a $\sim \exp(\tilde{\Delta})$ scaling in the measured τ_R . If one assumes the validity within a semiclassical picture of the Kramer's analysis, we see that the noise we are looking for needs be multiplicative, with a variance scaling linearly with Δ . Such kind of noise could be for instance produced by excess fluctuations in the phase of the laser field, which can be modeled as a frequency (i.e. detuning) jitter. The inclusion of these terms in the master equation is not straightforward and is an ongoing work, which will hopefully help us solve this issue.

Nevertheless, as we hypothesized that the scaling of the hysteresis area does not depend on the microscopic details of the model, but only on τ_R , which we experimentally characterized, the specific dependence of τ_R with Δ should not matter.

In Fig. 6.6-(e) we present a set of dynamical hysteresis experiment where we modulated the input power according to a sine sweep $P(t) \approx P_c(1 + 0.4 \sin(2\pi t/\tau_{Sw}))$. We repeated the experiment using the same nine values of the modulation frequency $\tau_{Sw}^{-1} = (10 - 500)$ kHz for ten different values of the laser detuning $\Delta = (0.83 - 1.34)\Gamma$. For each modulation and detuning, we calculated the hysteresis area (A_{Hyst}) from the averaged input-output power traces using Eq. (6.10). Rather than plotting A_{Hyst} as a

⁵ If \tilde{p}_D is only approximatively equal to \tilde{p}_B , the best estimate of the tunneling time is $\tau_R = \frac{1}{4} \left(\frac{\tau_D}{\tilde{p}_D} + \frac{\tau_B}{\tilde{p}_B} \right)$, see [227]. This linearization holds only in close vicinity to P_c .

function of τ_{Sw} for each detuning value (see the inset), we divided τ_{Sw} by the measured tunneling time τ_R at the corresponding detuning. Upon performing this scaling, all the data points collapse onto the same double-power law dependence on $\tau' = \tau_{Sw}/\tau_R$. A fit allows retrieving the exponents $\alpha \approx -1/3$ for $\tau' \lesssim 10$ and $\beta \approx -1$ for $\tau' \gtrsim 10$, the latter is again consistent within the uncertainty with the -1 universal exponent predicted in [230]. This experiment enforces the understanding of the scaling properties of the hysteresis area in terms of a competition of timescales. Quite surprisingly, we observe that also in the non-adiabatic power sweep region ($\tau' \lesssim 10$) the data points collapse quite well onto the same power law dependence. Indeed, the exponent α , is in principle non-universal, see Fig. 6.5-(e,g): this scaling analysis suggests that it might be the contrary. Some check whether α depends on the spectral components or amplitude of the modulation is anyway necessary, warranting some further research.

A detailed study of the critical exponents of this dissipative phase transition might help elucidating the relation between metastable phenomena in out-of equilibrium non-linear system and Ising-type systems at equilibrium [195, 410]. As numerical techniques based on the truncated Wigner approximation have been successfully employed to study dissipative phase transition in large ensembles (~ 200) of coupled microcavities [195, 197], it would be interesting to benchmark the scaling analysis proposed in this pages against their predictions. One question I personally find interesting is the following: If we measure locally (on a single resonator) the scaling properties of the tunneling time, what can we say about the scaling of other global properties of the system in vicinity of a dissipative phase transition ?

6.3 A parallel with stochastic thermodynamics

Nonlinear photonic systems experiencing sizable nonlinear effects for few dozens excitations operate in a phenomenologically rich semiclassical regime. Although the spontaneous fluctuations of the intracavity field generally do not produce nonclassical features, they can strongly modify the system dynamics. More specifically, system observables as the cavity occupation, are characterized by probability distributions whose variances and expectation values are roughly of the same order. Moreover, as the system can both dissipate in and receive excitations from the surrounding environment, its dynamics is intrinsically out-of-equilibrium.

This situation is common in several mesoscopic systems and stimulated early works in the 90s to extend the concepts of equilibrium macroscopic thermodynamics to small, out-of-equilibrium systems. For instance, the laws derived for macroscopic systems in the thermodynamic limit, were found to be verified only on average by mesoscopic objects [411]. In a series of seminal works, Gallavotti and Cohen [412], Jarzynski [413] and Crooks [414] derived generalized fluctuation-dissipation relations, transcending conventional linear response theory. Remarkably, these general relations can be formulated in terms of the trajectories the system describes in phase-space and find their roots in the microscopic time-reversal of the dynamics [415, 416, 417]. Stochastic thermodynamics considers an object coupled to a thermal bath, being solely interested in the description of a subset of the degrees of freedom which involves only the object. These degrees of freedom are collective (macroscopic) variables changing only slowly in comparison to some other (microscopic) ones. These fast variables are responsible for the stochastic evolution of the slow variables. The ability to readout the state of the macroscopic variables as a function of time is the only requirement to build a stochastic thermodynamic experiment, even if the microscopic details of the system are unknown.

Pioneering experiments using RNA filaments manipulated with optical tweezers [418], levitated colloidal particles [419, 420], driven two-level systems [421, 422], single-electron boxes [423, 424], optomechanical resonators [425] and superconducting qubits [426] supported these theoretical results (see [427] for a nice review). Quite strikingly, to the best of our knowledge, the experimental implementations and proposals based on photonic systems remain scarce [428], or consider geometries where dissipation plays a marginal role [429]. This seems even more surprising if we think that the noisy signal we record with a photodiode receiving the transmitted light from a cavity is a natural example of stochastic evolution of the collective variables of the system (here, the cavity occupation).

A possible reason behind this scarceness, is the difficulty in the univocal identification of thermodynamic observables describing both the dissipative nonlinear optical system and its bath. Indeed, in most of the above experimental realizations, the stochastic degrees of freedoms are the ones of a physical object. For instance, in such systems the definition of the environment temperature is natural. This is not the case for systems at optical frequencies where the number of thermal excitations can be usually neglected: the environment acts effectively as a zero temperature bath [201]. This limit prevents most of the intuitive parallels with mesoscopic systems connected with a thermal bath, as the classical thermodynamic quantities become singular for $T = 0$. When recovering a full quantum treatment of the optical system, the zero-point fluctuations cure all these divergences [430, 431, 432]. In this picture, fluctuations play the role of

a diffusion term, i.e. of an effective temperature of the bath, whose interplay with the nonlinear dynamics of the resonator may result in exotic features. Descriptions based on the density matrix of the system offer a consistent theoretical framework [430, 433]. However, from the experimental point of view, a full tomographic reconstruction of the density matrix of the systems is challenging. Alternative descriptions in terms of a stochastic unraveling of the master equation recently appeared, but have been applied only to the case of a two-level system [434, 435].

Rather than following a top-down approach relying on the quantum master equation, our initial idea was to start from the semiclassical Langevin equations describing the resonator dynamics in phase-space and to derive an operative definition of the thermodynamic quantities [417]. However, the results we obtained present still some inconsistencies at a theoretical level. We decided to take a step back and map the Kerr resonator to an even simpler and well-known example: a (classical) Logical Bit. In the next pages we will first describe such minimalistic model consisting of a two-state bit subject to random bit-flip events. Then, we will focus on the non-equilibrium entropy production when a periodic modulation of the input power is applied and verify whether an integral fluctuation theorem is verified for our system.

Drawing this parallel between stochastic thermodynamics and highly nonlinear photonic microcavities might pave the way to the exploration of out-of-equilibrium thermodynamics in a scalable and highly tunable platform. Furthermore, photonic platforms allow engineering dissipative couplings with other kind of baths, e.g. parametric or squeezed [335, 430, 436]. This almost unexplored playground for thermodynamics, may prove interesting for testing the ultimate bounds on the efficiency of nanoscale engines [437, 438].

6.3.1 The Logical Bit

In this section, we briefly introduce the idea of mapping the metastable Kerr resonator state to a Logical bit and define the relevant thermodynamic quantities at the single trajectory level. The mapping we propose consists in identifying the two metastable states of the Kerr resonator onto the two states $\sigma \in \{0, 1\}$ of a classical two-level system. To do so, we consider the median of the population at the critical drive strength, denoted n_c , to digitize the trajectory. If the cavity occupation at a given instant of time (n_t) is larger (smaller) than n_c we associate to it the state $\sigma_t = 1$ ($\sigma_t = 0$) of the logical bit. These states have energies $E_{1,0}$, which are eventually time-dependent and can be controlled via an external parameter. In this new picture, the metastable dynamics of the Kerr resonator can be seen as the result of random bit-flip events due to the stochastic interaction of the system with the environment. In the case of the logical bit we can always model the environment as a thermal bath with an effective inverse temperature $\beta = 1/k_B T_{\text{eff}}$, where k_B is the Boltzmann constant. These bit-flip events happen with an average rate Γ_{01} or Γ_{10} for the $0 \rightarrow 1$ and $1 \rightarrow 0$ transitions, respectively and can be time-dependent via some control parameter. We schematically illustrate the mapping in Fig. 6.7. For this toy model, at each time t , the canonical partition function reads

$$\mathcal{Z}(t) = e^{-\beta(t)E_0(t)} + e^{-\beta(t)E_1(t)} \quad (6.11)$$

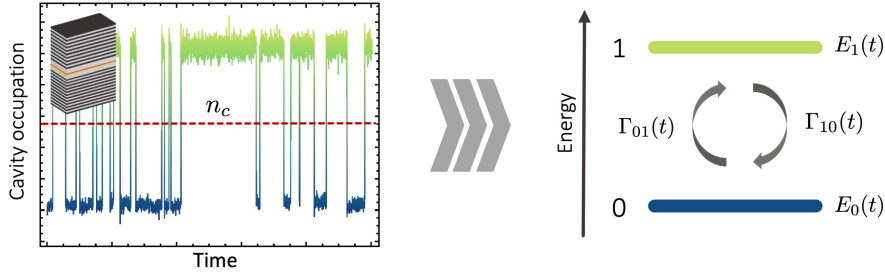


Figure 6.7: **Mapping proposal:** A threshold value of the cavity occupation (n_c) is used to digitize the photodiode signal as a function of time. The dark (bright) metastable states are identified with the $\sigma = 0$ ($\sigma = 1$) states of the bit with energy E_0 (E_1). The contact with a bath results in random bit flip events $0 \rightarrow 1$ ($1 \rightarrow 0$) with a rate Γ_{01} (Γ_{10}).

for some effective inverse temperature β . Since we are considering a two-level system, we can always define the effective inverse temperature via the transition rates between the states. Denoting $\Delta E(t) = E_1(t) - E_0(t)$, we have

$$\beta(t) = \frac{1}{\Delta E(t)} \log \left(\frac{\Gamma_{10}(t)}{\Gamma_{01}(t)} \right). \quad (6.12)$$

Using this relation, the transition rates Γ can be expressed in the form of thermal transition rates $\Gamma_{01} = \gamma \langle n \rangle$ and $\Gamma_{10} = \gamma (\langle n \rangle + 1)$ for the average number of thermal excitations at the transition energy $\langle n \rangle = (e^{\beta \Delta E} - 1)^{-1}$ and spontaneous decay rate $\gamma = \Gamma_{10} / \langle n \rangle$. Notice that the effective temperature defined within this mapping can also take unphysical values, for instance if $\Gamma_{01} > \Gamma_{10}$ follows $T_{\text{eff}} < 0$ and when $\Gamma_{01} = \Gamma_{10}$ the effective temperature of the bath is infinite. For this reason, in the following we consider $k_B = 1$ units, thus β becomes a parameter governing the partition function of the logical bit, but does not have the physical dimension of energy.

Let us now consider an experiment where the stochastic evolution of the system is monitored at a constant rate δt (i.e. the photodiode signal in the oscilloscope). At each sampling of the trajectory we can measure the state of the system, encoded in the vector $\sigma = (\sigma_0, \dots, \sigma_N)$, where σ_0 (σ_N) is the state at $t_{in} = 0$ ($t_{fin} = N\delta t$). Within typical framework of stochastic thermodynamics, heat Q is defined as energy changes of the system induced by the bath, while work W corresponds to energy changes due to the external controlled parameters (acting both on E_i and β). For the logical bit, when considering an infinitesimal temporal increment δt , this means

$$\begin{aligned} \delta Q_k &= [\beta_{k+1} E_{k+1}^\sigma(\sigma_{k+1}) - \beta_{k+1} E_{k+1}^\sigma(\sigma_k)] \\ \delta W_k &= [\beta_{k+1} (E_{k+1}^\sigma(\sigma_k) - \beta_k E_k^\sigma(\sigma_k))] \end{aligned} \quad (6.13)$$

where β_k is the effective inverse temperature at the time $t = k\delta t$ and $E_k^\sigma(\sigma_{k'})$ is the energy of each σ state at the time $t = k\delta t$ evaluated for the state $\sigma_{k'}$. Notice that we generally have to include β_k in the above formulas to account for protocols where the effective temperature of the bath is not constant. The total heat and work received by the system along the trajectory can be computed as the sum over these infinitesimal

increments. One can check for consistency that $W[\sigma] + Q[\sigma] = \beta_N E_N^\sigma - \beta_0 E_0^\sigma = \Delta U$, which is the first law of thermodynamics [434].

In the context of our experiments this might not be the best set of thermodynamic variables to work with. Indeed, the most straightforward control parameter would be the power incident on the resonator. As we have seen in the previous sections this can be directly linked to a change of the tunneling rates $\Gamma_{i \rightleftharpoons j}$ (cf. Sec. 6.1.1). However, in our mapping it is not clear if this also corresponds to an effective modification of ΔE , making the identification of the increments δQ_k and δW_k unclear. In this sense, the definition of entropy for a system presenting discrete states seems more advantageous, as it only relies on the knowledge of the stationary transition rates: a directly measurable quantity which is unambiguously defined. The probability of measuring a given trajectory $\sigma = (\sigma_0, \dots, \sigma_N)$ for a Markovian process is

$$P[\sigma] = P_0(\sigma_0) \prod_{k=1}^N P_k[\sigma'_k | \sigma_{k-1}] \quad (6.14)$$

Here $P_0(\sigma_0)$ is the probability that the system at time $t = 0$ is in the state σ_0 and $P_k[\sigma'_k | \sigma_{k-1}]$ is the conditional probability of finding the system in the state σ'_k at time $t = \delta tk$ knowing that it was found in state σ_{k-1} at the previous sampling of the dynamics. Assuming δt is small compared to the characteristic time where $\Gamma_{i \rightleftharpoons j}$ is changed, one has $P[\sigma' | \sigma] = \Gamma_{\sigma\sigma'} \delta t$ if $\sigma \neq \sigma'$ and $P[\sigma' | \sigma] = (1 - \Gamma_{\sigma\sigma'}) \delta t$ if $\sigma = \sigma'$. If we call $P_r[\sigma_r]$ the probability that the system follows the reversed trajectory $\sigma_r = (\sigma_N, \dots, \sigma_0)$ during the time-reversed transformation of the control parameter, we can define the entropy production as $\Delta s = \log(P[\sigma]/P_r[\sigma_r])$ [381]. Using then Eq. (6.9), one finds that the steady-state probabilities \tilde{P}_σ obey

$$\tilde{P}(\sigma) = \frac{\Gamma_{\sigma\sigma'}}{\Gamma_{\sigma\sigma'} + \Gamma_{\sigma'\sigma}}. \quad (6.15)$$

Inserting these relations in the definition of the entropy production finally yields

$$\Delta s[\sigma] = \log \left(\frac{P_0(\sigma_0)}{P_N(\sigma_N)} \right) + \sum_{k=1}^N \log \left(\frac{\tilde{P}_k(\sigma_k)}{\tilde{P}_k(\sigma_{k-1})} \right). \quad (6.16)$$

We stress that if the system is not in equilibrium at $t/\delta t = 0$ and $t/\delta t = N$ the probabilities in the first (boundary) term are not stationary ones. Nevertheless, by choosing a periodic drive protocol with deterministic and equal initial and final conditions, this boundary term vanishes. This means that we can calculate Δs using only the knowledge of the stationary probabilities \tilde{P} and of the state σ at each instant of time.

Using these definitions we want now to benchmark the mapping of the driven Kerr resonator onto a Logical bit against a general result of non-equilibrium stochastic thermodynamics: the Integral Fluctuation Theorem (IFT) for entropy. The theorem states that if one considers a general transformation over time of some control parameter (here the transition rates) and records a large number of trajectories, $\langle \exp(-\Delta s[\sigma]) \rangle_\sigma = 1$ [381, 416].

6.3.2 Measuring the entropy production

In order to estimate the dependence of the stationary probabilities as a function of the input power, we consider an adiabatic sweep of the pump power for a detuning $\Delta/\Gamma = 1.06$. The adiabaticity condition is ensured by taking a sine modulation of the input power $P(t) \approx P_c(1 + 0.2 \sin(2\pi t/\tau_{Sw}))$ with $\tau_{Sw}/\tau_R \approx 10^3$ (cf. Sec. 6.2.3). In Fig. 6.8-(a) we show the average cavity occupation as a function of input power for this quasi-adiabatic sweep. The data points corresponding to the increasing (FW) or decreasing (BW) power ramp completely overlap: the measured hysteresis area is zero within the experimental uncertainty. After validating the quasi-adiabaticity of this modulation protocol, we use the value of the average cavity occupation $\langle n \rangle$ at the critical input power P_c to digitize the single-shot trajectories: If $n(t) \geq n_c$ the system is in the state $\sigma_t = 1$ at time t otherwise, $\sigma_t = 0$. In order to estimate the stationary probability $\tilde{P}(\sigma)$ we acquired 10^2 single-shot trajectories using a quasi-adiabatic modulation of the input power. Each couple of values (P, n) has been collected in a histogram. Upon integrating the counts for each row (constant P) below and above n_c , we could estimate the stationary probabilities $\tilde{P}(0)$ and $\tilde{P}(1)$, respectively. Figure 6.8-(b) presents the result of this analysis, blue (green) markers corresponding to $\tilde{P}(0)$ ($\tilde{P}(1)$). It is convenient for later use to have an analytical expression for these stationary probabilities as a function of the input power. Provided that the two-mode approximation (6.9) of the density matrix is faithful, which we verified in Sec. 6.2.3, and $\Gamma\tau_R \gg 1$, the transition rates between the metastable states $\Gamma_{\sigma=\sigma'}$ scale as [227]

$$\Gamma_{\sigma=\sigma'}^{-1} = \tau_R e^{\pm\eta \frac{(P_c - P)}{P_c}} \quad (6.17)$$

with η some constant depending on the resonator parameters, τ_R the average switching time at the critical drive power P_c (here $\Gamma\tau_R \approx 1.7 \cdot 10^4$) and the sign in the exponent is positive for Γ_{10} and negative for Γ_{01} . Inserting these relations in the definition of the stationary probability Eq. (6.15) we can rewrite $\tilde{P}(\sigma) - \tilde{P}(\sigma') = 2\tilde{P}(\sigma) - 1$ as

$$\tilde{P}_P(\sigma) = \frac{1}{2} \left[\tanh \left(\pm\eta \frac{P - P_c}{P_c} \right) + 1 \right] \quad (6.18)$$

We use this relation to fit the measured stationary probabilities; the result is shown in Fig. 6.8-(b). We can now use this relation in combination with the the input (P_t) - output (n_t) trajectories to estimate the stochastic entropy production when the input power is modulated according to some modulation protocol using Eq. (6.16).

As previously mentioned, it is convenient to work in a situation where the boundary term in the entropy production is vanishing. This can be achieved by considering a cyclic modulation of the input power $P_0 = P_N$ where the initial (σ_0) and final (σ_N) states are equal. This request is fulfilled when modulating the input power using a cosine wave with an amplitude significantly larger than the metastability region. In Fig. 6.8-(c) we show a small portion of single-shot trajectories for the input power (gray line) and cavity occupation (color); here $\Delta = 1.06$ and the modulation period is $\tau_{Sw} = 50 \mu\text{s}$. We acquired long single-shot trajectories containing $\sim 10^3$ periods of the modulation protocol for several values of τ_{Sw} ranging between $50 \mu\text{s}$ and $2 \mu\text{s}$. For each dataset (constant τ_{Sw}) we used the averaged power and cavity occupation trajectories to extract the hysteresis area (cf. Sec. 6.2.2); the result is shown in Fig. 6.8-(d). We

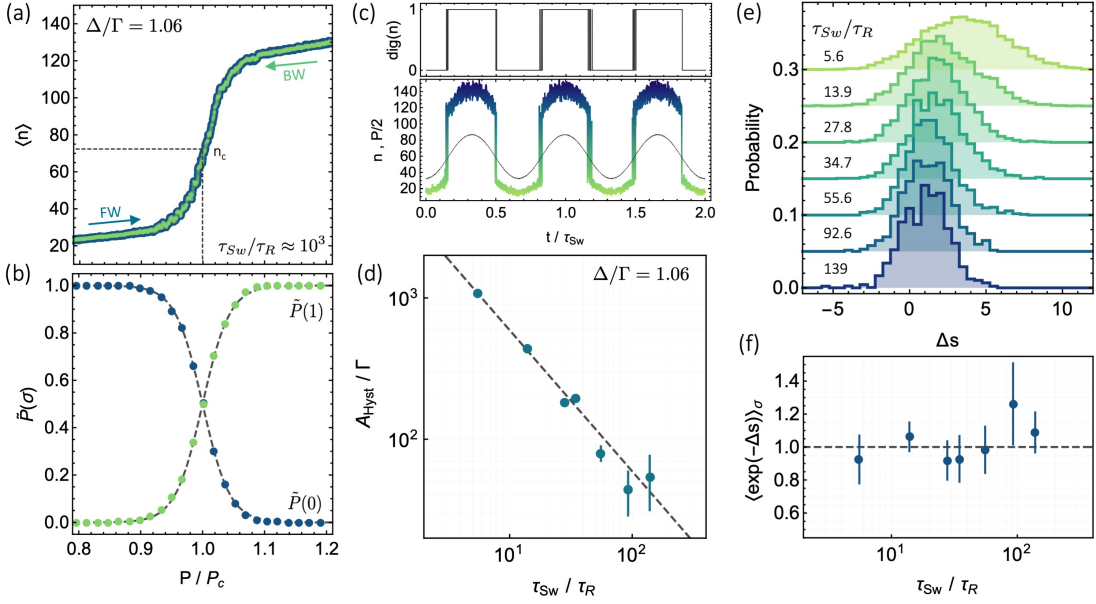


Figure 6.8: **Entropy production measurements:** (a) Average cavity occupation as a function of the input pump power. Data points in the increasing (FW) and decreasing (BW) part of the power ramp overlap demonstrating the power sweep is quasi-adiabatic ($\tau_{Sw}/\tau_R \approx 10^3$). The value $\langle n \rangle|_{P_c}$ defines the critical cavity occupation n_c used for the digitization of the trajectory. (b) Stationary probability $\tilde{P}(\sigma)$ as a function of the pump power. Dashed lines are fits with Eq. (6.18). (c) Example of three modulation periods of the input power P (gray) and corresponding single-shot trajectory of the cavity occupation n (color) are shown; $\text{dig}(n)$ is the digitization of the latter. (d) Average hysteresis area measured as a function of the power modulation period (τ_{Sw}) rescaled for the relaxation time ($\tau_R = 0.36(2) \mu\text{s}$). The dashed line is a power law fit with exponent -1 . (e) Histogram of the entropy production per modulation period for seven values of τ_{Sw} corresponding to panel (d). (f) Verification of the integral fluctuation theorem for the entropy.

observe that the average hysteresis area as a function of the rescaled sweep speed τ_{Sw}/τ_R spans roughly two decades and presents a scaling fairly interpolated by a power law fit with the -1 universal exponent (dashed line). For the slower modulation the average hysteresis area is very small and we can regard this power sweep protocol as quasi-adiabatic. The faster modulation instead corresponds to a non-adiabatic protocol of the control parameter (P), whose relative speed $\tau_{Sw}/\tau_R \approx 5.6$, corners the onset of the "classical" region for the scaling of the hysteresis area, see Fig. 6.6-(e).

Then, we used $n_c = 74$ as discrimination threshold for digitizing the cavity occupation trajectory ($\sigma_t = \text{dig}(n_t)$) as shown in Fig. 6.8-(c). For each modulation period, consisting of $N + 1$ values of the pump power P_k and logical bit state σ_k , we computed the infinitesimal entropy production using

$$\delta s_k = \log \left(\frac{(1 - \sigma_k) \tilde{P}_k(0) + \sigma_k \tilde{P}_k(1)}{(1 - \sigma_{k-1}) \tilde{P}_k(0) + \sigma_{k-1} \tilde{P}_k(1)} \right) \quad (6.19)$$

where $\tilde{P}_k(\sigma)$ is the compact notation for the stationary probability of finding the system

in the state σ if the input power is P_k . Finally, the total entropy production Δs over a cycle of the control parameter is obtained by summing over $k = 1, \dots, N$ the increment δs_k . Then, we repeat this procedure for each modulation cycle in the single-shot trajectory and bin the results in a histogram. The entropy production histograms obtained separately for each modulation speed are presented in Fig. 6.8-(e). Notice that we set a constant 0.05 vertical shift between each histogram to ease the visual comparison.

Interestingly we can see that in every histograms there is a significant portion of events where $\Delta s < 0$ within a cyclic transformation of the control parameter. This seem to conflict with the macroscopic formulation of the second law of thermodynamics, stating that $\Delta s \geq 0$ for a cyclic transformation, with the equality holding only for adiabatic processes [439]. As anticipated in the introduction to this chapter, this is just an apparent contradiction. Indeed, fluctuations are a lost feature in classical thermodynamics as a consequence of the thermodynamic limit. On the contrary, the thermodynamics variables of mesoscopic systems are characterized by a probability density whose variance is of the same order of its average. Some events may violate the laws holding for macroscopic systems, which however hold on average. Indeed, the expectation value of the entropy production histograms in Fig. 6.8-(e) is always positive. We can also observe that the average entropy production grows for faster sweeps, which is consistent with the macroscopic prediction. We also notice that the Δs distributions are distinctly non-Gaussian, asymmetric and heavy-tailed, this is a common situation in strongly-driven nonlinear systems [421, 423].

Finally, we test an integral fluctuation theorem (IFT) for the entropy production. The theorem states, under extremely general conditions, that the nonlinear expectation value $\langle \exp(-\Delta s) \rangle_\sigma$ equals 1, and is related to the symmetry under time-reversal of the microscopic dynamics generating the stochastic evolution of the system [381, 416, 440]. In Fig. 6.8-(f) we show the result of this nonlinear expectation value for each entropy production dataset, error-bars correspond to one standard deviation. Overall, we observe a fair agreement of the data points with the IFT prediction (dashed line) within the statistical uncertainty. Notice that the due to exponential the weight of some trajectories in the average becomes extremely large. As a result, the convergence to the expected value of $\langle \exp(-\Delta s) \rangle_\sigma$ is slower than for linear estimates and is affected by large statistical uncertainties, warranting the acquisition of a larger dataset.

In summary, these preliminary results validate the mapping of the Kerr resonator onto the physics of the logical bit for the range of modulation speeds explored in this dataset $\tau_{Sw}/\tau_R \sim (5 - 10^2)$. The next natural step would be to check for different detuning values the IFT. However, we think this is not necessary since we demonstrated in Sec. 6.2.3 that the scaling of the metastable dynamics as a function of Δ collapses when the modulation timescale τ_{Sw} is rescaled for the relaxation time τ_R . It could be more interesting to investigate cyclic but asymmetric drive ramps, checking whether there is an optimal cycle which minimizes the entropy production, or to verify the Landauer entropic bound for the erasure of a bit of information [424, 422, 441].

6.4 Summary and Perspectives

In this chapter we have investigated the metastable dynamics characterizing a single, confined mode of the electromagnetic field in a micropillar cavity hosting polariton excitations. We have first discussed how the interplay of dissipation and nonlinearities originates the metastability, which manifests in jumps of the cavity occupation between the two -otherwise stable- branches of the classical bistability. The average time between two consecutive switching events depends dramatically on the system parameters: for instance, we have shown in Sec. 6.2.3 that this time becomes exponentially large when increasing the laser detuning. More generally this switching dynamics is rapidly suppressed as the number of excitations in the systems tends towards infinity: this critical slowing of the dynamics relates to the onset of a dissipative phase-transition (DPT), see Sec. 6.1.2.

In order to probe the onset of this DPT, we performed dynamical hysteresis experiments where we studied the scaling of the average hysteresis area as a function of the speed of the input power modulation protocol (cf. Sec. 6.2.2). The experimental data shows that the hysteresis area closes for slower protocols as a consequence of fluctuations, following a double power-law dependence as a function of the sweep period (τ_{Sw}). The power law characterizing large scanning times exhibit a -1 exponent, independently of the laser detuning: this universal exponent is in agreement with theoretical predictions [230]. Analyzing the scaling of the input power region where the system responds non-adiabatically to the modulation, in the spirit of a Kibble-Zurek mechanism for dynamical phase transitions, we could reproduce the experimental results. In the thermodynamic limit, where the number of excitation in the cavity tends to infinity, the metastable relaxation timescale diverges and the onset of the -1 power can be observed only for infinitely slow modulations. The scaling of the hysteresis area thus follows a single power law: such algebraic behavior signals the onset of a DPT.

Interestingly, we could demonstrate that the hysteresis area measured for different power sweeps periods τ_{Sw} and laser detunings Δ , collapses on the same double power law dependence upon rescaling τ_{Sw} for the critical value of the metastability relaxational timescale τ_R . This seems to suggest that also the first power-law exponent is universal; in particular we find $\alpha \approx -1/3$ (cf. Sec. 6.2.3). It could be interesting to numerically and experimentally validate this observation in 2D lattices of microresonators, where an intriguing mapping to the equilibrium Ising model was recently highlighted [195].

In the second part of the chapter, we profit from the possibility of accessing at a single trajectory level the system dynamics to build a parallel between the metastable dynamics of the Kerr resonator and the one of a (classical) Logical Bit subject to random bit-flip events. This mapping allows us to circumvent some technical difficulties in the definition of thermodynamic variables for a photonic system. Indeed, for a two-level system, it is possible to build a simple and robust estimate for the entropy production, which relies only on the measurement of the stationary cavity occupation probabilities as a function of input power (cf. Sec. 6.3.1). We realize an experiment to test this idea, retrieving the entropy production distributions both for quasi-adiabatic and diabatic cyclic power modulation protocols. Although these experiments are still preliminary, we could demonstrate that stochastic entropy production verifies a general integral fluctuation theorem (cf. Sec. 6.3.2). This encouraging result supports the validity of the Kerr resonator - Logical Bit mapping.

We envisage the possibility of studying cyclic but asymmetric power ramps and check whether there is an optimal cycle which minimizes the average entropy production per cycle. These considerations might be important on the longer run to question whether passive nonlinear optical elements could be used to build integrated optical circuits with a computational or energetic advantage when compared with electronic solid state architectures [442, 443, 444]. More generally, this opens interesting perspectives for the exploration of the non-equilibrium thermodynamics of a mesoscopic system, profiting from the exquisite control of an integrated photonic platform. Furthermore, photonic systems naturally offer the possibility to engineer the dissipative coupling with other kind of baths, e.g. parametric or squeezed [335, 430, 436]. This is an almost unexplored playground for thermodynamics: engineering the system-environment interaction, may provide an insight on the ultimate efficiency bounds for nanoscale engines [437, 438].

Conclusion and Outlook

In this PhD dissertation we have investigated micron-sized semiconductor structures vertically defined by a Fabry-Perot cavity embedding a single quantum well and laterally patterned to emulate the physics of one or few coupled zero dimensional (photon) polariton boxes. Despite their apparent simplicity such elementary structures present an extremely rich phenomenology. Depending on the sample design and excitation scheme, the quantum well provides the microcavities optical gain or a resonant Kerr-type nonlinearity, which become sizable already for few excitations. The work concentrates on two main lines of research. 1) How to create and control chiral photonic currents in arrays of coupled microcavities. 2) Study intrinsic dynamical phenomena originating from the interplay of nonlinearities and dissipation in coherently driven microstructures.

Along the first line of research, we investigated arrays of coupled micropillar cavities arranged in a ring geometry presenting a discrete rotational symmetry (cf. Chap. 4). Harnessing an analogue spin-orbit coupling between the cavity-photon polarization (pseudo-spin) and its in-plane motion, we show that some of the optical modes present a wavefront with a net phase circulation. In other words, these modes possess a net orbital angular momentum (OAM), an in principle unbounded degree of freedom, which is both desirable for fundamental studies and technologically relevant [80, 268]. However, the modes presenting opposite OAM chirality always appear in energy-degenerate doublets, due to the mirror-symmetry of the cavity eigenmodes (by definition a chiral object can be distinguished from its mirror image). Profiting from the small degree of spin-polarization, surviving the relaxation processes of photo-generated carriers up to ~ 100 K, we can slightly bias the degree of circular polarization of the gain medium. In combination with the polarization properties of the optical modes, this allows implementing an OAM lasing scheme where the chirality can be optically controlled. The proposed lasing scheme is general as it relies only on two ingredients which are present in several micro and nanoscale photonic platforms, namely, a finite TE-TM polarization splitting in cavities presenting a C_{nv} symmetry and a mean to spin-polarize the gain medium. Furthermore, when investigating the gain saturation regime, we discovered a

bistability between modes presenting distinct OAM and polarization patterns. These findings could not only be interesting from the point of view of developing new structured light sources [58, 445] but more generally in the context of topological photonics [59]. Indeed, our structures presently embed a single QW, thus the lasing action occurred in the weak coupling regime. By altering the design of the heterostructure (e.g. embedding 12 QWs) we could repeat these experiments for the strong-coupling regime. In this case, the two spin-polarized exciton populations not only bias the overall gain of the circularly polarized eigenmodes of the system, but also affect their energy via the spin-dependent polariton-polariton and polariton-reservoir interactions, resulting in an analog Zeeman shift. The combination of these two ingredients may allow to trigger lasing in topologically protected edge states with both a tunable chirality and in absence of any magnetic field [60, 446, 447].

In Chap. 5 and 6, we have focused on the second line of research, characterizing two general dynamical out-of-equilibrium effects in coherently driven microcavities. One is the emergence of intrinsic parametric instabilities when two (or more) coupled microcavities are coherently driven (cf. Chap. 5). The second is the metastable dynamics of the intracavity field, activated by the interplay of stochastic dissipation processes and nonlinearities (cf. Chap. 6). In both cases, we investigate the simplest experimental setting where the phenomenon can be observed. We probed two coupled micropillar cavities or a single tightly confined polariton mode in a rectangular micropillar.

The mechanism responsible for the parametric instability relates to the opening of a resonant scattering channel from the pump toward two (or more) modes as their energy gets renormalized by the nonlinearity [330]. This mechanism is a general feature of strongly driven nonlinear resonators arrays, which can be theoretically addressed at the level of a linear stability analysis (cf. 3.3.1). Provided the polariton-polariton scattering rate is faster than losses, the instability seeds sustained parametric oscillations: the signal and idler fields are at the frequency of the nonlinear modes, thus inheriting their spatial profile. By imaging the emission pattern of signal and idler modes in the instability regime, we demonstrate the validity of this overall picture. In our experiments, unlike previously demonstrated triply resonant schemes involving microcavity polaritons [131, 128, 132, 361], the parametric process involves just two polariton modes, the pump not being in resonance with any of them. This configuration allows observing remarkably contrasted sidebands, where roughly 38% of the total radiated energy is stored, for a threshold power as low as few hundred microwatts. Given the broad range of applicability of these results and the inherent scalability of our integrated photonic platform, this work opens interesting possibilities for engineering the spatial modes of parametric oscillators [360]. For instance, if we consider a honeycomb arrangement of microcavities, a photonic analogue of graphene [49], the bandstructure is entirely symmetric with respect to the Dirac point energy. Pumping few linewidths above the Dirac-cone energy should trigger simultaneously parametric oscillations for all wavevectors. As opposing Dirac-cones in reciprocal space present opposite winding of the phase, we expect the generation of correlated photon pairs with a structured wavefront.

In Chap. 6, we have been interested in the metastable dynamics characterizing one mode of a highly nonlinear rectangular micropillar cavity. The metastability manifests in abrupt jumps of the cavity occupation between the two -otherwise stable- branches of the classical bistability. For specific driving conditions, the switching dynamics is much slower than any other characteristic time of the system. Moreover, the metastable dy-

namics is strongly suppressed as the number of excitations in the systems tends towards infinity: such critical slowing down of the dynamics relates to the onset of a dissipative phase-transition [193, 230]. Following a theoretical proposal, we use dynamical hysteresis experiments as a probe of the metastable dynamics of the system. Using a scaling analysis we are able to retrieve the exponents of the dissipative phase transition. Our results suggest that the hysteresis area follows a universal double power law dependence as a function of the ratio between the power modulation period τ_{Sw} and the metastability escape rate τ_R . The measured exponents are $\alpha \approx -1/3$ for $\tau_{Sw}/\tau_R \ll 1$ and $\beta \approx -1$ for $\tau_{Sw}/\tau_R \gg 1$. Interestingly, not only we could experimentally verify the universality of the exponent $\beta \approx -1$, consistently with the theoretical predictions [230], but our scaling analysis suggests that also $\alpha \approx -1/3$ might be universal. Even if our results are too preliminary for a claim, they warrant further investigations. Indeed, testing the universality of α could help elucidating an intriguing mapping existing between equilibrium Ising models and the metastable dynamics of 2D lattices of microcavities [195]. Finally, profiting from the possibility of accessing the system dynamics at a single trajectory level, we verified the possibility of mapping the metastable dynamics of the Kerr resonator onto a (classical) Logical Bit subject to random bit-flip events. Providing a proof-of-principle verification of an integral fluctuation theorem for the non-equilibrium entropy production [381], our preliminary results suggest an interesting parallel between the stochastic thermodynamics of mesoscopic objects and nonlinear photonic systems. The possibility of designing nearly arbitrary input drive protocols, combined with a single-shot readout of the system observables, could be used to test the ultimate efficiency bounds for nanoscale engines. On the longer term, a consistent formulation of a microscopic thermodynamic (and information) theory for passive nonlinear optical systems, might be important to address whether integrated optical circuits could enable a computational or energetic advantage when compared with present electronic microprocessor architectures [444].

On the short term it would be interesting to combine the two main lines of research presented in this dissertation by coherently exciting the chiral eigenmodes in ring-type photonic molecules. Indeed, we expect the interplay between the opposite circular polarization of the two chiral modes with the two spin-dependent polariton interaction channels to drive a metastable dynamics characterized by spontaneous symmetry breaking effects.

In order to fully exploit the versatility of a polariton platform for the emulation of strongly-correlated many-body phases, the achievement of two-body polariton interactions (U) comparable both with the cavity linewidth (Γ) and the intracavity coupling strength (J) is a major challenge. To this aim, one can either improve significantly the cavity linewidth Γ or find alternative solutions to enhance U . In this thesis we discussed the main factors presently limiting Γ in our platform: residual absorption in the cavity and the inhomogeneous broadening of the exciton transition. The former contribution can be minimized by employing an adiabatic cavity design [209], which allows reducing the thickness of GaAs present in the cavity, where we believe most of the optical absorption takes place. The latter is a technical problem which can be minimized working with thicker quantum wells while improving the interface quality and level of residual doping in the epitaxial growth machine.

In order to improve the interaction strength we see two possible avenues. In the first approach, pioneered in the group of A. Imamoglu, one keeps working with excitons in GaAs/InGaAs based quantum wells, but aims at modifying the interaction mechanisms.

For instance, indirect excitons can be formed by spatially separating electron and holes in adjacent quantum wells with resonantly coupled electronic levels [448]. This spatial separation, allows the build-up of a strong exciton dipole moment, endowing the system with enhanced long-range interactions [56]. Alternatively, polariton–polariton interactions can be strongly enhanced when the electrons of an additional 2D electron gas are initially in the fractional quantum Hall regime [337].

The second, would be to explore new materials, such as copper oxides, supporting giant Rydberg excitons [449]. In this systems the exciton Bohr radius, hence contact interactions, can be enhanced by almost two orders of magnitude ($a_B \sim \mu\text{m}$). Correspondingly, the radiative exciton decay rate decreases, hence the Rabi coupling to the photon, this eventually prevents to enter the strong coupling regime. This problem could be solved by employing an electromagnetically induced transparency (EIT) excitation scheme, as recently demonstrated by N. Jia and collaborators [450]. These materials are however not compatible with epitaxial techniques; therefore, the recent development of open cavities where the active material can be directly transferred on one of the cavity mirrors seems a viable option [46].

Publications

- S. R. K. Rodriguez, W. Casteels, F. Storme, N. Carlon Zambon, I. Sagnes, L. Le Gratiet, E. Galopin, A. Lemaître, A. Amo, C. Ciuti and J. Bloch, "Probing a Dissipative Phase Transition via Dynamical Optical Hysteresis". *Physical Review Letters* 118 (24), 247402 (2017).
- S. R. K. Rodriguez, V. Goblot, N. Carlon Zambon, A. Amo and J. Bloch, "Non-reciprocity and zero reflection in nonlinear cavities with tailored loss", *Physical Review A* 99 (1), 013851 (2019).
- N. Carlon Zambon*, P. St-Jean*, M. Milićević, A. Lemaître, A. Harouri, L. Le Gratiet, O. Bleu, D. D. Solnyshkov, G. Malpuech, I. Sagnes, S. Ravets, A. Amo and J. Bloch, "Optically controlling the emission chirality of microlasers", *Nature Photonics* 13 (4), 283-288 (2019).
- N. Carlon Zambon*, P. St-Jean*, M. Milićević, A. Lemaître, A. Harouri, L. Le Gratiet, I. Sagnes, S. Ravets, A. Amo and J. Bloch, "Orbital angular momentum bistability in a microlaser", *Optics Letters* 44 (18), 4531-4534 (2019).
- N. Carlon Zambon, S. R. K. Rodriguez, A. Lemaître, A. Harouri, L. Le Gratiet, I. Sagnes, P. St-Jean, S. Ravets, A. Amo and J. Bloch, "Parametric instability in coupled nonlinear microcavities", arXiv:1911.02816 (2019).

Bibliography

- [1] E. Fermi et al. *Studies of the Nonlinear Problems*. Tech. rep. May. Los Alamos, NM (United States): Los Alamos National Laboratory (LANL), May 1955. DOI: [10.2172/4376203](https://doi.org/10.2172/4376203) (cit. on p. 1).
- [2] S. Arora and B. Barak. *Computational Complexity: A Modern Approach*. January. Cambridge: Cambridge University Press, 2009, pp. 19–56. ISBN: 9780511804090. DOI: [10.1017/CB09780511804090](https://doi.org/10.1017/CB09780511804090) (cit. on p. 1).
- [3] R. Badii and A. Politi. *Complexity: Hierarchical Structures and Scaling in Physics*. Cambridge Nonlinear Science Series. Cambridge University Press, 1999. ISBN: 9780521663854 (cit. on p. 1).
- [4] S. Aaronson and A. Arkhipov. “The Computational Complexity of Linear Optics”. In: *Research in Optical Sciences*. Washington, D.C.: OSA, 2014, QTh1A.2. ISBN: 978-1-55752-995-4. DOI: [10.1364/QIM.2014.QTh1A.2](https://doi.org/10.1364/QIM.2014.QTh1A.2) (cit. on p. 2).
- [5] H. Wang et al. “Boson Sampling with 20 Input Photons and a 60-Mode Interferometer in a 10^{14} -Dimensional Hilbert Space”. In: *Physical Review Letters* 123.25 (Dec. 2019), p. 250503. ISSN: 0031-9007. DOI: [10.1103/PhysRevLett.123.250503](https://doi.org/10.1103/PhysRevLett.123.250503) (cit. on p. 2).
- [6] H. M. Wiseman. “The two Bell’s theorems of John Bell”. In: *Journal of Physics A: Mathematical and Theoretical* 47.42 (Oct. 2014), p. 424001. DOI: [10.1088/1751-8113/47/42/424001](https://doi.org/10.1088/1751-8113/47/42/424001) (cit. on p. 2).
- [7] C. Hempel et al. “Quantum Chemistry Calculations on a Trapped-Ion Quantum Simulator”. In: *Physical Review X* 8.3 (2018), p. 31022. ISSN: 21603308. DOI: [10.1103/PhysRevX.8.031022](https://doi.org/10.1103/PhysRevX.8.031022). arXiv: [1803.10238](https://arxiv.org/abs/1803.10238) (cit. on p. 2).
- [8] J. Orenstein. “Advances in the Physics of High-Temperature Superconductivity”. In: *Science* 288.5465 (Apr. 2000), pp. 468–474. ISSN: 00368075. DOI: [10.1126/science.288.5465.468](https://doi.org/10.1126/science.288.5465.468) (cit. on p. 2).
- [9] R. P. Feynman. “Simulating physics with computers”. In: *International Journal of Theoretical Physics* 21.6-7 (June 1982), pp. 467–488. ISSN: 0020-7748. DOI: [10.1007/BF02650179](https://doi.org/10.1007/BF02650179) (cit. on p. 2).
- [10] D. Deutsch. “Quantum Theory, the Church-Turing Principle and the Universal Quantum Computer”. In: *Proceedings of the Royal Society A: Mathematical, Physical and Engineering Sciences* 400.1818 (July 1985), pp. 97–117. ISSN: 1364-5021. DOI: [10.1098/rspa.1985.0070](https://doi.org/10.1098/rspa.1985.0070) (cit. on p. 2).

- [11] F. Arute et al. “Quantum supremacy using a programmable superconducting processor”. In: *Nature* 574.7779 (Oct. 2019), pp. 505–510. ISSN: 0028-0836. DOI: [10.1038/s41586-019-1666-5](https://doi.org/10.1038/s41586-019-1666-5). arXiv: [1911.00577](https://arxiv.org/abs/1911.00577) (cit. on p. 2).
- [12] S. Aaronson. “Opinion: Why Google’s Quantum Supremacy Milestone Matters”. In: *The New York Times* (Oct. 2019) (cit. on p. 2).
- [13] S. Lloyd. “Universal Quantum Simulators”. In: *Science* 273.5278 (Aug. 1996), pp. 1073–1078. ISSN: 0036-8075. DOI: [10.1126/science.273.5278.1073](https://doi.org/10.1126/science.273.5278.1073) (cit. on p. 2).
- [14] M. Kliesch et al. “Dissipative Quantum Church-Turing Theorem”. In: *Physical Review Letters* 107.12 (Sept. 2011), p. 120501. ISSN: 0031-9007. DOI: [10.1103/PhysRevLett.107.120501](https://doi.org/10.1103/PhysRevLett.107.120501) (cit. on p. 2).
- [15] D. Wecker et al. “Gate-count estimates for performing quantum chemistry on small quantum computers”. In: *Physical Review A* 90.2 (Aug. 2014), p. 022305. ISSN: 1050-2947. DOI: [10.1103/PhysRevA.90.022305](https://doi.org/10.1103/PhysRevA.90.022305) (cit. on p. 2).
- [16] E. Gibney. “Physics: Quantum computer quest”. In: *Nature* 516.7529 (Dec. 2014), pp. 24–26. ISSN: 0028-0836. DOI: [10.1038/516024a](https://doi.org/10.1038/516024a) (cit. on p. 2).
- [17] F. T. Chong, D. Franklin, and M. Martonosi. “Programming languages and compiler design for realistic quantum hardware”. In: *Nature* 549.7671 (Sept. 2017), pp. 180–187. ISSN: 0028-0836. DOI: [10.1038/nature23459](https://doi.org/10.1038/nature23459) (cit. on p. 2).
- [18] L. W. Cheuk et al. “Observation of spatial charge and spin correlations in the 2D Fermi-Hubbard model”. In: *Science* 353.6305 (2016), pp. 1260–1264. ISSN: 0036-8075. DOI: [10.1126/science.aag3349](https://doi.org/10.1126/science.aag3349) (cit. on p. 2).
- [19] H. Bernien et al. “Probing many-body dynamics on a 51-atom quantum simulator”. In: *Nature* 551.7682 (Nov. 2017), pp. 579–584. ISSN: 0028-0836. DOI: [10.1038/nature24622](https://doi.org/10.1038/nature24622) (cit. on p. 2).
- [20] T. Hensgens et al. “Quantum simulation of a Fermi–Hubbard model using a semiconductor quantum dot array”. In: *Nature* 548.7665 (Aug. 2017), pp. 70–73. ISSN: 0028-0836. DOI: [10.1038/nature23022](https://doi.org/10.1038/nature23022) (cit. on p. 2).
- [21] J. W. Britton et al. “Engineered two-dimensional Ising interactions in a trapped-ion quantum simulator with hundreds of spins”. In: *Nature* 484.7395 (Apr. 2012), pp. 489–492. ISSN: 0028-0836. DOI: [10.1038/nature10981](https://doi.org/10.1038/nature10981) (cit. on p. 2).
- [22] H. Labuhn et al. “Tunable two-dimensional arrays of single Rydberg atoms for realizing quantum Ising models”. In: *Nature* 534.7609 (June 2016), pp. 667–670. ISSN: 0028-0836. DOI: [10.1038/nature18274](https://doi.org/10.1038/nature18274) (cit. on p. 2).
- [23] T. Inagaki et al. “A coherent Ising machine for 2000-node optimization problems”. In: *Science* 354.6312 (Nov. 2016), pp. 603–606. ISSN: 0036-8075. DOI: [10.1126/science.aah4243](https://doi.org/10.1126/science.aah4243) (cit. on p. 2).
- [24] I. Bloch, J. Dalibard, and S. Nascimbène. “Quantum simulations with ultracold quantum gases”. In: *Nature Physics* 8.4 (Apr. 2012), pp. 267–276. ISSN: 1745-2473. DOI: [10.1038/nphys2259](https://doi.org/10.1038/nphys2259) (cit. on p. 2).
- [25] R. Blatt and C. F. Roos. “Quantum simulations with trapped ions”. In: *Nature Physics* 8.4 (Apr. 2012), pp. 277–284. ISSN: 1745-2473. DOI: [10.1038/nphys2252](https://doi.org/10.1038/nphys2252) (cit. on p. 2).
- [26] A. A. Houck, H. E. Türeci, and J. Koch. “On-chip quantum simulation with superconducting circuits”. In: *Nature Physics* 8.4 (Apr. 2012), pp. 292–299. ISSN: 1745-2473. DOI: [10.1038/nphys2251](https://doi.org/10.1038/nphys2251) (cit. on p. 2).
- [27] J. I. Cirac and P. Zoller. “Goals and opportunities in quantum simulation”. In: *Nature Physics* 8.4 (2012), pp. 264–266. ISSN: 1745-2481. DOI: [10.1038/nphys2275](https://doi.org/10.1038/nphys2275) (cit. on p. 2).

-
- [28] M. J. Kastoryano, F. Reiter, and A. S. Sørensen. “Dissipative Preparation of Entanglement in Optical Cavities”. In: *Physical Review Letters* 106.9 (Feb. 2011), p. 090502. ISSN: 0031-9007. DOI: [10.1103/PhysRevLett.106.090502](https://doi.org/10.1103/PhysRevLett.106.090502) (cit. on pp. 2, 42).
- [29] E. E. Wollman et al. “Kilopixel array of superconducting nanowire single-photon detectors”. In: *Optics Express* 27.24 (Nov. 2019), p. 35279. ISSN: 1094-4087. DOI: [10.1364/OE.27.035279](https://doi.org/10.1364/OE.27.035279) (cit. on p. 2).
- [30] M. Aaboud et al. “Evidence for light-by-light scattering in heavy-ion collisions with the ATLAS detector at the LHC”. In: *Nature Physics* 13.9 (Sept. 2017), pp. 852–858. ISSN: 1745-2473. DOI: [10.1038/nphys4208](https://doi.org/10.1038/nphys4208). arXiv: [1702.01625](https://arxiv.org/abs/1702.01625) (cit. on p. 2).
- [31] J. J. Hopfield. “Theory of the Contribution of Excitons to the Complex Dielectric Constant of Crystals”. In: *Physical Review* 112.5 (Dec. 1958), pp. 1555–1567. ISSN: 0031-899X. DOI: [10.1103/PhysRev.112.1555](https://doi.org/10.1103/PhysRev.112.1555) (cit. on pp. 3, 24, 25).
- [32] C. Weisbuch et al. “Observation of the coupled exciton-photon mode splitting in a semiconductor quantum microcavity”. In: *Physical Review Letters* 69.23 (Dec. 1992), pp. 3314–3317. ISSN: 0031-9007. DOI: [10.1103/PhysRevLett.69.3314](https://doi.org/10.1103/PhysRevLett.69.3314) (cit. on pp. 3, 25).
- [33] A. Imamoglu et al. “Nonequilibrium condensates and lasers without inversion: Exciton-polariton lasers”. In: *Physical Review A* 53.6 (June 1996), pp. 4250–4253. ISSN: 1050-2947. DOI: [10.1103/PhysRevA.53.4250](https://doi.org/10.1103/PhysRevA.53.4250) (cit. on pp. 3, 32).
- [34] F. Tassone and Y. Yamamoto. “Exciton-exciton scattering dynamics in a semiconductor microcavity and stimulated scattering into polaritons”. In: *Physical Review B* 59.16 (Apr. 1999), pp. 10830–10842. ISSN: 0163-1829. DOI: [10.1103/PhysRevB.59.10830](https://doi.org/10.1103/PhysRevB.59.10830) (cit. on pp. 3, 22, 27, 30, 52).
- [35] J. Kasprzak et al. “Bose–Einstein condensation of exciton polaritons”. In: *Nature* 443.7110 (Sept. 2006), pp. 409–414. ISSN: 0028-0836. DOI: [10.1038/nature05131](https://doi.org/10.1038/nature05131) (cit. on pp. 3, 32, 61).
- [36] C. Schneider et al. “An electrically pumped polariton laser”. In: *Nature* 497.7449 (May 2013), pp. 348–352. ISSN: 0028-0836. DOI: [10.1038/nature12036](https://doi.org/10.1038/nature12036) (cit. on pp. 3, 32).
- [37] I. Carusotto and C. Ciuti. “Quantum fluids of light”. In: *Reviews of Modern Physics* 85.1 (Feb. 2013), pp. 299–366. ISSN: 0034-6861. DOI: [10.1103/RevModPhys.85.299](https://doi.org/10.1103/RevModPhys.85.299) (cit. on pp. 3, 8, 13, 20, 22, 27–30, 35, 41, 42, 63, 64, 69, 114).
- [38] A. Amo et al. “Superfluidity of polaritons in semiconductor microcavities”. In: *Nature Physics* 5.11 (2009), pp. 805–810. ISSN: 17452473. DOI: [10.1038/nphys1364](https://doi.org/10.1038/nphys1364). arXiv: [0812.2748](https://arxiv.org/abs/0812.2748) (cit. on pp. 3, 30).
- [39] Q. Fontaine et al. “Observation of the Bogoliubov Dispersion in a Fluid of Light”. In: *Physical Review Letters* 121.18 (Oct. 2018), p. 183604. ISSN: 0031-9007. DOI: [10.1103/PhysRevLett.121.183604](https://doi.org/10.1103/PhysRevLett.121.183604) (cit. on p. 3).
- [40] G. Nardin et al. “Hydrodynamic nucleation of quantized vortex pairs in a polariton quantum fluid”. In: *Nature Physics* 7.8 (Aug. 2011), pp. 635–641. ISSN: 1745-2473. DOI: [10.1038/nphys1959](https://doi.org/10.1038/nphys1959) (cit. on pp. 3, 30).
- [41] D. Sanvitto et al. “All-optical control of the quantum flow of a polariton condensate”. In: *Nature Photonics* 5.10 (2011), pp. 610–614. ISSN: 17494885. DOI: [10.1038/nphoton.2011.211](https://doi.org/10.1038/nphoton.2011.211) (cit. on pp. 3, 30, 36).

- [42] A. Amo et al. “Polariton Superfluids Reveal Quantum Hydrodynamic Solitons”. In: *Science* 332.6034 (June 2011), pp. 1167–1170. ISSN: 0036-8075. DOI: [10.1126/science.1202307](https://doi.org/10.1126/science.1202307) (cit. on pp. 3, 30).
- [43] M. Sich et al. “Observation of bright polariton solitons in a semiconductor microcavity”. In: *Nature Photonics* 6.1 (Jan. 2012), pp. 50–55. ISSN: 1749-4885. DOI: [10.1038/nphoton.2011.267](https://doi.org/10.1038/nphoton.2011.267) (cit. on pp. 3, 30).
- [44] A. Amo et al. “Light engineering of the polariton landscape in semiconductor microcavities”. In: *Physical Review B* 82.8 (Aug. 2010), p. 081301. ISSN: 1098-0121. DOI: [10.1103/PhysRevB.82.081301](https://doi.org/10.1103/PhysRevB.82.081301) (cit. on pp. 3, 36).
- [45] C. Schneider et al. “Exciton-polariton trapping and potential landscape engineering”. In: *Reports on Progress in Physics* 80.1 (Jan. 2017), p. 016503. ISSN: 0034-4885. DOI: [10.1088/0034-4885/80/1/016503](https://doi.org/10.1088/0034-4885/80/1/016503) (cit. on p. 3).
- [46] L. C. Flatten, A. A. Trichet, and J. M. Smith. “Spectral engineering of coupled open-access microcavities”. In: *Laser and Photonics Reviews* 10.2 (2016), pp. 257–263. ISSN: 18638899. DOI: [10.1002/lpor.201500138](https://doi.org/10.1002/lpor.201500138) (cit. on pp. 3, 37, 156).
- [47] N. G. Berloff et al. “Realizing the classical XY Hamiltonian in polariton simulators”. In: *Nature Materials* 16.11 (Nov. 2017), pp. 1120–1126. ISSN: 1476-1122. DOI: [10.1038/nmat4971](https://doi.org/10.1038/nmat4971) (cit. on pp. 3, 4, 37).
- [48] V. Goblot et al. “Nonlinear Polariton Fluids in a Flatband Reveal Discrete Gap Solitons”. In: *Physical Review Letters* 123.11 (Sept. 2019), p. 113901. ISSN: 0031-9007. DOI: [10.1103/PhysRevLett.123.113901](https://doi.org/10.1103/PhysRevLett.123.113901). arXiv: [1905.03759](https://arxiv.org/abs/1905.03759) (cit. on pp. 3, 41, 43, 126).
- [49] T. Jacqmin et al. “Direct Observation of Dirac Cones and a Flatband in a Honeycomb Lattice for Polaritons”. In: *Physical Review Letters* 112.11 (Mar. 2014), p. 116402. ISSN: 0031-9007. DOI: [10.1103/PhysRevLett.112.116402](https://doi.org/10.1103/PhysRevLett.112.116402) (cit. on pp. 3, 41, 42, 154).
- [50] C. E. Whittaker et al. “Exciton Polaritons in a Two-Dimensional Lieb Lattice with Spin-Orbit Coupling”. In: *Physical Review Letters* 120.9 (Mar. 2018), p. 097401. ISSN: 0031-9007. DOI: [10.1103/PhysRevLett.120.097401](https://doi.org/10.1103/PhysRevLett.120.097401) (cit. on pp. 3, 39, 42, 126).
- [51] M. J. Hartmann, F. G. S. L. Brandão, and M. B. Plenio. “Strongly interacting polaritons in coupled arrays of cavities”. In: *Nature Physics* 2.12 (Dec. 2006), pp. 849–855. ISSN: 1745-2473. DOI: [10.1038/nphys462](https://doi.org/10.1038/nphys462) (cit. on pp. 4, 34, 111, 112).
- [52] I. Carusotto et al. “Fermionized Photons in an Array of Driven Dissipative Nonlinear Cavities”. In: *Physical Review Letters* 103.3 (July 2009), p. 033601. ISSN: 0031-9007. DOI: [10.1103/PhysRevLett.103.033601](https://doi.org/10.1103/PhysRevLett.103.033601) (cit. on pp. 4, 34, 112).
- [53] M. J. Hartmann. “Polariton Crystallization in Driven Arrays of Lossy Nonlinear Resonators”. In: *Physical Review Letters* 104.11 (Mar. 2010), p. 113601. ISSN: 0031-9007. DOI: [10.1103/PhysRevLett.104.113601](https://doi.org/10.1103/PhysRevLett.104.113601) (cit. on pp. 4, 43, 112).
- [54] A. Delteil et al. “Towards polariton blockade of confined exciton–polaritons”. In: *Nature Materials* 18.3 (Mar. 2019), pp. 219–222. ISSN: 1476-1122. DOI: [10.1038/s41563-019-0282-y](https://doi.org/10.1038/s41563-019-0282-y) (cit. on pp. 4, 122, 126, 135).
- [55] G. Muñoz-Matutano et al. “Emergence of quantum correlations from interacting fibre-cavity polaritons”. In: *Nature Materials* 18.3 (Mar. 2019), pp. 213–218. ISSN: 1476-1122. DOI: [10.1038/s41563-019-0281-z](https://doi.org/10.1038/s41563-019-0281-z) (cit. on pp. 4, 122, 126, 135).

- [56] E. Togan et al. “Enhanced Interactions between Dipolar Polaritons”. In: *Physical Review Letters* 121.22 (Nov. 2018), p. 227402. ISSN: 0031-9007. DOI: [10.1103/PhysRevLett.121.227402](https://doi.org/10.1103/PhysRevLett.121.227402) (cit. on pp. 4, 112, 126, 156).
- [57] D. Ballarini et al. “Polaritonic neuromorphic computing outperforms linear classifiers”. In: (Nov. 2019), pp. 1–14. arXiv: [1911.02923](https://arxiv.org/abs/1911.02923) (cit. on p. 4).
- [58] A. Forbes. “Structured Light from Lasers”. In: *Laser & Photonics Reviews* 1900140 (Oct. 2019), p. 1900140. ISSN: 1863-8880. DOI: [10.1002/lpor.201900140](https://doi.org/10.1002/lpor.201900140) (cit. on pp. 4, 76, 78, 105, 154).
- [59] T. Ozawa et al. “Topological photonics”. In: *Reviews of Modern Physics* 91.1 (Mar. 2019), p. 015006. ISSN: 0034-6861. DOI: [10.1103/RevModPhys.91.015006](https://doi.org/10.1103/RevModPhys.91.015006) (cit. on pp. 4, 154).
- [60] S. Klembt et al. “Exciton-polariton topological insulator”. In: *Nature* 562.7728 (Oct. 2018), pp. 552–556. ISSN: 0028-0836. DOI: [10.1038/s41586-018-0601-5](https://doi.org/10.1038/s41586-018-0601-5) (cit. on pp. 4, 126, 154).
- [61] N. Ismail et al. “Fabry-Pérot resonator: spectral line shapes, generic and related Airy distributions, linewidths, finesses, and performance at low or frequency-dependent reflectivity”. In: *Optics Express* 24.15 (2016), p. 16366. DOI: [10.1364/oe.24.016366](https://doi.org/10.1364/oe.24.016366) (cit. on p. 8).
- [62] L. Rayleigh. “On the Reflection of Light from a Regularly Stratified Medium”. In: *Proceedings of the Royal Society A: Mathematical, Physical and Engineering Sciences* 93.655 (Oct. 1917), pp. 565–577. ISSN: 1364-5021. DOI: [10.1098/rspa.1917.0040](https://doi.org/10.1098/rspa.1917.0040) (cit. on p. 9).
- [63] J. D. Joannopoulos et al. *Photonic Crystals*. Vol. 6. 2. Princeton University Press, Oct. 2011, p. 305. ISBN: 9781400828241. DOI: [10.2307/j.ctvcvcm4gz9](https://doi.org/10.2307/j.ctvcvcm4gz9) (cit. on pp. 9, 10, 78).
- [64] M. A. Afromowitz. “Refractive index of Ga_{1-x}Al_xAs”. In: *Solid State Communications* 15.1 (1974), pp. 59–63. ISSN: 00381098. DOI: [10.1016/0038-1098\(74\)90014-3](https://doi.org/10.1016/0038-1098(74)90014-3) (cit. on p. 10).
- [65] S. Gehrsitz et al. “The refractive index of Al_xGa_{1-x}As below the band gap: Accurate determination and empirical modeling”. In: *Journal of Applied Physics* 87.11 (2000), pp. 7825–7837. ISSN: 00218979. DOI: [10.1063/1.373462](https://doi.org/10.1063/1.373462) (cit. on p. 10).
- [66] D. C. Reynolds et al. “Refractive index, n , and dispersion, $-dn/d\lambda$, of GaAs at 2 K determined from Fabry-Pérot cavity oscillations”. In: *Journal of Applied Physics* 61.1 (Jan. 1987), pp. 342–345. ISSN: 0021-8979. DOI: [10.1063/1.338828](https://doi.org/10.1063/1.338828) (cit. on p. 11).
- [67] H. G. Grimmeiss and B. Monemar. “Temperature dependence of the refractive index of AIAs and AIP”. In: *Physica Status Solidi (a)* 5.1 (Apr. 1971), pp. 109–114. ISSN: 00318965. DOI: [10.1002/pssa.2210050111](https://doi.org/10.1002/pssa.2210050111) (cit. on p. 11).
- [68] M. D. Sturge. “Optical absorption of gallium arsenide between 0.6 and 2.75 eV”. In: *Physical Review* 127.3 (1962), pp. 768–773. ISSN: 0031899X. DOI: [10.1103/PhysRev.127.768](https://doi.org/10.1103/PhysRev.127.768) (cit. on pp. 11, 94).
- [69] C. C. Katsidis and D. I. Siapkas. “General transfer-matrix method for optical multilayer systems with coherent, partially coherent, and incoherent interference”. In: *Applied Optics* 41.19 (July 2002), p. 3978. ISSN: 0003-6935. DOI: [10.1364/AO.41.003978](https://doi.org/10.1364/AO.41.003978) (cit. on p. 11).
- [70] V. Savona. *Confined Photon Systems*. Ed. by H. Benisty et al. Vol. 531. Lecture Notes in Physics. Berlin, Heidelberg: Springer Berlin Heidelberg, 1999, pp. 173–

242. ISBN: 978-3-540-66435-2. DOI: [10.1007/BFb0104378](https://doi.org/10.1007/BFb0104378) (cit. on pp. [11](#), [20](#), [21](#), [23](#), [29](#), [36](#), [53](#)).
- [71] G. Panzarini et al. “Exciton-light coupling in single and coupled semiconductor microcavities: Polariton dispersion and polarization splitting”. In: *Phys. Rev. B* 59.7 (1999), pp. 5082–5089 (cit. on pp. [11](#), [12](#), [23](#), [82](#)).
- [72] R. P. Stanley et al. “Ultrahigh finesse microcavity with distributed Bragg reflectors”. In: *Applied Physics Letters* 65.15 (Oct. 1994), pp. 1883–1885. ISSN: 0003-6951. DOI: [10.1063/1.112877](https://doi.org/10.1063/1.112877) (cit. on pp. [11](#), [12](#)).
- [73] J. Pohl et al. “Reduction of absorption losses in MOVPE-grown AlGaAs Bragg mirrors”. In: *Optics Letters* 43.15 (Aug. 2018), p. 3522. ISSN: 0146-9592. DOI: [10.1364/OL.43.003522](https://doi.org/10.1364/OL.43.003522) (cit. on pp. [11](#), [35](#)).
- [74] A. Kavokin, G. Malpuech, and M. Glazov. “Optical Spin Hall Effect”. In: *Physical Review Letters* 95.13 (Sept. 2005), p. 136601. ISSN: 0031-9007. DOI: [10.1103/PhysRevLett.95.136601](https://doi.org/10.1103/PhysRevLett.95.136601) (cit. on pp. [13](#), [46](#), [49](#), [82](#)).
- [75] K. V. Kavokin et al. “Quantum Theory of Spin Dynamics of Exciton-Polaritons in Microcavities”. In: *Physical Review Letters* 92.1 (Jan. 2004), p. 017401. ISSN: 0031-9007. DOI: [10.1103/PhysRevLett.92.017401](https://doi.org/10.1103/PhysRevLett.92.017401) (cit. on pp. [13](#), [86](#)).
- [76] C. Leyder et al. “Observation of the optical spin Hall effect”. In: *Nature Physics* 3.9 (Sept. 2007), pp. 628–631. ISSN: 1745-2473. DOI: [10.1038/nphys676](https://doi.org/10.1038/nphys676) (cit. on pp. [14](#), [46](#)).
- [77] M. Maragkou et al. “Optical analogue of the spin Hall effect in a photonic cavity”. In: *Optics Letters* 36.7 (Apr. 2011), p. 1095. ISSN: 0146-9592. DOI: [10.1364/OL.36.001095](https://doi.org/10.1364/OL.36.001095) (cit. on pp. [14](#), [46](#)).
- [78] K. Lekenta et al. “Tunable optical spin Hall effect in a liquid crystal microcavity”. In: *Light: Science & Applications* 7.1 (Dec. 2018), p. 74. ISSN: 2047-7538. DOI: [10.1038/s41377-018-0076-z](https://doi.org/10.1038/s41377-018-0076-z) (cit. on p. [14](#)).
- [79] S. Dufferwiel et al. “Spin Textures of Exciton-Polaritons in a Tunable Microcavity with Large TE-TM Splitting”. In: *Physical Review Letters* 115.24 (Dec. 2015), p. 246401. ISSN: 0031-9007. DOI: [10.1103/PhysRevLett.115.246401](https://doi.org/10.1103/PhysRevLett.115.246401) (cit. on pp. [14](#), [49](#), [79](#)).
- [80] K. Y. Bliokh et al. “Spin-orbit interactions of light”. In: *Nature Photonics* 9.12 (Dec. 2015), pp. 796–808. ISSN: 1749-4885. DOI: [10.1038/nphoton.2015.201](https://doi.org/10.1038/nphoton.2015.201) (cit. on pp. [14](#), [77–79](#), [153](#)).
- [81] P. Y. Yu and M. Cardona. *Fundamentals of Semiconductors*. Vol. 59. Graduate Texts in Physics 6. Berlin, Heidelberg: Springer Berlin Heidelberg, 2010, pp. 442–443. ISBN: 978-3-642-00709-5. DOI: [10.1007/978-3-642-00710-1](https://doi.org/10.1007/978-3-642-00710-1) (cit. on pp. [14–17](#), [20](#)).
- [82] F. M. Bickelhaupt and E. J. Baerends. “Kohn-Sham Density Functional Theory: Predicting and Understanding Chemistry”. In: *Reviews in Computational Chemistry*. John Wiley & Sons, Ltd, 2007, pp. 1–86. ISBN: 9780470125922. DOI: [10.1002/9780470125922.ch1](https://doi.org/10.1002/9780470125922.ch1) (cit. on p. [14](#)).
- [83] R. Car and M. Parrinello. “Unified Approach for Molecular Dynamics and Density-Functional Theory”. In: *Physical Review Letters* 55.22 (Nov. 1985), pp. 2471–2474. ISSN: 0031-9007. DOI: [10.1103/PhysRevLett.55.2471](https://doi.org/10.1103/PhysRevLett.55.2471) (cit. on p. [14](#)).
- [84] C. S. Wang and B. M. Klein. “First-principles electronic structure of Si, Ge, GaP, GaAs, ZnS, and ZnSe. II. Optical properties”. In: *Phys. Rev. B* 24.6 (Sept. 1981), pp. 3417–3429. DOI: [10.1103/PhysRevB.24.3417](https://doi.org/10.1103/PhysRevB.24.3417) (cit. on pp. [14](#), [16](#)).

- [85] J. M. Luttinger and W. Kohn. “Motion of Electrons and Holes in Perturbed Periodic Fields”. In: *Physical Review* 97.4 (Feb. 1955), pp. 869–883. ISSN: 0031-899X. DOI: [10.1103/PhysRev.97.869](https://doi.org/10.1103/PhysRev.97.869) (cit. on p. 14).
- [86] G. Bastard. *Wave mechanics applied to semiconductor heterostructures*. United States: John Wiley and Sons Inc, 1990. ISBN: 0-471-21708-1 (cit. on pp. 14–16, 18, 20, 21, 86).
- [87] S. Richard, F. Aniel, and G. Fishman. “Energy-band structure of Ge, Si, and GaAs: A thirty-band k·p method”. In: *Physical Review B* 70.23 (2004), pp. 1–6. ISSN: 10980121. DOI: [10.1103/PhysRevB.70.235204](https://doi.org/10.1103/PhysRevB.70.235204) (cit. on pp. 14, 15).
- [88] Z. M. Fang et al. “Photoluminescence of InSb, InAs, and InAsSb grown by organometallic vapor phase epitaxy”. In: *Journal of Applied Physics* 67.11 (June 1990), pp. 7034–7039. ISSN: 0021-8979. DOI: [10.1063/1.345050](https://doi.org/10.1063/1.345050) (cit. on p. 16).
- [89] S. Paul, J. B. Roy, and P. K. Basu. “Empirical expressions for the alloy composition and temperature dependence of the band gap and intrinsic carrier density in $\text{Ga}_x\text{In}_{1-x}\text{As}$ ”. In: *Journal of Applied Physics* 69.2 (1991), pp. 827–829. ISSN: 00218979. DOI: [10.1063/1.348919](https://doi.org/10.1063/1.348919) (cit. on pp. 16, 17).
- [90] M. Cardona. “Electron Effective Masses of InAs and GaAs as a Function of Temperature and Doping”. In: *Physical Review* 121.3 (Feb. 1961), pp. 752–758. ISSN: 0031-899X. DOI: [10.1103/PhysRev.121.752](https://doi.org/10.1103/PhysRev.121.752) (cit. on p. 16).
- [91] S. Adachi. “Material parameters of $\text{In}_{1-x}\text{Ga}_x\text{As}_y\text{P}_{1-y}$ and related binaries”. In: *Journal of Applied Physics* 53.12 (Dec. 1982), pp. 8775–8792. ISSN: 0021-8979. DOI: [10.1063/1.330480](https://doi.org/10.1063/1.330480) (cit. on p. 16).
- [92] M. Levinshstein, S. Rumyantsev, and M. Shur. *Handbook Series on Semiconductor Parameters*. Vol. 1. WORLD SCIENTIFIC, Nov. 1996. ISBN: 978-981-02-2934-4. DOI: [10.1142/2046-vol1](https://doi.org/10.1142/2046-vol1) (cit. on p. 16).
- [93] R. Atanasov et al. “Exciton properties and optical response in InGaAs/GaAs strained quantum wells”. In: *Physical Review B* 50.19 (Nov. 1994), pp. 14381–14388. DOI: [10.1103/PhysRevB.50.14381](https://doi.org/10.1103/PhysRevB.50.14381) (cit. on pp. 17, 19, 21).
- [94] J. Reithmaier et al. “Band offset in elastically strained InGaAs/GaAs multiple quantum wells determined by optical absorption and electronic Raman scattering”. In: *Applied Physics Letters* 56.6 (Feb. 1990), pp. 536–538. ISSN: 0003-6951. DOI: [10.1063/1.102737](https://doi.org/10.1063/1.102737) (cit. on p. 17).
- [95] J. Barnes et al. “Characterization of GaAs/InGaAs quantum wells using photocurrent spectroscopy”. In: *Journal of Applied Physics* 79.10 (May 1996), pp. 7775–7779. ISSN: 0021-8979. DOI: [10.1063/1.362383](https://doi.org/10.1063/1.362383) (cit. on p. 17).
- [96] V. I. Zubkov et al. “Determination of band offsets in strained InGaAs/GaAs quantum wells by capacitance-voltage profiling and Schrödinger-Poisson self-consistent simulation”. In: *Physical Review B* 70.7 (Aug. 2004), p. 075312. ISSN: 1098-0121. DOI: [10.1103/PhysRevB.70.075312](https://doi.org/10.1103/PhysRevB.70.075312) (cit. on p. 17).
- [97] G. Bastard et al. “Exciton binding energy in quantum wells”. In: *Physical Review B* 26.4 (Aug. 1982), pp. 1974–1979. DOI: [10.1103/PhysRevB.26.1974](https://doi.org/10.1103/PhysRevB.26.1974) (cit. on p. 18).
- [98] K. J. Moore et al. “Observations and calculations of the exciton binding energy in (In,Ga)As/GaAs strained-quantum-well heterostructures”. In: *Physical Review B* 41.2 (1990), pp. 1090–1094. ISSN: 01631829. DOI: [10.1103/PhysRevB.41.1090](https://doi.org/10.1103/PhysRevB.41.1090) (cit. on pp. 18, 19).
- [99] L. C. Andreani and A. Pasquarello. “Accurate theory of excitons in GaAs-GaAlAs quantum wells”. In: *Physical Review B* 42.14 (Nov. 1990), pp. 8928–8938. ISSN: 0163-1829. DOI: [10.1103/PhysRevB.42.8928](https://doi.org/10.1103/PhysRevB.42.8928) (cit. on pp. 20, 21).

- [100] M. Wouters. “Resonant polariton-polariton scattering in semiconductor microcavities”. In: *Physical Review B* 76.4 (July 2007), p. 045319. ISSN: 1098-0121. DOI: [10.1103/PhysRevB.76.045319](https://doi.org/10.1103/PhysRevB.76.045319) (cit. on pp. 20, 22).
- [101] H. Haug and S. W. Koch. *Quantum Theory of the Optical and Electronic Properties of Semiconductors*. WORLD SCIENTIFIC, Jan. 2009. ISBN: 978-981-283-883-4. DOI: [10.1142/7184](https://doi.org/10.1142/7184) (cit. on pp. 20, 22).
- [102] A. Klein and E. R. Marshalek. “Boson realizations of Lie algebras with applications to nuclear physics”. In: *Reviews of Modern Physics* 63.2 (Apr. 1991), pp. 375–558. ISSN: 0034-6861. DOI: [10.1103/RevModPhys.63.375](https://doi.org/10.1103/RevModPhys.63.375) (cit. on p. 22).
- [103] M. COMBESCOT, O. BETBEDERMATIBET, and F. DUBIN. “The many-body physics of composite bosons”. In: *Physics Reports* 463.5-6 (July 2008), pp. 215–320. ISSN: 03701573. DOI: [10.1016/j.physrep.2007.11.003](https://doi.org/10.1016/j.physrep.2007.11.003) (cit. on p. 22).
- [104] S. Schmitt-Rink, D. Chemla, and D. Miller. “Linear and nonlinear optical properties of semiconductor quantum wells”. In: *Advances in Physics* 38.2 (Jan. 1989), pp. 89–188. ISSN: 0001-8732. DOI: [10.1080/00018738900101102](https://doi.org/10.1080/00018738900101102) (cit. on p. 22).
- [105] G. Rochat et al. “Excitonic Bloch equations for a two-dimensional system of interacting excitons”. In: *Physical Review B* 61.20 (May 2000), pp. 13856–13862. ISSN: 0163-1829. DOI: [10.1103/PhysRevB.61.13856](https://doi.org/10.1103/PhysRevB.61.13856) (cit. on p. 22).
- [106] L. Kappei et al. “Direct Observation of the Mott Transition in an Optically Excited Semiconductor Quantum Well”. In: *Physical Review Letters* 94.14 (Apr. 2005), p. 147403. ISSN: 0031-9007. DOI: [10.1103/PhysRevLett.94.147403](https://doi.org/10.1103/PhysRevLett.94.147403) (cit. on p. 22).
- [107] C. Ciuti et al. “Role of the exchange of carriers in elastic exciton-exciton scattering in quantum wells”. In: *Physical Review B* 58.12 (Sept. 1998), pp. 7926–7933. ISSN: 0163-1829. DOI: [10.1103/PhysRevB.58.7926](https://doi.org/10.1103/PhysRevB.58.7926) (cit. on pp. 22, 27).
- [108] M. M. Glazov et al. “Polariton-polariton scattering in microcavities: A microscopic theory”. In: *Physical Review B* 80.15 (Oct. 2009), p. 155306. ISSN: 1098-0121. DOI: [10.1103/PhysRevB.80.155306](https://doi.org/10.1103/PhysRevB.80.155306) (cit. on pp. 22, 52).
- [109] M. Vladimirova et al. “Polariton-polariton interaction constants in microcavities”. In: *Physical Review B* 82.7 (Aug. 2010), p. 075301. ISSN: 1098-0121. DOI: [10.1103/PhysRevB.82.075301](https://doi.org/10.1103/PhysRevB.82.075301) (cit. on pp. 22, 28).
- [110] E. Estrecho et al. “Direct measurement of polariton-polariton interaction strength in the Thomas-Fermi regime of exciton-polariton condensation”. In: *Physical Review B* 100.3 (July 2019), p. 035306. ISSN: 2469-9950. DOI: [10.1103/PhysRevB.100.035306](https://doi.org/10.1103/PhysRevB.100.035306) (cit. on p. 22).
- [111] V. Savona et al. “Quantum well excitons in semiconductor microcavities: Unified treatment of weak and strong coupling regimes”. In: *Solid State Communications* 93.9 (Mar. 1995), pp. 733–739. ISSN: 00381098. DOI: [10.1016/0038-1098\(94\)00865-5](https://doi.org/10.1016/0038-1098(94)00865-5) (cit. on pp. 23, 24).
- [112] Y. Xu, R. K. Lee, and A. Yariv. “Quantum analysis and the classical analysis of spontaneous emission in a microcavity”. In: *Physical Review A* 61.3 (Feb. 2000), p. 033807. ISSN: 1050-2947. DOI: [10.1103/PhysRevA.61.033807](https://doi.org/10.1103/PhysRevA.61.033807) (cit. on pp. 23, 24).
- [113] S. R.-K. Rodriguez. “Classical and quantum distinctions between weak and strong coupling”. In: *European Journal of Physics* 37.2 (Mar. 2016), p. 025802. ISSN: 0143-0807. DOI: [10.1088/0143-0807/37/2/025802](https://doi.org/10.1088/0143-0807/37/2/025802) (cit. on pp. 23, 24, 114).

- [114] L. Novotny. “Strong coupling, energy splitting, and level crossings: A classical perspective”. In: *American Journal of Physics* 78.11 (2010), pp. 1199–1202. ISSN: 0002-9505. DOI: [10.1119/1.3471177](https://doi.org/10.1119/1.3471177) (cit. on p. 24).
- [115] E. M. Purcell. “Spontaneous Emission Probabilities at Radio Frequencies”. In: *Confined Electrons and Photons: New Physics and Applications*. Ed. by E. Burstein and C. Weisbuch. Boston, MA: Springer US, 1946, p. 839. ISBN: 978-1-4615-1963-8. DOI: [10.1007/978-1-4615-1963-8_40](https://doi.org/10.1007/978-1-4615-1963-8_40) (cit. on p. 24).
- [116] M.-A. Miri and A. Alù. “Exceptional points in optics and photonics”. In: *Science* 363.6422 (Jan. 2019), eaar7709. ISSN: 0036-8075. DOI: [10.1126/science.aar7709](https://doi.org/10.1126/science.aar7709) (cit. on p. 24).
- [117] L. Feng, R. El-Ganainy, and L. Ge. “Non-Hermitian photonics based on parity–time symmetry”. In: *Nature Photonics* 11.12 (Dec. 2017), pp. 752–762. ISSN: 1749-4885. DOI: [10.1038/s41566-017-0031-1](https://doi.org/10.1038/s41566-017-0031-1) (cit. on p. 24).
- [118] T. Niemczyk et al. “Beyond the Jaynes-Cummings model: circuit QED in the ultrastrong coupling regime”. In: *Nature Physics* 6.10 (2010), pp. 772–776. ISSN: 1745-2473. DOI: [10.1038/nphys1730](https://doi.org/10.1038/nphys1730). arXiv: [1003.2376](https://arxiv.org/abs/1003.2376) (cit. on p. 24).
- [119] G. Scalari et al. “Ultrastrong coupling of the cyclotron transition of a 2D electron gas to a THz metamaterial”. In: *Science* 335.6074 (2012), pp. 1323–1326. ISSN: 10959203. DOI: [10.1126/science.1216022](https://doi.org/10.1126/science.1216022) (cit. on p. 24).
- [120] D. De Bernardis et al. “Breakdown of gauge invariance in ultrastrong-coupling cavity QED”. In: *Physical Review A* 98.5 (Nov. 2018), p. 053819. ISSN: 2469-9926. DOI: [10.1103/PhysRevA.98.053819](https://doi.org/10.1103/PhysRevA.98.053819) (cit. on p. 24).
- [121] P. Forn-Díaz et al. “Ultrastrong coupling regimes of light-matter interaction”. In: *Reviews of Modern Physics* 91.2 (2019), p. 25005. ISSN: 0034-6861. DOI: [10.1103/revmodphys.91.025005](https://doi.org/10.1103/revmodphys.91.025005) (cit. on p. 24).
- [122] A. Frisk Kockum et al. “Ultrastrong coupling between light and matter”. In: *Nature Reviews Physics* 1.1 (2019), pp. 19–40. ISSN: 2522-5820. DOI: [10.1038/s42254-018-0006-2](https://doi.org/10.1038/s42254-018-0006-2) (cit. on p. 24).
- [123] J. Rogel-Salazar. “The Gross–Pitaevskii equation and Bose–Einstein condensates”. In: *European Journal of Physics* 34.2 (Mar. 2013), pp. 247–257. ISSN: 0143-0807. DOI: [10.1088/0143-0807/34/2/247](https://doi.org/10.1088/0143-0807/34/2/247) (cit. on pp. 27, 28).
- [124] L. Pitaevskii and S. Stringari. *Bose-Einstein condensation and superfluidity*. International series of monographs on physics. Oxford: Oxford University Press, 2016. DOI: [10.1093/acprof:oso/9780198758884.001.0001](https://doi.org/10.1093/acprof:oso/9780198758884.001.0001) (cit. on pp. 27, 28, 63, 67).
- [125] M. Brambilla et al. “Transverse laser patterns. II. Variational principle for pattern selection, spatial multistability, and laser hydrodynamics”. In: *Physical Review A* 43.9 (May 1991), pp. 5114–5120. ISSN: 1050-2947. DOI: [10.1103/PhysRevA.43.5114](https://doi.org/10.1103/PhysRevA.43.5114) (cit. on p. 28).
- [126] K. Staliunas. “Laser Ginzburg-Landau equation and laser hydrodynamics”. In: *Physical Review A* 48.2 (Aug. 1993), pp. 1573–1581. ISSN: 1050-2947. DOI: [10.1103/PhysRevA.48.1573](https://doi.org/10.1103/PhysRevA.48.1573) (cit. on p. 28).
- [127] C. Ciuti and I. Carusotto. “Input-output theory of cavities in the ultrastrong coupling regime: The case of time-independent cavity parameters”. In: *Physical Review A* 74.3 (Sept. 2006), p. 033811. ISSN: 1050-2947. DOI: [10.1103/PhysRevA.74.033811](https://doi.org/10.1103/PhysRevA.74.033811) (cit. on p. 29).
- [128] P. G. Savvidis et al. “Angle-Resonant Stimulated Polariton Amplifier”. In: *Physical Review Letters* 84.7 (Feb. 2000), pp. 1547–1550. ISSN: 0031-9007. DOI: [10.1103/PhysRevLett.84.1547](https://doi.org/10.1103/PhysRevLett.84.1547) (cit. on pp. 30, 113, 126, 154).

- [129] M. Saba et al. “High-temperature ultrafast polariton parametric amplification in semiconductor microcavities”. In: *Nature* 414.6865 (Dec. 2001), pp. 731–735. ISSN: 0028-0836. DOI: [10.1038/414731a](https://doi.org/10.1038/414731a) (cit. on p. 30).
- [130] J. J. Baumberg et al. “Parametric oscillation in a vertical microcavity: A polariton condensate or micro-optical parametric oscillation”. In: *Physical Review B* 62.24 (Dec. 2000), R16247–R16250. ISSN: 0163-1829. DOI: [10.1103/PhysRevB.62.R16247](https://doi.org/10.1103/PhysRevB.62.R16247) (cit. on p. 30).
- [131] R. M. Stevenson et al. “Continuous Wave Observation of Massive Polariton Redistribution by Stimulated Scattering in Semiconductor Microcavities”. In: *Physical Review Letters* 85.17 (Oct. 2000), pp. 3680–3683. ISSN: 0031-9007. DOI: [10.1103/PhysRevLett.85.3680](https://doi.org/10.1103/PhysRevLett.85.3680) (cit. on pp. 30, 113, 126, 154).
- [132] C. Diederichs et al. “Parametric oscillation in vertical triple microcavities”. In: *Nature* 440.7086 (Apr. 2006), pp. 904–907. ISSN: 0028-0836. DOI: [10.1038/nature04602](https://doi.org/10.1038/nature04602) (cit. on pp. 30, 113, 126, 154).
- [133] A. Baas et al. “Optical bistability in semiconductor microcavities”. In: *Physical Review A* 69.2 (2004), p. 023809. ISSN: 1050-2947. DOI: [10.1103/PhysRevA.69.023809](https://doi.org/10.1103/PhysRevA.69.023809). arXiv: [0306473 \[cond-mat\]](https://arxiv.org/abs/0306473) (cit. on pp. 30, 122).
- [134] J. P. Karr et al. “Squeezing in semiconductor microcavities in the strong-coupling regime”. In: *Physical Review A* 69.3 (Mar. 2004), p. 031802. ISSN: 1050-2947. DOI: [10.1103/PhysRevA.69.031802](https://doi.org/10.1103/PhysRevA.69.031802) (cit. on p. 30).
- [135] E. Giacobino et al. “Polariton-generated intensity squeezing in semiconductor micropillars”. In: *Nature Communications* 5.1 (2014), pp. 1–7. DOI: [10.1038/ncomms4260](https://doi.org/10.1038/ncomms4260) (cit. on pp. 30, 130).
- [136] M. Romanelli et al. “Four Wave Mixing Oscillation in a Semiconductor Microcavity: Generation of Two Correlated Polariton Populations”. In: *Physical Review Letters* 98.10 (Mar. 2007), p. 106401. ISSN: 0031-9007. DOI: [10.1103/PhysRevLett.98.106401](https://doi.org/10.1103/PhysRevLett.98.106401) (cit. on pp. 30, 113, 126).
- [137] I. Carusotto and C. Ciuti. “Probing Microcavity Polariton Superfluidity through Resonant Rayleigh Scattering”. In: *Physical Review Letters* 93.16 (Oct. 2004), p. 166401. ISSN: 0031-9007. DOI: [10.1103/PhysRevLett.93.166401](https://doi.org/10.1103/PhysRevLett.93.166401) (cit. on p. 30).
- [138] G. Lerario et al. “Room-temperature superfluidity in a polariton condensate”. In: *Nature Physics* 13.9 (Sept. 2017), pp. 837–841. ISSN: 1745-2473. DOI: [10.1038/nphys4147](https://doi.org/10.1038/nphys4147) (cit. on p. 30).
- [139] V. Savona et al. “Theory of polariton photoluminescence in arbitrary semiconductor microcavity structures”. In: *Physical Review B* 53.19 (May 1996), pp. 13051–13062. ISSN: 0163-1829. DOI: [10.1103/PhysRevB.53.13051](https://doi.org/10.1103/PhysRevB.53.13051) (cit. on pp. 30, 32).
- [140] F. Tassone et al. “Bottleneck effects in the relaxation and photoluminescence of microcavity polaritons”. In: *Physical Review B* 56.12 (Sept. 1997), pp. 7554–7563. ISSN: 0163-1829. DOI: [10.1103/PhysRevB.56.7554](https://doi.org/10.1103/PhysRevB.56.7554) (cit. on p. 30).
- [141] G. Malpuech et al. “Polariton lasing by exciton-electron scattering in semiconductor microcavities”. In: *Physical Review B* 65.15 (Apr. 2002), p. 153310. ISSN: 0163-1829. DOI: [10.1103/PhysRevB.65.153310](https://doi.org/10.1103/PhysRevB.65.153310) (cit. on pp. 30, 32).
- [142] R. Houdré et al. “Measurement of Cavity-Polariton Dispersion Curve from Angle-Resolved Photoluminescence Experiments”. In: *Physical Review Letters* 73.15 (Oct. 1994), pp. 2043–2046. ISSN: 0031-9007. DOI: [10.1103/PhysRevLett.73.2043](https://doi.org/10.1103/PhysRevLett.73.2043) (cit. on pp. 31, 59).

- [143] J.-J. Greffet et al. “Light Emission by Nonequilibrium Bodies: Local Kirchhoff Law”. In: *Physical Review X* 8.2 (Apr. 2018), p. 021008. ISSN: 2160-3308. DOI: [10.1103/PhysRevX.8.021008](https://doi.org/10.1103/PhysRevX.8.021008) (cit. on p. 32).
- [144] H. Deng, H. Haug, and Y. Yamamoto. “Exciton-polariton Bose-Einstein condensation”. In: *Reviews of Modern Physics* 82.2 (May 2010), pp. 1489–1537. ISSN: 0034-6861. DOI: [10.1103/RevModPhys.82.1489](https://doi.org/10.1103/RevModPhys.82.1489) (cit. on pp. 32, 80).
- [145] D. Porras et al. “Polariton dynamics and Bose-Einstein condensation in semiconductor microcavities”. In: *Physical Review B* 66.8 (Aug. 2002), p. 085304. ISSN: 0163-1829. DOI: [10.1103/PhysRevB.66.085304](https://doi.org/10.1103/PhysRevB.66.085304) (cit. on p. 32).
- [146] S. Kéna-Cohen and S. R. Forrest. “Room-temperature polariton lasing in an organic single-crystal microcavity”. In: *Nature Photonics* 4.6 (June 2010), pp. 371–375. ISSN: 1749-4885. DOI: [10.1038/nphoton.2010.86](https://doi.org/10.1038/nphoton.2010.86) (cit. on p. 32).
- [147] J. D. Plumhof et al. “Room-temperature Bose-Einstein condensation of cavity exciton-polaritons in a polymer”. In: *Nature Materials* 13.3 (Mar. 2014), pp. 247–252. ISSN: 1476-1122. DOI: [10.1038/nmat3825](https://doi.org/10.1038/nmat3825) (cit. on p. 32).
- [148] M. Wouters and I. Carusotto. “Excitations in a Nonequilibrium Bose-Einstein Condensate of Exciton Polaritons”. In: *Physical Review Letters* 99.14 (Oct. 2007), p. 140402. ISSN: 0031-9007. DOI: [10.1103/PhysRevLett.99.140402](https://doi.org/10.1103/PhysRevLett.99.140402) (cit. on p. 32).
- [149] N. Bobrovska, E. A. Ostrovskaya, and M. Matuszewski. “Stability and spatial coherence of nonresonantly pumped exciton-polariton condensates”. In: *Physical Review B - Condensed Matter and Materials Physics* 90.20 (2014), pp. 1–6. ISSN: 1550235X. DOI: [10.1103/PhysRevB.90.205304](https://doi.org/10.1103/PhysRevB.90.205304) (cit. on p. 32).
- [150] T. C. Liew et al. “Instability-induced formation and nonequilibrium dynamics of phase defects in polariton condensates”. In: *Physical Review B - Condensed Matter and Materials Physics* 91.8 (2015), pp. 1–12. ISSN: 1550235X. DOI: [10.1103/PhysRevB.91.085413](https://doi.org/10.1103/PhysRevB.91.085413) (cit. on p. 32).
- [151] F. Baboux et al. “Unstable and stable regimes of polariton condensation”. In: *Optica* 5.10 (Oct. 2018), p. 1163. ISSN: 2334-2536. DOI: [10.1364/OPTICA.5.001163](https://doi.org/10.1364/OPTICA.5.001163) (cit. on p. 32).
- [152] Y. Sun et al. “Bose-Einstein Condensation of Long-Lifetime Polaritons in Thermal Equilibrium”. In: *Physical Review Letters* 118.1 (Jan. 2017), p. 016602. ISSN: 0031-9007. DOI: [10.1103/PhysRevLett.118.016602](https://doi.org/10.1103/PhysRevLett.118.016602) (cit. on p. 32).
- [153] J. Klaers et al. “Bose-Einstein condensation of photons in an optical microcavity”. In: *Nature* 468.7323 (2010), pp. 545–548. ISSN: 00280836. DOI: [10.1038/nature09567](https://doi.org/10.1038/nature09567) (cit. on p. 32).
- [154] M. Kardar, G. Parisi, and Y. C. Zhang. “Dynamic scaling of growing interfaces”. In: *Physical Review Letters* 56.9 (1986), pp. 889–892. ISSN: 00319007. DOI: [10.1103/PhysRevLett.56.889](https://doi.org/10.1103/PhysRevLett.56.889) (cit. on p. 33).
- [155] K. Ji, V. N. Gladilin, and M. Wouters. “Temporal coherence of one-dimensional nonequilibrium quantum fluids”. In: *Physical Review B* 91.4 (Jan. 2015), p. 045301. ISSN: 1098-0121. DOI: [10.1103/PhysRevB.91.045301](https://doi.org/10.1103/PhysRevB.91.045301) (cit. on p. 33).
- [156] D. Squizzato, L. Canet, and A. Minguzzi. “Kardar-Parisi-Zhang universality in the phase distributions of one-dimensional exciton-polaritons”. In: *Physical Review B* 97.19 (May 2018), p. 195453. ISSN: 2469-9950. DOI: [10.1103/PhysRevB.97.195453](https://doi.org/10.1103/PhysRevB.97.195453) (cit. on p. 33).
- [157] A. D. Greentree et al. “Quantum phase transitions of light”. In: *Nature Physics* 2.12 (Dec. 2006), pp. 856–861. ISSN: 1745-2473. DOI: [10.1038/nphys466](https://doi.org/10.1038/nphys466) (cit. on pp. 34, 111, 112).

- [158] D. G. Angelakis, M. F. Santos, and S. Bose. “Photon-blockade-induced Mott transitions and XY spin models in coupled cavity arrays”. In: *Physical Review A* 76.3 (Sept. 2007), 031805(R). ISSN: 1050-2947. DOI: [10.1103/PhysRevA.76.031805](https://doi.org/10.1103/PhysRevA.76.031805) (cit. on pp. 34, 112).
- [159] D. Gerace et al. “The quantum-optical Josephson interferometer”. In: *Nature Physics* 5.4 (Apr. 2009), pp. 281–284. ISSN: 1745-2473. DOI: [10.1038/nphys1223](https://doi.org/10.1038/nphys1223) (cit. on pp. 34, 112).
- [160] V. Savona et al. “Optical properties of microcavity polaritons”. In: *Phase Transitions* 68.1 (Feb. 1999), pp. 169–279. ISSN: 0141-1594. DOI: [10.1080/01411599908224518](https://doi.org/10.1080/01411599908224518) (cit. on pp. 34–36).
- [161] R. Houdré, R. P. Stanley, and M. Iliegemts. “Vacuum-field Rabi splitting in the presence of inhomogeneous broadening: Resolution of a homogeneous linewidth in an inhomogeneously broadened system”. In: *Physical Review A* 53.4 (Apr. 1996), pp. 2711–2715. ISSN: 1050-2947. DOI: [10.1103/PhysRevA.53.2711](https://doi.org/10.1103/PhysRevA.53.2711) (cit. on p. 35).
- [162] M. Gross and S. Haroche. “Superradiance: An essay on the theory of collective spontaneous emission”. In: *Physics Reports* 93.5 (Dec. 1982), pp. 301–396. ISSN: 03701573. DOI: [10.1016/0370-1573\(82\)90102-8](https://doi.org/10.1016/0370-1573(82)90102-8) (cit. on p. 35).
- [163] I. Diniz et al. “Strongly coupling a cavity to inhomogeneous ensembles of emitters: Potential for long-lived solid-state quantum memories”. In: *Physical Review A* 84.6 (Dec. 2011), p. 063810. ISSN: 1050-2947. DOI: [10.1103/PhysRevA.84.063810](https://doi.org/10.1103/PhysRevA.84.063810) (cit. on pp. 35, 36, 61, 121).
- [164] S. Putz et al. “Protecting a spin ensemble against decoherence in the strong-coupling regime of cavity QED”. In: *Nature Physics* 10.10 (Oct. 2014), pp. 720–724. ISSN: 1745-2473. DOI: [10.1038/nphys3050](https://doi.org/10.1038/nphys3050) (cit. on p. 36).
- [165] J. D. Breeze et al. “Room-temperature cavity quantum electrodynamics with strongly coupled Dicke states”. In: *npj Quantum Information* 3.1 (Dec. 2017), p. 40. ISSN: 2056-6387. DOI: [10.1038/s41534-017-0041-3](https://doi.org/10.1038/s41534-017-0041-3) (cit. on p. 36).
- [166] G. Scuri et al. “Large Excitonic Reflectivity of Monolayer MoSe₂ Encapsulated in Hexagonal Boron Nitride”. In: *Physical Review Letters* 120.3 (2018), p. 37402. ISSN: 10797114. DOI: [10.1103/PhysRevLett.120.037402](https://doi.org/10.1103/PhysRevLett.120.037402) (cit. on p. 36).
- [167] D. S. Wild et al. “Quantum Nonlinear Optics in Atomically Thin Materials”. In: *Physical Review Letters* 121.12 (Sept. 2018), p. 123606. ISSN: 0031-9007. DOI: [10.1103/PhysRevLett.121.123606](https://doi.org/10.1103/PhysRevLett.121.123606) (cit. on p. 36).
- [168] S. Zeytinoglu and A. İmamoğlu. “Interaction-induced photon blockade using an atomically thin mirror embedded in a microcavity”. In: *Physical Review A* 98.5 (Nov. 2018), p. 051801. ISSN: 2469-9926. DOI: [10.1103/PhysRevA.98.051801](https://doi.org/10.1103/PhysRevA.98.051801) (cit. on p. 36).
- [169] R. Balili et al. “Bose-Einstein Condensation of Microcavity Polaritons in a Trap”. In: *Science* 316.5827 (2007), pp. 1007–1010. ISSN: 0036-8075. DOI: [10.1126/science.1140990](https://doi.org/10.1126/science.1140990) (cit. on p. 36).
- [170] E. A. Cerda-Méndez et al. “Polariton Condensation in Dynamic Acoustic Lattices”. In: *Physical Review Letters* 105.11 (Sept. 2010), p. 116402. ISSN: 0031-9007. DOI: [10.1103/PhysRevLett.105.116402](https://doi.org/10.1103/PhysRevLett.105.116402) (cit. on p. 36).
- [171] E. A. Cerda-Méndez et al. “Exciton-Polariton Gap Solitons in Two-Dimensional Lattices”. In: *Physical Review Letters* 111.14 (Oct. 2013), p. 146401. ISSN: 0031-9007. DOI: [10.1103/PhysRevLett.111.146401](https://doi.org/10.1103/PhysRevLett.111.146401) (cit. on p. 36).

- [172] E. Wertz et al. “Spontaneous formation and optical manipulation of extended polariton condensates”. In: *Nature Physics* 6.11 (Nov. 2010), pp. 860–864. ISSN: 1745-2473. DOI: [10.1038/nphys1750](https://doi.org/10.1038/nphys1750) (cit. on p. 36).
- [173] R. Dall et al. “Creation of Orbital Angular Momentum States with Chiral Polaritonic Lenses”. In: *Physical Review Letters* 113.20 (Nov. 2014), p. 200404. ISSN: 0031-9007. DOI: [10.1103/PhysRevLett.113.200404](https://doi.org/10.1103/PhysRevLett.113.200404) (cit. on p. 36).
- [174] C. W. Lai et al. “Coherent zero-state and π -state in an exciton–polariton condensate array”. In: *Nature* 450.7169 (Nov. 2007), pp. 529–532. ISSN: 0028-0836. DOI: [10.1038/nature06334](https://doi.org/10.1038/nature06334) (cit. on p. 37).
- [175] B. Zhang et al. “Zero-dimensional polariton laser in a subwavelength grating-based vertical microcavity”. In: *Light: Science & Applications* 3.1 (Jan. 2014), e135–e135. ISSN: 2047-7538. DOI: [10.1038/lsa.2014.16](https://doi.org/10.1038/lsa.2014.16) (cit. on p. 37).
- [176] R. I. Kaitouni et al. “Engineering the spatial confinement of exciton polaritons in semiconductors”. In: *Physical Review B* 74.15 (Oct. 2006), p. 155311. ISSN: 1098-0121. DOI: [10.1103/PhysRevB.74.155311](https://doi.org/10.1103/PhysRevB.74.155311) (cit. on p. 37).
- [177] B. Besga et al. “Polariton Boxes in a Tunable Fiber Cavity”. In: *Physical Review Applied* 3.1 (Jan. 2015), p. 014008. ISSN: 2331-7019. DOI: [10.1103/PhysRevApplied.3.014008](https://doi.org/10.1103/PhysRevApplied.3.014008) (cit. on p. 37).
- [178] D. Najer et al. “A gated quantum dot far in the strong-coupling regime of cavity-QED at optical frequencies”. In: (Dec. 2018). arXiv: [1812.08662](https://arxiv.org/abs/1812.08662) (cit. on pp. 37, 52).
- [179] D. N. Basov, M. M. Fogler, and F. J. de Abajo. “Polaritons in van der Waals materials”. In: *Science* 354.6309 (2016). ISSN: 0036-8075. DOI: [10.1126/science.aag1992](https://doi.org/10.1126/science.aag1992) (cit. on p. 37).
- [180] L. C. Flatten et al. “Electrically tunable organic–inorganic hybrid polaritons with monolayer WS₂”. In: *Nature Communications* 8.1 (Apr. 2017), p. 14097. ISSN: 2041-1723. DOI: [10.1038/ncomms14097](https://doi.org/10.1038/ncomms14097). arXiv: [1608.05274](https://arxiv.org/abs/1608.05274) (cit. on p. 37).
- [181] J. Bloch et al. “Strong-coupling regime in pillar semiconductor microcavities”. In: *Superlattices and Microstructures* 22.3 (Oct. 1997), pp. 371–374. ISSN: 07496036. DOI: [10.1006/spmi.1996.0317](https://doi.org/10.1006/spmi.1996.0317) (cit. on p. 37).
- [182] T. Gutbrod et al. “Weak and strong coupling of photons and excitons in photonic dots”. In: *Physical Review B* 57.16 (Apr. 1998), pp. 9950–9956. ISSN: 0163-1829. DOI: [10.1103/PhysRevB.57.9950](https://doi.org/10.1103/PhysRevB.57.9950) (cit. on p. 37).
- [183] A. Amo and J. Bloch. “Exciton–polaritons in lattices: A non-linear photonic simulator”. In: *Comptes Rendus Physique* 17.8 (Oct. 2016), pp. 934–945. ISSN: 16310705. DOI: [10.1016/j.crhy.2016.08.007](https://doi.org/10.1016/j.crhy.2016.08.007) (cit. on p. 37).
- [184] M. A. M. Marte and S. Stenholm. “Paraxial light and atom optics: The optical Schrödinger equation and beyond”. In: *Physical Review A* 56.4 (Oct. 1997), pp. 2940–2953. ISSN: 1050-2947. DOI: [10.1103/PhysRevA.56.2940](https://doi.org/10.1103/PhysRevA.56.2940) (cit. on pp. 38, 47, 48).
- [185] C. Cohen-Tannoudji, B. Diu, and F. Laloe. *Mécanique Quantique*. Vol.2. EDP sciences, 2018. ISBN: 9782759822850 (cit. on p. 39).
- [186] M. Galbiati et al. “Polariton Condensation in Photonic Molecules”. In: *Physical Review Letters* 108.12 (Mar. 2012), p. 126403. ISSN: 0031-9007. DOI: [10.1103/PhysRevLett.108.126403](https://doi.org/10.1103/PhysRevLett.108.126403) (cit. on p. 39).
- [187] V. G. Sala et al. “Spin-Orbit Coupling for Photons and Polaritons in Microstructures”. In: *Physical Review X* 5.1 (Mar. 2015), p. 11034. ISSN: 2160-3308. DOI: [10.1103/PhysRevX.5.011034](https://doi.org/10.1103/PhysRevX.5.011034) (cit. on pp. 39, 79, 80, 82, 83).

- [188] P. St-Jean et al. “Lasing in topological edge states of a one-dimensional lattice”. In: *Nature Photonics* 11.10 (2017), pp. 651–656. ISSN: 17494893. DOI: [10.1038/s41566-017-0006-2](https://doi.org/10.1038/s41566-017-0006-2). arXiv: [1704.07310](https://arxiv.org/abs/1704.07310) (cit. on pp. 39, 42).
- [189] F. Mangussi et al. “Multi-orbital tight binding model for cavity-polariton lattices”. In: (July 2019), pp. 1–14. arXiv: [1907.13621](https://arxiv.org/abs/1907.13621) (cit. on pp. 40, 41, 83).
- [190] M. Milićević et al. “Edge states in polariton honeycomb lattices”. In: *2D Materials* 2.3 (Aug. 2015), p. 034012. ISSN: 2053-1583. DOI: [10.1088/2053-1583/2/3/034012](https://doi.org/10.1088/2053-1583/2/3/034012). arXiv: [1504.05761](https://arxiv.org/abs/1504.05761) (cit. on pp. 41, 42).
- [191] M. Greiner et al. “Quantum phase transition from a superfluid to a Mott insulator in a gas of ultracold atoms”. In: *Nature* 415.6867 (Jan. 2002), pp. 39–44. ISSN: 0028-0836. DOI: [10.1038/415039a](https://doi.org/10.1038/415039a) (cit. on pp. 42, 112).
- [192] W. S. Bakr et al. “Probing the Superfluid-to-Mott Insulator Transition at the Single-Atom Level”. In: *Science* 329.5991 (July 2010), pp. 547–550. ISSN: 0036-8075. DOI: [10.1126/science.1192368](https://doi.org/10.1126/science.1192368) (cit. on pp. 42, 112).
- [193] E. M. Kessler et al. “Dissipative phase transition in a central spin system”. In: *Physical Review A* 86.1 (July 2012), p. 012116. ISSN: 1050-2947. DOI: [10.1103/PhysRevA.86.012116](https://doi.org/10.1103/PhysRevA.86.012116) (cit. on pp. 43, 71, 133, 139, 155).
- [194] H. J. Carmichael. “Breakdown of Photon Blockade: A Dissipative Quantum Phase Transition in Zero Dimensions”. In: *Physical Review X* 5.3 (Sept. 2015), p. 031028. ISSN: 2160-3308. DOI: [10.1103/PhysRevX.5.031028](https://doi.org/10.1103/PhysRevX.5.031028) (cit. on p. 43).
- [195] M. Foss-Feig et al. “Emergent equilibrium in many-body optical bistability”. In: *Physical Review A* 95.4 (Apr. 2017), p. 043826. ISSN: 2469-9926. DOI: [10.1103/PhysRevA.95.043826](https://doi.org/10.1103/PhysRevA.95.043826) (cit. on pp. 43, 69, 71, 112, 143, 151, 155).
- [196] M. Biondi et al. “Nonequilibrium gas-liquid transition in the driven-dissipative photonic lattice”. In: *Physical Review A* 96.4 (Oct. 2017), p. 043809. ISSN: 2469-9926. DOI: [10.1103/PhysRevA.96.043809](https://doi.org/10.1103/PhysRevA.96.043809) (cit. on pp. 43, 112, 133).
- [197] F. Vicentini et al. “Critical slowing down in driven-dissipative Bose-Hubbard lattices”. In: *Physical Review A* 97.1 (Jan. 2018), p. 013853. ISSN: 2469-9926. DOI: [10.1103/PhysRevA.97.013853](https://doi.org/10.1103/PhysRevA.97.013853) (cit. on pp. 43, 69, 133, 143).
- [198] A. Belavin et al. “Relaxation of Quantum Systems with Equidistant Spectra”. In: *Soviet Journal of Experimental and Theoretical Physics* 29 (Jan. 1969), p. 145 (cit. on p. 43).
- [199] G. Lindblad. “On the generators of quantum dynamical semigroups”. In: *Communications in Mathematical Physics* 48.2 (June 1976), pp. 119–130. ISSN: 0010-3616. DOI: [10.1007/BF01608499](https://doi.org/10.1007/BF01608499) (cit. on pp. 43, 44, 132).
- [200] A. O. Caldeira and A. J. Leggett. “Influence of Dissipation on Quantum Tunneling in Macroscopic Systems”. In: *Physical Review Letters* 46.4 (Jan. 1981), pp. 211–214. ISSN: 0031-9007. DOI: [10.1103/PhysRevLett.46.211](https://doi.org/10.1103/PhysRevLett.46.211) (cit. on p. 43).
- [201] H.-P. Breuer and F. Petruccione. *The Theory of Open Quantum Systems*. Vol. 53. 9. Cambridge: Oxford University Press, Jan. 2007, pp. 1–30. ISBN: 9780199213900. DOI: [10.1093/acprof:oso/9780199213900.001.0001](https://doi.org/10.1093/acprof:oso/9780199213900.001.0001). arXiv: [arXiv:1011.1669v3](https://arxiv.org/abs/1011.1669v3) (cit. on pp. 44, 45, 144).
- [202] C. Navarrete-Benlloch. “Open systems dynamics: Simulating master equations in the computer”. In: (Apr. 2015), pp. 1–18. arXiv: [1504.05266](https://arxiv.org/abs/1504.05266) (cit. on p. 45).
- [203] K. Macieszczak et al. “Towards a Theory of Metastability in Open Quantum Dynamics”. In: *Physical Review Letters* 116.24 (June 2016), p. 240404. ISSN: 0031-9007. DOI: [10.1103/PhysRevLett.116.240404](https://doi.org/10.1103/PhysRevLett.116.240404) (cit. on pp. 45, 70).

- [204] F. Minganti et al. “Spectral theory of Liouvillians for dissipative phase transitions”. In: *Physical Review A* 98.4 (Oct. 2018), p. 042118. ISSN: 2469-9926. DOI: [10.1103/PhysRevA.98.042118](https://doi.org/10.1103/PhysRevA.98.042118) (cit. on pp. 45, 132).
- [205] C. Yeh, L. Casperson, and W. P. Brown. “Scalar-wave approach for single-mode inhomogeneous fiber problems”. In: *Applied Physics Letters* 34.7 (Apr. 1979), pp. 460–462. ISSN: 00036951. DOI: [10.1063/1.90834](https://doi.org/10.1063/1.90834) (cit. on p. 47).
- [206] W. Shin and S. Fan. “Accelerated solution of the frequency-domain Maxwell’s equations by engineering the eigenvalue distribution of the operator”. In: *Optics Express* 21.19 (Sept. 2013), p. 22578. ISSN: 1094-4087. DOI: [10.1364/OE.21.022578](https://doi.org/10.1364/OE.21.022578) (cit. on p. 49).
- [207] Yen-Chung Chiang, Yih-Peng Chiou, and Hung-Chun Chang. “Improved full-vectorial finite-difference mode solver for optical waveguides with step-index profiles”. In: *Journal of Lightwave Technology* 20.8 (Aug. 2002), pp. 1609–1618. ISSN: 0733-8724. DOI: [10.1109/JLT.2002.800292](https://doi.org/10.1109/JLT.2002.800292) (cit. on p. 49).
- [208] Y. Zhang and M. Lončar. “Submicrometer diameter micropillar cavities with high quality factor and ultrasmall mode volume”. In: *Optics Letters* 34.7 (Apr. 2009), p. 902. ISSN: 0146-9592. DOI: [10.1364/OL.34.000902](https://doi.org/10.1364/OL.34.000902) (cit. on p. 52).
- [209] M. Lerner et al. “Bloch-Wave Engineering of Quantum Dot Micropillars for Cavity Quantum Electrodynamics Experiments”. In: *Physical Review Letters* 108.5 (Jan. 2012), p. 057402. ISSN: 0031-9007. DOI: [10.1103/PhysRevLett.108.057402](https://doi.org/10.1103/PhysRevLett.108.057402) (cit. on pp. 52, 155).
- [210] F. R. Lamberti et al. “Nanomechanical resonators based on adiabatic periodicity-breaking in a superlattice”. In: *Applied Physics Letters* 111.17 (Oct. 2017), p. 173107. ISSN: 0003-6951. DOI: [10.1063/1.5000805](https://doi.org/10.1063/1.5000805) (cit. on p. 52).
- [211] A. Y. Cho and J. R. Arthur. “Molecular beam epitaxy”. In: *Progress in Solid State Chemistry* 10 (1975), pp. 157–191. ISSN: 0079-6786. DOI: [https://doi.org/10.1016/0079-6786\(75\)90005-9](https://doi.org/10.1016/0079-6786(75)90005-9) (cit. on p. 54).
- [212] K. Murphy et al. “Experimental detection of optical vortices with a Shack-Hartmann wavefront sensor”. In: *Optics Express* 18.15 (July 2010), p. 15448. ISSN: 1094-4087. DOI: [10.1364/OE.18.015448](https://doi.org/10.1364/OE.18.015448) (cit. on p. 61).
- [213] D. Najer et al. “A gated quantum dot strongly coupled to an optical microcavity”. In: *Nature* 575.7784 (Nov. 2019), pp. 622–627. ISSN: 0028-0836. DOI: [10.1038/s41586-019-1709-y](https://doi.org/10.1038/s41586-019-1709-y) (cit. on p. 63).
- [214] R. W. Boyd. “Quantum-Mechanical Theory of the Nonlinear Optical Susceptibility”. In: *Nonlinear Optics*. Ed. by R. W. Boyd. Third Edit. Burlington: Elsevier, 2008, pp. 135–206. ISBN: 978-0-12-369470-6. DOI: [10.1016/B978-0-12-369470-6.00003-4](https://doi.org/10.1016/B978-0-12-369470-6.00003-4) (cit. on pp. 63, 64, 66, 113).
- [215] E. Hairer and G. Wanner. *Geometric Numerical Integration*. Vol. 31. Springer Series in Computational Mathematics. Berlin/Heidelberg: Springer-Verlag, 2006, p. 644. ISBN: 3-540-30663-3. DOI: [10.1007/3-540-30666-8](https://doi.org/10.1007/3-540-30666-8) (cit. on p. 64).
- [216] H. M. Gibbs. “STEADY-STATE MODEL OF OPTICAL BISTABILITY”. In: *Optical Bistability: Controlling Light with Light*. Ed. by H. M. Gibbs. Elsevier, 1985, pp. 19–92. ISBN: 978-0-12-281940-7. DOI: [10.1016/B978-0-12-281940-7.50007-X](https://doi.org/10.1016/B978-0-12-281940-7.50007-X) (cit. on pp. 66, 122, 127).
- [217] P. Glendinning. *Stability, Instability and Chaos*. Cambridge Texts in Applied Mathematics. Cambridge: Cambridge University Press, 1994. ISBN: 9780511626296. DOI: [10.1017/CB09780511626296](https://doi.org/10.1017/CB09780511626296) (cit. on p. 67).

- [218] M. C. Cross and P. C. Hohenberg. “Pattern formation outside of equilibrium”. In: *Reviews of Modern Physics* 65.3 (July 1993), pp. 851–1112. ISSN: 0034-6861. DOI: [10.1103/RevModPhys.65.851](https://doi.org/10.1103/RevModPhys.65.851) (cit. on pp. 67, 98, 111, 113).
- [219] E. C. G. Sudarshan. “Equivalence of Semiclassical and Quantum Mechanical Descriptions of Statistical Light Beams”. In: *Physical Review Letters* 10.7 (Apr. 1963), pp. 277–279. ISSN: 0031-9007. DOI: [10.1103/PhysRevLett.10.277](https://doi.org/10.1103/PhysRevLett.10.277) (cit. on p. 68).
- [220] K. E. Cahill and R. J. Glauber. “Density Operators and Quasiprobability Distributions”. In: *Physical Review* 177.5 (Jan. 1969), pp. 1882–1902. ISSN: 0031-899X. DOI: [10.1103/PhysRev.177.1882](https://doi.org/10.1103/PhysRev.177.1882) (cit. on p. 68).
- [221] K. Husimi. “Some formal properties of the density matrix”. In: *Proc. Phys. Math. Soc. Jpn.* 22 (1940), p. 264. DOI: https://doi.org/10.11429/ppmsj1919.22.4_264 (cit. on p. 68).
- [222] H. J. Carmichael. *Statistical Methods in Quantum Optics 1*. 1st ed. Vol. 123. 2. Berlin, Heidelberg: Springer Berlin Heidelberg, 1999. ISBN: 978-3-642-08133-0. DOI: [10.1007/978-3-662-03875-8](https://doi.org/10.1007/978-3-662-03875-8) (cit. on pp. 68, 69, 114).
- [223] K. Vogel and H. Risken. “Quasiprobability distributions in dispersive optical bistability”. In: *Phys. Rev. A* 39.9 (May 1989), pp. 4675–4683. DOI: [10.1103/PhysRevA.39.4675](https://doi.org/10.1103/PhysRevA.39.4675) (cit. on p. 68).
- [224] A. Sinatra, C. Lobo, and Y. Castin. “The truncated Wigner method for Bose-condensed gases: limits of validity and applications”. In: *Journal of Physics B: Atomic, Molecular and Optical Physics* 35.17 (Sept. 2002), pp. 3599–3631. ISSN: 0953-4075. DOI: [10.1088/0953-4075/35/17/301](https://doi.org/10.1088/0953-4075/35/17/301) (cit. on p. 69).
- [225] P. D. Drummond and D. F. Walls. “Quantum theory of optical bistability. I. Nonlinear polarisability model”. In: *Journal of Physics A: Mathematical and General* 13.2 (Feb. 1980), pp. 725–741. ISSN: 0305-4470. DOI: [10.1088/0305-4470/13/2/034](https://doi.org/10.1088/0305-4470/13/2/034) (cit. on pp. 70, 127, 130).
- [226] R. Roy et al. “First-Passage-Time Distributions under the Influence of Quantum Fluctuations in a Laser”. In: *Physical Review Letters* 45.18 (Nov. 1980), pp. 1486–1490. ISSN: 0031-9007. DOI: [10.1103/PhysRevLett.45.1486](https://doi.org/10.1103/PhysRevLett.45.1486) (cit. on pp. 70, 127, 130, 140).
- [227] H. Risken et al. “Quantum tunneling in dispersive optical bistability”. In: *Physical Review A* 35.4 (Feb. 1987), pp. 1729–1739. ISSN: 0556-2791. DOI: [10.1103/PhysRevA.35.1729](https://doi.org/10.1103/PhysRevA.35.1729) (cit. on pp. 70, 131, 132, 137, 140, 142, 148).
- [228] C. Rackauckas and Q. Nie. *Adaptive methods for stochastic differential equations via natural embeddings and rejection sampling with memory*. 2017. DOI: [10.3934/dcdsb.2017133](https://doi.org/10.3934/dcdsb.2017133) (cit. on p. 70).
- [229] F. Vicentini et al. “Optimal stochastic unraveling of disordered open quantum systems: Application to driven-dissipative photonic lattices”. In: *Physical Review A* 99.3 (Mar. 2019), p. 032115. ISSN: 2469-9926. DOI: [10.1103/PhysRevA.99.032115](https://doi.org/10.1103/PhysRevA.99.032115) (cit. on pp. 70, 133).
- [230] W. Casteels, R. Fazio, and C. Ciuti. “Critical dynamical properties of a first-order dissipative phase transition”. In: *Physical Review A* 95.1 (Jan. 2017), p. 012128. ISSN: 2469-9926. DOI: [10.1103/PhysRevA.95.012128](https://doi.org/10.1103/PhysRevA.95.012128) (cit. on pp. 71, 127, 133, 134, 137–139, 143, 151, 155).
- [231] M. Fitzpatrick et al. “Observation of a Dissipative Phase Transition in a One-Dimensional Circuit QED Lattice”. In: *Physical Review X* 7.1 (Feb. 2017), p. 011016. ISSN: 2160-3308. DOI: [10.1103/PhysRevX.7.011016](https://doi.org/10.1103/PhysRevX.7.011016) (cit. on pp. 71, 133, 139, 140).

- [232] S. R. K. Rodriguez et al. “Probing a Dissipative Phase Transition via Dynamical Optical Hysteresis”. In: *Physical Review Letters* 118.24 (June 2017), p. 247402. ISSN: 0031-9007. DOI: [10.1103/PhysRevLett.118.247402](https://doi.org/10.1103/PhysRevLett.118.247402) (cit. on pp. 71, 127).
- [233] N. Carlon Zambon et al. “Optically controlling the emission chirality of micro-lasers”. In: *Nature Photonics* 13.4 (Apr. 2019), pp. 283–288. ISSN: 1749-4885. DOI: [10.1038/s41566-019-0380-z](https://doi.org/10.1038/s41566-019-0380-z) (cit. on pp. 75, 80).
- [234] N. Carlon Zambon et al. “Orbital angular momentum bistability in a micro-laser”. In: *Optics Letters* 44.18 (Sept. 2019), p. 4531. ISSN: 0146-9592. DOI: [10.1364/OL.44.004531](https://doi.org/10.1364/OL.44.004531) (cit. on p. 75).
- [235] J. Hecht. “A short history of laser development”. In: *Applied Optics* 49.25 (Sept. 2010), F99. ISSN: 0003-6935. DOI: [10.1364/AO.49.000F99](https://doi.org/10.1364/AO.49.000F99) (cit. on p. 76).
- [236] T. P. Heavner et al. “First accuracy evaluation of NIST-F2”. In: *Metrologia* 51.3 (June 2014), pp. 174–182. ISSN: 0026-1394. DOI: [10.1088/0026-1394/51/3/174](https://doi.org/10.1088/0026-1394/51/3/174) (cit. on p. 76).
- [237] T. W. Hänsch. “Nobel Lecture: Passion for precision”. In: *Reviews of Modern Physics* 78.4 (Nov. 2006), pp. 1297–1309. ISSN: 0034-6861. DOI: [10.1103/RevModPhys.78.1297](https://doi.org/10.1103/RevModPhys.78.1297) (cit. on p. 76).
- [238] P. Del’Haye et al. “Optical frequency comb generation from a monolithic microresonator”. In: *Nature* 450.7173 (Dec. 2007), pp. 1214–1217. ISSN: 0028-0836. DOI: [10.1038/nature06401](https://doi.org/10.1038/nature06401) (cit. on pp. 76, 111).
- [239] J. M. Dudley, G. Genty, and S. Coen. “Supercontinuum generation in photonic crystal fiber”. In: *Reviews of Modern Physics* 78.4 (Oct. 2006), pp. 1135–1184. ISSN: 0034-6861. DOI: [10.1103/RevModPhys.78.1135](https://doi.org/10.1103/RevModPhys.78.1135) (cit. on p. 76).
- [240] M. Hentschel et al. “Attosecond metrology”. In: *Nature* 414.6863 (Nov. 2001), pp. 509–513. ISSN: 0028-0836. DOI: [10.1038/35107000](https://doi.org/10.1038/35107000) (cit. on p. 76).
- [241] D. Strickland. “Nobel Lecture: Generating high-intensity ultrashort optical pulses”. In: *Reviews of Modern Physics* 91.3 (July 2019), p. 030502. ISSN: 0034-6861. DOI: [10.1103/RevModPhys.91.030502](https://doi.org/10.1103/RevModPhys.91.030502) (cit. on p. 76).
- [242] T. Juhasz et al. “Corneal refractive surgery with femtosecond lasers”. In: *IEEE Journal of Selected Topics in Quantum Electronics* 5.4 (1999), pp. 902–910. ISSN: 1077260X. DOI: [10.1109/2944.796309](https://doi.org/10.1109/2944.796309) (cit. on p. 76).
- [243] W. R. Zipfel, R. M. Williams, and W. W. Webb. “Nonlinear magic: multiphoton microscopy in the biosciences”. In: *Nature Biotechnology* 21.11 (Nov. 2003), pp. 1369–1377. ISSN: 1087-0156. DOI: [10.1038/nbt899](https://doi.org/10.1038/nbt899) (cit. on p. 76).
- [244] D. G. Ouzounov et al. “Soliton pulse compression in photonic band-gap fibers.” In: *Optics Express* 13.16 (2005), p. 6153. ISSN: 1094-4087. DOI: [10.1364/OPEX.13.006153](https://doi.org/10.1364/OPEX.13.006153) (cit. on p. 76).
- [245] V. Bagnoud and J. D. Zuegel. “Independent phase and amplitude control of a laser beam by use of a single-phase-only spatial light modulator”. In: *Optics Letters* 29.3 (Feb. 2004), p. 295. ISSN: 0146-9592. DOI: [10.1364/OL.29.000295](https://doi.org/10.1364/OL.29.000295) (cit. on p. 76).
- [246] I. Moreno et al. “Complete polarization control of light from a liquid crystal spatial light modulator”. In: *Optics Express* 20.1 (Jan. 2012), p. 364. ISSN: 1094-4087. DOI: [10.1364/OE.20.000364](https://doi.org/10.1364/OE.20.000364) (cit. on p. 76).
- [247] R.-J. Essiambre et al. “Breakthroughs in Photonics 2012: Space-Division Multiplexing in Multimode and Multicore Fibers for High-Capacity Optical Communication”. In: *IEEE Photonics Journal* 5.2 (Apr. 2013), pp. 0701307–0701307. ISSN: 1943-0655. DOI: [10.1109/JPHOT.2013.2253091](https://doi.org/10.1109/JPHOT.2013.2253091) (cit. on p. 76).

- [248] A. P. Mosk et al. “Controlling waves in space and time for imaging and focusing in complex media”. In: *Nature Photonics* 6.5 (May 2012), pp. 283–292. ISSN: 1749-4885. DOI: [10.1038/nphoton.2012.88](https://doi.org/10.1038/nphoton.2012.88) (cit. on p. 76).
- [249] G. Makey et al. “Breaking crosstalk limits to dynamic holography using orthogonality of high-dimensional random vectors”. In: *Nature Photonics* 13.4 (Apr. 2019), pp. 251–256. ISSN: 1749-4885. DOI: [10.1038/s41566-019-0393-7](https://doi.org/10.1038/s41566-019-0393-7) (cit. on p. 76).
- [250] A. J. Caley et al. “Diffractive optical elements for high gain lasers with arbitrary output beam profiles”. In: *Optics Express* 15.17 (2007), p. 10699. ISSN: 1094-4087. DOI: [10.1364/OE.15.010699](https://doi.org/10.1364/OE.15.010699) (cit. on p. 76).
- [251] H. Kogelnik and T. Li. “Laser Beams and Resonators”. In: *Applied Optics* 5.10 (Oct. 1966), p. 1550. ISSN: 0003-6935. DOI: [10.1364/AO.5.001550](https://doi.org/10.1364/AO.5.001550) (cit. on p. 77).
- [252] S. Ngcobo et al. “A digital laser for on-demand laser modes”. In: *Nature Communications* 4.1 (Oct. 2013), p. 2289. ISSN: 2041-1723. DOI: [10.1038/ncomms3289](https://doi.org/10.1038/ncomms3289) (cit. on p. 77).
- [253] C. V. Raman and S. Bhagavantam. “Experimental Proof of the Spin of the Photon”. In: *Nature* 129.3244 (Jan. 1932), pp. 22–23. ISSN: 0028-0836. DOI: [10.1038/129022a0](https://doi.org/10.1038/129022a0) (cit. on p. 77).
- [254] F. Belinfante. “On the current and the density of the electric charge, the energy, the linear momentum and the angular momentum of arbitrary fields”. In: *Physica* 7.5 (May 1940), pp. 449–474. ISSN: 00318914. DOI: [10.1016/S0031-8914\(40\)90091-X](https://doi.org/10.1016/S0031-8914(40)90091-X) (cit. on pp. 77, 101).
- [255] L. Allen et al. “Orbital angular momentum of light and the transformation of Laguerre-Gaussian laser modes”. In: *Physical Review A* 45.11 (June 1992), pp. 8185–8189. ISSN: 1050-2947. DOI: [10.1103/PhysRevA.45.8185](https://doi.org/10.1103/PhysRevA.45.8185) (cit. on pp. 77, 78, 105).
- [256] M. Padgett. “Helically Phased Beams, and Analogies with Polarization”. In: *Twisted Photons*. Weinheim, Germany: Wiley-VCH Verlag GmbH & Co. KGaA, Mar. 2011. Chap. 2, pp. 25–35. ISBN: 9783527635368. DOI: [10.1002/9783527635368.ch3](https://doi.org/10.1002/9783527635368.ch3) (cit. on pp. 77, 78).
- [257] R. Fickler et al. “Quantum entanglement of angular momentum states with quantum numbers up to 10,010”. In: *Proceedings of the National Academy of Sciences* 113.48 (Nov. 2016), pp. 13642–13647. ISSN: 0027-8424. DOI: [10.1073/pnas.1616889113](https://doi.org/10.1073/pnas.1616889113) (cit. on p. 78).
- [258] G. Gibson et al. “Free-space information transfer using light beams carrying orbital angular momentum”. In: *Optics Express* 12.22 (Nov. 2004), p. 5448. ISSN: 1094-4087. DOI: [10.1364/OPEX.12.005448](https://doi.org/10.1364/OPEX.12.005448) (cit. on p. 78).
- [259] J. Wang et al. “Terabit free-space data transmission employing orbital angular momentum multiplexing”. In: *Nature Photonics* 6.7 (July 2012), pp. 488–496. ISSN: 1749-4885. DOI: [10.1038/nphoton.2012.138](https://doi.org/10.1038/nphoton.2012.138) (cit. on p. 78).
- [260] N. Bozinovic et al. “Terabit-Scale Orbital Angular Momentum Mode Division Multiplexing in Fibers”. In: *Science* 340.6140 (June 2013), pp. 1545–1548. ISSN: 0036-8075. DOI: [10.1126/science.1237861](https://doi.org/10.1126/science.1237861) (cit. on p. 78).
- [261] A. E. Willner et al. “Optical communications using orbital angular momentum beams”. In: *Advances in Optics and Photonics* 7.1 (Mar. 2015), p. 66. ISSN: 1943-8206. DOI: [10.1364/AOP.7.000066](https://doi.org/10.1364/AOP.7.000066) (cit. on p. 78).

- [262] G. Vallone et al. “Free-Space Quantum Key Distribution by Rotation-Invariant Twisted Photons”. In: *Physical Review Letters* 113.6 (Aug. 2014), p. 60503. ISSN: 0031-9007. DOI: [10.1103/PhysRevLett.113.060503](https://doi.org/10.1103/PhysRevLett.113.060503) (cit. on p. 78).
- [263] A. Sit et al. “High-dimensional intracity quantum cryptography with structured photons”. In: *Optica* 4.9 (Sept. 2017), p. 1006. ISSN: 2334-2536. DOI: [10.1364/OPTICA.4.001006](https://doi.org/10.1364/OPTICA.4.001006) (cit. on p. 78).
- [264] M. Erhard et al. “Twisted photons: new quantum perspectives in high dimensions”. In: *Light: Science & Applications* 7.3 (Mar. 2018), p. 17146. ISSN: 2047-7538. DOI: [10.1038/lsa.2017.146](https://doi.org/10.1038/lsa.2017.146) (cit. on p. 78).
- [265] D. Cozzolino et al. “Orbital Angular Momentum States Enabling Fiber-based High-dimensional Quantum Communication”. In: *Physical Review Applied* 11.6 (June 2019), p. 064058. ISSN: 2331-7019. DOI: [10.1103/PhysRevApplied.11.064058](https://doi.org/10.1103/PhysRevApplied.11.064058). arXiv: [1803.10138](https://arxiv.org/abs/1803.10138) (cit. on p. 78).
- [266] D. Kaszlikowski et al. “Violations of Local Realism by Two Entangled N - Dimensional Systems Are Stronger than for Two Qubits”. In: *Physical Review Letters* 85.21 (Nov. 2000), pp. 4418–4421. ISSN: 0031-9007. DOI: [10.1103/PhysRevLett.85.4418](https://doi.org/10.1103/PhysRevLett.85.4418) (cit. on p. 78).
- [267] N. J. Cerf et al. “Security of Quantum Key Distribution Using d -Level Systems”. In: *Physical Review Letters* 88.12 (Mar. 2002), p. 127902. ISSN: 0031-9007. DOI: [10.1103/PhysRevLett.88.127902](https://doi.org/10.1103/PhysRevLett.88.127902) (cit. on p. 78).
- [268] D. Cozzolino et al. “High-Dimensional Quantum Communication: Benefits, Progress, and Future Challenges”. In: *Advanced Quantum Technologies* 1900038 (Oct. 2019), p. 1900038. ISSN: 2511-9044. DOI: [10.1002/qute.201900038](https://doi.org/10.1002/qute.201900038). arXiv: [1910.07220](https://arxiv.org/abs/1910.07220) (cit. on pp. 78, 153).
- [269] J. H. Poynting. “The Wave Motion of a Revolving Shaft, and a Suggestion as to the Angular Momentum in a Beam of Circularly Polarised Light”. In: *Proceedings of the Royal Society A: Mathematical, Physical and Engineering Sciences* 82.557 (July 1909), pp. 560–567. ISSN: 1364-5021. DOI: [10.1098/rspa.1909.0060](https://doi.org/10.1098/rspa.1909.0060) (cit. on p. 78).
- [270] R. A. Beth. “Mechanical Detection and Measurement of the Angular Momentum of Light”. In: *Physical Review* 50.2 (July 1936), pp. 115–125. ISSN: 0031-899X. DOI: [10.1103/PhysRev.50.115](https://doi.org/10.1103/PhysRev.50.115) (cit. on p. 78).
- [271] H. He et al. “Direct Observation of Transfer of Angular Momentum to Absorptive Particles from a Laser Beam with a Phase Singularity”. In: *Physical Review Letters* 75.5 (July 1995), pp. 826–829. ISSN: 0031-9007. DOI: [10.1103/PhysRevLett.75.826](https://doi.org/10.1103/PhysRevLett.75.826) (cit. on p. 78).
- [272] N. B. Simpson et al. “Mechanical equivalence of spin and orbital angular momentum of light: an optical spanner”. In: *Optics Letters* 22.1 (Jan. 1997), p. 52. ISSN: 0146-9592. DOI: [10.1364/OL.22.000052](https://doi.org/10.1364/OL.22.000052) (cit. on p. 78).
- [273] D. G. Grier. “A revolution in optical manipulation”. In: *Nature* 424.6950 (Aug. 2003), pp. 810–816. ISSN: 0028-0836. DOI: [10.1038/nature01935](https://doi.org/10.1038/nature01935) (cit. on p. 78).
- [274] D. Gao et al. “Optical manipulation from the microscale to the nanoscale: fundamentals, advances and prospects”. In: *Light: Science & Applications* 6.9 (Sept. 2017), e17039–e17039. ISSN: 2047-7538. DOI: [10.1038/lsa.2017.39](https://doi.org/10.1038/lsa.2017.39) (cit. on p. 78).
- [275] R. Reimann et al. “GHz Rotation of an Optically Trapped Nanoparticle in Vacuum”. In: *Physical Review Letters* 121.3 (July 2018), p. 033602. ISSN: 0031-9007. DOI: [10.1103/PhysRevLett.121.033602](https://doi.org/10.1103/PhysRevLett.121.033602) (cit. on p. 78).

- [276] M. G. Donato et al. “Polarization-dependent optomechanics mediated by chiral microresonators”. In: *Nature Communications* 5.1 (May 2014), p. 3656. ISSN: 2041-1723. DOI: [10.1038/ncomms4656](https://doi.org/10.1038/ncomms4656) (cit. on p. 78).
- [277] M. Aspelmeyer, T. J. Kippenberg, and F. Marquardt. “Cavity optomechanics”. In: *Reviews of Modern Physics* 86.4 (Dec. 2014), pp. 1391–1452. ISSN: 0034-6861. DOI: [10.1103/RevModPhys.86.1391](https://doi.org/10.1103/RevModPhys.86.1391) (cit. on p. 78).
- [278] R. Fickler et al. “Quantum Entanglement of High Angular Momenta”. In: *Science* 338.6107 (Nov. 2012), pp. 640–643. ISSN: 0036-8075. DOI: [10.1126/science.1227193](https://doi.org/10.1126/science.1227193) (cit. on p. 78).
- [279] D. Collins et al. “Bell Inequalities for Arbitrarily High-Dimensional Systems”. In: *Physical Review Letters* 88.4 (Jan. 2002), p. 40404. ISSN: 0031-9007. DOI: [10.1103/PhysRevLett.88.040404](https://doi.org/10.1103/PhysRevLett.88.040404) (cit. on p. 78).
- [280] V. V. Kotlyar et al. “Generation of phase singularity through diffracting a plane or Gaussian beam by a spiral phase plate”. In: *Journal of the Optical Society of America A* 22.5 (May 2005), p. 849. ISSN: 1084-7529. DOI: [10.1364/JOSAA.22.000849](https://doi.org/10.1364/JOSAA.22.000849) (cit. on p. 78).
- [281] F. Cardano and L. Marrucci. “Spin-orbit photonics”. In: *Nature Photonics* 9.12 (Dec. 2015), pp. 776–778. ISSN: 1749-4885. DOI: [10.1038/nphoton.2015.232](https://doi.org/10.1038/nphoton.2015.232) (cit. on p. 78).
- [282] F. Bouchard et al. “Optical spin-to-orbital angular momentum conversion in ultra-thin metasurfaces with arbitrary topological charges”. In: *Applied Physics Letters* 105.10 (Sept. 2014), p. 101905. ISSN: 0003-6951. DOI: [10.1063/1.4895620](https://doi.org/10.1063/1.4895620) (cit. on p. 78).
- [283] A. Arbabi et al. “Dielectric metasurfaces for complete control of phase and polarization with subwavelength spatial resolution and high transmission”. In: *Nature Nanotechnology* 10.11 (Nov. 2015), pp. 937–943. ISSN: 1748-3387. DOI: [10.1038/nnano.2015.186](https://doi.org/10.1038/nnano.2015.186) (cit. on p. 78).
- [284] R. C. Devlin et al. “Arbitrary spin-to-orbital angular momentum conversion of light”. In: *Science* 358.6365 (Nov. 2017), pp. 896–901. ISSN: 0036-8075. DOI: [10.1126/science.aao5392](https://doi.org/10.1126/science.aao5392) (cit. on p. 78).
- [285] Y. Xu et al. “Reconfiguring structured light beams using nonlinear metasurfaces”. In: *Optics Express* 26.23 (Nov. 2018), p. 30930. ISSN: 1094-4087. DOI: [10.1364/OE.26.030930](https://doi.org/10.1364/OE.26.030930). arXiv: [1805.07327](https://arxiv.org/abs/1805.07327) (cit. on p. 78).
- [286] L. Marrucci, C. Manzo, and D. Paparo. “Optical Spin-to-Orbital Angular Momentum Conversion in Inhomogeneous Anisotropic Media”. In: *Physical Review Letters* 96.16 (Apr. 2006), p. 163905. ISSN: 0031-9007. DOI: [10.1103/PhysRevLett.96.163905](https://doi.org/10.1103/PhysRevLett.96.163905) (cit. on p. 78).
- [287] D. Naidoo et al. “Controlled generation of higher-order Poincaré sphere beams from a laser”. In: *Nature Photonics* 10.5 (May 2016), pp. 327–332. ISSN: 1749-4885. DOI: [10.1038/nphoton.2016.37](https://doi.org/10.1038/nphoton.2016.37) (cit. on p. 78).
- [288] Y.-W. Huang et al. “Versatile total angular momentum generation using cascaded J-plates”. In: *Optics Express* 27.5 (Mar. 2019), p. 7469. ISSN: 1094-4087. DOI: [10.1364/OE.27.007469](https://doi.org/10.1364/OE.27.007469) (cit. on p. 78).
- [289] R. N. Hall et al. “Coherent Light Emission From GaAs Junctions”. In: *Physical Review Letters* 9.9 (Nov. 1962), pp. 366–368. ISSN: 0031-9007. DOI: [10.1103/PhysRevLett.9.366](https://doi.org/10.1103/PhysRevLett.9.366) (cit. on p. 78).
- [290] K. Iga. “Surface-emitting laser-its birth and generation of new optoelectronics field”. In: *IEEE Journal of Selected Topics in Quantum Electronics* 6.6 (Nov.

- 2000), pp. 1201–1215. ISSN: 1077-260X. DOI: [10.1109/2944.902168](https://doi.org/10.1109/2944.902168) (cit. on p. 78).
- [291] E. Yablonovitch. “Inhibited Spontaneous Emission in Solid-State Physics and Electronics”. In: *Physical Review Letters* 58.20 (May 1987), pp. 2059–2062. ISSN: 0031-9007. DOI: [10.1103/PhysRevLett.58.2059](https://doi.org/10.1103/PhysRevLett.58.2059) (cit. on p. 78).
- [292] J. D. Joannopoulos, P. R. Villeneuve, and S. Fan. “Photonic crystals: putting a new twist on light”. In: *Nature* 386.6621 (Mar. 1997), pp. 143–149. ISSN: 0028-0836. DOI: [10.1038/386143a0](https://doi.org/10.1038/386143a0) (cit. on p. 78).
- [293] X. Cai et al. “Integrated Compact Optical Vortex Beam Emitters”. In: *Science* 338.6105 (Oct. 2012), pp. 363–366. ISSN: 0036-8075. DOI: [10.1126/science.1226528](https://doi.org/10.1126/science.1226528) (cit. on p. 79).
- [294] P. Miao et al. “Orbital angular momentum microlaser”. In: *Science* 353.6298 (July 2016), pp. 464–467. ISSN: 0036-8075. DOI: [10.1126/science.aaf8533](https://doi.org/10.1126/science.aaf8533) (cit. on p. 79).
- [295] B. Peng et al. “Chiral modes and directional lasing at exceptional points.” In: *Proceedings of the National Academy of Sciences of the United States of America* 113.25 (June 2016), pp. 6845–6850. ISSN: 1091-6490. DOI: [10.1073/pnas.1603318113](https://doi.org/10.1073/pnas.1603318113) (cit. on p. 79).
- [296] S. Michaelis de Vasconcellos et al. “Spatial, spectral, and polarization properties of coupled micropillar cavities”. In: *Applied Physics Letters* 99.10 (Sept. 2011), p. 101103. ISSN: 0003-6951. DOI: [10.1063/1.3632111](https://doi.org/10.1063/1.3632111) (cit. on p. 82).
- [297] Y. Yafet. “g Factors and Spin-Lattice Relaxation of Conduction Electrons”. In: *Solid State Physics - Advances in Research and Applications*. Vol. 14. C. 1963, pp. 1–98. DOI: [10.1016/S0081-1947\(08\)60259-3](https://doi.org/10.1016/S0081-1947(08)60259-3) (cit. on p. 86).
- [298] G. E. Pikus and A. N. Titkov. “CHAPTER 3 - Spin Relaxation under Optical Orientation in Semiconductors”. In: *Optical Orientation*. Ed. by F. MEIER and B. P. ZAKHARCHENYA. Vol. 8. Modern Problems in Condensed Matter Sciences. Elsevier, 1984, pp. 73–131. DOI: <https://doi.org/10.1016/B978-0-444-86741-4.50008-1> (cit. on p. 86).
- [299] M. Z. Maialle, E. A. de Andrada e Silva, and L. J. Sham. “Exciton spin dynamics in quantum wells”. In: *Physical Review B* 47.23 (June 1993), pp. 15776–15788. ISSN: 0163-1829. DOI: [10.1103/PhysRevB.47.15776](https://doi.org/10.1103/PhysRevB.47.15776) (cit. on p. 86).
- [300] F.-k. Hsu et al. “Ultrafast spin-polarized lasing in a highly photoexcited semiconductor microcavity at room temperature”. In: *Physical Review B* 91.19 (May 2015), p. 195312. ISSN: 1098-0121. DOI: [10.1103/PhysRevB.91.195312](https://doi.org/10.1103/PhysRevB.91.195312) (cit. on pp. 87, 94).
- [301] H. Ando, T. Sogawa, and H. Gotoh. “Photon-spin controlled lasing oscillation in surface-emitting lasers”. In: *Applied Physics Letters* 73.5 (July 1998), p. 566. ISSN: 0003-6951. DOI: [10.1063/1.121857](https://doi.org/10.1063/1.121857) (cit. on p. 87).
- [302] Y. Arakawa and A. Yariv. “Quantum well lasers—Gain, spectra, dynamics”. In: *IEEE Journal of Quantum Electronics* 22.9 (Sept. 1986), pp. 1887–1899. ISSN: 0018-9197. DOI: [10.1109/JQE.1986.1073185](https://doi.org/10.1109/JQE.1986.1073185) (cit. on p. 91).
- [303] T. Takahashi, M. Nishioka, and Y. Arakawa. “Differential gain of GaAs/AlGaAs quantum well and modulation-doped quantum well lasers”. In: *Applied Physics Letters* 58.1 (Jan. 1991), pp. 4–6. ISSN: 0003-6951. DOI: [10.1063/1.104440](https://doi.org/10.1063/1.104440) (cit. on p. 91).
- [304] G. Agrawal. “Effect of gain and index nonlinearities on single-mode dynamics in semiconductor lasers”. In: *IEEE Journal of Quantum Electronics* 26.11 (1990), pp. 1901–1909. ISSN: 00189197. DOI: [10.1109/3.62109](https://doi.org/10.1109/3.62109) (cit. on p. 95).

- [305] A. S. Desyatnikov, Y. S. Kivshar, and L. Torner. “Optical vortices and vortex solitons”. In: *Progress in Optics* 47 (Jan. 2005), pp. 291–391. ISSN: 0079-6638. DOI: [10.1016/S0079-6638\(05\)47006-7](https://doi.org/10.1016/S0079-6638(05)47006-7) (cit. on p. 96).
- [306] C. L. Tang, A. Schremer, and T. Fujita. “Bistability in two-mode semiconductor lasers via gain saturation”. In: *Applied Physics Letters* 51.18 (Nov. 1987), pp. 1392–1394. ISSN: 0003-6951. DOI: [10.1063/1.98686](https://doi.org/10.1063/1.98686) (cit. on p. 97).
- [307] H. Kawaguchi et al. “Ultrafast switching in polarization-bistable laser diodes”. In: *Optics Letters* 17.2 (Jan. 1992), p. 130. ISSN: 0146-9592. DOI: [10.1364/OL.17.000130](https://doi.org/10.1364/OL.17.000130) (cit. on p. 97).
- [308] H. Kawaguchi. “Bistable laser diodes and their applications: state of the art”. In: *IEEE Journal of Selected Topics in Quantum Electronics* 3.5 (1997), pp. 1254–1270. ISSN: 1077260X. DOI: [10.1109/2944.658606](https://doi.org/10.1109/2944.658606) (cit. on p. 97).
- [309] A. Amo et al. “Interplay of exciton and electron-hole plasma recombination on the photoluminescence dynamics in bulk GaAs”. In: *Physical Review B* 73.3 (Jan. 2006), p. 035205. ISSN: 1098-0121. DOI: [10.1103/PhysRevB.73.035205](https://doi.org/10.1103/PhysRevB.73.035205) (cit. on p. 98).
- [310] K. Chan, H. Li, and C. Chan. “Optical gain of interdiffused InGaAs-As and AlGaAs-GaAs quantum wells”. In: *IEEE Journal of Quantum Electronics* 34.1 (1998), pp. 157–165. ISSN: 00189197. DOI: [10.1109/3.655019](https://doi.org/10.1109/3.655019) (cit. on p. 98).
- [311] A. Allain et al. “Electrical contacts to two-dimensional semiconductors”. In: *Nature Materials* 14.12 (Dec. 2015), pp. 1195–1205. ISSN: 1476-1122. DOI: [10.1038/nmat4452](https://doi.org/10.1038/nmat4452) (cit. on p. 99).
- [312] A. Fainstein et al. “Strong Optical-Mechanical Coupling in a Vertical GaAs/AlAs Microcavity for Subterahertz Phonons and Near-Infrared Light”. In: *Physical Review Letters* 110.3 (Jan. 2013), p. 037403. ISSN: 0031-9007. DOI: [10.1103/PhysRevLett.110.037403](https://doi.org/10.1103/PhysRevLett.110.037403) (cit. on p. 100).
- [313] E. F. Fenton et al. “Spin-optomechanical coupling between light and a nanofiber torsional mode”. In: *Optics Letters* 43.7 (Apr. 2018), p. 1534. ISSN: 0146-9592. DOI: [10.1364/OL.43.001534](https://doi.org/10.1364/OL.43.001534) (cit. on p. 100).
- [314] C. F. Fong et al. “Scheme for media conversion between electronic spin and photonic orbital angular momentum based on photonic nanocavity”. In: *Optics Express* 26.16 (Aug. 2018), p. 21219. ISSN: 1094-4087. DOI: [10.1364/OE.26.021219](https://doi.org/10.1364/OE.26.021219). arXiv: [1806.00223](https://arxiv.org/abs/1806.00223) (cit. on p. 100).
- [315] P. Lodahl et al. “Chiral quantum optics”. In: *Nature* 541.7638 (Jan. 2017), pp. 473–480. ISSN: 0028-0836. DOI: [10.1038/nature21037](https://doi.org/10.1038/nature21037). arXiv: [1608.00446](https://arxiv.org/abs/1608.00446) (cit. on p. 100).
- [316] K. Lechner. *Classical Electrodynamics*. UNITEXT for Physics. Cham: Springer International Publishing, Feb. 2018. ISBN: 978-3-319-91808-2. DOI: [10.1007/978-3-319-91809-9](https://doi.org/10.1007/978-3-319-91809-9) (cit. on pp. 101–103).
- [317] G. Milione et al. “Higher Order Pancharatnam-Berry Phase and the Angular Momentum of Light”. In: *Physical Review Letters* 108.19 (May 2012), p. 190401. ISSN: 0031-9007. DOI: [10.1103/PhysRevLett.108.190401](https://doi.org/10.1103/PhysRevLett.108.190401) (cit. on p. 105).
- [318] P. B. Monteiro, P. A. M. Neto, and H. M. Nussenzveig. “Angular momentum of focused beams: Beyond the paraxial approximation”. In: *Physical Review A* 79.3 (Mar. 2009), p. 033830. ISSN: 1050-2947. DOI: [10.1103/PhysRevA.79.033830](https://doi.org/10.1103/PhysRevA.79.033830). arXiv: [0902.3214](https://arxiv.org/abs/0902.3214) (cit. on p. 105).
- [319] M. S. Dresselhaus, G. Dresselhaus, and A. (Jorio. *Group theory : application to the physics of condensed matter*. Springer-Verlag, 2008, p. 582. ISBN: 9783540328995 (cit. on p. 107).

- [320] P. Hamel et al. “Spontaneous mirror-symmetry breaking in coupled photonic-crystal nanolasers”. In: *Nature Photonics* 9.5 (May 2015), pp. 311–315. ISSN: 1749-4885. DOI: [10.1038/nphoton.2015.65](https://doi.org/10.1038/nphoton.2015.65) (cit. on pp. 111, 112).
- [321] K. G. Lagoudakis et al. “Coherent Oscillations in an Exciton-Polariton Josephson Junction”. In: *Physical Review Letters* 105.12 (Sept. 2010), p. 120403. ISSN: 0031-9007. DOI: [10.1103/PhysRevLett.105.120403](https://doi.org/10.1103/PhysRevLett.105.120403) (cit. on pp. 111, 112).
- [322] A. F. Adiyatullin et al. “Periodic squeezing in a polariton Josephson junction”. In: *Nature Communications* 8.1 (Dec. 2017), p. 1329. ISSN: 2041-1723. DOI: [10.1038/s41467-017-01331-8](https://doi.org/10.1038/s41467-017-01331-8) (cit. on pp. 111, 112).
- [323] S. R. K. Rodriguez et al. “Interaction-induced hopping phase in driven-dissipative coupled photonic microcavities”. In: *Nature Communications* 7.1 (Sept. 2016), p. 11887. ISSN: 2041-1723. DOI: [10.1038/ncomms11887](https://doi.org/10.1038/ncomms11887) (cit. on pp. 111, 112, 122).
- [324] L. A. Orozco, A. T. Rosenberger, and H. J. Kimble. “Intrinsic Dynamical Instability in Optical Bistability with Two-Level Atoms”. In: *Physical Review Letters* 53.27 (Dec. 1984), pp. 2547–2550. ISSN: 0031-9007. DOI: [10.1103/PhysRevLett.53.2547](https://doi.org/10.1103/PhysRevLett.53.2547) (cit. on pp. 111, 115).
- [325] L. A. Lugiato et al. “Bistability, self-pulsing and chaos in optical parametric oscillators”. In: *Il Nuovo Cimento D* 10.8 (Aug. 1988), pp. 959–977. ISSN: 03926737. DOI: [10.1007/BF02450197](https://doi.org/10.1007/BF02450197) (cit. on pp. 111, 115).
- [326] T. J. Kippenberg, S. M. Spillane, and K. J. Vahala. “Kerr-Nonlinearity Optical Parametric Oscillation in an Ultrahigh-Q Toroid Microcavity”. In: *Physical Review Letters* 93.8 (Aug. 2004), p. 083904. ISSN: 0031-9007. DOI: [10.1103/PhysRevLett.93.083904](https://doi.org/10.1103/PhysRevLett.93.083904) (cit. on p. 111).
- [327] B. J. M. Hausmann et al. “Diamond nonlinear photonics”. In: *Nature Photonics* 8.5 (May 2014), pp. 369–374. ISSN: 1749-4885. DOI: [10.1038/nphoton.2014.72](https://doi.org/10.1038/nphoton.2014.72) (cit. on p. 111).
- [328] M. Pu et al. “Efficient frequency comb generation in AlGaAs-on-insulator”. In: *Optica* 3.8 (Aug. 2016), p. 823. ISSN: 2334-2536. DOI: [10.1364/OPTICA.3.000823](https://doi.org/10.1364/OPTICA.3.000823) (cit. on p. 111).
- [329] X. Ji et al. “Ultra-low-loss on-chip resonators with sub-milliwatt parametric oscillation threshold”. In: *Optica* 4.6 (June 2017), p. 619. ISSN: 2334-2536. DOI: [10.1364/OPTICA.4.000619](https://doi.org/10.1364/OPTICA.4.000619) (cit. on p. 111).
- [330] D. Sarchi et al. “Coherent dynamics and parametric instabilities of microcavity polaritons in double-well systems”. In: *Physical Review B* 77.12 (Mar. 2008), p. 125324. ISSN: 1098-0121. DOI: [10.1103/PhysRevB.77.125324](https://doi.org/10.1103/PhysRevB.77.125324) (cit. on pp. 111, 112, 114, 116, 117, 122, 125, 126, 154).
- [331] N. C. Zambon et al. “Parametric instability in coupled nonlinear microcavities”. In: 39.4 (Nov. 2019), pp. 1–6. arXiv: [1911.02816](https://arxiv.org/abs/1911.02816) (cit. on p. 111).
- [332] T. Calarco, R. Fazio, and P. Mataloni, eds. *Quantum Simulators*. SeriesProc. 2018. ISBN: 978-1-61499-856-3 (cit. on p. 112).
- [333] S. Diehl et al. “Quantum states and phases in driven open quantum systems with cold atoms”. In: *Nature Physics* 4.11 (Nov. 2008), pp. 878–883. ISSN: 1745-2473. DOI: [10.1038/nphys1073](https://doi.org/10.1038/nphys1073) (cit. on p. 112).
- [334] J. Lebreuilly et al. “Stabilizing strongly correlated photon fluids with non-Markovian reservoirs”. In: *Physical Review A* 96.3 (2017), pp. 1–15. ISSN: 24699934. DOI: [10.1103/PhysRevA.96.033828](https://doi.org/10.1103/PhysRevA.96.033828) (cit. on p. 112).

- [335] R. Ma et al. “A dissipatively stabilized Mott insulator of photons”. In: *Nature* 566.7742 (2019), pp. 51–57. ISSN: 14764687. DOI: [10.1038/s41586-019-0897-9](https://doi.org/10.1038/s41586-019-0897-9). arXiv: [1807.11342](https://arxiv.org/abs/1807.11342) (cit. on pp. [112](#), [133](#), [145](#), [152](#)).
- [336] R. O. Umucalllar and I. Carusotto. “Fractional quantum hall states of photons in an array of dissipative coupled cavities”. In: *Physical Review Letters* 108.20 (2012), pp. 1–5. ISSN: 00319007. DOI: <https://arxiv.org/abs/1907.05872> (cit. on p. [112](#)).
- [337] P. Knüppel et al. “Nonlinear optics in the fractional quantum Hall regime”. In: *Nature* 572.7767 (Aug. 2019), pp. 91–94. ISSN: 0028-0836. DOI: [10.1038/s41586-019-1356-3](https://doi.org/10.1038/s41586-019-1356-3) (cit. on pp. [112](#), [156](#)).
- [338] M. Abbarchi et al. “Macroscopic quantum self-trapping and Josephson oscillations of exciton polaritons”. In: *Nature Physics* 9.5 (May 2013), pp. 275–279. ISSN: 1745-2473. DOI: [10.1038/nphys2609](https://doi.org/10.1038/nphys2609) (cit. on p. [112](#)).
- [339] S. Rahimzadeh Kalaleh Rodriguez et al. “Nonlinear Polariton Localization in Strongly Coupled Driven-Dissipative Microcavities”. In: *ACS Photonics* 5.1 (Jan. 2018), pp. 95–99. ISSN: 2330-4022. DOI: [10.1021/acsphotonics.7b00721](https://doi.org/10.1021/acsphotonics.7b00721) (cit. on p. [112](#)).
- [340] C. Vaneph et al. “Observation of the Unconventional Photon Blockade in the Microwave Domain”. In: *Physical Review Letters* 121.4 (July 2018), p. 043602. ISSN: 0031-9007. DOI: [10.1103/PhysRevLett.121.043602](https://doi.org/10.1103/PhysRevLett.121.043602) (cit. on p. [112](#)).
- [341] W. Casteels and C. Ciuti. “Quantum entanglement in the spatial-symmetry-breaking phase transition of a driven-dissipative Bose-Hubbard dimer”. In: *Physical Review A* 95.1 (2017), pp. 1–5. ISSN: 24699934. DOI: [10.1103/PhysRevA.95.013812](https://doi.org/10.1103/PhysRevA.95.013812). arXiv: [1607.02578](https://arxiv.org/abs/1607.02578) (cit. on pp. [112](#), [114](#)).
- [342] F. Melde. “Ueber die Erregung stehender Wellen eines fadenförmigen Körpers”. In: *Annalen der Physik und Chemie* 185.2 (1860), pp. 193–215. ISSN: 00033804. DOI: [10.1002/andp.18601850202](https://doi.org/10.1002/andp.18601850202) (cit. on p. [113](#)).
- [343] S. Fauve et al. “Parametric instability of a liquid-vapor interface close to the critical point”. In: *Physical Review Letters* 68.21 (May 1992), pp. 3160–3163. ISSN: 0031-9007. DOI: [10.1103/PhysRevLett.68.3160](https://doi.org/10.1103/PhysRevLett.68.3160) (cit. on p. [113](#)).
- [344] M. Faraday. “On a Peculiar Class of Acoustical Figures; and on Certain Forms Assumed by Groups of Particles upon Vibrating Elastic Surfaces”. In: *Philosophical Transactions of the Royal Society of London* 121.1831 (1831), pp. 299–340. ISSN: 0261-0523. DOI: [10.1098/rstl.1831.0018](https://doi.org/10.1098/rstl.1831.0018) (cit. on p. [113](#)).
- [345] L. Rayleigh. “On the Maintenance of Vibrations by Forces of Double Frequency, and on the Propagation of Waves through a Medium endowed with a Periodic Structure.” In: *Philosophical Magazine and Journal of Science* 24.147 (1887), pp. 145–159. DOI: [10.1080/14786430310001611644](https://doi.org/10.1080/14786430310001611644) (cit. on p. [113](#)).
- [346] W. B. Case. “The pumping of a swing from the standing position”. In: *American Journal of Physics* 64.3 (Mar. 1996), pp. 215–220. ISSN: 0002-9505. DOI: [10.1119/1.18209](https://doi.org/10.1119/1.18209) (cit. on p. [113](#)).
- [347] J. A. Giordmaine and R. C. Miller. “Tunable Coherent Parametric Oscillation in LiNb at Optical Frequencies”. In: *Physical Review Letters* 14.24 (June 1965), pp. 973–976. ISSN: 0031-9007. DOI: [10.1103/PhysRevLett.14.973](https://doi.org/10.1103/PhysRevLett.14.973) (cit. on p. [113](#)).
- [348] J. Hansryd et al. “Fiber-based optical parametric amplifiers and their applications”. In: *IEEE Journal on Selected Topics in Quantum Electronics* 8.3 (2002), pp. 506–520. ISSN: 1077260X. DOI: [10.1109/JSTQE.2002.1016354](https://doi.org/10.1109/JSTQE.2002.1016354) (cit. on p. [113](#)).

-
- [349] T. Yamamoto et al. “Flux-driven Josephson parametric amplifier”. In: *Applied Physics Letters* 93.4 (2008), pp. 2–5. ISSN: 00036951. DOI: [10.1063/1.2964182](https://doi.org/10.1063/1.2964182). arXiv: [0808.1386](https://arxiv.org/abs/0808.1386) (cit. on p. 113).
- [350] M. Hatridge et al. “Dispersive magnetometry with a quantum limited SQUID parametric amplifier”. In: *Physical Review B - Condensed Matter and Materials Physics* 83.13 (2011), pp. 1–8. ISSN: 10980121. DOI: [10.1103/PhysRevB.83.134501](https://doi.org/10.1103/PhysRevB.83.134501). arXiv: [1003.2466](https://arxiv.org/abs/1003.2466) (cit. on p. 113).
- [351] Y. Okawachi et al. “Octave-spanning frequency comb generation in a silicon nitride chip”. In: *Optics Letters* 36.17 (Sept. 2011), p. 3398. ISSN: 0146-9592. DOI: [10.1364/OL.36.003398](https://doi.org/10.1364/OL.36.003398) (cit. on p. 113).
- [352] P. Del’Haye et al. “Octave Spanning Tunable Frequency Comb from a Microresonator”. In: *Physical Review Letters* 107.6 (Aug. 2011), p. 063901. ISSN: 0031-9007. DOI: [10.1103/PhysRevLett.107.063901](https://doi.org/10.1103/PhysRevLett.107.063901) (cit. on p. 113).
- [353] T. Udem, R. Holzwarth, and T. W. Hänsch. *Optical frequency metrology*. 2002. DOI: [10.1038/416233a](https://doi.org/10.1038/416233a) (cit. on p. 113).
- [354] A. Heidmann et al. “Observation of Quantum Noise Reduction on Twin Laser Beams”. In: *Physical Review Letters* 59.22 (Nov. 1987), pp. 2555–2557. ISSN: 0031-9007. DOI: [10.1103/PhysRevLett.59.2555](https://doi.org/10.1103/PhysRevLett.59.2555). arXiv: [arXiv:1011.1669v3](https://arxiv.org/abs/1011.1669v3) (cit. on p. 113).
- [355] A. Dutt et al. “On-Chip Optical Squeezing”. In: *Physical Review Applied* 3.4 (Apr. 2015), p. 044005. ISSN: 2331-7019. DOI: [10.1103/PhysRevApplied.3.044005](https://doi.org/10.1103/PhysRevApplied.3.044005) (cit. on p. 113).
- [356] A. Schönbeck, F. Thies, and R. Schnabel. “13 dB squeezed vacuum states at 1550 nm from 12 mW external pump power at 775 nm”. In: *Optics Letters* 43.1 (Jan. 2018), p. 110. ISSN: 0146-9592. DOI: [10.1364/OL.43.000110](https://doi.org/10.1364/OL.43.000110) (cit. on p. 113).
- [357] M. D. Reid and P. D. Drummond. “Quantum correlations of phase in nondegenerate parametric oscillation”. In: *Physical Review Letters* 60.26 (1988), pp. 2731–2733. ISSN: 00319007. DOI: [10.1103/PhysRevLett.60.2731](https://doi.org/10.1103/PhysRevLett.60.2731) (cit. on p. 113).
- [358] Z. Y. Ou et al. “Realization of the Einstein-Podolsky-Rosen”. In: *Physical Review Letters* (1992). ISSN: 0031-9007. DOI: [10.1103/PhysRevLett.68.3663](https://doi.org/10.1103/PhysRevLett.68.3663) (cit. on p. 113).
- [359] M. Martinelli et al. “Experimental study of the spatial distribution of quantum correlations in a confocal optical parametric oscillator”. In: *Physical Review A* 67.023808 (2003), pp. 1–9. ISSN: 1050-2947. DOI: [10.1103/PhysRevA.67.023808](https://doi.org/10.1103/PhysRevA.67.023808). arXiv: [0210023](https://arxiv.org/abs/0210023) [quant-ph] (cit. on p. 113).
- [360] S. Mittal, E. A. Goldschmidt, and M. Hafezi. “A topological source of quantum light”. In: *Nature* 561.7724 (Sept. 2018), pp. 502–506. ISSN: 0028-0836. DOI: [10.1038/s41586-018-0478-3](https://doi.org/10.1038/s41586-018-0478-3) (cit. on pp. 113, 126, 154).
- [361] L. Ferrier et al. “Polariton parametric oscillation in a single micropillar cavity”. In: *Applied Physics Letters* 97.3 (July 2010), p. 031105. ISSN: 0003-6951. DOI: [10.1063/1.3466902](https://doi.org/10.1063/1.3466902) (cit. on pp. 113, 126, 154).
- [362] I. Carusotto and C. Ciuti. “Spontaneous microcavity-polariton coherence across the parametric threshold: Quantum Monte Carlo studies”. In: *Physical Review B* 72.12 (Sept. 2005), p. 125335. ISSN: 1098-0121. DOI: [10.1103/PhysRevB.72.125335](https://doi.org/10.1103/PhysRevB.72.125335) (cit. on p. 114).
- [363] B. Ségard et al. “Multimode instability in optical bistability”. In: *Physical Review A* 39.2 (Jan. 1989), pp. 703–722. ISSN: 0556-2791. DOI: [10.1103/PhysRevA.39.703](https://doi.org/10.1103/PhysRevA.39.703) (cit. on p. 115).

- [364] O. Lafont et al. “Origins and control of the polarization splitting in exciton-polaritons microwires”. In: (Oct. 2016), pp. 6–9. arXiv: [1610.04856](https://arxiv.org/abs/1610.04856) (cit. on p. 118).
- [365] S. Michaelis de Vasconcellos et al. “Spatial, spectral, and polarization properties of coupled micropillar cavities”. In: *Applied Physics Letters* 99.10 (Sept. 2011), p. 101103. ISSN: 0003-6951. DOI: [10.1063/1.3632111](https://doi.org/10.1063/1.3632111) (cit. on p. 119).
- [366] H. M. Gibbs et al. “Optical bistability in semiconductors”. In: *Applied Physics Letters* 35.6 (Sept. 1979), pp. 451–453. ISSN: 0003-6951. DOI: [10.1063/1.91157](https://doi.org/10.1063/1.91157) (cit. on p. 122).
- [367] P. M. Walker et al. “Dark Solitons in High Velocity Waveguide Polariton Fluids”. In: *Physical Review Letters* 119.9 (Aug. 2017), p. 097403. ISSN: 0031-9007. DOI: [10.1103/PhysRevLett.119.097403](https://doi.org/10.1103/PhysRevLett.119.097403) (cit. on p. 122).
- [368] C. Lledó, T. K. Mavrogordatos, and M. H. Szymańska. “Driven Bose-Hubbard dimer under nonlocal dissipation: A bistable time crystal”. In: *Physical Review B* 100.5 (Aug. 2019), p. 054303. ISSN: 2469-9950. DOI: [10.1103/PhysRevB.100.054303](https://doi.org/10.1103/PhysRevB.100.054303) (cit. on p. 125).
- [369] K. Seibold, R. Rota, and V. Savona. *A dissipative time crystal in an asymmetric non-linear photonic dimer*. Oct. 2019. arXiv: [1910.03499](https://arxiv.org/abs/1910.03499) (cit. on p. 125).
- [370] C. Ciuti, P. Schwendimann, and A. Quattropani. “Parametric luminescence of microcavity polaritons”. In: *Physical Review B* 63.4 (Jan. 2001), 041303(R). ISSN: 0163-1829. DOI: [10.1103/PhysRevB.63.041303](https://doi.org/10.1103/PhysRevB.63.041303) (cit. on p. 126).
- [371] Z. Wang et al. “Quantum Dynamics of a Few-Photon Parametric Oscillator”. In: *Physical Review X* 9.2 (June 2019), p. 021049. ISSN: 2160-3308. DOI: [10.1103/PhysRevX.9.021049](https://doi.org/10.1103/PhysRevX.9.021049) (cit. on p. 126).
- [372] T. Karzig et al. “Topological Polaritons”. In: *Physical Review X* 5.3 (July 2015), p. 031001. ISSN: 2160-3308. DOI: [10.1103/PhysRevX.5.031001](https://doi.org/10.1103/PhysRevX.5.031001) (cit. on p. 126).
- [373] K. Ikeda. “Multiple-valued stationary state and its instability of the transmitted light by a ring cavity system”. In: *Optics Communications* 30.2 (Aug. 1979), pp. 257–261. ISSN: 00304018. DOI: [10.1016/0030-4018\(79\)90090-7](https://doi.org/10.1016/0030-4018(79)90090-7) (cit. on p. 126).
- [374] D. D. Solnyshkov et al. “Chaotic Josephson oscillations of exciton-polaritons and their applications”. In: *Physical Review B* 80.23 (Dec. 2009), p. 235303. ISSN: 1098-0121. DOI: [10.1103/PhysRevB.80.235303](https://doi.org/10.1103/PhysRevB.80.235303) (cit. on p. 126).
- [375] H. H. Adamyán, S. B. Manvelyan, and G. Y. Kryuchkyan. “Chaos in a double driven dissipative nonlinear oscillator”. In: *Physical Review E* 64.4 (Sept. 2001), p. 046219. ISSN: 1063-651X. DOI: [10.1103/PhysRevE.64.046219](https://doi.org/10.1103/PhysRevE.64.046219) (cit. on p. 126).
- [376] M. Žnidarič et al. “Thermalization and ergodicity in one-dimensional many-body open quantum systems”. In: *Physical Review E* 81.5 (May 2010), p. 051135. ISSN: 1539-3755. DOI: [10.1103/PhysRevE.81.051135](https://doi.org/10.1103/PhysRevE.81.051135) (cit. on p. 126).
- [377] R. Bonifacio and L. A. Lugiato. “Photon Statistics and Spectrum of Transmitted Light in Optical Bistability”. In: *Physical Review Letters* 40.15 (Apr. 1978), pp. 1023–1027. ISSN: 0031-9007. DOI: [10.1103/PhysRevLett.40.1023](https://doi.org/10.1103/PhysRevLett.40.1023) (cit. on pp. 127, 130).
- [378] F. T. Hioe and S. Singh. “Correlations, transients, bistability, and phase-transition analogy in two-mode lasers”. In: *Physical Review A* 24.4 (Oct. 1981), pp. 2050–2074. ISSN: 0556-2791. DOI: [10.1103/PhysRevA.24.2050](https://doi.org/10.1103/PhysRevA.24.2050) (cit. on pp. 127, 130, 132).

- [379] P. Lett et al. “Macroscopic Quantum Fluctuations and First-Order Phase Transition in a Laser”. In: *Physical Review Letters* 47.26 (Dec. 1981), pp. 1892–1895. ISSN: 0031-9007. DOI: [10.1103/PhysRevLett.47.1892](https://doi.org/10.1103/PhysRevLett.47.1892) (cit. on pp. 127, 132).
- [380] W. Casteels et al. “Power laws in the dynamic hysteresis of quantum nonlinear photonic resonators”. In: *Physical Review A* 93.3 (Mar. 2016), p. 033824. ISSN: 2469-9926. DOI: [10.1103/PhysRevA.93.033824](https://doi.org/10.1103/PhysRevA.93.033824). arXiv: [1509.02118](https://arxiv.org/abs/1509.02118) (cit. on pp. 127, 134, 138).
- [381] U. Seifert. “Entropy Production along a Stochastic Trajectory and an Integral Fluctuation Theorem”. In: *Physical Review Letters* 95.4 (July 2005), p. 040602. ISSN: 0031-9007. DOI: [10.1103/PhysRevLett.95.040602](https://doi.org/10.1103/PhysRevLett.95.040602) (cit. on pp. 127, 147, 150, 155).
- [382] H. M. Gibbs, S. L. McCall, and T. N. C. Venkatesan. “Differential Gain and Bistability Using a Sodium-Filled Fabry-Perot Interferometer”. In: *Physical Review Letters* 36.19 (May 1976), pp. 1135–1138. ISSN: 0031-9007. DOI: [10.1103/PhysRevLett.36.1135](https://doi.org/10.1103/PhysRevLett.36.1135) (cit. on p. 130).
- [383] J. A. Goldstone and E. Garmire. “Intrinsic Optical Bistability in Nonlinear Media”. In: *Physical Review Letters* 53.9 (Aug. 1984), pp. 910–913. ISSN: 0031-9007. DOI: [10.1103/PhysRevLett.53.910](https://doi.org/10.1103/PhysRevLett.53.910) (cit. on p. 130).
- [384] G. Rempe et al. “Optical bistability and photon statistics in cavity quantum electrodynamics”. In: *Physical Review Letters* 67.13 (Sept. 1991), pp. 1727–1730. ISSN: 0031-9007. DOI: [10.1103/PhysRevLett.67.1727](https://doi.org/10.1103/PhysRevLett.67.1727) (cit. on p. 130).
- [385] V. R. Almeida and M. Lipson. “Optical bistability on a silicon chip”. In: *Optics Letters* 29.20 (Oct. 2004), p. 2387. ISSN: 0146-9592. DOI: [10.1364/OL.29.002387](https://doi.org/10.1364/OL.29.002387) (cit. on p. 130).
- [386] G. A. Wurtz, R. Pollard, and A. V. Zayats. “Optical bistability in nonlinear surface-plasmon polaritonic crystals”. In: *Physical Review Letters* 97.5 (2006), pp. 1–4. ISSN: 00319007. DOI: [10.1103/PhysRevLett.97.057402](https://doi.org/10.1103/PhysRevLett.97.057402) (cit. on p. 130).
- [387] J. Kerckhoff, M. A. Armen, and H. Mabuchi. “Remnants of semiclassical bistability in the few-photon regime of cavity QED”. In: *Optics Express* 19.24 (Nov. 2011), p. 24468. ISSN: 1094-4087. DOI: [10.1364/OE.19.024468](https://doi.org/10.1364/OE.19.024468) (cit. on p. 130).
- [388] H. Abbaspour et al. “Effect of a noisy driving field on a bistable polariton system”. In: *Physical Review B* 92.16 (Oct. 2015), p. 165303. ISSN: 1098-0121. DOI: [10.1103/PhysRevB.92.165303](https://doi.org/10.1103/PhysRevB.92.165303) (cit. on p. 130).
- [389] K. Vogel and H. Risken. “Quantum-tunneling rates and stationary solutions in dispersive optical bistability”. In: *Physical Review A* 38.5 (Sept. 1988), pp. 2409–2422. ISSN: 0556-2791. DOI: [10.1103/PhysRevA.38.2409](https://doi.org/10.1103/PhysRevA.38.2409) (cit. on pp. 131, 142).
- [390] H. Risken and K. Vogel. “Quantum tunneling rates in dispersive optical bistability for low cavity damping”. In: *Physical Review A* 38.3 (Aug. 1988), pp. 1349–1357. ISSN: 0556-2791. DOI: [10.1103/PhysRevA.38.1349](https://doi.org/10.1103/PhysRevA.38.1349) (cit. on pp. 131, 142).
- [391] R. M. Wilson et al. “Collective phases of strongly interacting cavity photons”. In: *Phys. Rev. A* 94.3 (Sept. 2016), p. 33801. DOI: [10.1103/PhysRevA.94.033801](https://doi.org/10.1103/PhysRevA.94.033801) (cit. on p. 132).
- [392] T. Schneider, G. Srinivasan, and C. P. Enz. “Phase Transitions and Soft Modes”. In: *Physical Review A* 5.3 (Mar. 1972), pp. 1528–1536. ISSN: 0556-2791. DOI: [10.1103/PhysRevA.5.1528](https://doi.org/10.1103/PhysRevA.5.1528) (cit. on pp. 132, 133).
- [393] K. Binder. “Theory of first-order phase transitions”. In: *Reports on Progress in Physics* 50.7 (July 1987), pp. 783–859. ISSN: 0034-4885. DOI: [10.1088/0034-4885/50/7/001](https://doi.org/10.1088/0034-4885/50/7/001) (cit. on p. 132).

- [394] M. Fabrizio. “Ice-water and liquid-vapor phase transitions by a Ginzburg–Landau model”. In: *Journal of Mathematical Physics* 49.10 (Oct. 2008), p. 102902. ISSN: 0022-2488. DOI: [10.1063/1.2992478](https://doi.org/10.1063/1.2992478) (cit. on p. 132).
- [395] S. L. Sondhi et al. “Continuous quantum phase transitions”. In: *Reviews of Modern Physics* 69.1 (Jan. 1997), pp. 315–333. ISSN: 0034-6861. DOI: [10.1103/RevModPhys.69.315](https://doi.org/10.1103/RevModPhys.69.315) (cit. on p. 133).
- [396] S. Sachdev. “Quantum Criticality: Competing Ground States in Low Dimensions”. In: *Science* 288.5465 (Apr. 2000), pp. 475–480. ISSN: 00368075. DOI: [10.1126/science.288.5465.475](https://doi.org/10.1126/science.288.5465.475) (cit. on p. 133).
- [397] M. Vojta. “Quantum phase transitions”. In: *Reports on Progress in Physics* 66.12 (Dec. 2003), pp. 2069–2110. ISSN: 0034-4885. DOI: [10.1088/0034-4885/66/12/R01](https://doi.org/10.1088/0034-4885/66/12/R01) (cit. on p. 133).
- [398] H. J. Carmichael. “Analytical and numerical results for the steady state in cooperative resonance fluorescence”. In: *Journal of Physics B: Atomic and Molecular Physics* 13.18 (Sept. 1980), pp. 3551–3575. ISSN: 0022-3700. DOI: [10.1088/0022-3700/13/18/009](https://doi.org/10.1088/0022-3700/13/18/009) (cit. on p. 133).
- [399] M. J. Bhaseen et al. “Dynamics of nonequilibrium Dicke models”. In: *Physical Review A* 85.1 (Jan. 2012), p. 013817. ISSN: 1050-2947. DOI: [10.1103/PhysRevA.85.013817](https://doi.org/10.1103/PhysRevA.85.013817) (cit. on p. 133).
- [400] B. Öztop et al. “Excitations of optically driven atomic condensate in a cavity: theory of photodetection measurements”. In: *New Journal of Physics* 14.8 (Aug. 2012), p. 085011. ISSN: 1367-2630. DOI: [10.1088/1367-2630/14/8/085011](https://doi.org/10.1088/1367-2630/14/8/085011) (cit. on p. 133).
- [401] J. M. Fink et al. “Observation of the Photon-Blockade Breakdown Phase Transition”. In: *Physical Review X* 7.1 (Jan. 2017), p. 011012. ISSN: 2160-3308. DOI: [10.1103/PhysRevX.7.011012](https://doi.org/10.1103/PhysRevX.7.011012). arXiv: [1607.04892](https://arxiv.org/abs/1607.04892) (cit. on pp. 133, 139).
- [402] T. Fink et al. “Signatures of a dissipative phase transition in photon correlation measurements”. In: *Nature Physics* 14.4 (Apr. 2018), pp. 365–369. ISSN: 1745-2473. DOI: [10.1038/s41567-017-0020-9](https://doi.org/10.1038/s41567-017-0020-9) (cit. on pp. 133, 140).
- [403] C. N. Luse and A. Zangwill. “Discontinuous scaling of hysteresis losses”. In: *Physical Review E* 50.1 (July 1994), pp. 224–226. ISSN: 1063-651X. DOI: [10.1103/PhysRevE.50.224](https://doi.org/10.1103/PhysRevE.50.224) (cit. on p. 138).
- [404] P. Jung et al. “Scaling law for dynamical hysteresis”. In: *Physical Review Letters* 65.15 (Oct. 1990), pp. 1873–1876. ISSN: 0031-9007. DOI: [10.1103/PhysRevLett.65.1873](https://doi.org/10.1103/PhysRevLett.65.1873) (cit. on p. 138).
- [405] J. Dziarmaga. “Dynamics of a quantum phase transition and relaxation to a steady state”. In: *Advances in Physics* 59.6 (Nov. 2010), pp. 1063–1189. ISSN: 0001-8732. DOI: [10.1080/00018732.2010.514702](https://doi.org/10.1080/00018732.2010.514702) (cit. on p. 138).
- [406] F. Letscher et al. “Bistability Versus Metastability in Driven Dissipative Rydberg Gases”. In: *Physical Review X* 7.2 (May 2017), p. 021020. ISSN: 2160-3308. DOI: [10.1103/PhysRevX.7.021020](https://doi.org/10.1103/PhysRevX.7.021020) (cit. on p. 139).
- [407] L. Pickup et al. “Optical Bistability under Nonresonant Excitation in Spinor Polariton Condensates”. In: *Physical Review Letters* 120.22 (May 2018), p. 225301. ISSN: 0031-9007. DOI: [10.1103/PhysRevLett.120.225301](https://doi.org/10.1103/PhysRevLett.120.225301) (cit. on p. 139).
- [408] H. Kramers. “Brownian motion in a field of force and the diffusion model of chemical reactions”. In: *Physica* 7.4 (Apr. 1940), pp. 284–304. ISSN: 00318914. DOI: [10.1016/S0031-8914\(40\)90098-2](https://doi.org/10.1016/S0031-8914(40)90098-2) (cit. on pp. 141, 142).

- [409] P. Hanggi. “Escape from a metastable state”. In: *Journal of Statistical Physics* 42.1-2 (Jan. 1986), pp. 105–148. ISSN: 0022-4715. DOI: [10.1007/BF01010843](https://doi.org/10.1007/BF01010843) (cit. on pp. [141](#), [142](#)).
- [410] J. T. Young et al. “Non-equilibrium fixed points of coupled Ising models”. In: (Mar. 2019), pp. 1–33. arXiv: [1903.02569](https://arxiv.org/abs/1903.02569) (cit. on p. [143](#)).
- [411] C. Bustamante, J. Liphardt, and F. Ritort. “The Nonequilibrium Thermodynamics of Small Systems”. In: *Physics Today* 58.7 (July 2005), pp. 43–48. ISSN: 0031-9228. DOI: [10.1063/1.2012462](https://doi.org/10.1063/1.2012462) (cit. on p. [144](#)).
- [412] G. Gallavotti and E. G. D. Cohen. “Dynamical Ensembles in Nonequilibrium Statistical Mechanics”. In: *Physical Review Letters* 74.14 (Apr. 1995), pp. 2694–2697. ISSN: 0031-9007. DOI: [10.1103/PhysRevLett.74.2694](https://doi.org/10.1103/PhysRevLett.74.2694) (cit. on p. [144](#)).
- [413] C. Jarzynski. “Equilibrium free-energy differences from nonequilibrium measurements: A master-equation approach”. In: *Physical Review E* 56.5 (Nov. 1997), pp. 5018–5035. ISSN: 1063-651X. DOI: [10.1103/PhysRevE.56.5018](https://doi.org/10.1103/PhysRevE.56.5018). arXiv: [9707325](https://arxiv.org/abs/9707325) [[cond-mat](#)] (cit. on p. [144](#)).
- [414] G. E. Crooks. “Entropy production fluctuation theorem and the nonequilibrium work relation for free energy differences”. In: *Physical Review E* 60.3 (Sept. 1999), pp. 2721–2726. ISSN: 1063-651X. DOI: [10.1103/PhysRevE.60.2721](https://doi.org/10.1103/PhysRevE.60.2721) (cit. on p. [144](#)).
- [415] T. Speck and U. Seifert. “The Jarzynski relation, fluctuation theorems, and stochastic thermodynamics for non-Markovian processes”. In: *Journal of Statistical Mechanics: Theory and Experiment* 2007.09 (Sept. 2007), pp. L09002–L09002. ISSN: 1742-5468. DOI: [10.1088/1742-5468/2007/09/L09002](https://doi.org/10.1088/1742-5468/2007/09/L09002) (cit. on p. [144](#)).
- [416] U. Seifert. “Stochastic thermodynamics, fluctuation theorems and molecular machines”. In: *Reports on Progress in Physics* 75.12 (Dec. 2012), p. 126001. ISSN: 0034-4885. DOI: [10.1088/0034-4885/75/12/126001](https://doi.org/10.1088/0034-4885/75/12/126001) (cit. on pp. [144](#), [147](#), [150](#)).
- [417] S. Borlenghi et al. “Entropy production for complex Langevin equations”. In: *Physical Review E* 96.1 (July 2017), p. 012150. ISSN: 2470-0045. DOI: [10.1103/PhysRevE.96.012150](https://doi.org/10.1103/PhysRevE.96.012150). arXiv: [arXiv:1704.01566v2](https://arxiv.org/abs/1704.01566v2) (cit. on pp. [144](#), [145](#)).
- [418] D. Collin et al. “Verification of the Crooks fluctuation theorem and recovery of RNA folding free energies”. In: *Nature* 437.7056 (Sept. 2005), pp. 231–234. ISSN: 0028-0836. DOI: [10.1038/nature04061](https://doi.org/10.1038/nature04061) (cit. on p. [144](#)).
- [419] V. Blickle et al. “Einstein Relation Generalized to Nonequilibrium”. In: *Physical Review Letters* 98.21 (May 2007), p. 210601. ISSN: 0031-9007. DOI: [10.1103/PhysRevLett.98.210601](https://doi.org/10.1103/PhysRevLett.98.210601). arXiv: [arXiv:0704.2283v1](https://arxiv.org/abs/0704.2283v1) (cit. on p. [144](#)).
- [420] P. Jop, A. Petrosyan, and S. Ciliberto. “Work and dissipation fluctuations near the stochastic resonance of a colloidal particle”. In: *{EPL} (Europhysics Letters)* 81.5 (Feb. 2008), p. 50005. DOI: [10.1209/0295-5075/81/50005](https://doi.org/10.1209/0295-5075/81/50005) (cit. on p. [144](#)).
- [421] S. Schuler et al. “Experimental Test of the Fluctuation Theorem for a Driven Two-Level System with Time-Dependent Rates”. In: *Physical Review Letters* 94.18 (May 2005), p. 180602. ISSN: 0031-9007. DOI: [10.1103/PhysRevLett.94.180602](https://doi.org/10.1103/PhysRevLett.94.180602) (cit. on pp. [144](#), [150](#)).
- [422] L. L. Yan et al. “Single-Atom Demonstration of the Quantum Landauer Principle”. In: *Physical Review Letters* 120.21 (May 2018), p. 210601. ISSN: 0031-9007. DOI: [10.1103/PhysRevLett.120.210601](https://doi.org/10.1103/PhysRevLett.120.210601) (cit. on pp. [144](#), [150](#)).
- [423] J. V. Koski et al. “Distribution of entropy production in a single-electron box”. In: *Nature Physics* 9.10 (Oct. 2013), pp. 644–648. ISSN: 1745-2473. DOI: [10.1038/nphys2711](https://doi.org/10.1038/nphys2711) (cit. on pp. [144](#), [150](#)).

- [424] J. V. Koski et al. “Experimental realization of a Szilard engine with a single electron”. In: *Proceedings of the National Academy of Sciences* 111.38 (Sept. 2014), pp. 13786–13789. ISSN: 0027-8424. DOI: [10.1073/pnas.1406966111](https://doi.org/10.1073/pnas.1406966111). arXiv: [1402.5907](https://arxiv.org/abs/1402.5907) (cit. on pp. 144, 150).
- [425] M. Brunelli et al. “Experimental Determination of Irreversible Entropy Production in out-of-Equilibrium Mesoscopic Quantum Systems”. In: *Physical Review Letters* 121.16 (Oct. 2018), p. 160604. ISSN: 0031-9007. DOI: [10.1103/PhysRevLett.121.160604](https://doi.org/10.1103/PhysRevLett.121.160604) (cit. on p. 144).
- [426] N. Cottet et al. “Observing a quantum Maxwell demon at work”. In: *Proceedings of the National Academy of Sciences* 114.29 (2017), pp. 7561–7564. DOI: [10.1073/pnas.1704827114](https://doi.org/10.1073/pnas.1704827114). arXiv: [1702.05161](https://arxiv.org/abs/1702.05161) (cit. on p. 144).
- [427] S. Ciliberto. “Experiments in Stochastic Thermodynamics: Short History and Perspectives”. In: *Physical Review X* 7.2 (2017), pp. 16–21. DOI: [10.1103/physrevx.7.021051](https://doi.org/10.1103/physrevx.7.021051) (cit. on p. 144).
- [428] M. Marconi et al. “Far-from-Equilibrium Route to Superthermal Light in Bimodal Nanolasers”. In: *Physical Review X* 8.1 (Jan. 2018), p. 011013. ISSN: 2160-3308. DOI: [10.1103/PhysRevX.8.011013](https://doi.org/10.1103/PhysRevX.8.011013) (cit. on p. 144).
- [429] F. O. Wu, A. U. Hassan, and D. N. Christodoulides. “Thermodynamic theory of highly multimoded nonlinear optical systems”. In: *Nature Photonics* 13.11 (Nov. 2019), pp. 776–782. ISSN: 1749-4885. DOI: [10.1038/s41566-019-0501-8](https://doi.org/10.1038/s41566-019-0501-8) (cit. on p. 144).
- [430] J. P. Santos, G. T. Landi, and M. Paternostro. “Wigner Entropy Production Rate”. In: *Physical Review Letters* 118.22 (June 2017), p. 220601. ISSN: 0031-9007. DOI: [10.1103/PhysRevLett.118.220601](https://doi.org/10.1103/PhysRevLett.118.220601). arXiv: [1706.01145](https://arxiv.org/abs/1706.01145) (cit. on pp. 144, 145, 152).
- [431] S. Deffner. “Quantum entropy production in phase space”. In: *EPL (Europhysics Letters)* 103.3 (Aug. 2013), p. 30001. ISSN: 0295-5075. DOI: [10.1209/0295-5075/103/30001](https://doi.org/10.1209/0295-5075/103/30001). arXiv: [arXiv:1307.3183v2](https://arxiv.org/abs/1307.3183v2) (cit. on p. 144).
- [432] M. Campisi, P. Talkner, and P. Hänggi. “Fluctuation Theorem for Arbitrary Open Quantum Systems”. In: *Physical Review Letters* 102.21 (May 2009), p. 210401. ISSN: 0031-9007. DOI: [10.1103/PhysRevLett.102.210401](https://doi.org/10.1103/PhysRevLett.102.210401). arXiv: [0902.3879](https://arxiv.org/abs/0902.3879) (cit. on p. 144).
- [433] K. Funo and H. T. Quan. “Path Integral Approach to Quantum Thermodynamics”. In: *Physical Review Letters* 121.4 (July 2018), p. 040602. ISSN: 0031-9007. DOI: [10.1103/PhysRevLett.121.040602](https://doi.org/10.1103/PhysRevLett.121.040602). arXiv: [1708.05113](https://arxiv.org/abs/1708.05113) (cit. on p. 145).
- [434] C. Elouard et al. “The role of quantum measurement in stochastic thermodynamics”. In: *npj Quantum Information* 3.1 (Dec. 2017), p. 9. ISSN: 2056-6387. DOI: [10.1038/s41534-017-0008-4](https://doi.org/10.1038/s41534-017-0008-4). arXiv: [1607.02404](https://arxiv.org/abs/1607.02404) (cit. on pp. 145, 147).
- [435] G. P. Martins, N. K. Bernardes, and M. F. Santos. “Continuous monitoring of energy in quantum open systems”. In: *Physical Review A* 99.3 (Mar. 2019), p. 032124. ISSN: 2469-9926. DOI: [10.1103/PhysRevA.99.032124](https://doi.org/10.1103/PhysRevA.99.032124). arXiv: [1811.00819](https://arxiv.org/abs/1811.00819) (cit. on p. 145).
- [436] J. Wang, J. He, and Y. Ma. “Finite-time performance of a quantum heat engine with a squeezed thermal bath”. In: *Phys. Rev. E* 100.5 (Nov. 2019), p. 52126. DOI: [10.1103/PhysRevE.100.052126](https://doi.org/10.1103/PhysRevE.100.052126) (cit. on pp. 145, 152).
- [437] C. Elouard et al. “Probing quantum fluctuation theorems in engineered reservoirs”. In: *New Journal of Physics* 19.10 (Oct. 2017), p. 103011. ISSN: 1367-2630. DOI: [10.1088/1367-2630/aa7fa2](https://doi.org/10.1088/1367-2630/aa7fa2) (cit. on pp. 145, 152).

-
- [438] W. Niedenzu et al. “Quantum engine efficiency bound beyond the second law of thermodynamics”. In: *Nature Communications* 9.1 (Dec. 2018), p. 165. ISSN: 2041-1723. DOI: [10.1038/s41467-017-01991-6](https://doi.org/10.1038/s41467-017-01991-6). arXiv: [1703.02911](https://arxiv.org/abs/1703.02911) (cit. on pp. [145](#), [152](#)).
- [439] M. Kardar. *Statistical Physics of Particles*. Cambridge: Cambridge University Press, 2007. ISBN: 9780511815898. DOI: [10.1017/CB09780511815898](https://doi.org/10.1017/CB09780511815898) (cit. on p. [150](#)).
- [440] F. Liu and Z.-c. Ou-Yang. “Generalized integral fluctuation theorem for diffusion processes”. In: *Physical Review E* 79.6 (June 2009), p. 060107. ISSN: 1539-3755. DOI: [10.1103/PhysRevE.79.060107](https://doi.org/10.1103/PhysRevE.79.060107) (cit. on p. [150](#)).
- [441] A. Bérut et al. “Experimental verification of Landauer’s principle linking information and thermodynamics”. In: *Nature* 483.7388 (Mar. 2012), pp. 187–189. ISSN: 0028-0836. DOI: [10.1038/nature10872](https://doi.org/10.1038/nature10872) (cit. on p. [150](#)).
- [442] M. F. Yanik, S. Fan, and M. Soljačić. “High-contrast all-optical bistable switching in photonic crystal microcavities”. In: *Applied Physics Letters* 83.14 (Oct. 2003), pp. 2739–2741. ISSN: 0003-6951. DOI: [10.1063/1.1615835](https://doi.org/10.1063/1.1615835) (cit. on p. [152](#)).
- [443] T. Tanabe et al. “Fast bistable all-optical switch and memory on a silicon photonic crystal on-chip”. In: *Optics Letters* 30.19 (Oct. 2005), p. 2575. ISSN: 0146-9592. DOI: [10.1364/OL.30.002575](https://doi.org/10.1364/OL.30.002575) (cit. on p. [152](#)).
- [444] D. Dai, J. Bauters, and J. E. Bowers. “Passive technologies for future large-scale photonic integrated circuits on silicon: polarization handling, light non-reciprocity and loss reduction”. In: *Light: Science & Applications* 1.3 (Mar. 2012), e1–e1. ISSN: 2047-7538. DOI: [10.1038/lsa.2012.1](https://doi.org/10.1038/lsa.2012.1) (cit. on pp. [152](#), [155](#)).
- [445] Y. Shen et al. “Optical vortices 30 years on: OAM manipulation from topological charge to multiple singularities”. In: *Light: Science and Applications* 8.1 (2019). ISSN: 20477538. DOI: [10.1038/s41377-019-0194-2](https://doi.org/10.1038/s41377-019-0194-2) (cit. on p. [154](#)).
- [446] B. Bahari et al. “Nonreciprocal lasing in topological cavities of arbitrary geometries”. In: *Science* 358.6363 (Nov. 2017), pp. 636–640. ISSN: 0036-8075. DOI: [10.1126/science.aao4551](https://doi.org/10.1126/science.aao4551) (cit. on p. [154](#)).
- [447] M. A. Bandres et al. “Topological insulator laser: Experiments”. In: *Science* 359.6381 (Mar. 2018), eaar4005. ISSN: 0036-8075. DOI: [10.1126/science.aar4005](https://doi.org/10.1126/science.aar4005) (cit. on p. [154](#)).
- [448] P. Cristofolini et al. “Coupling Quantum Tunneling with Cavity Photons”. In: *Science* 336.6082 (May 2012), pp. 704–707. ISSN: 0036-8075. DOI: [10.1126/science.1219010](https://doi.org/10.1126/science.1219010) (cit. on p. [156](#)).
- [449] T. Kazimierczuk et al. “Giant Rydberg excitons in the copper oxide Cu₂O”. In: *Nature* 514.7522 (Oct. 2014), pp. 343–347. ISSN: 0028-0836. DOI: [10.1038/nature13832](https://doi.org/10.1038/nature13832) (cit. on p. [156](#)).
- [450] N. Jia et al. “A strongly interacting polaritonic quantum dot”. In: *Nature Physics* 14.6 (June 2018), pp. 550–554. ISSN: 1745-2473. DOI: [10.1038/s41567-018-0071-6](https://doi.org/10.1038/s41567-018-0071-6) (cit. on p. [156](#)).

Titre : Chiralité et dynamique non-linéaire dans les microcavité a polariton

Mots clés : Polaritons de cavité, Fluides quantiques, Non-linéarité, Microstructures, Spectroscopie optique

Résumé : Les microcavités en semiconducteurs, définies par une cavité Fabry Pérot planaire contenant un puits quantique, permettent de confiner fortement à la fois la lumière et les excitations électroniques. Dans ces hétérostructures, la lumière et la matière interagissent si fortement que les excitations fondamentales du système sont décrites par des quasi-particules hybrides lumière-matière appelées polaritons excitoniques. Les polaritons héritent les propriétés de leurs deux constituants élémentaires : la partie photonique peut être structurée spatialement en sculptant à l'échelle micrométrique l'indice de réfraction du matériau par lithographie et gravure ; la composante excitonique donne au système une très forte non-linéarité Kerr. Dans cette thèse, nous avons utilisé ces deux propriétés pour réaliser une ingénierie du mode photonique grâce à des micropiliers couplés, et sonder plusieurs facettes de leurs propriétés non-linéaires. Dans une première partie du travail, nous étudions des microcavités couplées disposées en anneau. Tirant profit d'un couplage spin-orbite synthétique et de la possibilité de polariser en spin le gain optique, nous avons démontré une émission laser dans des modes présentant un moment orbital angulaire (OAM) fini, dont la chiralité peut être contrôlée optiquement. De plus, nous mettons en évidence un comportement bistable original du microlaser, qui implique des modes présentant des valeurs différentes du OAM ainsi que des textures de polarisation différentes. Dans la deuxième partie de la thèse, nous explorons la dynamique non-linéaire du système sous pompage cohérent. Nous déclenchons une instabilité paramétrique dans des résonateurs couplés, et analysons en détails le mécanisme physique sous-jacent. Dans le régime instable, nous observons l'établissement d'oscillations paramétriques qui donnent lieu à des bandes latérales très brillantes et contrastées dans le spectre d'émission. Enfin dans la dernière partie du travail, nous étudions un régime de métastabilité optique dans un résonateur fortement non-linéaire. Ce régime se manifeste par l'apparition de sauts aléatoires entre deux valeurs du nombre moyen de photons dans le résonateur. Pour certaines conditions de pompage, nous observons un ralentissement critique de la dynamique métastable, signature d'une transition de phase dissipative. Par des expériences d'hystérésis dynamique, nous évaluons les exposants critiques de cette transition de phase. Finalement, nous proposons une correspondance ("mapping") entre la dynamique métastable d'un résonateur Kerr, et les renversements aléatoires dans le temps d'un bit logique. Nous pouvons alors définir et mesurer la production d'entropie lors d'une trajectoire unique d'une expérience d'hystérésis dynamique. Ces mesures nous ont permis de valider, dans le cadre de cette correspondance, le théorème intégral de fluctuations pour la production d'entropie hors équilibre. Ce travail couvre une grande variété de sujets, d'aspects les plus fondamentaux de la dynamique non linéaire dans un système photonique, à des idées innovantes pour réaliser des dispositifs photoniques, qui pourraient dans le futur être optimisés pour un fonctionnement à température ambiante.

Title : Chirality and nonlinear dynamics in polariton microresonators

Keywords : Cavity polaritons, Quantum fluids, Nonlinearity, Microstructures, Optical spectroscopy

Abstract : Semiconductor microresonators, defined by a planar Fabry-Perot cavity embedding a quantum well, allow tightly confining both optical and electronic excitations. In these heterostructures, light and matter interact so rapidly that the fundamental excitations of the system can be effectively described as hybrid light-matter quasiparticles, called exciton-polaritons. Polaritons inherit properties from both their elementary constituents: the photonic modes can be tailored by molding the refractive index landscape via dry etching processing, while the excitonic component endows the system with a large Kerr nonlinearity. In this thesis, we take advantage of these two key features to engineer the photon modes using coupled micropillar resonators, and probe diverse non-linear phenomena. In the first part of this work, we consider coupled microcavities arranged in a ring geometry. Harnessing an analogue spin-orbit coupling and the ability to spin-polarize the optical gain, we demonstrate lasing in modes carrying a net orbital angular momentum (OAM), with a chirality which can be optically controlled. In addition, we evidence a bistable behaviour of the microlaser, involving modes presenting distinct OAM values and polarization patterns. In the second part of the thesis, we concentrate on the nonlinear dynamics of the system under coherent pumping. We trigger a parametric instability in coupled nonlinear resonator, and investigate the underlying mechanism. In the unstable regime, we observe the onset of sustained parametric oscillations, which presence is revealed by the appearance of bright and contrasted sidebands in the emission spectrum. In the last part of the thesis, we investigate the optical metastability a highly nonlinear single micropillar cavity, which manifests in stochastic jumps of the cavity occupation between the two -otherwise stable-branches of the classical bistability. For specific driving conditions, we observe a critical slowing down of the metastable dynamics, which is associated to the onset of a dissipative phase transition. Using a scaling analysis involving dynamical hysteresis experiments, we retrieve the critical exponents of the phase transition. Finally, we propose a mapping of the metastable dynamics of a Kerr resonator onto a logical bit subject to random bit-flip events. We can define and measure the entropy production at a single trajectory level during dynamical hysteresis experiments. These measurements allow us validating an integral fluctuation theorem for the non-equilibrium entropy production. This work covers a variety of topics, from fundamental non-linear dynamics in a photonic system, to novel ideas for realizing optical devices, which could eventually operate at room temperature.